Atom–cavity interactions and gray molasses in a bow–tie resonator

Hodei Eneriz

université de BORDEAUX

THÈSE PRÉSENTÉE

POUR OBTENIR LE GRADE DE

DOCTEUR DE

L'UNIVERSITÉ DE BORDEAUX

ÉCOLE DOCTORALE SPI

LASERS, MATIÈRE, NANOSCIENCES

Par Hodei ENERIZ

INTERACTIONS ATOME-CAVITÉ ET MÉLASSE GRISE DANS UN RÉSONATEUR EN NŒUD PAPILLON

ATOM-CAVITY INTERACTIONS AND GRAY MOLASSES IN A BOW-TIE RESONATOR

Sous la direction de : Philippe BOUYER
Co-directeur : Andrea BERTOLDI

Soutenue le 17 janvier 2022

Membres du jury :

M. PISTOLESI, Fabio	Directeur de Recherche	LOMA	Président
Mme HUGBART, Mathilde	Chargée de Recherche	INPHYNI	Rapporteuse
M. CHICIREANU, Radu	Chargé de Recherche	PhLAM	Rapporteur
Mme PRUVOST, Laurence	Directrice de Recherche	LAC	Examinatrice
M. BOUYER, Philippe	Directeur de Recherche	LP2N	Directeur de thèse
M. BERTOLDI, Andrea	Ingénieur de Recherche	LP2N	Co-directeur de thèse

Titre : Interactions atome–cavité et mélasse grise dans un résonateur en nœud papillon

Résumé : Cette thèse s'intéresse à l'étude des interactions entre les atomes froids et la lumière laser à l'intérieur d'une cavité en nœud papillon. Des atomes ultrafroids de ^{87}Rb sont chargées au centre de la cavité en forme de croix à 1560 nm, où un piège dipolaire à hors résonance lointaine (FORT) est créé.

Le refroidissement d'un gaz atomique à des températures ultrafroides nécessite un processus en plusieurs étapes : piège magneto–optique (MOT); refroidissement sub—Doppler ; chargement dans un piège magnétique ou optique conservateur ; et souvent le refroidissement par évaporation. Les schémas de refroidissement sub–Doppler impliquant des états sombres sont devenus une technique puissante : ils sont connus sous le nom de mélasse grise.

Dans ce contexte, nous montrons que le refroidissement avec états sombres dans une condition Raman hyperfine à deux photons peut être utilisé en combinaison avec un FORT lorsque de forts décalages de lumière différentiels sont présents. De plus, nous utilisons cette technique pour refroidir l'ensemble atomique dans le FORT en désaccordant davantage les faisceaux Raman vers le rouge.

Dans une autre série d'expériences, nous exploitons le caractère doublement résonant de la cavité, à la fois à 1560 et 780 nm, pour explorer l'interaction entre les atomes et la cavité. Dans l'expérience, l'injection continue de lumière laser à 780 nm a été possible grâce à des améliorations sur le verrouillage en fréquence du laser 1560 nm sur la cavité, où les atomes ultrafroids chargés dans le FORT peuvent interagir de façon collective avec la lumière à 780 nm.

En utilisant des techniques à deux photons similaires à celles démontrées dans le scénario de la mélasse grise, nous injectons des impulsions Raman dans la cavité et observons des processus d'échange de photons inter–bras dans cavité induits par les atomes que nous caractérisons en analysant les distributions de quantité de mouvement produits sur les nuages atomiques ultrafroids.

Mots clés : Atomes froids en cavité optique, Piège dipolaire à résonance lointaine, Refroidissement par mélasses grises, Etats sombres, Transitions de Raman

Title : Atom–cavity interactions and gray molasses in a bow–tie resonator

Abstract : This thesis investigates the interactions between cold atoms and laser light inside a bow–tie cavity. Ultracold ^{87}Rb atoms are charged at the center of the cross–shaped cavity at 1560 nm, where a far off–resonant dipole trap (FORT) is created.

Cooling of an atomic gas to ultracold temperatures requires a multistage process: laser cooling in a magneto–optical trap (MOT); sub–Doppler cooling; loading into a conservative magnetic or optical trap; and often evaporative cooling. Sub–Doppler cooling schemes involving dark states have emerged as a powerful technique: they are known as gray molasses.

In this context, we show that dark state cooling in a hyperfine two–photon Raman condition can be used in combination with FORT when strong differential light shifts are present. Additionally, we utilize this technique to cool the atomic ensemble in the FORT by further detuning the Raman beams to the red.

In another set of experiments, we exploit the doubly resonant character of the cavity, both at 1560 and 780 nm, to explore the interaction between the atoms and the cavity. Experimentally, continuous 780 nm laser light injection has been obtained by improving the 1560 nm frequency lock to the cavity, where ultracold atoms loaded into the FORT can collectively interact with the 780 nm light.

By using similar two–photon techniques to the ones demonstrated in the gray molasses scenario, we inject Raman pulses into the cavity and observe atom–induced cavity inter–arm photon exchange processes which we characterize by analyzing the produced momentum distributions on the ultracold atomic clouds.

Keywords : Cold atoms in optical cavities, Far off–resonant dipole trap, Gray molasses cooling, Dark states, Raman transitions

Université de Bordeaux – Institut d'Optique d'Aquitaine, 1 Rue François Mitterrand - 33400 TALENCE.

&

CNRS – UMR 5298 – Laboratoire Photonique, Numérique et Nanosciences (LP2N)

à mon aita

Remerciements

Voilà venu le moment des remerciements. C'est un exercice difficile de remercier et de résumer en quelques lignes ces intenses dernières années, mais je vais m'efforcer de le faire au mieux.

Je remercie tout d'abord Mathilde Hugbart et Radu Chicireanu d'avoir accepté la lourde tâche d'être les rapporteurs de ce manuscrit. Merci ensuite à mes examinateurs Fabio Pistolesi et Laurence Pruvost qui tant au distanciel qu'au présentiel ont posé des questions très pertinentes.

Je vous remercie également Andrea Bertoldi et Philippe Bouyer pour la confiance que vous m'avez accordée en m'offrant ce travail de thèse. Ta lecture attentive du manuscrit Andrea, a permis d'introduire de grandes améliorations.

Devang Naik a joué un rôle très important dans mon apprentissage pendant ces années. Ta longue expérience en tant que postdoc et tes capacités pédagogiques ont eu une grande influence sur ma recherche. Je te souhaite un fantastique avenir que ce soit en France ou en Angleterre. En parlant de l'Angleterre, je dois ma reconnaissance également à Max Carey le marin, qui nous a rendu visite à deux reprises pendant quelques mois depuis Southampton au début de ma thèse. Même si tu venais plutôt en Eurostar qu'en bateau, je te souhaite une très bonne continuation en terres australiennes Max. Je ne peux pas finir ce paragraphe sans mentionner Grigor Kuyumjyan qui même sans overlap entre nous deux dans la manip, m'a donné de très bons conseils pour mon doctorat. Les anciens sont partis et les nouveaux sont arrivés: Geovan Santana de Figueiredo et Luisa Loranca ont pris en main leurs expériences respectives avec une très grande motivation, personne ne pourrait dire le contraire. Que la force soit avec vous pour la suite !

Dans notre groupe d'atomes froids j'ai également eu la chance de croiser beaucoup d'autres personnes. Romain Veyron avec qui j'ai pu manger et discuter pendant des centaines des repas au restau du CNRS; Grégoire Lefèvre, grâce à qui j'ai appris à danser la salsa et la bachata, je n'aurais jamais imaginé qu'un parisien allait m'enseigner la danse latine, merci à vous deux. Chen–Hao, Jean–Baptiste, Vincent, Guillaume, Adèle, Dylan, Joseph, Brynle, Xianhao–Zou, Celia, Martin, Romain, Vincent, Simon et Simon, je n'oublierai jamais les moments que l'on a partagés ensemble.

Ma famille m'a toujours appuyé de l'autre côté de la frontière. Cette frontière qui des fois semble être si proche mais qui en réalité est très lointaine tant en TER qu'en TGV. Un jour on aura un train direct Bordeaux-Donostia qui nous facilitera un peu la tâche. Maman, cela sera un peu plus compliqué de venir à Nice qu'à Bordeaux mais tu gagneras quelques degrés de température et la pluie sera moins abondante aussi tu verras bientôt. Merci d'être là.

Un événement majeur est venu perturber l'expérience début 2020. La COVID–19 a malheureusement beaucoup retardé notre progrès expérimental au labo, mais nous a donné aussi le temps de faire des activités différentes et de mener une vie en toute simplicité et tranquillité à la maison. Cela nous a permis de passer un peu plus de temps à la cuisine et de prendre le temps de préparer des omelettes aux pommes de terre et pas qu'aux pommes de terre. C'était le temps où l'on pouvait se concentrer sans être interrompues. Des centaines d'heures

et des jours pendant lesquels j'ai été très heureux à côté de toi Amandine, cette thèse est aussi le résultat de ton amour et de ta générosité.

Contents

Introduction

Interaction between light and matter is a fascinating subject of research, intriguing to physicist through most of the twentieth century. Key milestones in trying to explain observed phenomena include M. Planck's law of black–body radiation and A. Einstein's explanation of the photoelectric effect, which triggered the invention of quantum mechanics by W. Heisenberg and E. Schrödinger, among others. While the wave character of subatomic matter became clear at the time, the particle character of electromagnetic radiation was not completely ascertained until a few decades later [1], when phenomena such as light antibunching [2] and sub–Poissonian light [3] were observed.

Coupling atoms to cavity resonant light allows to explore light–matter interactions in a fundamentally different way as compared to free space. The modification of the rate of spontaneous emission of an atom by the environment was already pointed out by E. M. Purcell [4] in the mid 40s of the past century, an effect which was detected for Rydberg atoms in microwave cavities almost 40 years later [5]. The full potential of coupling atoms to cavities has been farther exploited with the advent of atom cooling techniques developed in the 80s and the 90s which allowed to produce Bose–Einstein condensates (BECs) [6, 7] in dilute gases. The many body quantum character of this phenomenon, which is often manifested in samples made of hundreds of thousands or even many millions of atoms [8, 9], forming a single macroscopic matter wave, has been more recently combined with optical cavities [10, 11], to study collective quantum effects [12, 13], and other phenomena on the border between classical and quantum physics [14].

As a first step, the work presented in this thesis focuses on ultracold ^{87}Rb atoms coupled to a bow–tie optical cavity. A large part of the work has been devoted to improving the mode matching and the frequency lock of the laser radiation to the cavity as well as its laser power

stabilization, which afforded us to implement novel atom cooling techniques based on gray molasses. These techniques help to increase the number of atoms loaded onto the intracavity far–off resonance dipole trap (FORT) [15], and facilitate the obtention of higher phase–space density (PSD) atomic clouds.

In another line of research, the improved electronics and optics has permitted to continuously inject 780 nm wavelength laser light into the bow–tie cavity, and make it interact with ultracold atoms loaded onto the dipole trap. These atoms, which have been previously cooled down farther after the gray molasses stage by using a FORT evaporation ramp, can interact strongly with the cavity light. The geometry of the cavity, which imposes a 90 degrees angle between simultaneous 780 light pulses, produces scattering events which are detected by absorption imaging of the ultracold atoms.

Thesis outline

In parallel to the two lines of research this thesis treats, one focused on gray molasses cooling and FORT loading of atoms, the other on atom–cavity interactions, the manuscript has also been organized to easily identify the results. These are presented in the two final chapters before the conclusion, while the previous four chapters are mostly devoted to theory and technical aspects of our experiment.

The theoretical framework and background needed to understand gray molasses cooling as well as other cooling techniques at use in the experiment are presented in Chapter 1. In Chapter 2 the experimental apparatus we use to apply these cooling techniques is presented, along with the description of a recently introduced imaging device. In Chapter 3 the high finesse bow–tie cavity is described, focusing on the utility of 780 and especially 1560 nm lights for the purpose of cold atom manipulation. Details about the electronics we use to frequency lock the radiation to the bow–tie cavity as well as to control other intracavity laser parameters are also explained therein. Chapter 4 is entirely devoted to atom–cavity interactions we are interested in studying utilizing the 780 nm resonance of the cavity, while the theoretical ground providing the framework for the most recent atom–cavity coupling results we found is also set there.

Finally, the results we got during my PhD work are divided between Chapter 5 which presents the ones already published [16], and Chapter 6 where we show more recent ones dealing with atom cavity interactions obtained during the last few months.

Chapter 1

Laser cooling techniques on the D_2 line of ^{87}Rb

The cooling of atomic gases to ultracold temperatures requires a multistage process: laser cooling in a magneto–optical trap (MOT); sub–Doppler cooling; loading into a conservative magnetic or optical trap; and finally, evaporative cooling, which is usually necessary to get phase–space densities (PSD) required by Bose–Einstein Condensates (BECs). The sub–Doppler cooling phase typically uses light red detuned from the $F \rightarrow F' + 1$ cycling transition of the D_2 line $nS_{1/2} \rightarrow nP_{3/2}$ for alkali atoms, and is explained in terms of polarization gradient cooling [17]. In this chapter we describe a powerful alternative involving dark states, which allow to cool down atoms inside and outside a dipole trap before initializing the evaporation process in our experiment. These dark states are coherent superpositions of internal and external states, decoupled from the optical field, whose creation does not require $F \rightarrow F' + 1$ cycling transitions but rather any transitions of the $F \rightarrow F' \leqslant F$ form obeying the angular momentum selection rules.

We shall describe in the first two introductory sections the basic theory behind the experimental techniques we use involving the force exerted by laser light and magnetic fields to slow the atomic motion. It will be in the third section where more sophisticated ones involving the combination of dark and bright states will be introduced.

1.1 Cooling by photon–scattering

In this section we detail the cooling techniques and apparatus used in our experiment to get cold atoms, presenting briefly the underlying physics principles. We start our description by a presentation of the fundamental mechanism that explains atom cooling above the Doppler limit and extend it to the case of counter–propagating laser beams which balance each other to constitute optical molasses.

It follows from conservation of momentum that when an atom approaching a monochromatic beam absorbs radiation, its momentum changes at a rate at which light delivers energy to the atom divided by the speed of light c. In the center of momentum frame for a single atom and an incident photon, the absorbed photon gives a kick in the direction opposite to the atom's motion, while photons emitted spontaneously can go in any direction. Therefore the average over many emission events has no effect on the momentum of the atom, in contrast to absorbed photons which always impart momentum on the same direction. The average imparted force is called the scattering force and equals,

$$F_{scatt} = \frac{\hbar\omega}{c} R_{scatt}, \tag{1.1}$$

where R_{scatt} is the scattering rate and ω the angular frequency of the scattered photons. This force depends not only on the beam intensity, but also on the detuning of photons from the frequency of the transition being addressed.

1.1.1 Semiclassical treatment of the interaction of a two–level atom with a laser

The scattering rate R_{scatt} can be derived quantum mechanically by using the optical Bloch equations [18], also called the Maxwell-Bloch equations. Before presenting them, we shall also show how an atom interacts coherently with monochromatic radiation when spontaneous emission is negligible, which allows quantum superpositions not to be destroyed. For an atom with only two energy levels E_1 and E_2, which are unperturbed eigenvalues of a Hamiltonian H_0, we consider a time dependent perturbation potential which represents the interaction of the atom with a laser in the dipole approximation. This approximation holds

when the spatial variation of the electric field $\boldsymbol{E}_0$ at the scale of the size of the atom is negligible, which is reasonable for wavelengths in the visible range. Then,

$$H = H_0 + V(t) = H_0 - q\boldsymbol{r}\cdot\boldsymbol{E}_0\cos(\omega t), \tag{1.2}$$

is the total Hamiltonian, q the charge of an electron, and $\boldsymbol{r}$ the position of the single electron with respect to the atom's center of mass. By moving into the interaction picture, defined by

$$|\Psi(\boldsymbol{r},t)\rangle_I \equiv e^{\frac{iH_0t}{\hbar}}|\Psi(\boldsymbol{r},t)\rangle, \tag{1.3}$$

where $|\Psi(\boldsymbol{r},t)\rangle = c_1(t)|1\rangle e^{-iE_1t/\hbar} + c_2(t)|2\rangle e^{-iE_2t/\hbar}$ is the wavefunction at time t in the Schrödinger picture, we can substitute $|\Psi(\boldsymbol{r},t)\rangle_I = c_1(t)|1\rangle + c_2(t)|2\rangle$ in $i\hbar\partial_t|\Psi(\boldsymbol{r},t)\rangle_I = V_I(t)|\Psi(\boldsymbol{r},t)\rangle_I$, with $V_I(t) = e^{\frac{iH_0t}{\hbar}}V(t)e^{\frac{-iH_0t}{\hbar}}$, to obtain the equations of motion

$$i\hbar\dot{c_m}(t) = \sum_n V_{mn}(t)e^{\frac{i(E_m-E_n)t}{\hbar}}c_n(t), \tag{1.4}$$

where $V_{mn}(t) = \langle m|V(t)|n\rangle = -q\langle m|\boldsymbol{r}\cdot\boldsymbol{E}_0\cos(\omega t)|n\rangle$.

Given that the electric dipole operator is an odd function of $\boldsymbol{r}$, only states with different parities are coupled by it. Therefore, diagonal elements in V_{mn} are zero and Eq. 1.4 leads to two coupled first order differential equations, namely,

$$i\dot{c_1}(t) = \Omega\cos(\omega t)e^{-i\omega_0t}c_2(t) = \frac{\Omega}{2}\left[e^{-i(\omega+\omega_0)t} + e^{i(\omega-\omega_0)t}\right]c_2(t), \tag{1.5a}$$

$$i\dot{c_2}(t) = \Omega^*\cos(\omega t)e^{i\omega_0t}c_1(t) = \frac{\Omega^*}{2}\left[e^{-i(\omega+\omega_0)t} + e^{i(\omega-\omega_0)t}\right]c_1(t), \tag{1.5b}$$

where $\omega_0 = \frac{E_2-E_1}{\hbar}$ and $\Omega = -\langle 1|q\boldsymbol{r}\cdot\boldsymbol{E}_0|2\rangle/\hbar$.

By calculating what the form of the induced electric dipole moment is on the atom, we intend to show how it responds to the applied field ignoring, for now, the effect of spontaneous emission. We consider radiation linearly polarized along the x-axis, and then the expectation value of the dipole moment's magnitude reads

$$\begin{aligned}\langle d(t)\rangle &= \langle\Psi(\boldsymbol{r},t)|qx|\Psi(\boldsymbol{r},t)\rangle,\\ &= q\left[c_2^*(t)c_1(t)X_{21}e^{i\omega_0t} + c_1^*(t)c_2(t)X_{12}e^{-i\omega_0t}\right],\end{aligned} \tag{1.6}$$

where q is the charge of the electron, and $X_{12} = (X_{21})^* = \langle 1|x|2\rangle$, while diagonal elements of the dipole operator vanish for systems with an inversion center as it is the case for atoms. The coherences $c_1^*(t)c_2(t)$ and $c_2^*(t)c_1(t)$, and the populations $|c_1(t)|^2$ and $|c_2(t)|^2$, form the

interaction picture density matrix at time t,

$$\rho_I(t) = |\Psi(t)\rangle_I \langle\Psi(t)|_I = \begin{pmatrix} |c_1(t)|^2 & c_2^*(t)c_1(t) \\ c_1^*(t)c_2(t) & |c_2(t)|^2 \end{pmatrix} = \begin{pmatrix} \rho_{11} & \rho_{12} \\ \rho_{21} & \rho_{22} \end{pmatrix}. \tag{1.7}$$

We can instead write the dipole moment in a rotating frame showing how the atom responds at frequency ω explicitly. By defining the detuning $\delta \equiv \omega - \omega_0$, we redefine the coherences $\tilde{\rho}_{12} = \rho_{12}e^{-i\delta t}$ and $\tilde{\rho}_{21} = \rho_{21}e^{i\delta t}$ so that

$$d_{rot}(t) = qX_{12}\left(\tilde{\rho}_{12}e^{i\omega t} + \tilde{\rho}_{21}e^{-i\omega t}\right) = X_{12}\left[u\cos(\omega t) - v\sin(\omega t)\right], \tag{1.8}$$

where $u = \tilde{\rho}_{21} + \tilde{\rho}_{12}$ and $v = i\left(\tilde{\rho}_{21} - \tilde{\rho}_{12}\right)$ are in–phase and quadrature with the laser components respectively. Moreover, we also define the population difference $w \equiv \rho_{11} - \rho_{22}$.

At this point, we make an approximation which consists in neglecting the complex exponential terms which have an exponent proportional to $\omega + \omega_0$ in Eqs. 1.5. This is known as the rotating wave approximation, and relies on the fact that when $|\delta|, \Omega \ll \omega_0$, then the faster oscillating terms do not affect the dynamics. Under this assumption, which implies Ω be real, Eqs. 1.5 can be rewritten as

$$\begin{aligned} \dot{u} &= \delta v, \\ \dot{v} &= -\delta u + \Omega w, \\ \dot{w} &= -\Omega v. \end{aligned} \tag{1.9}$$

This rewriting is useful, since u, v and w can be interpreted as components of a vector pointing at the surface of a sphere, called the Bloch sphere, on which any state of a two–level atom can be represented.

To make the model more realistic, we shall introduce a damping term that accounts for the effect of spontaneous emission, and then a steady state solution explaining the scattering force can be found. Because of $\rho_{11} + \rho_{22} = 1$, we have $\dot{\rho_{22}} = -\dot{\rho_{11}}$ and $\dot{w} = -2\dot{\rho_{22}}$, so that $\dot{\rho_{22}} = \Omega v/2$, which by considering a damping term Γ gets modified to give,

$$\dot{\rho_{22}} = \frac{\Omega}{2}v - \Gamma\rho_{22}. \tag{1.10}$$

This means that in the absence of the laser producing Ω, the population in the excited state will decay exponentially as $\rho_{22}(t) = \rho_{22}(0)e^{-\Gamma t}$.

How the two other expressions in Eq. 1.9 get affected by the damping can be understood

by looking at the equation of motion of a classical damped harmonic oscillator of natural frequency ω_0 driven by a oscillatory force $F\cos(\omega t)$,

$$\ddot{x} + \beta\dot{x} + \omega_0^2 x = \frac{F}{m}\cos(\omega t). \tag{1.11}$$

Here β is the damping constant and m the mass of the object subjected to the oscillation. By trying the solution

$$x = U(t)\cos(\omega t) - V(t)\sin(\omega t), \tag{1.12}$$

and equating terms depending on in-phase and quadrature components we get

$$\begin{aligned} \dot{U} &= (\omega - \omega_0)V - \frac{\beta}{2}U, \\ \dot{V} &= -(\omega - \omega_0)U - \frac{\beta}{2}V - \frac{F}{2m\omega}, \end{aligned} \tag{1.13}$$

where $\ddot{U}$ and $\ddot{V}$ have been neglected and $\dot{V} \ll \omega V$ considered. These are valid assumptions when the envelope produced by the damping varies slowly as compared to the period of the oscillator [19].

Now using results in Eqs. 1.10 and 1.13, and by comparison with the quantum Eq. 1.9 we write,

$$\begin{aligned} \dot{u} &= \delta v - \frac{\Gamma}{2}u, \\ \dot{v} &= -\delta u + \Omega w - \frac{\Gamma}{2}v, \\ \dot{w} &= -\Omega v - \Gamma(w - 1). \end{aligned} \tag{1.14}$$

These are the optical Bloch equations and describe the interaction of a two–level atom with radiation close to resonance and decaying by spontaneous emission.

We are interested in the steady-state solution of these equations because we want to calculate the average force the atom is subjected to. By setting $\dot{u} = \dot{v} = \dot{w} = 0$, and solving the system of three linear equations we get,

$$\begin{pmatrix} u \\ v \\ w \end{pmatrix} = \frac{1}{\delta^2 + \Omega^2/2 + \Gamma^2/4} \begin{pmatrix} \Omega\delta \\ \Omega\Gamma/2 \\ \delta^2 + \Gamma^2/4 \end{pmatrix}, \tag{1.15}$$

and,

$$\rho_{22} = \frac{1 - w}{2} = \frac{\Omega^2/4}{\delta^2 + \Omega^2/2 + \Gamma^2/4}. \tag{1.16}$$

Thus the scattering rate produced by the process of absorption followed by spontaneous emission for a two–level atom can be written as

$$R_{scatt} = \Gamma\rho_{22} = \frac{\Gamma}{2}\frac{\Omega^2/2}{\delta^2 + \Omega^2/2 + \Gamma^2/4}. \tag{1.17}$$

1.1.2 Saturation intensity and scattering force

We have seen above that the damping created by spontaneous emission makes the atom settle down to a steady state. But from absorption also comes stimulated emission, which in the case of a two–level atom is easily understood by looking at the exchange symmetry between the labels 1 and 2. This makes transitions from 2 to 1 be driven at the same rate as the reverse process.

Considering now N as the number of atoms per unit of volume, with N_1 in the ground state and N_2 in the excited one, energy conservation in the steady state requires absorption be offset by the stimulated emission process in the following way,

$$(N_1 - N_2)\sigma(\omega)I = N_2 A_{21}\hbar\omega, \tag{1.18}$$

where $\sigma(\omega)$ is the cross–section per atom, I the intensity of the laser and A_{21} the Einstein coefficient for spontaneous emission. The left–hand side of Eq. 1.18 is the rate of energy absorption per unit of volume, while on the right–hand side we find the scattered energy rate out of the laser beam which drives the process.

Now from Eq. 1.18 and using $N_1 + N_2 = N$, the population difference per unit of volume can be written as,

$$N_1 - N_2 = \frac{N}{1 + I/I_s(\omega)}, \tag{1.19}$$

where,

$$I_s(\omega) = \frac{A_{21}\hbar\omega}{2\sigma(\omega)}, \tag{1.20}$$

is the saturation intensity. We also have from $w = \rho_{11} - \rho_{22} = (N_1 - N_2)/N$ that,

$$N_1 - N_2 = N\frac{\delta^2 + \Gamma^2/4}{\delta^2 + \Omega^2/2 + \Gamma^2/4} = \frac{N}{1 + 2\Omega^2/(4\delta^2 + \Gamma^2)}, \tag{1.21}$$

which by substitution in Eq. 1.19 gives $I/I_s(\omega_0) = 2\Omega^2/\Gamma^2$ for a laser resonant with the

transition. Using this result and Eq. 1.17, the scattering force in Eq. 1.1 can be written as,

$$F_{scatt} = \frac{\hbar\omega}{c}\frac{\Gamma}{2}\frac{\Omega^2/2}{\delta^2 + \Omega^2/2 + \Gamma^2/4} = \frac{\hbar\omega}{c}\frac{\Gamma}{2}\frac{I/I_s^0}{1 + I/I_s^0 + 4\delta^2/\Gamma^2}, \tag{1.22}$$

where $I_s^0 \equiv I_s(\omega_0)$.

1.1.3 The optical molasses technique

To reduce the momentum spread of atoms along the three directions of space, one can arrange lasers along the three main axis. The optical molasses technique [20] relies on counter–propagating lasers that balance their forces for stationary atoms on all the three axes, whereas for moving atoms the Doppler effect produces an imbalance as we show bellow.

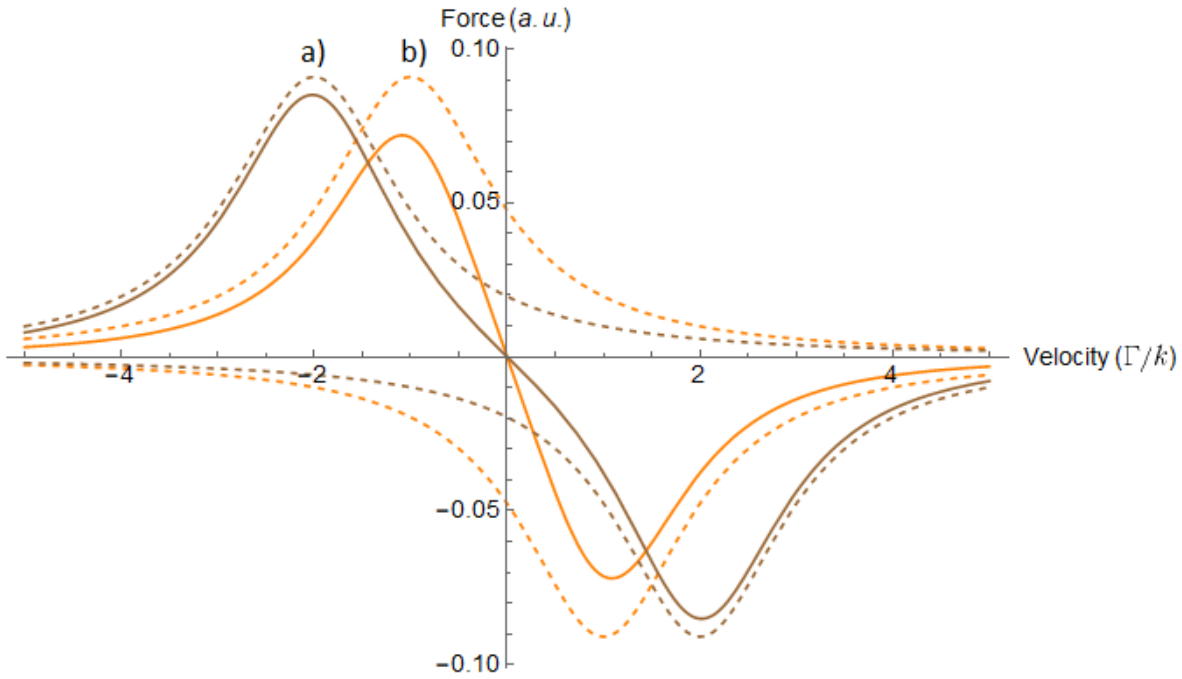

Figure 1.1: Force exerted by each of the counter-propagating lasers (dotted lines) and both together (solid lines) on a two–level atom as a function of velocity for $I/I_s^0 = 0.1$. In a) $\delta = -\Gamma$, while in b) $\delta = -\Gamma/2$.

In the following, when considering the frequency detuning $\delta = \omega - \omega_0$ from resonance, we shall take into account the Doppler frequency shift kv of an atom moving at a velocity of magnitude v on the axis parallel to two counter–propagating lasers. The total force produced

by lasers of equal frequency $\omega < \omega_0$, i.e. red–detuned, is then,

$$\begin{aligned} F_{mol} &= F_{scatt}(\omega_0 - \omega + kv) - F_{scatt}(\omega_0 - \omega - kv) \\ &= F_{scatt}(\delta - kv) - F_{scatt}(\delta + kv) \\ &= \frac{\hbar\omega}{c}\frac{\Gamma}{2}\left[\frac{I/I_s^0}{1 + I/I_s^0 + 4(\delta - kv)^2/\Gamma^2} - \frac{I/I_s^0}{1 + I/I_s^0 + 4(\delta + kv)^2/\Gamma^2}\right]. \end{aligned} \tag{1.23}$$

It is clear from Eq. 1.23, that the Doppler shift increases the scattering force against an atom propagating in the opposite direction of the momentum imparted by a beam. Although the scattering force is also present for an atom moving in the same direction as the momentum of either beam, the net force is less favorable for the one moving in the opposite direction as can be seen in Fig. 1.1, where the efficiency of the optical molasses cooling technique is apparent for a certain velocity capture window.

The cooling down of atoms by means of scattering force introduced in this subsection works well above a certain bound for temperature, limited by recoil kicks spontaneous emission produces in any direction. This effect is responsible for a velocity random walk, and sets a theoretical Doppler cooling limit which depends on the damping parameter Γ giving the linewidth of the two–level atom described in this section. As long as the laser linewidth is narrower than the linewidth Γ, which is not hard to achieve for cooling transitions in alkali atoms, the temperature limit is given by [21],

$$T_D = \frac{\hbar\Gamma}{2k_B}, \tag{1.24}$$

which is known as the Doppler limit. In the case of ^{87}Rb this is $\simeq 150\ \mu$K. However, temperature measurements using different methods showed in early experiments [22] that optical molasses are able to cool atoms down below the Doppler temperature limit. We present a particular example of this phenomenon in Sec. 1.3.

We shall introduce in the next section, a powerful technique which does not allow for sub–Doppler cooling, but which is of vital importance in order to trap a large number of atoms at the initial stage of the trapping and cooling procedure.

1.2 The magneto–optical trapping technique

By adding a quadrupole magnetic field with a linear gradient along the propagation direction of the lasers, a trapping character can be added to the cooling setup via the Zeeman effect. The technique is known as magneto–optical trapping (MOT)[23], and has been used extensively in our experiment beyond the usual first step for producing large clouds of cold atoms, to the point of being the only cooling technique at use to load atoms into the far off–resonant dipole trap (FORT) for a long time until my arrival in the experiment. This was due to the difficulty of turning off the MOT magnetic fields fast, since being the coils producing them attached to the bow–tie cavity support, the cavity mirrors do also suffer from large oscillations which would unlock the frequency lock of the 1560 nm laser to the cavity. The problem was solved at the beginning of my PhD thanks to the enhancements we implemented in the PDH electronics governing the lock (see Ann. B.).

Currently, MOT magnetic fields are extinguished in $\sim$2 ms once the initial 2DMOT, 3DMOT and compressed MOT (cMOT) stages are performed (see Sec. 5.1).

1.2.1 Principle of the MOT

The main advantage of the MOT with respect to the optical molasses technique we described in the previous section is that the MOT captures atoms as opposed to a pure optical molasses which only slows them down, thanks to a combination of damping and trapping produced by the Zeeman effect. This makes the MOT easy to load, and although it is not able to cool atoms down to temperatures as low as the optical molasses does, it creates much denser clouds of atoms containing larger numbers of them.

Mathematically, the MOT is explained by incorporating the Zeeman shifts caused by a quadrupole magnetic field into Eq. 1.23. Given that the Zeeman effect shifts opposite sign m_F sublevels in opposite directions, the polarization of the lasers in the MOT needs to be oppositely circular on each of the counterpropagating beams in order to obtain a configuration where the cooling beams address transitions involving $\Delta m_F = +1$ on one and $\Delta m_F = -1$ on the opposite side of the point where the magnetic field vanishes (see Fig. 1.2). We can then

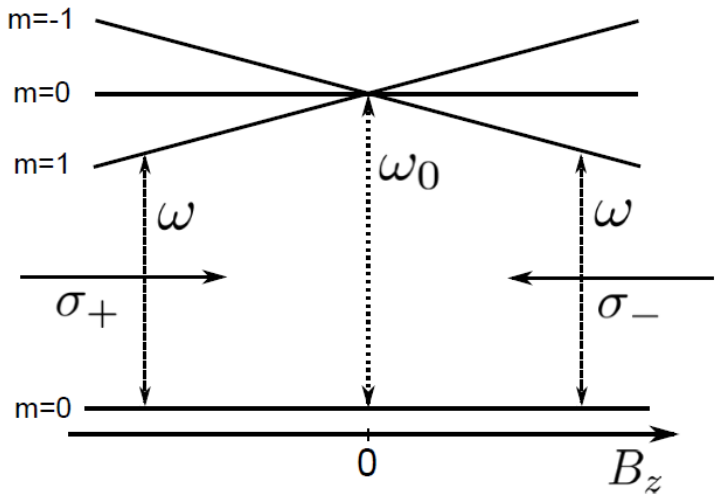

Figure 1.2: Zeeman splitting produced by a linear magnetic field along the quantization axis z, on the excited state $F = 1$ of bare energy $\hbar\omega_0$ greater than the ground state $F = 0$. Circular oppositely polarized pair of counterpropagating lasers of angular frequency ω are represented by horizontal arrows.

write the force along the z axis on which the counterpropagating lasers lay as,

$$F_{MOT} = F^{\sigma^+}_{scatt}(\omega_0 - \omega + kv + \alpha z) - F^{\sigma^-}_{scatt}(\omega_0 - \omega - kv - \alpha z), \tag{1.25}$$

where $\alpha = \frac{g\mu_B}{\hbar}\frac{dB}{dz}$, and g, μ_B, and z are the Landé g–factor, the Bohr magneton and the displacement parallel to the laser beam with origin on the point where $B = 0$, respectively. One can plot the force in Eq. 1.25 to get the same dependence as the one in Fig. 1.1, not only on velocity v, but now also on displacement z. Therefore, on top of the slowing force, in the MOT case there is also a position dependent restoring force which pushes cold atoms to the trap center.

In our experiment, we implement a 2D and a 3DMOT on ^{87}Rb atoms by using a slightly red–detuned laser on the $|5S_{1/2}, F = 2\rangle \rightarrow |5P_{3/2}, F' = 3\rangle$ transition of the D_2 line, where the prime symbol accounts for the final state. Quadrupolar magnetic fields created by coils in anti–Helmoltz configuration provide the needed linear dependence on the magnetic field along three orthogonal axes (see Sec. 2.1).

1.3 The gray molasses cooling technique

We mentioned in Subsec. 1.1.3 that experiments in the late 80s of the past century showed the optical molasses technique can cool down atoms below the Doppler limit. Now in this section, we present a particular example of this phenomenon which explains the sub–Doppler cooling mechanisms implemented in our experiment.

1.3.1 Coherent population trapping in a dark state

It was discovered in 1976 that an atom put in a superposition of quantum states can remain dark indefinitely thanks to the destructive interference produced by two lasers coupling two different ground state levels to a common upper level [24]. These three levels and their interaction with light can be treated in a similar way as we did for the case of the two–level atom in Subsec. 1.1.1. Known as Λ–type system (see Fig. 1.3), its Hamiltonian for two lasers

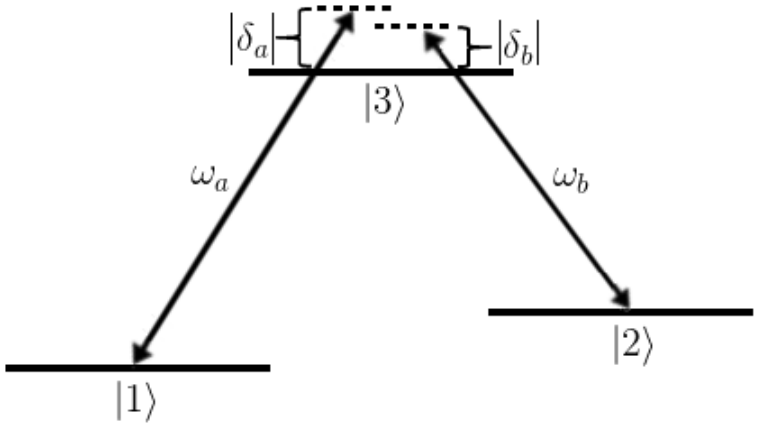

Figure 1.3: Λ–type system where $|1\rangle$ and $|2\rangle$ are non–degenerate. Lasers with frequencies ω_a and ω_b are tuned δ_a and δ_b off–resonance from $|1\rangle \longleftrightarrow |3\rangle$ and $|2\rangle \longleftrightarrow |3\rangle$ transitions, respectively.

with frequencies ω_a and ω_b linearly polarized along the x direction reads

$$H = H_0 + V(t) = \frac{H_0}{2} - \frac{qx}{2}\left(\epsilon_a e^{i\omega_a t} + \epsilon_b e^{i\omega_b t}\right) + H.c., \tag{1.26}$$

where ϵ_a and ϵ_b are the magnitudes of the electric fields for each of the lasers, and $H.c.$ stands for Hermitian conjugate. H_0 has now unperturbed eingenvalues $E_1 = \hbar\omega_1$, $E_2 = \hbar\omega_2$

and $E_3 = \hbar\omega_3$, so that the wavefunction

$$|\Psi(\boldsymbol{r},t)\rangle = c_1(t)|1\rangle e^{-iE_1t/\hbar} + c_2(t)|2\rangle e^{-iE_2t/\hbar} + c_3(t)|3\rangle e^{-iE_3t/\hbar}, \tag{1.27}$$

describes the state of the system in the Schrödinger picture again at time t. Using 1.4 as done previously for the two–level atom, and allowing only $|1\rangle \longleftrightarrow |3\rangle$ and $|2\rangle \longleftrightarrow |3\rangle$ dipole transitions, we get by using the rotating wave approximation the equations of motion

$$i\dot{c_1}(t) = \frac{\Omega_a^*}{2}e^{i\delta_a t}c_3(t), \tag{1.28a}$$

$$i\dot{c_2}(t) = \frac{\Omega_b^*}{2}e^{i\delta_b t}c_3(t), \tag{1.28b}$$

$$i\dot{c_3}(t) = \frac{\Omega_a}{2}e^{-i\delta_a t}c_1(t) + \frac{\Omega_b}{2}e^{-i\delta_b t}c_2(t), \tag{1.28c}$$

with $\Omega_a = -\langle 1|qx\epsilon_a|3\rangle/\hbar$, $\Omega_b = -\langle 2|qx\epsilon_b|3\rangle/\hbar$, $\delta_a = \omega_3 - \omega_1 - \omega_a$ and $\delta_b = \omega_3 - \omega_2 - \omega_b$ laser amplitudes and detunings.

The system of Eqs. 1.28 has an easy solution when $\delta_a = \delta_b \equiv \delta$. This can be seen by writing the linear combinations of amplitudes

$$r(t) = \frac{\Omega_b}{\Omega}c_1(t) - \frac{\Omega_a}{\Omega}c_2(t), \tag{1.29a}$$

$$s(t) = \frac{\Omega_a}{\Omega}c_1(t) + \frac{\Omega_b}{\Omega}c_2(t), \tag{1.29b}$$

with $\Omega = \sqrt{|\Omega_a|^2 + |\Omega_b|^2}$. Taking the time derivatives of both and using Eqs. 1.28a and 1.28b, we get

$$\dot{r}(t,\delta) = \frac{\Omega_b}{\Omega}\dot{c_1}(t,\delta) - \frac{\Omega_a}{\Omega}\dot{c_2}(t,\delta) = 0, \tag{1.30a}$$

$$\dot{s}(t,\delta) = \frac{\Omega_a}{\Omega}\dot{c_1}(t,\delta) + \frac{\Omega_b}{\Omega}\dot{c_2}(t,\delta) = -i\Omega e^{i\delta t}c_3(t,\delta), \tag{1.30b}$$

which means that the linear superposition of ground states $|D\rangle = (\Omega_b/\Omega)|1\rangle - (\Omega_a/\Omega)|2\rangle$ is entirely decoupled to the excited state by the lasers. This is called a dark state and is a perfect trap if one considers atoms at zero velocity, i.e. a state prepared initially on that superposition will remain there. If one additionally considers spontaneous emission from the excited state $|3\rangle$ to any of the ground states, large populations can be trapped in the dark steady–state $|D\rangle$ in a few lifetimes $1/\Gamma$, an effect known as coherent population trapping (CPT) [25].

This effect, however, does not produce any cooling by itself, and it was years later that its potential utility for reaching temperatures well below the Doppler limit was discovered [26]. It was found in particular, that the more fundamental temperature limit related to the recoil

associated to a single spontaneous emission process becomes relevant. This temperature is called the recoil limit [27] and is defined as,

$$T_r = \frac{\hbar^2 k^2}{k_B m}, \tag{1.31}$$

where k is the momentum of the spontaneously emitted photon, and m the mass of the atom.

1.3.1.1 Velocity–selective coherent population trapping

In Subsec. 1.1.3, we introduced two counter–propagating equal frequency lasers to explain how the optical molasses technique works. Now we consider the same situation but additionally, we quantize the motion of the two–level atom in order to explain how velocity–selective coherent population trapping (VSCPT) works. A quantum mechanical description of the atomic motion is required in this case since the reached momentum distributions can be arbitrarily narrow [28].

A velocity selection mechanism is apparent from the two–photon resonance condition $\delta_a = \delta_b \equiv \delta$ introduced in Subsec. 1.3.1. Indeed, in the case of counter–propagating lasers, opposite Doppler shifts will appear for an atom moving on the lasers' axes. If we consider, for simplicity, the two ground states of the atom are degenerate with momenta of magnitude $p \pm \hbar k$, where $\hbar k$ is the momentum of a single photon, and the counter–propagating lasers are oppositely circularly polarized, then for linear and angular momentum conservation to hold, each beam can couple only certain states (see Fig. 1.4). Neglecting spontaneous emission, the three states which we name $|1_+, p + \hbar k\rangle$, $|1_-, p - \hbar k\rangle$ and $|2, p\rangle$, form a closed family that can be labeled by p. In order to take the kinetic energy of the atom into account, we introduce now a new term in the free Hamiltonian H_0 of 1.3.1. Besides, on the time–dependent part we also introduce the phase dependence of each beam on the propagation direction as required by the more rigorous quantum treatment of the atomic motion. The total Hamiltonian then reads

$$H = H_0 + V(t) = \frac{\boldsymbol{p}^2}{2m} + V_0 - \boldsymbol{d} \cdot \boldsymbol{E}(z, t), \tag{1.32}$$

where m is the mass of the atom, and V_0 contains the unperturbed energy eigenvalues $E_{1\pm} = 0$

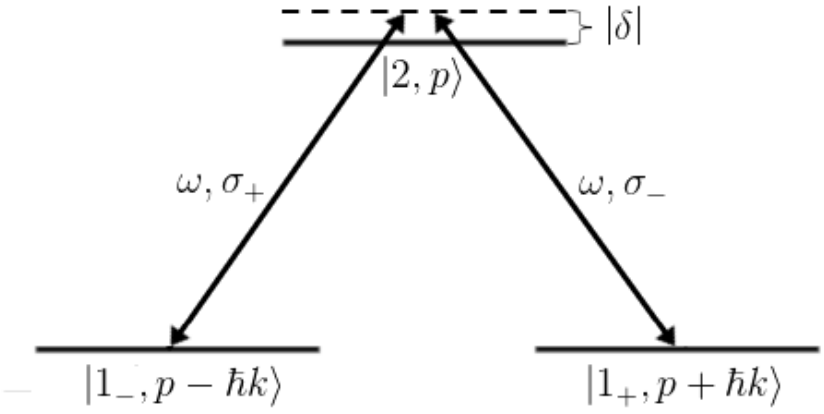

Figure 1.4: Λ–type system where $|1_+,p+\hbar k\rangle$ and $|1_-,p-\hbar k\rangle$ are degenerate, and can only couple to σ_- and σ_+ laser beams, respectively. Lasers with same frequency ω are tuned δ off–resonance from $|1_\pm,p\pm\hbar k\rangle \longleftrightarrow |2,p\rangle$. The excited state can emit to both by stimulated emission, and it completes the three states family, coupling to other different states not being possible as long as spontaneous emission is neglected.

and $E_2=\hbar\omega_0$. Finally, $\boldsymbol{d}$ is the electric dipole-moment operator, and

$$\boldsymbol{E}(z,t)=\left(\frac{\hat{\mathbf{x}}+i\hat{\mathbf{y}}}{2\sqrt{2}}\right)\epsilon_+e^{i(\omega t-kz)}+\left(\frac{\hat{\mathbf{x}}-i\hat{\mathbf{y}}}{2\sqrt{2}}\right)\epsilon_-e^{i(\omega t+kz)}+c.c., \tag{1.33}$$

with $\epsilon_\pm$ the magnitudes of the electric field corresponding to $\sigma_\pm$ polarized beams respectively.

As in 1.3.1, we have that only $|1_+,p+\hbar k\rangle \longleftrightarrow |2,p\rangle$ and $|1_-,p-\hbar k\rangle \longleftrightarrow |2,p\rangle$ dipole transitions are allowed, but now this assumption is reinforced by conservation of linear and angular momentum. On the other hand, the operator z only acts on the external degree of freedom of the atoms, and similarly to momentum being a generator of translations in position space, the inverse is also true, i.e.

$$e^{\pm ikz}=\sum_p e^{\pm ikz}|p\rangle\langle p|=\sum_p |p\pm\hbar k\rangle\langle p|. \tag{1.34}$$

In the rotating wave approximation, this transforms the potential $V(t)$ into the momentum–dependent basis as follows,

$$\begin{aligned} V(t) &= |2\rangle\langle 1_-|\frac{\hbar\Omega_+}{2}e^{i(kz-\omega t)}+|2\rangle\langle 1_+|\frac{\hbar\Omega_-}{2}e^{-i(kz+\omega t)}+H.c. \\ &= \sum_p \frac{\hbar}{2}|2,p\rangle\left(\langle 1_-,p-\hbar k|\Omega_+ + \langle 1_+,p+\hbar k|\Omega_-\right)e^{-i\omega t}+H.c., \end{aligned} \tag{1.35}$$

where $\Omega_\pm=-\epsilon_\pm\langle 1_\mp,p\mp\hbar k|\boldsymbol{d}\cdot(\hat{\mathbf{x}}\pm i\hat{\mathbf{y}})|2,p\rangle/\sqrt{2}\hbar$. Eq. 1.32 looks then very similar to Eq. 1.26

in spite of this more sophisticated basis, and we can also consider the corresponding dark and bright states [29]

$$|D,p\rangle = \frac{\Omega_-}{\Omega}|1_-,p-\hbar k\rangle - \frac{\Omega_+}{\Omega}|1_+,p+\hbar k\rangle, \tag{1.36a}$$

$$|B,p\rangle = \frac{\Omega_-^*}{\Omega}|1_-,p-\hbar k\rangle + \frac{\Omega_+^*}{\Omega}|1_+,p+\hbar k\rangle, \tag{1.36b}$$

where now $\Omega = \sqrt{\Omega_-^*\Omega_- + \Omega_+^*\Omega_+}$. Using Eq. 1.35 we find

$$\langle 2,p|V(t)|D,p\rangle = 0, \tag{1.37a}$$

$$\langle 2,p|V(t)|B,p\rangle = \frac{\hbar\Omega}{2}e^{-i\omega t}, \tag{1.37b}$$

which shows that the bright state in 1.36b is the only one coupled to the excited state directly by the lasers. One finds, however, a momentum dependent equation of motion

$$\frac{d}{dt}\langle D,p|\rho|D,p\rangle = \frac{-i2kp\Omega_+\Omega_-}{m\Omega^2}\langle D,p|\rho|B,p\rangle + c.c., \tag{1.38}$$

where ρ is the density operator describing the closed family of states with momentum p, and c.c. stands for complex conjugate. Eq. 1.38 means that an atom in a dark state $|D,p\rangle$ can be transferred into a bright state $|B,p\rangle$ when $p \neq 0$, an effect produced by the kinetic term in the free Hamiltonian H_0, and once in the bright state, it can also be transferred into the excited state $|2,p\rangle$.

A dark state will be a stationary state of the total Hamiltonian in Eq. 1.32 only when both degenerate ground states have equal kinetic energies $(\hbar k)^2/(2m)$, something that occurs when both superposition components have opposite momenta $\pm\hbar k$. Thus coherent population trapping is indeed velocity-selective, p/m being the velocity of the excited state, and where trapped atoms are those for which $p = 0$.

This treatment finally explains the role of polarization in the vicinity of atoms in the creation of dark sates. A pair of counter–propagating circularly polarized beams with opposite polarizations produces a linearly polarized total field along the propagation axis. This is easily seen from Eq. 1.33, by making both circular polarization beam intensities $\epsilon_+ = \epsilon_- \equiv \epsilon$. The electric field produced by the two counter–propagating lasers then reads,

$$\begin{aligned} \boldsymbol{E}(z,t) &= \frac{\epsilon}{\sqrt{2}}\left[\hat{\mathbf{x}}\cos(\omega t+kz) + \hat{\mathbf{y}}\sin(\omega t+kz) + \hat{\mathbf{x}}\cos(\omega t-kz) - \hat{\mathbf{y}}\sin(\omega t-kz)\right], \\ &= \sqrt{2}\epsilon\left[\hat{\mathbf{x}}\cos kz + \hat{\mathbf{y}}\sin kz\right]\cos\omega t, \end{aligned} \tag{1.39}$$

which forms a polarization gradient field with linear polarization at every point along z although this rotates uniformly through π as z changes by half a wavelength. On the other hand, Eq.1.37a shows that the dipole moment $\langle 2,p|\boldsymbol{d}|D,p\rangle$ is perpendicular to the electric field for all z, which means that for the completely delocalized dark state $|D,p\rangle$ the dipole moment will also form an helix moving at velocity p/m, but orthogonally polarized with respect to the electric field $\boldsymbol{E}(z,t)$. It will remain indefinitely orthogonal only if $|D,p=0\rangle = |1_-,-\hbar k\rangle/\sqrt{2} - e^{i\phi}|1_+,\hbar k\rangle/\sqrt{2}$, while for $p \neq 0$ the associated slowly drifting de Broglie wave will be destroyed.

VSCPT looks very promising for reaching extremely low temperatures, but it suffers from a main problem [28]: the random character of spontaneous emission makes part of the atoms diffuse towards high momentum values where the Doppler detuning prevents them from being in the two–photon resonance condition $\delta_a = \delta_b \equiv \delta$ and thus will no longer have a chance of being trapped into dark states. Therefore, only a small fraction of the atoms ends up being stopped to velocities on the order of the recoil limit. A solution to this problem was found by introducing a mechanism that adds a damping force into the system which increases the cooling efficiency of the VSCPT mechanism [30, 31].

1.3.2 Gray molasses cooling: combining dark and bright states

Gray molasses cooling is a technique that combines the VSCPT effect, with another sub–Doppler cooling mechanism known as polarization gradient cooling [17]. This mechanism explains sub–Doppler cooling by taking into account the additional complexity multilevel atoms posses as compared to the two–level atom studied in Subsec. 1.1.1. One needs to consider, in particular, the Zeeman structure of alkali atoms and how linearly and circularly polarized laser light interacts with it as we did in Subsec. 1.2 for the MOT case. In polarization gradient cooling, however, no external magnetic field is considered, while the laser polarization plays a more subtle role.

Nonetheless, a clarifying picture of the gray molasses cooling mechanism can be obtained by considering the non–adiabatic passage of three–level atoms from one of the ground states to the other while moving parallel to a standing wave, without the need of taking into ac-

count any Zeeman structure. In its general description, non–adiabatic passage explains the transformation from the initial quantum state to a linear combination of states of a light shifted Hamiltonian, which sum to adapt to the initial probability density. In the case of atoms passing through a polarization gradient, this happens as the atoms' response to the change of polarization at low intensity lags behind the adiabatic one sufficiently slow atoms have. Mathematically, it is a weak coupling regime to the lasers which allows to adiabatically eliminate the excited state and derive an effective Hamiltonian [32] where the effect of the coupling to that state is taken into account by adding energy shifts and couplings.

A relevant example for us on which we can apply adiabatic elimination is the three–level Λ–type system we studied in Subsec. 1.3.1. We consider thus the wave function in Eq. 1.27 and we transform it to a rotating frame defined by

$$|\Psi(\boldsymbol{r},t)\rangle \longrightarrow |\Psi(\boldsymbol{r},t)\rangle_{\Lambda} \equiv e^{\frac{i\Lambda t}{\hbar}}|\Psi(\boldsymbol{r},t)\rangle, \tag{1.40}$$

where [33],

$$\Lambda = \frac{1}{2}\begin{pmatrix} \delta_0 & 0 & 0 \\ 0 & 2\omega_a - 2\omega_b - \delta_0 & 0 \\ 0 & 0 & \omega_a - 2\Delta \end{pmatrix}, \tag{1.41}$$

with $\delta_0 \equiv \delta_a - \delta_b$ and $\Delta \equiv (\delta_a + \delta_b)/2$. This transformation now makes the Schrödinger picture Hamiltonian in Eq. 1.26 take the form

$$H_{\Lambda} = \frac{\hbar}{2}\begin{pmatrix} -\delta_0 & 0 & \Omega_a^* \\ 0 & \delta_0 & \Omega_b^* \\ \Omega_a & \Omega_b & 2\Delta \end{pmatrix}. \tag{1.42}$$

The separation between the ground states is thus given by an energy difference $\hbar\delta_0$, while the excited state lays $\hbar\Delta$ above from midway between the ground states. The corresponding system of differential equations can be then written as

$$i\dot{\alpha}(t) = -\frac{\delta_0}{2}\alpha(t) + \frac{\Omega_a^*}{2}\gamma(t), \tag{1.43a}$$

$$i\dot{\beta}(t) = \frac{\delta_0}{2}\beta(t) + \frac{\Omega_b^*}{2}\gamma(t), \tag{1.43b}$$

$$i\dot{\gamma}(t) = \frac{\Omega_a}{2}\alpha(t) + \frac{\Omega_b}{2}\beta(t) + \Delta\gamma(t). \tag{1.43c}$$

At this point, we make the weak coupling assumption $|\Omega_a|, |\Omega_b| \ll |\Delta|$, as well as $|\delta_0| \ll |\Delta|$

which implies the excited state lays very far away in energy compared to the energy separation between ground states. Under these assumptions, if the system is initially prepared at $|\Psi(\boldsymbol{r},0)\rangle = \alpha_0|1\rangle + \beta_0|2\rangle$, the excited state will not be populated and can be eliminated from the problem by taking $\dot{\gamma} = 0$. From Eq. 1.43c then,

$$\gamma(t) = -\frac{\Omega_a}{2\Delta}\alpha(t) - \frac{\Omega_b}{2\Delta}\beta(t), \tag{1.44}$$

and thus the system gets reduced to

$$i\dot{\alpha}(t) = -\left(\frac{\delta_0}{2} + \frac{|\Omega_a|^2}{4\Delta}\right)\alpha(t) - \frac{\Omega_a^*\Omega_b}{4\Delta}\beta(t), \tag{1.45a}$$

$$i\dot{\beta}(t) = \left(\frac{\delta_0}{2} - \frac{|\Omega_b|^2}{4\Delta}\right)\beta(t) - \frac{\Omega_b^*\Omega_a}{4\Delta}\alpha(t). \tag{1.45b}$$

Equivalently, an effective two–level Hamiltonian,

$$H_{eff} = -\hbar\begin{pmatrix} \frac{\delta_0}{2} + \frac{|\Omega_a|^2}{4\Delta} & \frac{\Omega_a^*\Omega_b}{4\Delta} \\ \frac{\Omega_b^*\Omega_a}{4\Delta} & -\frac{\delta_0}{2} + \frac{|\Omega_b|^2}{4\Delta} \end{pmatrix}, \tag{1.46}$$

describing two–photon transitions between the ground states can be written. The effective Hamiltonian in Eq. 1.46 introduces shifts proportional to the intensities of the laser fields. In the limit $\omega_2 \longrightarrow \omega_1$ and $\omega_b \longrightarrow \omega_a$, its eigenvalues for equal amplitude lasers $|\Omega_b| = |\Omega_a| \equiv |\Omega_0|$ are $\lambda_D = 0$ and $\lambda_B = -\hbar|\Omega_0|^2/(2\Delta)$, where subindexes D and B stand for dark and bright states again, respectively. When $\omega_a = \omega_b > \omega_3 - \omega_{1,2}$, then $\Delta < 0$, and thus the energy of the bright state lies above that of the dark's one for blue–detuned lasers from the ground to the excited state transitions.

So far in this subsection, we have neglected for both lasers the effect of polarization on the Λ–system. If we consider counter–propagating equal frequency and amplitude lasers which are linearly polarized enclosing a given angle between the directions of the polarization, generally a polarization gradient will form. If both lasers are identically polarized along the x direction however, a standing wave will form along the propagation direction z, with the electric field taking the form,

$$\boldsymbol{E}(z,t) = \hat{\mathbf{x}}\epsilon\left[\cos(\omega t - kz) + \cos(\omega t + kz)\right] = 2\hat{\mathbf{x}}\epsilon\cos(kz)\cos(\omega t), \tag{1.47}$$

where ϵ is the amplitude of the electric field.

One can define a space dependent amplitude $\Omega_{sw}(z) = \sqrt{2}\Omega_0\cos(kz)$, and the light shifted

bright state's energy will be modulated along the propagation direction z as follows,

$$E_B(z) = -\hbar\frac{|\Omega_{sw}(z)|^2}{2\Delta} = -\hbar\left[1+\cos\left(2kz\right)\right]\frac{|\Omega_0|^2}{2\Delta}, \tag{1.48}$$

i.e. with a period of one half the wavelength λ of the laser radiation (see Fig. 1.5).

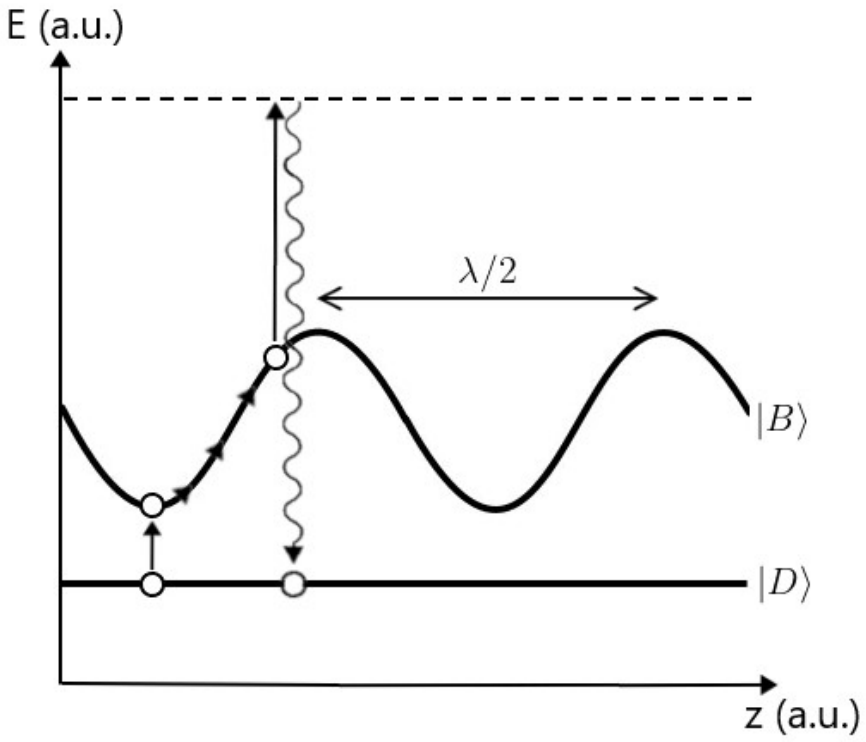

Figure 1.5: Energy shifts induced by the standing wave in Eq. 1.47 on the dark and bright states. Population is transferred from the former to the latter via non–adiabatic passage, which primarily occurs on the valleys of Eq. 1.48. By climbing the hill, kinetic energy is converted to potential energy, while dissipation happens through spontaneously emitted photons which are more energetic than absorbed ones for atoms moving at right velocities.

Therefore, atoms moving at velocities on the order of $\lambda\Gamma'/4$, where Γ' is the mean scattering rate along the low intensity standing wave ($|\Omega_0| \ll |\Delta|$), are most probably subjected to a cycle connecting a bright state at the top of the potential hill with a dark one which is at lower energy and thus makes the atoms lose energy. The transfer from dark to bright states in turn is more probable when the energies of the latter ones are on the valleys of Eq. 1.48. The probability takes the form [31],

$$P_{DB}(z) \propto \frac{\hbar^2k^2v^2\sin^2\phi}{E_B^2\left[1+\cos\left(2kz\right)\cos\phi\right]^2}, \tag{1.49}$$

where $v \ll \Gamma/k$, with Γ the linewidth of the transition, is the velocity at which the atoms move, and ϕ the angle linear polarizations are enclosing.

With long optical pumping times $\tau_p = 1/\Gamma' \gg 1/\Gamma$ that takes for an atom to be transferred from one ground Zeeman substate to another, atoms with much smaller velocities than the Doppler–limited one can be achieved by reducing the laser power, for which in principle there is no fundamental limit. While VSCPT produces coherences between Zeeman sublevels, we have seen that they not only show population imbalances, but that they are also subjected to different light–shifts as the atoms move along polarization gradients, inducing changes on the atoms' internal equilibrium states and producing friction. This process allows to accumulate a large fraction of the atoms in dark states, and thus to narrow the total momentum spread.

Gray molasses cooling proved to be useful in cooling down different alkali atoms such as cesium [34] or rubidium [35] and also helium [36] already in the mid 90s. More recently it has attracted a renewed interest for cooling lighter alkali species such as lithium, sodium and potassium as we shall show in the next Subsec. 1.3.3.

1.3.3 Gray molasses cooling in a hyperfine Λ–scheme

The complexity of the hyperfine structure of real alkali atoms with respect to the ideal Λ–type system presented in Subsec. 1.3.2 cannot be underestimated. This complexity comes from the Zeeman sublevels of hyperfine states which prevent the system be straightforwardly modeled as a three–level system. If one considers for simplicity state $|2\rangle$ in Fig. 1.3 is composed of a degenerate doublet, then radiation of frequency ω_b coupling them to state $|3\rangle$ can accumulate atoms in a Λ–type CPT state between levels 2 and 3. In other words, state $|2\rangle$ possesses inner coherence between its degenerate sublevels, an effect that makes the analysis of gray molasses in real multi–Zeeman–sublevel atoms extraordinarily complex.

The first experiments using gray molasses were based on the creation of Zeeman dark states (ZDSs) that use counter–propagating oppositely polarized light and blue–detuned lasers [37] so that the bright states, due to their positive light shift (see Subsec. 1.3.2), have energy always higher than the unshifted dark states. The commonly used $F = 2 \rightarrow F' = 2$ atomic transition, for example, can lead to inverted–W type dark states, i.e. linear superposi-

tions of $F = 2$ Zeeman sublevels with different momenta of the form [38],

$$|\text{ZDS}, p\rangle = \frac{1}{\sqrt{3}} \left[|(2,-2), p - 2\hbar k\rangle - |(2,0), p\rangle + |(2,2), p + 2\hbar k\rangle \right], \tag{1.50}$$

where $(2, m_F)$ denotes Zeeman sublevels in $F = 2$.

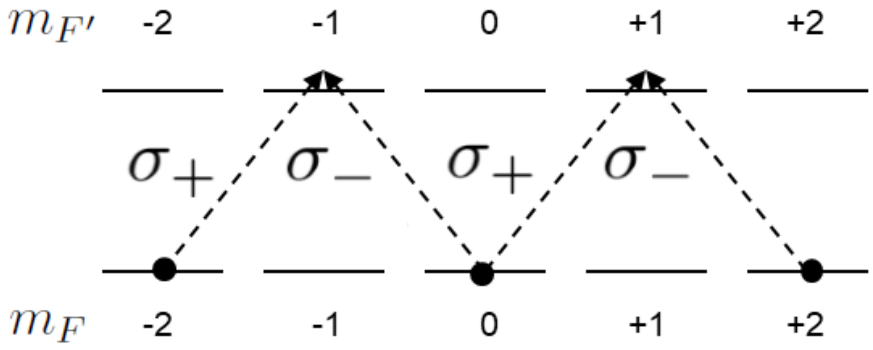

Figure 1.6: Inverted–W type ZDS, where non–primed and primed sub–indices correspond to ground and excited states respectively.

Given that ZDSs are not eigenstates of the momentum operator, dephasing will occur on a timescale on the order of the one associated to the inverse of the kinetic energy. Even for atoms at $p = 0$, the associated dephasing timescale will be $m/(2\hbar k^2) \simeq 10\,\mu$s and thus free evolution will turn ZDSs into bright fast compared to atom cooling timescales.

Furthermore, the presence of a repumper laser, essential to counter off–resonant optical pumping into the $F = 1$ hyperfine manifold and keep atoms resonant with the $F = 2 \rightarrow F' = 2$ transition, spoils these ZDSs, limiting the cooling efficacy of the process. That is why in our experiment, in order to avoid this detrimental effect as well as to explore the generation of other kinds of dark states, we introduced an hyperfine gray molasses scheme based on a repumper in the Raman condition with the cooler laser. This condition involves the simultaneous absorption and emission of two photons by an atom [39], with the energy difference given by the hyperfine splitting of the ground state. Consequently, both energy and momentum are interchanged with the atoms, and given that this occurs via single scattering events, photons not only need to share a fixed frequency difference but also a fixed relative phase, which requires phase coherence between the two involved beams.

In terms of what we presented in the Λ–type system in Subsec. 1.3.1, our scheme relies

on making the difference between frequencies ω_a and ω_b close to the one separating the two hyperfine states in the ground $nS_{1/2}$ manifold of alkali atoms [40, 41]. The approach described below allows to address the corresponding two transitions with the same detuning ($\delta_a = \delta_b \equiv \delta$) from the common excited level. Moreover, in our case, we had to adapt the scheme to cool atoms in the presence of the FORT, in order to load it and even cool the atoms loaded onto such trap (see Sec. 5.3).

In the context of atom cooling, the hyperfine Λ–scheme was first envisaged for sub–Doppler cooling of fermionic ^{40}K [42] by using blue–detuned lasers with respect to its D_1 line as an alternative to cooling on the D_2 line, since the narrow hyperfine structure of $4P_{3/2}$ with respect to the natural linewidth makes sub–Doppler cooling problematic on its closed transition. Lithium also suffers from the same problem, with the hyperfine splitting of $2P_{3/2}$ being even narrower. In this case it was bosonic ^{7}Li the species on which the hyperfine Λ–scheme was first applied on the D_1 line, achieving equal success [43]. More recently, it has also been applied on the D_1 line of ^{23}Na [44].

A distinctive feature of the hyperfine Λ–scheme with respect to the standard red–detuned sub–Doppler cooling is that the transition addressed by the cooler does not satisfy the condition $F \rightarrow F' + 1$ as imposed by the cycling transition, but rather verifies $F \rightarrow F' \leqslant F$ due to the fact that selection rules imposed on the repumper do not allow this to address a transition corresponding to the higher excited state the cooler usually addresses. This enables sub–Doppler cooling via hyperfine dark states (HDSs), states which are superpositions of Zeeman sublevels belonging to distinct hyperfine manifolds, and which are the ones we exploit to load the FORT in the presence of large excited state light shifts produced in our apparatus (see Subsec. 5.3.1).

We focus next on the specific case of hyperfine Λ–type cooling of ^{87}Rb atoms, since this is the species we use in our experiment.

1.3.3.1 Hyperfine Λ–scheme gray molasses cooling in ^{87}Rb

All the three previously mentioned realizations of hyperfine gray molasses cooling were realized on the D_1 line of ^{7}Li, ^{23}Na and ^{40}K. This was not the case for ^{87}Rb [45], which possesses a large hyperfine $5P_{3/2}$ separation and thus allows to address the

$|5S_{1/2}, F = 1, 2\rangle \rightarrow |5P_{3/2}, F' = 2\rangle$ transitions without causing too much transfer to other hyperfine manifolds. A great advantage of this feature in rubidium is that the same laser can be used for both standard red–detuned and gray molasses cooling, with no need of an additional laser source at 795 nm as it would be required to address the D_1 line of ^{87}Rb. Moreover, the repumper needed for standard red–detuned cooling can be most conveniently substituted when operating in gray molasses cooling mode, since the repumper needed for the former is typically operated on resonance to the $|5S_{1/2}, F = 1\rangle \rightarrow |5P_{3/2}, F' = 2\rangle$ transition, while the latter critically needs to be on the blue side of the transition (see Subsec. 1.3.2) as the cooler does.

By phase–modulating the cooler beam with an EOM at the hyperfine splitting frequency $\delta_{hf}^{^{87}Rb} = 2\pi \times 6.83468$ GHz, a rempumping sideband can be created at the Raman condition. Mathematically, the magnitude of the output field produced by the EOM can be expressed as,

$$E_{out}(t) = E_c e^{i[\omega_c t + \beta \sin(\omega_m t)]} = E_c e^{i\omega_c t} \sum_{m=-\infty}^{\infty} J_m(\beta) e^{i\omega_m t}, \tag{1.51}$$

where E_c and ω_c are respectively the amplitude and the frequency of the incident cooler laser field, $\omega_m \simeq \delta_{hf}^{^{87}Rb}$ is the modulation frequency at which the EOM is driven with β modulation amplitude, and $J_m(\beta)$ are Bessel functions of the first kind.

Here, we are interested in the weak modulation limit $\beta \ll 1$ where the output field can be approximated by

$$E_{out}(t) \approx E_c \left[J_0(\beta) e^{i\omega_c t} + J_1(\beta) e^{i(\omega_c + \omega_m)t} + J_{-1}(\beta) e^{i(\omega_c - \omega_m)t} \right]. \tag{1.52}$$

The field coming out from the EOM then provides us not only with a higher frequency repumping sideband, but also with an additional lower frequency sideband which does not play a relevant role since its frequency is almost 7 GHz red–detuned from the cooler transition and will thus not produce any detrimental effect on the atoms.

In practice, the modulation signal is created by an Anritsu 68017C frequency synthesizer, which allows to select both the frequency and the amplitude of the radio frequency (RF) signal. Both modulation amplitude and frequency were optimized by looking at the loading efficiency into the dipole FORT produced at 1560 nm wavelength. This process, along with the previous cooling stages, is described in detail in Sec. 5.1. The optical table containing the EOM for the phase modulation at the hyperfine splitting frequency in turn, is described in

the following Chapter 2, where the laser setup producing the previous cooling stages is also described.

Chapter 2

780 nm optical table and side imaging system

Since the conception of the experiment, all the optical components producing 780 nm light have been positioned on a single breadboard, where small enhancements or simple substitution of aging components such as lasers, have been implemented. During my PhD however, we had to introduce a few important changes among which the free–space EOM producing the repumping sideband for the gray molasses stands out.

The 780 nm laser frequencies created on the breadboard table need to be transmitted to a different table which using fibers where the vacuum chambers and the bow–tie cavity under ultra–high vacuum (UHV) are installed. The atoms are loaded at the center of the cavity and imaged from above via a high–resolution imaging system which was set up on the axis orthogonal to the plane where the four cavity mirrors are positioned. The cold atoms are detected through absorption imaging both on this system as well as using an additional one on a side of the vacuum chamber where a new telescope and a camera have been introduced. We describe this new setup in detail in the final section of this chapter. In the previous two sections, we shall describe the technique and the components producing the laser and magnetic fields we use to cool down the atoms.

2.1 Retroreflected 3DMOT setup and Raman repumper

Although the $|5S_{1/2}, F = 2\rangle \rightarrow |5P_{3/2}, F' = 3\rangle$ cooler transition of the D_2 line is closed, i.e. the electric dipole selection rule $\Delta F = 0, \pm 1$ prevents atoms from falling to $|5S_{1/2}, F = 1\rangle$, in practice, there is some off–resonant $|5S_{1/2}, F = 2\rangle \rightarrow |5P_{3/2}, F' = 2\rangle$ open transition occurring. Therefore, there is some possibility for ^{87}Rb atoms to decay spontaneously to $|5S_{1/2}, F = 1\rangle$, which is a dark state with respect to cooler light. In order to repopulate the $|5S_{1/2}, F = 2\rangle$ state an additional repumper laser resonant on the $|5S_{1/2}, F = 1\rangle \rightarrow |5P_{3/2}, F' = 2\rangle$ open transition is used, which sends atoms back to the cooling cycle.

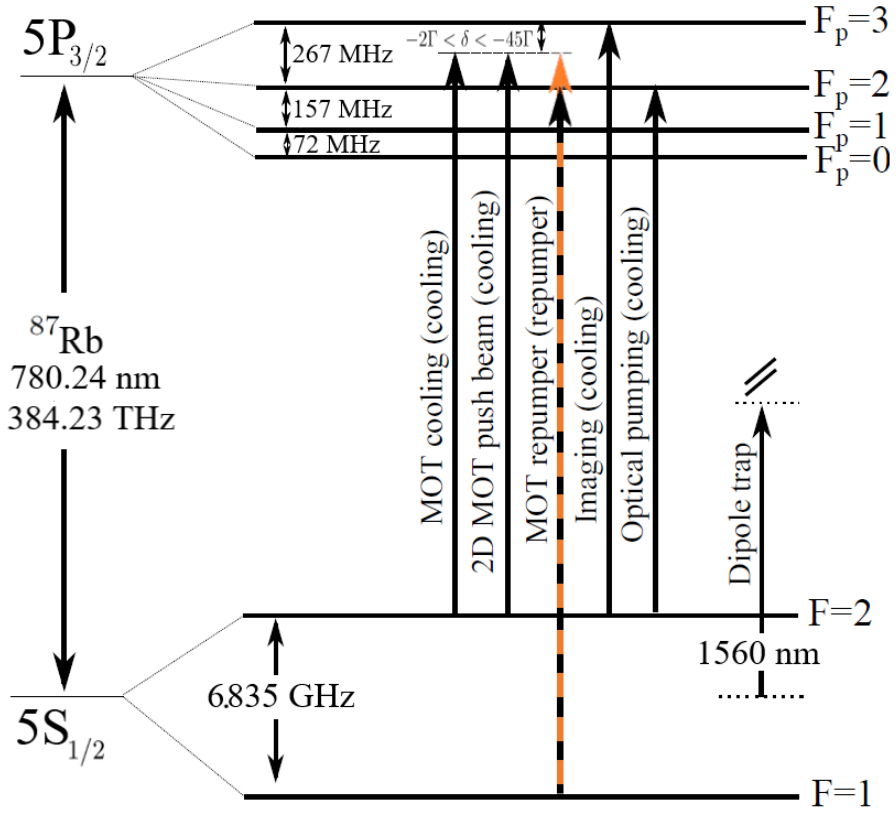

Figure 2.1: Level structure of the D_2 line in ^{87}Rb along with the lasers that are used in our experiment. The coherent repumper created by a free–space EOM is shown in orange.

The level structure of the D_2 line as well as the laser frequencies that are involved in our experiment are depicted in Fig. 2.1. The arrow in orange, in particular, shows the laser

that is responsible for the phase–locked repumper, which is derived via sideband by a free–space EOM (QUBIG, model PM10–NIR), modulated at a frequency close to $5S_{1/2}$'s hyperfine splitting ~ 6.835 GHz.

The optical table producing all the light beams needed for the MOT, compressed MOT (cMOT) and subsequent bright and gray molasses techniques in our experiment, on the other hand, is depicted in Fig. 2.2.

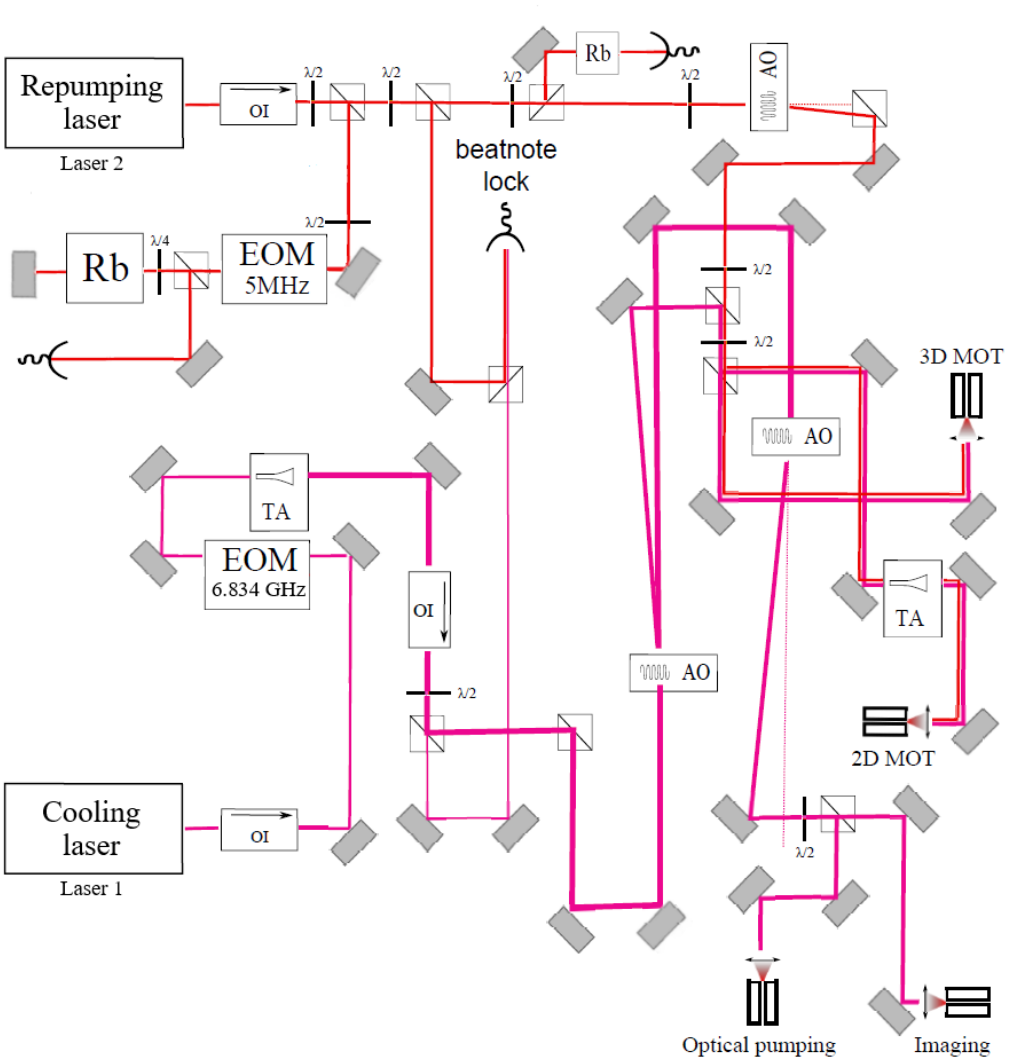

Figure 2.2: General view of the optical table in our experiment producing the 780 nm radiation needed for cooling ^{87}Rb on the D_2 line. Main enhancement during my PhD include a free–space EOM producing sidebands close to $5S_{1/2}$'s hyperfine splitting ~ 6.835 GHz introduced before the first tapered amplifier (TA), and simplification of the SAS lock of the repumper [46] via a retro–reflected geometry, to the absolute frequency reference provided by a rubidium vapor cell.

Since the introduction of the free–space EOM at the beginning of my PhD, the cooler and ordinary repumper lights can be produced using either a single or two different lasers. These two lasers which we call laser 1 and laser 2 respectively, and their relative frequency difference are depicted in the context of the D_2 line level structure of ^{87}Rb in Fig. 2.3. Laser 2 is exactly on the crossover between the transitions $|5S_{1/2}, F = 1\rangle \rightarrow |5P_{3/2}, F' = 1\rangle$ and $|5S_{1/2}, F = 1\rangle \rightarrow |5P_{3/2}, F' = 2\rangle$, thanks to a saturated absorption spectroscopy (SAS) lock, whose error signal along with the one obtained from the repumper's transmission through a rubidium vapor cell is shown in Fig. 2.4. The ~ 78.5 MHz shift that separates the repumper transition's upper $|5P_{3/2}, F' = 2\rangle$ level from the $|5P_{3/2}, F' = 1, 2\rangle$ crossover is created via an AOM, which also allows for optical power control.

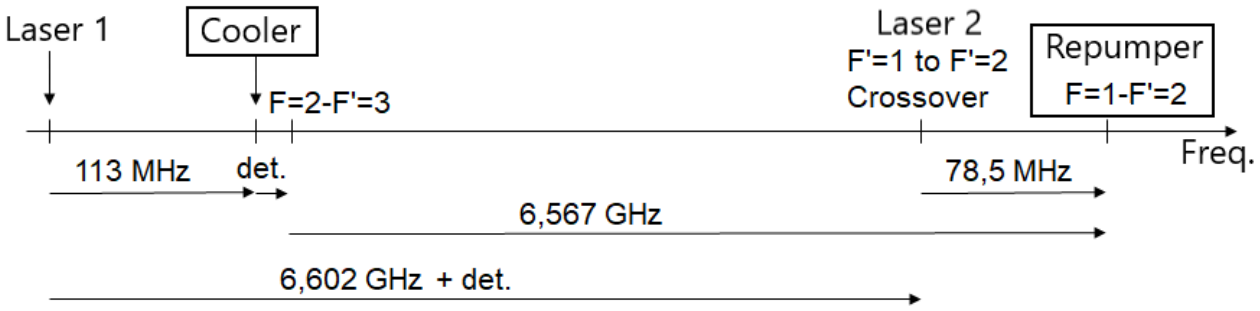

Figure 2.3: Relative frequency differences between the sources producing the MOT lasers as well as the final cooler and repumper radiations atoms see in our experiment referenced to transitions of the D_2 line in ^{87}Rb.

Laser 1 on the other hand is frequency locked to laser 2 using a beatnote lock, with the detected optical signal being mixed with a stable Yttrium Iron Garnet (YIG) microwave oscillator (Giga-tronics, model LPO-0408), to convert the frequency down to a hundreds of MHz level. A farther reduction by a factor of 512 in frequency is obtained by a voltage divider, before feeding the signal through a frequency to voltage converter (FVC, Analog Devices, model AD650) in order to linearly convert the frequency to a voltage. Finally a proportional integral (PI) controller circuit produces the error signal which is fed onto the lasers current.

Even though before, the error signal used to be subtracted with a controllable reference voltage that allowed to modify the frequency locking point, more recently the reference voltage has been applied to the summing input on the current controller of the YIG oscillator. This alternative was tested when the circuitry after the FVC was found to be malfunctioning,

and given that it worked well, the new solution was finally kept.

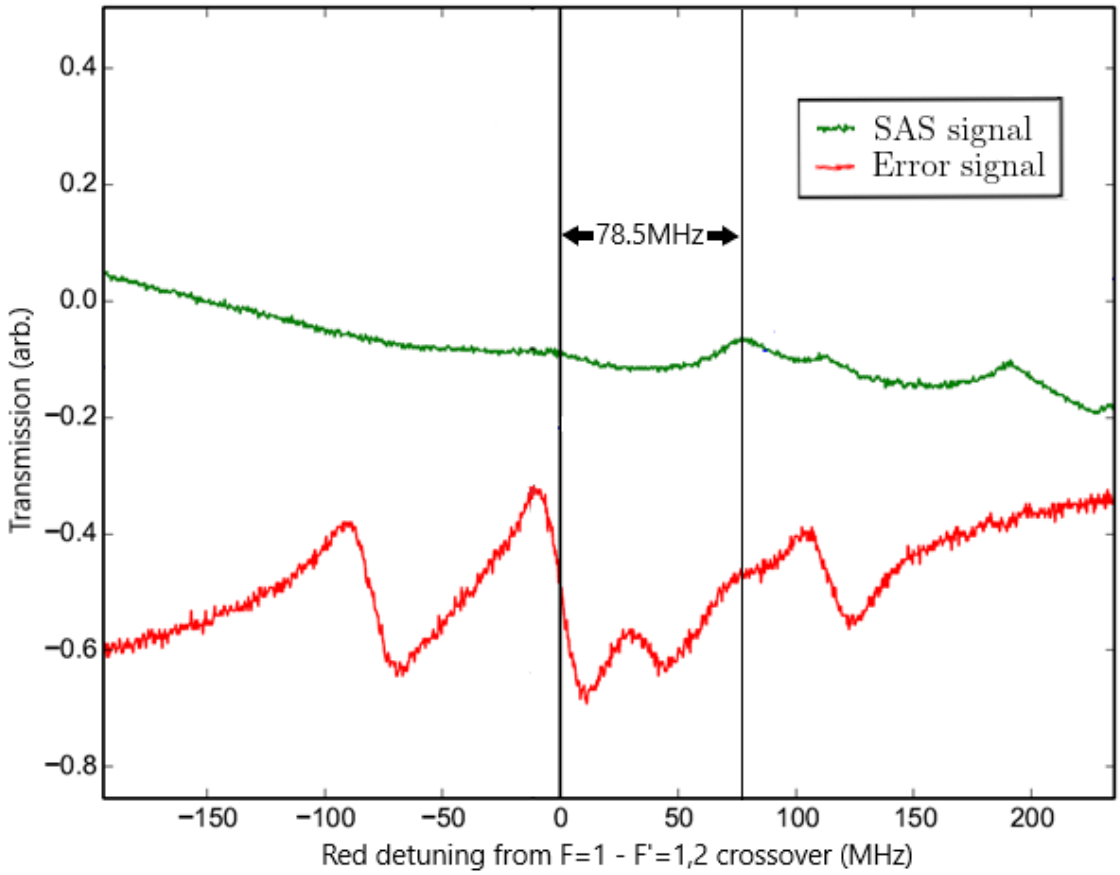

Figure 2.4: Repumper error signal in red and corresponding SAS signal in green red–shifted by ~ 78.5 MHz, which corresponds to the shift that separates the repumper transition's upper $|5P_{3/2}, F' = 2\rangle$ level from the $|5P_{3/2}, F' = 1, 2\rangle$ crossover in the D_2 line of ^{87}Rb. This shift is the frequency difference between the repumper light the atoms see in the SAS lock vapor cell and the one the atoms see in the MOT.

Thanks to the beatnote lock, laser 1 is set to be detuned to the red from laser 2 by a frequency of ~ 6.6 GHz, plus the desired red detuning from the $|5S_{1/2}, F = 2\rangle \rightarrow |5P_{3/2}, F' = 3\rangle$ transition for the cooler, which at the MOT stage we set to three times the natural linewidth $\Gamma_{D_2} = 2\pi\times$ 6.067 MHz (the damping term in Sec. 1.1) of the D_2 line. However, the YIG oscillator's upper frequency limit permits us to control the detuning over a range of more than half a GHz, which allows addressing frequencies spanning both $|5S_{1/2}, F = 2\rangle \rightarrow |5P_{3/2}, F' = 3\rangle$ and $|5S_{1/2}, F = 2\rangle \rightarrow |5P_{3/2}, F' = 2\rangle$ transitions, at hundreds of MHz steps in less than 1 ms. This is particularly useful for our gray molasses scheme, for which large detuning mod-

ifications towards the red are needed, the faster the better. On the other extreme, Laser 1 is red–detuned a minimum of 113 MHz from the cooling transition since an additional AOM at this frequency is used to get a beam which is closer to resonance with the cooling transition, and which also allows controlling the optical power of the cooler light depending on whether a MOT, cMOT or optical molasses is needed. Finally, there is one more AOM that introduces a ~ 123 MHz shift on laser 1 to get a beam on resonance with the cooling transition for imaging purposes, as depicted in Fig. 2.1.

On the optical power side, the cooler undergoes amplification by a tapered amplifier (TA), and the output is split and injected into two polarization maintaining (PM) fibers with both cooler and repumper lights each. Before the amplification stage, laser 1 also passes through the free–space EOM needed to provide the frequency component that implements the repumper in the gray molasses stage. There is finally an additional TA that allows to farther amplify part of the cooler and repumper lights before injecting them into the 2DMOT setup. This setup is described in Sec. 2.2.

To provide MOT light through all the three directions of space needed in the 3DMOT, two Schäfter + Kirchhoff one–to–three splitters is used, and then fiber couplers from the same brand are used to collimate light at a 6.75 mm waist. Four beams and their reflections are shown in Fig. 2.5, while two more beams going into and out of the page, and which are not retroreflected, are not shown. The retroflected pairs are aligned off–axis, since there is no geometry allowing to make a beam and its reflected counterpart colinear with the other pair if one wants all the beams to cross at the 3DMOT region. These configuration, however, allows for power recycling and is also nearly symmetric thanks to the double pairs close to each axis. This last feature nearly cancels the shadow effect produced by the cloud which makes the retroreflected beam weaker, although a small force towards the left side in Fig. 2.5 is still present in principle. This comes from the smaller angle between the beams on the right hand side before retroreflection, a small asymmetry which the retroreflected setup cannot get rid off. The power imbalance produced by retroreflection is not very important at the molasses stage when sub–doppler cooling mechanisms enter into action [20, 47].

During my PhD, different lasers have been used to play the role of laser 1 and laser 2. When I arrived, both frequencies were created using 780 nm New Focus external-cavity diode

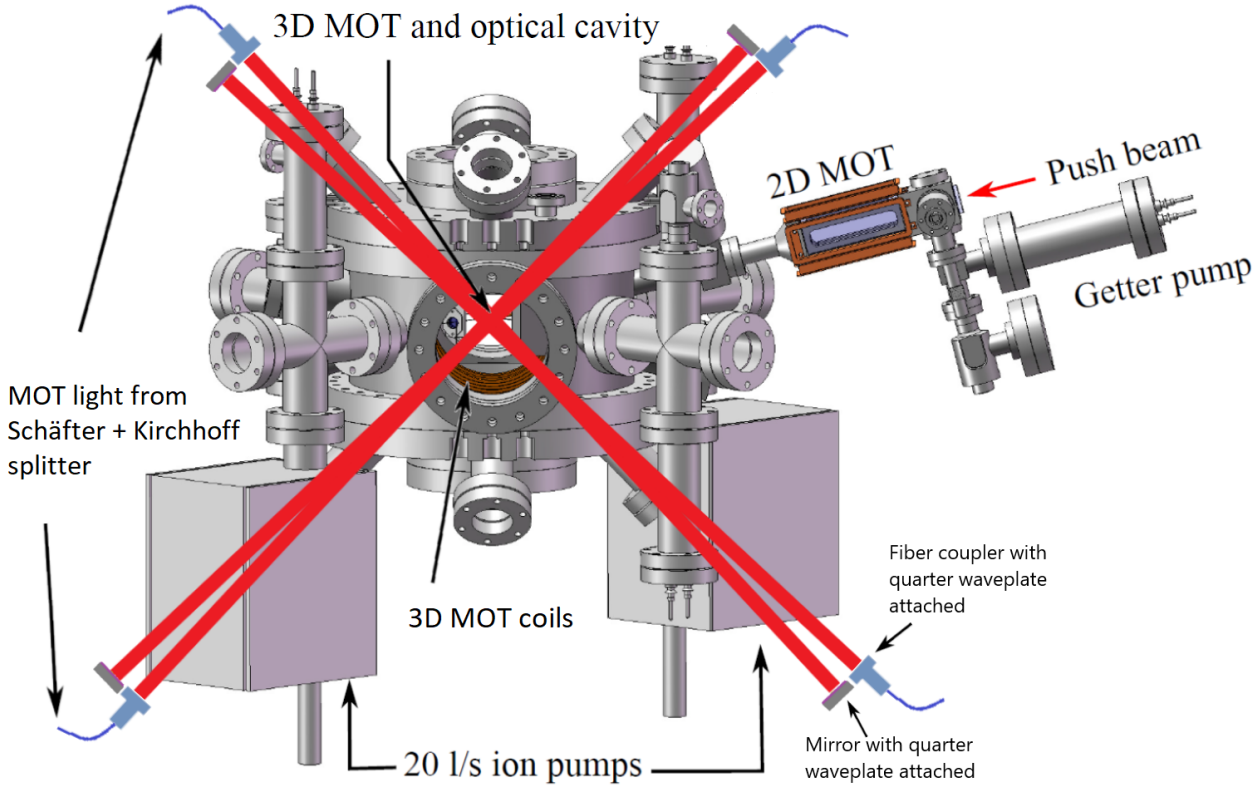

Figure 2.5: Retroreflected 3DMOT beams and their respective fiber couplers and mirrors, along with the overview of the complete vacuum system on the background. Two beams going perpendicularly into and out of the page, which were installed in ordinary MOT configuration i.e. no refroreflection, are not reported, while the MOT coils which are aligned in the same direction are partly visible behind the science chamber window. These coils produce a quadrupole magnetic field thanks to coils in anti–Helmoltz configuration which implies a zero magnetic field at the center, while for small displacements from there the modulus of B increases linearly in every direction.

lasers (ECDL), but they both broke down at different stages of the research. First, laser 1 had to be substituted by a 780 nm Sacher ECDL, and then the New Focus on laser 2 was replaced by a 1560 nm Koheras Adjustik fiber laser, frequency doubled by a periodically poled lithium niobate (PPLN) NTT Electronics doubler. This happened when the lasing threshold of the New Focus laser was found at a too high bias current for operating the repumper consistently. More recently, the Sacher laser suffered from the same problem, and then a second PPLN (NTT Electronics) frequency doubled solution, combined with a 1560 nm Eblana Photonics fibered diode, was installed on the cooler part as well.

2.2 2DMOT loading and lifetime in the science chamber

In the first place, in order to get a 2DMOT, one needs a source that creates a sufficiently large vapor pressure. The solution envisaged in our experiment was to use a glass cell which contains solid rubidium and which is broken by mechanical pressure on a metallic finger once the system has been put under ultra high–vacuum. At this stage, the rubidium in the broken cell is under the same vacuum to which the 2DMOT chamber is subjected to. This chamber, shown on the top right of Fig. 2.5, creates the atomic flux needed to charge the 3DMOT under UHV, which is separated by a differential vacuum stage.

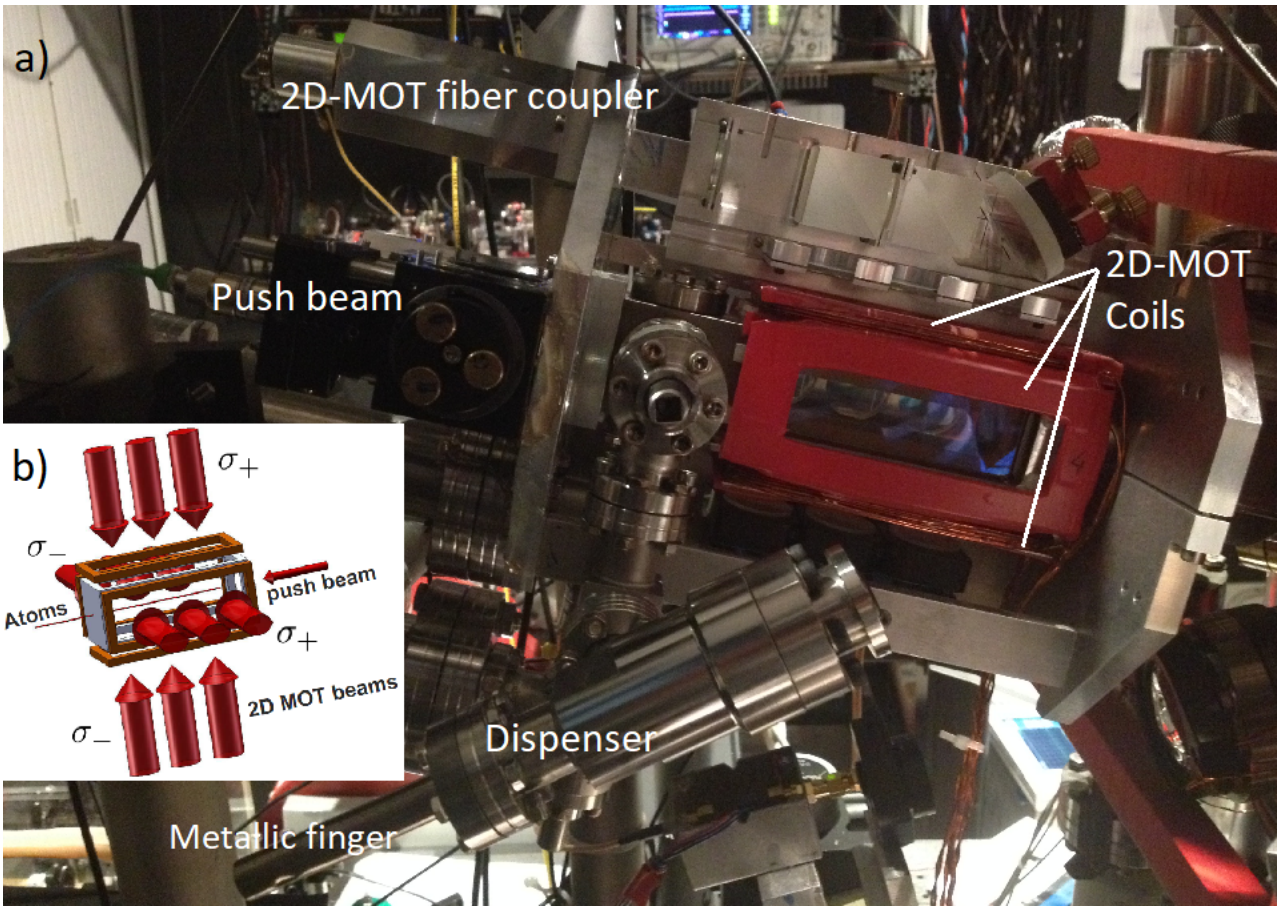

Figure 2.6: a) shows the 2DMOT chamber and the metallic finger containing the glass one inside (see Fig. 2.7). In b) 2DMOT design schematics from the opposite side view, where the configuration of the oppositely circular polarizations is shown.

The optical system is composed of two pairs of retroreflected beams and a push beam coming from a OZ Optics one–to–three splitter. The latter forces the jet of atoms to circulate

towards the 3DMOT chamber, which is our science chamber. Fiber couplers, mirrors and attached quarter wave plates provide the collimation and handedness needed for the magnetic field produced by two pairs of rectangular coils (see Fig. 2.6), which produce a gradient in the transverse direction and a zero field at equal distance from the coils. These are fed by currents produced via four separate power supplies.

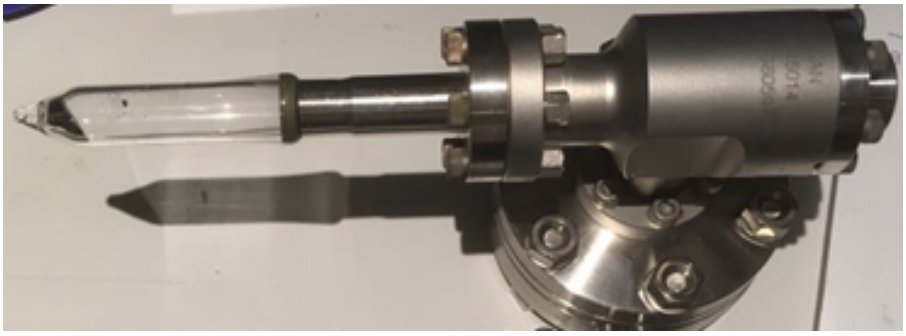

Figure 2.7: New rubidium cell before it was introduced in the setup.

The metallic finger which is used to apply pressure on the glass finger containing the rubidium (see Fig. 2.7), can be heated up using a heating resistive band in order to enhance the rubidium transfer to the MOT area. It was necessary for us to do so after we found difficulties in getting a fluorescence signal in the 2DMOT chamber. It finally became clear that we were not having enough rubidium, and therefore had to replace the rubidium glass cell itself and restore the vacuum pressure needed in the 2DMOT chamber. This process can take several weeks, but fortunately, the UHV in the 3DMOT chamber was not affected during the whole process thanks to a valve between both chambers which allows to isolate the science chamber from the rest of the vacuum setup.

To be sure that the system was working well after the rubidium cell substitution, however, we decided to test the performance of the 3DMOT by looking at the decay of the fluorescence emitted by atom clouds when the conductance channel between the 2D and 3DMOT chambers was blocked in two different ways. First, by stopping the laser light in the 2DMOT setup via shutter; and second, by closing the all metal valve separating the 2D and 3DMOT chambers manually, as fast as possible. The results of both procedures, as well as the respective exponential fits are visible in Fig. 2.8. Blocking the 2DMOT beams produces a longer lifetime of 38.2 s than the 24.1 s attained when closing the metallic valve, which indicates

the existence of a significant flux of atoms at sufficiently low temperatures being transferred from the 2DMOT to the science chamber even in the absence of the 2DMOT beams and the push when the valve is kept open.

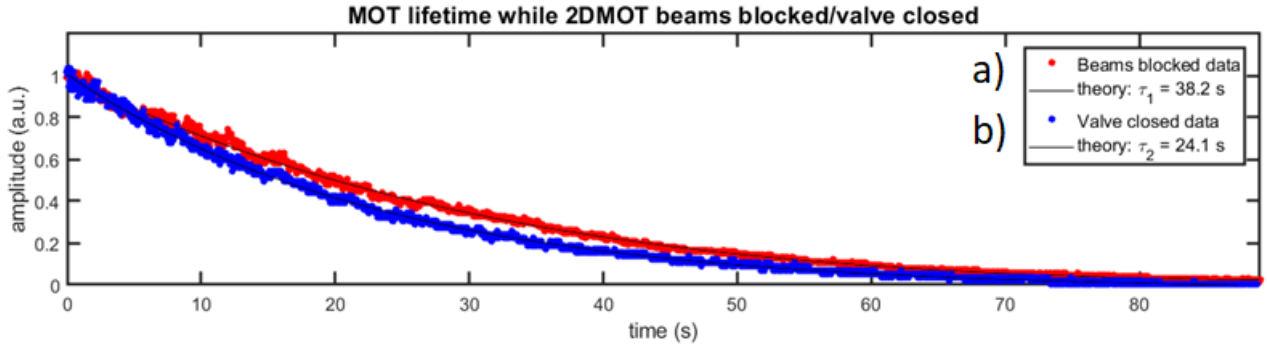

Figure 2.8: 3D–MOT lifetime after 5 seconds loading. In a) 2DMOT beams are shutter blocked; in b) the conductance channel between the 2D and 3DMOT chambers is physically blocked via the all metal valve.

The behavior of the conductance channel between the 2D and 3DMOT chambers is of critical importance in our experiment for an additional reason as we discovered at a later stage of the research. This is related to the lifetime of the atoms loaded into the dipole trap which could be doubled up to $\sim$6 s once the heating resistive bands where turned off. The effect is not surprising given the existence of a large flux of atoms present even when the 2DMOT light is blocked, but such a large detrimental effect was not suspected at the beginning.

The dipole trap allows us to achieve the coldest temperatures and the largest phase–space densities (PSD) in our experiment via evaporative cooling, and its working principle is explained in Subsec. 3.2.2.

2.3 Imaging system for cavity alignment and temperature calibration

Near–resonant light with the atomic transition allows to image the atoms and get information about their density and temperature [48]. In the absorption imaging technique, this is done

by detecting the reduction of light intensity produced by the atoms when they absorb the imaging laser. The atomic shadow is detected on a charge–coupled device (CCD) camera, which in our experiment was installed above the cavity and the vacuum chamber in order to image the atoms from the top and have a two dimensional view of the horizontal plane defined by the cavity arms [49].

During our research however, a new imaging setup has been introduced on the side for two main reasons. First, there was some uncertainty on whether the cavity arms were well aligned or not, since this had not been verified for at least a couple of years before the beginning of my PhD. The side imaging allows to determine the quality of the alignment straightforwardly by looking how the atoms in the dipole trap behave. We discovered the alignment was completely off thanks to this imaging system (see Subsec. 3.2.2). Second, having an imaging system detecting the atoms from the side provides us with a clear reference for the time–of–flight (TOF) imaging [22], with the free fall induced by Earth's gravity. Subsec. 2.3.3 shows how we have utilized it in order to ascertain the calibration of the size of atomic clouds in our experiment.

2.3.1 Absorption imaging and TOF technique

Absorption imaging gives a direct measure of the atomic cloud density integrated along a given direction. The attenuation of the imaging laser can be studied using the Beer–Lambert law which states that this is characterized by the scattering cross–section of each particle, and the particle density in the medium. If the laser propagates along direction z, its intensity after crossing an infinitesimally thin sheet will decrease following,

$$-\frac{dI}{I} = n(x,y)\sigma(\omega)dz, \tag{2.1}$$

where $n(x,y)$ is the atomic density and $\sigma(\omega)$ is the cross–section of the atoms, with $\sigma(\omega_0)$ being the one on resonance at which we operate. Assuming low saturation ($I \ll I_s$) we can integrate Eq. 2.1 to get the optical density (OD),

$$\text{OD}(x,y) \simeq -\ln\left[\frac{I(x,y) - I_{back}(x,y)}{I_0(x,y) - I_{back}(x,y)}\right], \tag{2.2}$$

where $I_0(x,y)$ is the laser intensity before entering the medium and $I_{back}(x,y)$ is the background noise intensity of the CCD which we detect and substract for each experimental run.

In practice then, in order to obtain the atomic density profile, we take three images in the following order. First, $I(x, y)$ is detected after it crosses the atomic cloud; then a second image without the atoms is taken for the same intensity $I_0(x, y)$; and finally a third image with neither the atoms nor the imaging beam is detected, which gives the CCD background noise.

The optical density profile can be fitted to measure the size of the cloud, and by repeating the measurement for the size after different amounts of expansion time, the momentum distribution of the atomic ensemble can also be obtained. This allows to calculate the temperature of cold atomic samples directly as long as they are sufficiently diluted ($\rho a^3 \ll 1$ with a the scattering length) for quantum effects to be negligible. Considering the initial atomic density profile is Gaussian, we can assume a Maxwell–Boltzmann velocity distribution and the Gaussian radius of the atomic cloud will expand following [50],

$$\sigma_c(t) = \sqrt{\sigma_0^2 + \frac{k_B T}{m} t^2}, \tag{2.3}$$

where σ_0 is the initial radius of the cloud, T the temperature of the sample and m the mass of one atom.

Additionally, once the atoms are released from the trapping potential to image them after a given TOF, Earth's gravity will attract them towards the ground. This effect is highly useful to obtain an absolute calibration of size and therefore of temperature in the atomic sample as mentioned above. We shall describe it in detail below after introducing our new imaging setup.

2.3.2 New imaging system in folded configuration

The imaging system we describe in the following is the one we installed during my PhD, while the older one which is still the main imaging device for characterizing the atomic samples is described elsewhere [46]. However, the set of Zeiss Fluar microscope objectives (x5, x10 and x20 magnifications) in front of the one–inch mirror and the CCD (see Fig. 2.9) is still the same as the one installed in the older setup and is interchanged between both imaging systems depending on the magnification needed.

The vacuum chamber imposes a working distance of 190 mm which is the distance be-

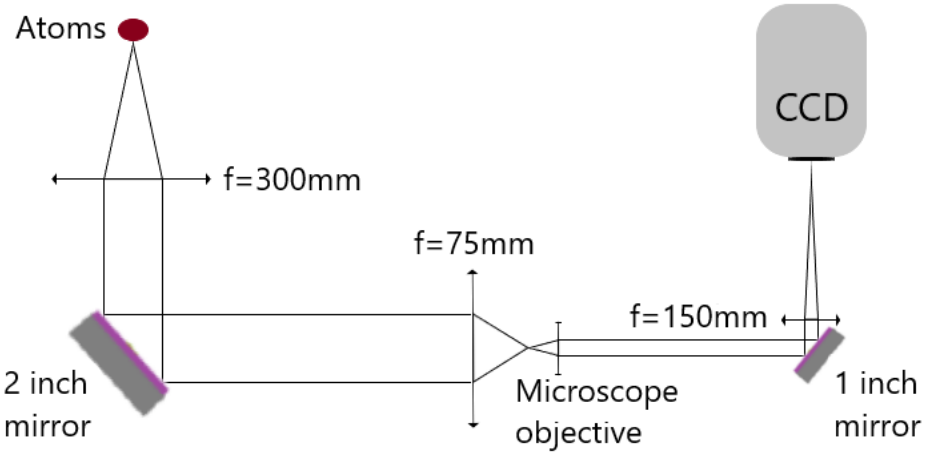

Figure 2.9: Side imaging system is made of two–inch folded telescope and mirror, microscope objective, and CCD which is 260 mm away from the objective.

tween the center of the cavity and the lateral window on the chamber. This window however must allow for one of the non–reflected 3DMOT beams to go into the vacuum, which means the two–inch optics telescope cannot be arbitrarily close to the window. The first lens of the telescope is then installed 300 mm away from the cavity center and thus the MOT beam is free to enter the chamber without touching the telescope. The telescope lens closest to the microscope objective, on the other hand, has a focal length of 75 mm which results in a telescope magnification of $M = f/f_e = 300/75 = 4$. Besides, the limited length available on both the common large breadboard and the smaller one on which the side imaging system and the coupler for the MOT beam are installed, gives no choice but to introduce a two–inch mirror between the two lenses making up the telescope. There is a second smaller one–inch mirror between the microscope objective and the CCD, and then the whole imaging setup can be installed on the same small breadboard.

Finally, the CCD camera detecting the shadow left by the atoms in our science chamber is an Andor iXon Ultra 897, which is simultaneously triggered along with the CCD on the main imaging setup.

2.3.3 Temperature calibration via free fall trajectory fit of the atomic cloud

On Earth's surface, in the particular case of Bordeaux, gravitational acceleration is well approximated by the value $g = 9.806$ m/s^2. Therefore, free fall of an atomic cloud is a good reference to estimate easily its size provided a long enough observation time of the free falling atoms.

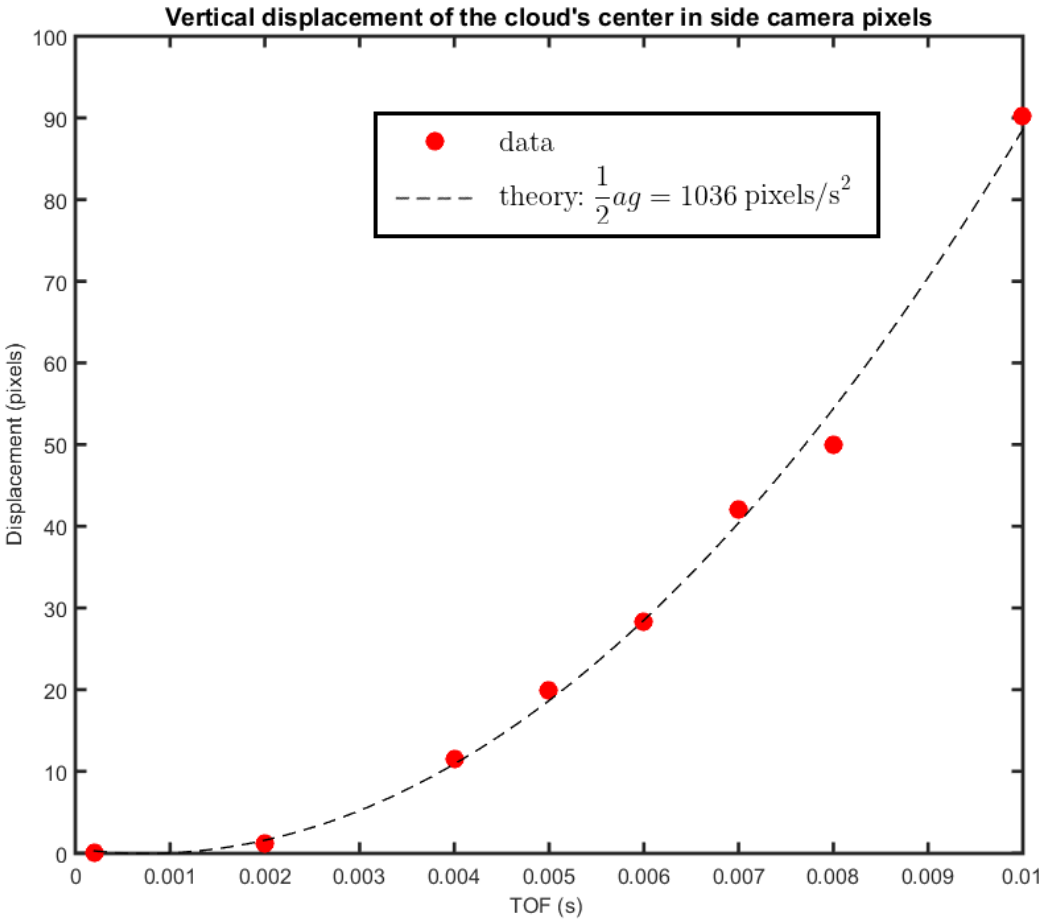

Figure 2.10: TOF data and parabolic fit used to calibrate the temperature of the atoms obtained after an evaporation ramp duration of 5.1 s (see Subsec. 3.2.2).

In the side imaging system introduced during my PhD, a good compromise between resolution and observation time is obtained using the intermediate magnification available, that is with a x10 Zeiss Fluar microscope objective. The observation time is then limited to 10

ms TOF, since using a longer TOF makes atoms go too far down to be captured by the CCD. Therefore, the parabolic fit of the data we took used samples falling down for a maximum of 10 ms (see Fig. 2.10).

Integrating acceleration twice with respect to time, while considering initial conditions at which the cloud of atoms is static we get,

$$y(t) = \frac{1}{2}agt^2, \tag{2.4}$$

where a is a free fitting parameter. From the fit, $a = 211.2$ pixels/m was obtained and by dividing the Gaussian radii in pixel units by the parameter, one gets the size of the atomic cloud in meters.

We also measured atomic clouds under the same conditions using the main imaging system with the same x10 Zeiss Fluar microscope objective used on the side imaging, and then the conversion factor between the old and the new standards could be found. We found that according to the gravity calibration, the control system monitoring the data obtained from the main imaging system was overestimating the size of the atomic clouds by approximately 20 %. This is because information about the control system parameters giving the correct calibration for a given microscope objective got lost over the years.

The conversion factor by which the size displayed on the computer controlling the main imaging system had to be multiplied is 0.845, which according to Eq. 2.3 means the temperatures were in reality approximately 30 % lower than the ones being recorded before the gravity calibration.

2.4 Concluding remarks

In this chapter, we have described the optical table producing 780 nm laser light in detail. This is motivated by the enhancements that have been introduced on this table during my PhD to produce the repumping sideband for the gray molasses. On the other hand, a new imaging system monitoring the position of the atoms along the vertical axis has been also described, together with a relevant application related to the correct determination of the size and thus the temperature of the atomic clouds in our experiment. A more critical aspect

for trapping the atoms and interacting with them via the cavity modes at 780 nm, namely the alignment of the intracavity arms at the crossing region, will be treated in Subsec. 3.2.2.

Other minor changes introduced during my PhD on the 780 nm breadboard table include the frequency control of the cooling laser via the beatnote lock, which now relies on a direct current control of the YIG oscillator, and the simplification of the repumper's SAS lock which is now implemented using a retro–reflected geometry.

Chapter 3

High finesse bi-resonant bow-tie cavity

The high finesse cavity is the central component of our experiment. This is due to two main reasons: first, the cavity permits to create a deep far off–resonant dipole trap (FORT) thanks to the enhancement of the 1560 nm field therein; second, the coherent coupling of the atoms inside the cavity to closer to resonance light, which is one of the two main achievements reported in this thesis. These two reasons where behind the motivation of constructing a cavity which can be excited at two wavelengths: at 1560 nm for the dipole trap, and at 780 nm for the coherent coupling. However, most of the properties of the cavity are common to both wavelengths, and can be then described without the need of specifying which particular one we are referring to. Therefore, we start this chapter by presenting the general properties of the cavity and we shall later describe specific features corresponding to one or the other light only when it is required to do so.

To begin with, we analyze the geometry and mode structure of the cavity by deriving the modes of the resonator. We study next the relationship between injected laser and amplification inside the cavity thanks to the measurement of the finesses at 1560 nm and at 780 nm later on. After a detailed analysis of the dipole trap parameters we finally show how to maintain the laser on resonance with the cavity mode and how to keep injected power constant in time.

3.1 Geometry and mode structure

The bow–tie geometry of the cavity was chosen at its conception stage to achieve favorable conditions to create degenerate gases. This was done by choosing a butterfly cavity close to a concentric configuration which permits power to concentrate in the center and increase confinement along all spacial directions. In this way, large trap frequencies needed for condensation can be achieved over a large volume.

3.1.1 Mechanical structure

The cavity was built from four spherical mirrors of 100 mm radius of curvature and 1/2 inch diameter each. The mirrors are positioned so as to create a square, each of the four intracavity sides measuring 63.64 mm, so that the diagonal is 90.00 mm long, that is, 10 % shorter than the radius of curvature of the mirrors, and then the cavity resonance is in the stable regime. Two mirrors are positioned on fixed mounts while the other two can be controlled either by picomotors or by piezo–electric actuators. The former are meant for coarse micrometer precision displacements along two axes while the latter provide finer adjustment along three axes in the nanometer region. The picomotor controlling the horizontal axis was damaged when the ultra-high vacuum chamber where the cavity is kept was baked-out at the construction stage of the experiment. Therefore, during the entire duration of my PhD, we used either the piezo–electric actuators or the vertical axis picomotor control, which is fortunately controlling the critical direction in what the cavity arm alignment is concerned (see Subsec. 3.2.2).

Mirrors and piezo–electric actuators are mounted on a titanium flange for low magnetic field environment purposes, since not only it supports the cavity but also the coils that create the 3 dimensional magneto-optical trap (3D–MOT). All this is contained inside the ultra-high vacuum chamber (see Fig. 3.1).

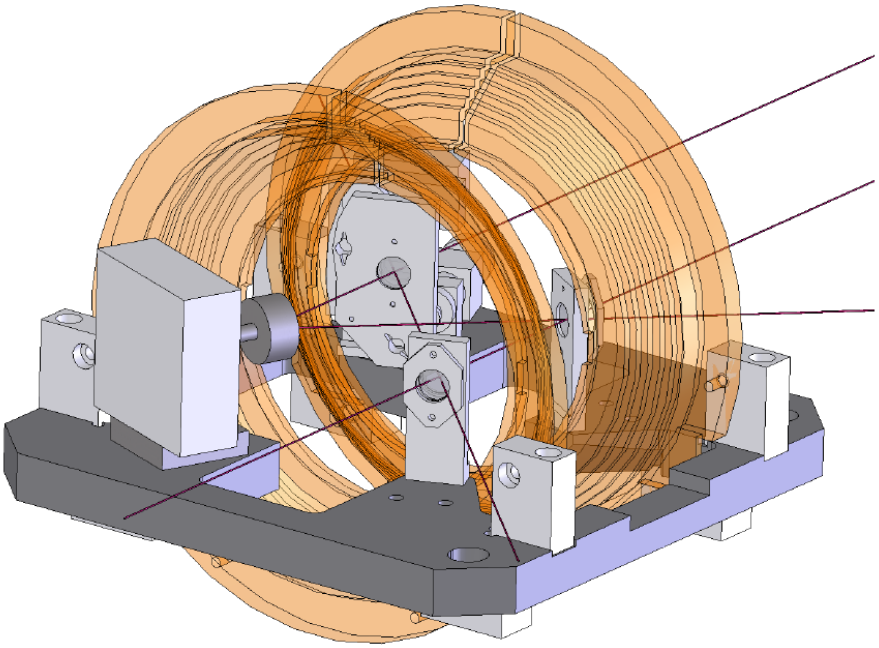

Figure 3.1: General view of the cavity and 3DMOT coils which appear in orange. The piezo–electrically controlled mirror is the one on the left while the picomotor controlled one appears on the back [46].

3.1.2 Mode structure in the paraxial approximation

Getting the modes of the electric field that resonate in our bow-tie cavity requires considering some approximations. The starting point is the wave equation for the electric field in vacuum

$$\left(\nabla^2 - \frac{1}{c^2}\frac{\partial^2}{\partial t^2}\right)\boldsymbol{E}(\boldsymbol{r},t) = 0, \tag{3.1}$$

which is derived from the Maxwell equations in charge–free space. Separating the dependence in space and time variables as $\boldsymbol{E}(\boldsymbol{r})$ and $\boldsymbol{F}(t)$ we get

$$\frac{\nabla^2\boldsymbol{E}(\boldsymbol{r})}{\boldsymbol{E}(\boldsymbol{r})} = \frac{1}{c^2\boldsymbol{F}(t)}\frac{d^2\boldsymbol{F}(t)}{dt^2}, \tag{3.2}$$

which is generally true if and only if both sides equal a constant. This leads to two independent equations, one which contains the time dependence, and the other which depends on the space variables and gives the form of the electric field in the cavity once the correct boundary conditions are applied. The latter is the Helmholtz equation for $\mathbf{E}(\mathbf{r})$ which reads

$$\nabla^2\boldsymbol{E}(\boldsymbol{r}) + k^2\boldsymbol{E}(\boldsymbol{r}) = 0, \tag{3.3}$$

where $k = \omega/c$ is the dispersion relation and c the speed of light in vacuum.

The optical power inside the cavity is closely confined along the propagation axis, in other

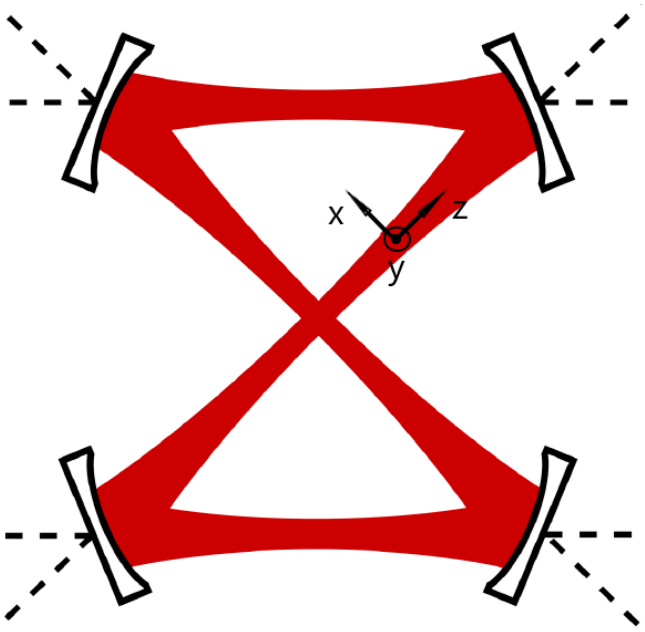

Figure 3.2: Definition of cavity axes, with x and z on the cavity plane, whereas y is orthogonal to this plane.

words, we are restricted to modes propagating along the direction through which light can be injected, namely, the z-axis. Therefore, we continue our analysis making use of the paraxial approximation, which means that transverse variations are small while propagation along the z-axis is considered. On the other hand, we will consider the scalar paraxial Helmholtz equation, since no fields are allowed in the direction of propagation by the electromagnetic wave equation, while we assume polarization degrees of freedom can be treated separately. We then consider parallel to the cavity plane linear polarization (see Fig. 3.2),

$$\boldsymbol{E}(\boldsymbol{r}) = E(\boldsymbol{r})\hat{x} = U(\boldsymbol{r})e^{-ikz}\hat{x}, \tag{3.4}$$

where $U(\boldsymbol{r})$ is the amplitude of the electric field. This choice of polarization produces no interference between perpendicular beams on the center of the cavity [51]. The paraxial Helmholtz equation then reads,

$$\begin{aligned}
\nabla^2 E(\boldsymbol{r}) + k^2 E(\boldsymbol{r}) &= \left(\partial_x^2 + \partial_y^2\right) U(\boldsymbol{r})e^{-ikz} + \partial_z\left[e^{-ikz}\partial_z U(\boldsymbol{r}) - ikU(\boldsymbol{r})e^{-ikz}\right] + k^2 U(\boldsymbol{r})e^{-ikz} \\
&= \nabla_\perp^2 U(\boldsymbol{r})e^{-ikz} + e^{-ikz}\partial_z^2 U(\boldsymbol{r}) - i2kU(\boldsymbol{r})e^{-ikz} \\
&\approx \nabla_\perp^2 U(\boldsymbol{r})e^{-ikz} - i2kU(\boldsymbol{r})e^{-ikz} = 0,
\end{aligned} \tag{3.5}$$

where $\partial_z^2 U(\boldsymbol{r}) \ll k\partial_z U(\boldsymbol{r})$ in the paraxial approximation has been applied.

The mirrors in the cavity break the rotational symmetry along the transverse direction, which is broken in laser resonators due to optical components at non–zero angles against the beam propagation direction. Therefore, transverse electromagnetic modes (TEM) with rectangular symmetry are a natural decomposition for solutions to Eq. 3.5 for us. These are Hermite–Gaussian modes which we present below for the specific case of our cavity.

Given that our cavity is composed of out of axis spherical mirrors and thus their focal distance changes for parallel and perpedicular to the cavity plane orientations, the modes are necessarily astigmatic, implying horizontal and vertical beam profiles evolve differently upon propagation. A consequence of this astigmatism is the fact that $\mathrm{TEM_{mn}}$ and $\mathrm{TEM_{nm}}$ modes are no longer equivalent under a $90°$ rotation, and are non-degenerate allowing thus for independent excitation. By trying a separable product of functions of x and y [52],

$$U(x,y,z) = g(x,z)h(y,z)e^{-ip(z)}, \tag{3.6}$$

as a solution of Eq. 3.5, a decomposition in terms of Hermite–Gauss orthonormal functions of the following form can be found,

$$U_{mn} = \frac{U_0 w_0^{\parallel} w_0^{\perp}}{w_{\parallel}(z) w_{\perp}(z)} H_m\left(\frac{\sqrt{2}x}{w_{\parallel}(z)}\right) H_n\left(\frac{\sqrt{2}y}{w_{\perp}(z)}\right) e^{i\left[\phi_{mn} - \frac{k}{2}\left(\frac{x^2}{R_{\parallel}(z)} + \frac{y^2}{R_{\perp}(z)}\right)\right] - \frac{x^2}{w_{\parallel}^2(z)} - \frac{y^2}{w_{\perp}^2(z)}}, \tag{3.7}$$

where $H_m(x)$ and $H_n(y)$ are Hermite polynomials with non–negative integers m and n, $R_{\parallel/\perp}(z)$ the parallel and perpendicular wavefront curvatures, $w_0^{\parallel/\perp}$ and $w_{\parallel/\perp}(z)$ the parallel and perpendicular to cavity plane waists and Gaussian beam radii respectively, and finally

$$\phi_{mn} = \left(m + \frac{1}{2}\right)\arctan\left(\frac{z}{z_R{}^{\parallel}}\right) + \left(n + \frac{1}{2}\right)\arctan\left(\frac{z}{z_R{}^{\perp}}\right), \tag{3.8}$$

the Gouy phase. Here $z_R{}^{\parallel/\perp} = \pi\left(w_0^{\parallel/\perp}\right)^2/\lambda$ are the parallel and perpendicular to cavity plane Rayleigh ranges respectively, and $\lambda = 2\pi c/\omega$ the wavelenght of the radiation.

3.1.2.1 Fundamental mode geometry in the paraxial approximation

Obtaining the geometrical properties of the fundamental mode is of particular utility since both the 1560 nm radiation at which the FORT is created, as well as the 780 nm light which we use for coherent atom-light interactions, are operated predominantly on this fundamental mode.

In the paraxial approximation, ray transfer matrix analysis can be used, a method which

allows to solve problems involving paraxial rays. This way, one can describe the ray at any point of the propagation axis z provided the distance y that separates the point from the propagation axis, as well as the angle θ the ray describes with this axis are known. Each of the components, and whole optical systems themselves, can be represented by a ray transfer matrix, also known as ABCD matrix whose four elements determine the evolution of the complex radius of curvature [53]

$$q(z) = \left(\frac{1}{R(z)} - i \frac{\lambda}{\pi w^2(z)} \right)^{-1}, \tag{3.9}$$

along the propagation axis. It evolves following

$$q(z') = \frac{Aq(z) + B}{Cq(z) + D}, \tag{3.10}$$

while the output plane can be related to the input one by a linear transformation which allows for the matrix expression,

$$\begin{pmatrix} y' \\ \theta' \end{pmatrix} = \begin{pmatrix} A & B \\ C & D \end{pmatrix} \begin{pmatrix} y \\ \theta \end{pmatrix}. \tag{3.11}$$

Here primed elements correspond to the output ray vector while the ones on which the transfer matrix is acting correspond to the input one.

To get the transfer matrix of our cavity, we can multiply each of the elements composing it. To start with, using the fact that the radius of curvature r of a spherical mirror is twice its focal length f, one can write,

$$M_m = \begin{pmatrix} 1 & 0 \\ \frac{-1}{f} & 1 \end{pmatrix} = \begin{pmatrix} 1 & 0 \\ \frac{-2}{r} & 1 \end{pmatrix}, \tag{3.12}$$

for each of the cavity mirrors. Given that there are no other components in the cavity, the only additional matrices needed are the ones corresponding to free intracavity propagation over a distance d,

$$M_p(d) = \begin{pmatrix} 1 & d \\ 0 & 1 \end{pmatrix}. \tag{3.13}$$

Choosing the origin of the propagation direction at the crossing of the cavity arms $z = 0$ and denoting by $d = s$ a side of the square the cavity represents we get

$$M_c = M_p(\frac{s}{\sqrt{2}}) M_m(R) M_p(s) M_m(R) M_p(\sqrt{2}s) M_m(R) M_p(s) M_m(R) M_p(\frac{s}{\sqrt{2}}), \tag{3.14}$$

which would be valid for both the horizontal and vertical transverse directions if the reflec-

$\lambda\ (nm)$	${w_0}^{\parallel/\perp}\ (\mu m)$	${z_R}^{\parallel/\perp}\ (mm)$
1560	81, 128	13.2, 33
780	57.2, 90.5	13.2, 33

Table 3.1: Parallel and perpendicular to cavity plane waists and Rayleigh ranges for 1560 and 780 nm radiations along the cross arms (see Fig. 3.2)

tions in our cavity did not occur out of axis. However, to account for the astigmatism present in our cavity, we need to treat each of the two transverse axes using separate ABCD matrices corresponding to different complex radius of curvature $q_{\parallel}(z)$ and $q_{\perp}(z)$. If θ is the angle of incidence with respect to the normal to the tangent plane to the point at center of the mirror, then $f_{\parallel} = r\cos(\theta)/2$ and $f_{\perp} = r/2\cos\theta$ which will thus define two distinct expressions ${M_c}^{\parallel/\perp}$ for our cavity.

To match the cavity resonance two conditions must be satisfied: (i) the mode amplitude needs to maintain its shape on the roundtrip; and (ii) the phase shift needs to be an integer multiple of 2π over the distance $\Delta z = L = 2s + 2\sqrt{2}s = 307.28$ mm. Mathematically,

$$q_{\parallel/\perp}(z = L) = q_{\parallel/\perp}(z = 0), \tag{3.15}$$

which by using Eq. 3.10 implies

$$q_{\parallel/\perp}(0) = \frac{A_{\parallel/\perp} q_{\parallel/\perp}(0) + B_{\parallel/\perp}}{C_{\parallel/\perp} q_{\parallel/\perp}(0) + D_{\parallel/\perp}}. \tag{3.16}$$

Separating the real and imaginary parts, and substituting the matrix elements from Eq. 3.14 as well as the two concerned wavelengths resonant with our cavity in Eq. 3.9, we get two pairs of ordinary algebraic equations among which we focus on the imaginary ones. These provide us with the waists along the two orthogonal directions perpendicular to the cavity propagation axis, for each of the wavelengths. Besides, from the waists we get the Rayleigh ranges which are not wavelength dependent.

The parallel and perpendicular Gaussian beam widths for the fundamental mode at any given distance from the cavity center can be then calculated using the formula

$$w_{\parallel/\perp}(z) = {w_0}^{\parallel/\perp} \sqrt{1 + \left(\frac{z}{{z_R}^{\parallel/\perp}}\right)^2}, \tag{3.17}$$

where ${w_0}^{\parallel/\perp}$ and ${z_R}^{\parallel/\perp}$ are again the parallel and perpendicular to cavity plane waists and Rayleigh ranges, respectively. For our cavity, their theoretical values are given in Tab. 3.1.

A numerical plot of Eq. 3.17 is shown in Fig. 3.3 a) for as far as half a meter from the

$\lambda\ (nm)$	${w_0}^{\parallel/\perp}\ (\mu m)$	${z_R}^{\parallel/\perp}\ (mm)$
1560	283, 204	161, 84
780	200, 144	161, 84

Table 3.2: Parallel and perpendicular to cavity plane waists and Rayleigh ranges on the two parallel sides of the cavity for 1560 and 780 nm radiations (see Fig. 3.2).

cavity center, which is approximately the distance at which we monitor the beam profile of the radiation leaking out of the cavity. In b) the evolution of the fundamental mode profile inside the cavity is shown for a full intracavity trip.

The vertical to horizontal cross–section ratio is found to be $\simeq 63$ % at the typical monitoring distance, which makes the elliptical character of the profile apparent with the naked eye. We next explain the procedure we followed in order to compensate for this effect so as to correctly mode–match the fundamental mode, with the purpose of increasing the coupling efficiency of the laser to our bow–tie cavity.

3.1.2.2 Fundamental mode matching optics and coupling efficiency

Our approach to optimally mode match the injected radiation to the fundamental cavity mode was to use two optical telescopes at the injection stage: an ordinary one, which was the only one used in the experiment before my arrival, is adjusted to match the vertical radius of the beam to that of the cavity profile, leaving the horizontal radius of the beam the same as the vertical one; while the second one, made of a pair of cylindrical lenses, compensates for the horizontal radius of the beam once the ordinary telescope has been optimally positioned.

During my PhD we increased the coupling efficiency at both 1560 and 780 nm for which the cavity is resonant. At the beginning, a big effort was made on enhancing the whole 1560 nm injection system with the objective of achieving a more stable intracavity FORT. The main limitation of the previous setup was the fragility of the frequency lock to low–frequency cavity vibrations. These would unlock the laser if the magnetic field needed for creating the MOT was switched off on a timescale of less than few milliseconds. Given that fast switching of the MOT is needed for creating a true molasses stage loading the dipole trap most efficiently, building a more robust frequency lock was the main objective during the first few months of my PhD (see Sec. 3.3). On the other hand, injecting 780 nm radiation entailed starting the

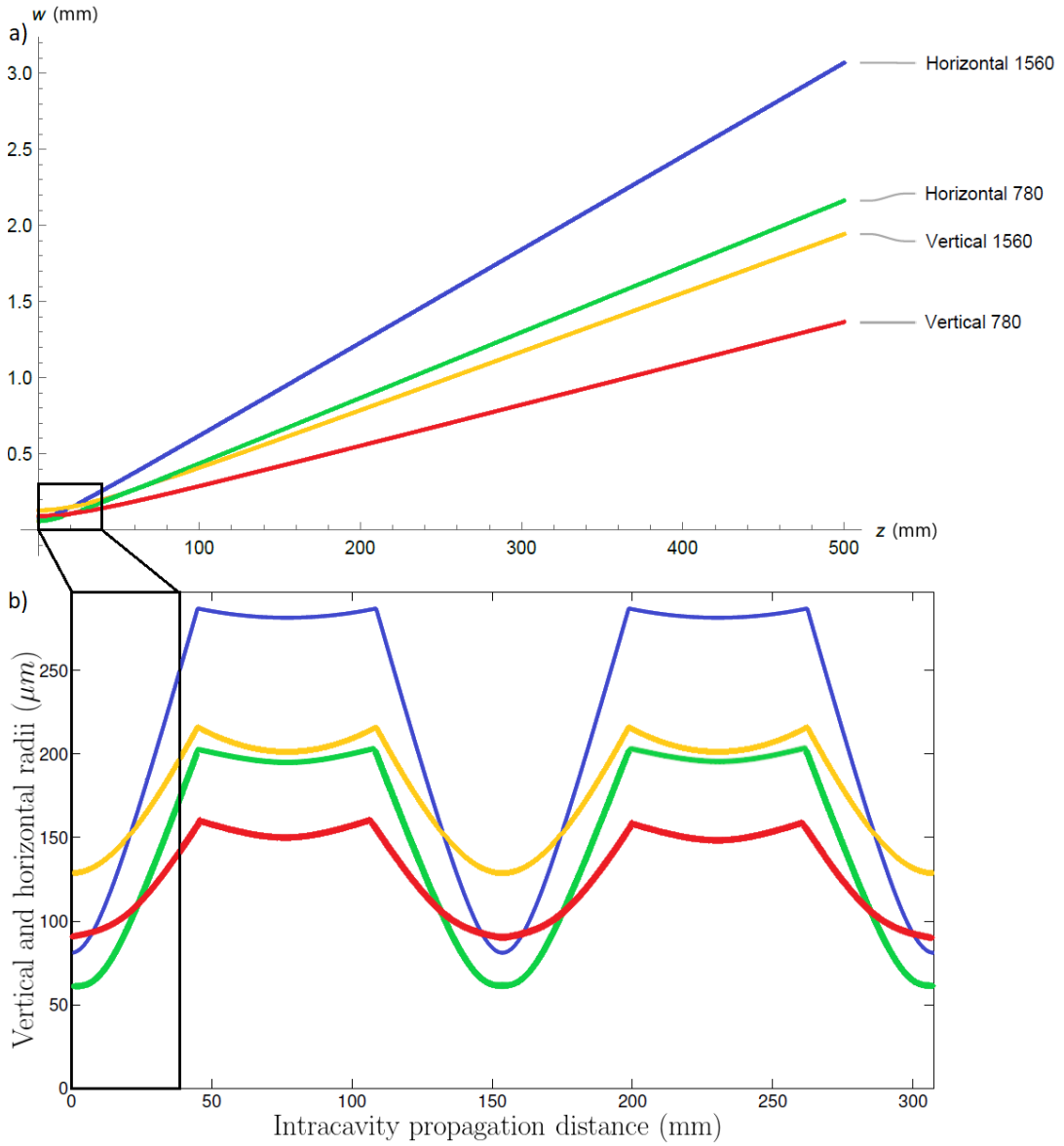

Figure 3.3: Theoretical evolution with distance from the cavity center of horizontal and vertical cross-sections of the fundamental mode, for both 1560 and 780 nm wavelengths; in a) for radiation leaking out of the cavity according to Eq. 3.17; and in b) intracavity propagation along a full trip.

work from scratch since the 780 nm resonance of the cavity had never been exploited during previous research in our experiment. We started working on the injection of 780 nm laser light at a later stage of the research, when observing atom–cavity coupling became the main objective.

The closest to the horizontal to vertical ratio of beam radii we could find in the market for the ratio between horizontal to vertical focal lengths of the lenses was 67 %. They were acquired at Thorlabs at both 50-75 mm and 100-150 mm focal length combinations. The first pair was used to inject 1560 nm radiation, while the distance between the lenses on the second one was found easier to optimize for fine mode matching at 780 nm light, given the lower coupling efficiency of the cavity at this wavelength.

The coupling efficiency of the injected light is of critical importance not only to get a clean error signal for the frequency lock of the laser to the cavity, but also to maximize the power injected into the cavity given the limited amount of power available at the amplifier. For the particular four mirror geometry of our bow–tie cavity and once the laser power inside has reached the steady state, the coupling efficiency can be calculated by solving the following set of three simple ordinary algebraic equations for the power,

$$P_{tot} = P_{inj} + P_{refl}, \tag{3.18a}$$

$$P_D = P_{refl} + P_{loss}, \tag{3.18b}$$

$$P_{inj} = 4P_{loss}, \tag{3.18c}$$

where P_{tot}, P_{inj}, P_{refl}, P_D and P_{loss} are the total laser power produced; the injected power inside the cavity; the reflected power out of the injection mirror; the detected power on the photodetector monitoring the reflection path; and the power leaking out of the cavity on each of the mirrors respectively. Solving for P_{inj}/P_{tot} we get the coupling efficiency in terms of the detected power on the reflection path,

$$\frac{P_{inj}}{P_{tot}} = \frac{4}{3}\left(1 - \frac{P_D}{P_{tot}}\right), \tag{3.19}$$

which is monitored on an oscilloscope where the depth of the reflection dip over the absolute reflection value is measured (see Fig. 3.4). After optimizing both the ordinary and cylindrical telescope distances sequentially, $P_{inj}/P_{tot} = 46 \pm 2$ % was achieved, which is $\simeq 25$ % greater than the one obtained before installing the new telescope [46].

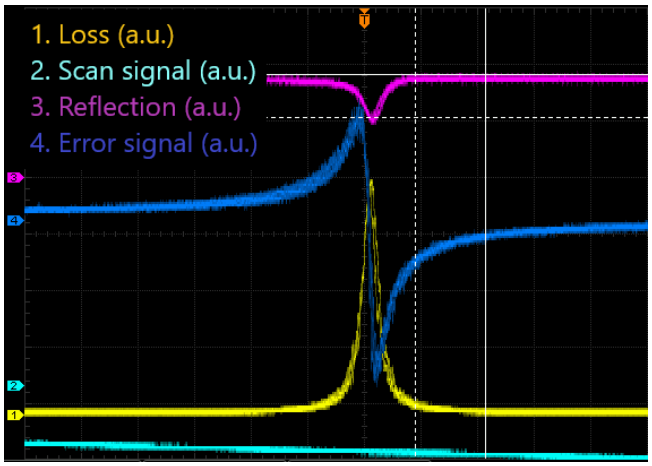

Figure 3.4: Reflection dip in violet shows 46 ± 2 % coupling efficiency according to Eq. 3.19. Corresponding transmission signal through the cavity (loss) in yellow, Pound–Drever–Hall signal in dark blue (see Sec. 3.3) and laser bias current scan signal in light blue are also shown.

In practice, the main physical consequence of the enhanced coupling efficiency is that less power will be needed at the injection in order to achieve the same intracavity power. Previously reported conversion factors between the power injected and the dipole trap frequencies thus need to be updated. However, for our calculations of FORT trap frequencies (see Subsec. 3.2.2), it is rather the transmitted power the one which is monitored to get an estimation of the power inside, as the ratio between them does not depend on the coupling efficiency. More importantly, the transmitted power can easily be measured without disturbing the injection of laser radiation into the bow–tie cavity.

3.1.2.3 Higher order cavity modes

The ABCD matrix coefficients and the complex radius of curvature $q_{\parallel}(z)$ and $q_{\perp}(z)$ defined earlier in Eq. 3.1.2 determine another important parameter of the cavity, namely the frequencies of each and every mode at which the resonator can be excited both longitudinally and transversely [53],

$$\omega^{p}_{mn} = \frac{c}{L}\left[p + \left(\frac{m}{2\pi} + \frac{1}{4\pi}\right)\mathrm{Arg}\left(A_{\parallel} + \frac{B_{\parallel}}{q_0^{\parallel}}\right) + \left(\frac{n}{2\pi} + \frac{1}{4\pi}\right)\mathrm{Arg}\left(A_{\perp} + \frac{B_{\perp}}{q_0^{\perp}}\right)\right]. \tag{3.20}$$

Here Arg is the argument function and p is an integer corresponding to the longitudinal mode order, while m and n are the same integers as in Eqs. 3.7 and 3.8 that is, the transverse mode

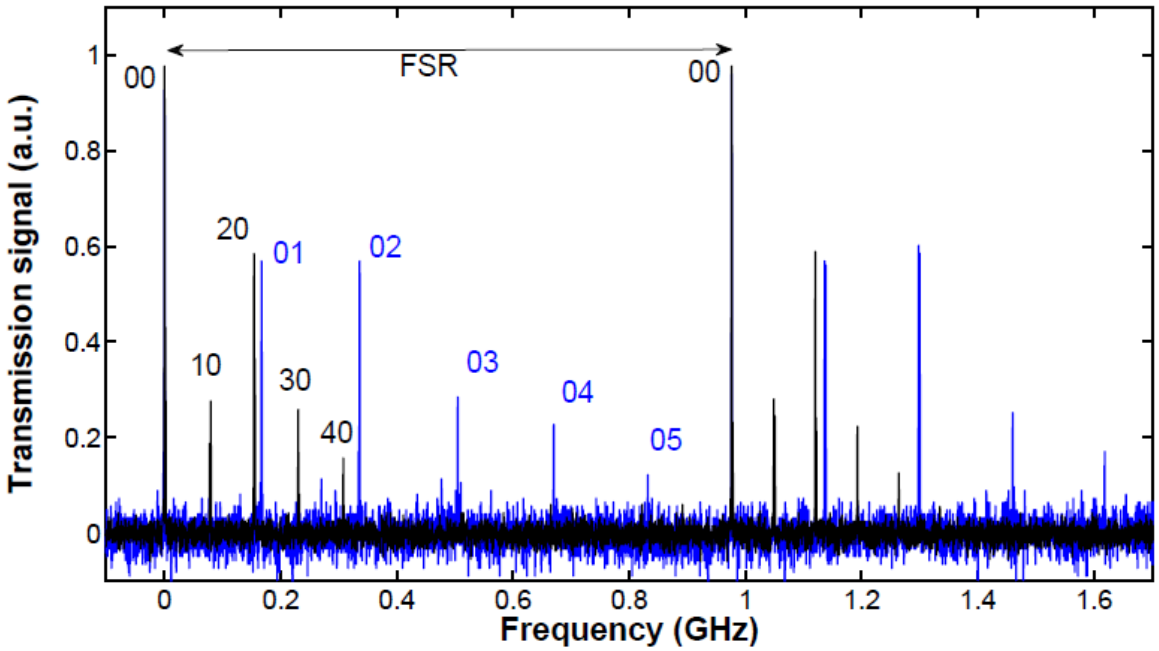

Figure 3.5: Cavity transmission signal as a function of injection frequency. $\mathrm{TEM}_{\mathrm{m0}}$ parallel and $\mathrm{TEM}_{\mathrm{0n}}$ perpendicular to the cavity plane transverse modes are shown in black and blue respectively [51]

orders corresponding to a given $\mathrm{TEM}_{\mathrm{mn}}$ mode. Finally, $q_0^{\parallel/\perp} \equiv q_{\parallel/\perp}(0)$.

The frequency spacing between two longitudinal modes p and p' of equal transverse mode order m and n, is $\Delta p \equiv p - p'$ times the free spectral range (FSR) of the cavity. This can be measured by injecting a laser into the cavity, and detecting the transmission of the carrier and the sidebands produced via phase–modulation simultaneously (see also Sec. 3.5 for data involving a similar procedure at 780 nm), using a sweep on the current control of the laser. The EOM modulation frequency that maximizes the transmission of the overlapped peaks corresponds to the FSR. Using this method a value of $\Delta\omega_{\mathrm{FSR}} = 2\pi \times (976.20 \pm 0.05)$ MHz was achieved [46]. It is worth mentioning that this value of FSR is in good accordance with the expected length of an intracavity trip. Indeed, $L = 2\pi \times c/\Delta\omega_{\mathrm{FSR}} = 307.10 \pm 0.02$ mm, where c is the speed of light in vacuum, while summing the theoretical values of the two diagonals and the two sides of the square in our bow-tie cavity (see Subsec. 3.1.1) we find the value for the intracavity trip $L_{th} = 2 \times 63.64$ mm $+ 2 \times 90.00$ mm $= 307.28$ mm.

Finally, the dependence of the mode frequencies on the complex radius of curvature and

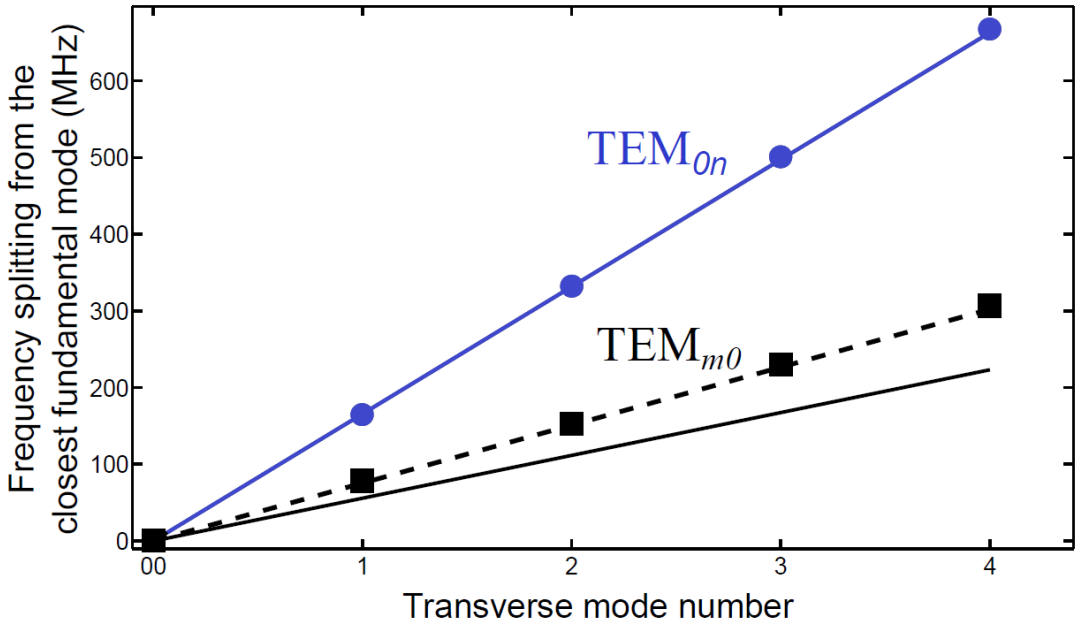

Figure 3.6: Transverse mode frequency spacing following Eq. 3.20 for the close to concentric cavity configuration present at our cavity. $\mathrm{TEM_{m0}}$ parallel and $\mathrm{TEM_{0n}}$ perpendicular to the cavity plane transverse mode dependence in m and n are shown in black and blue respectively. Parallel direction measurements show a discrepancy between theoretical prediction and true spacing [52].

the ABCD matrix coefficients means that the measurement of higher order mode frequencies of the cavity provides valuable information to characterize its geometric parameters. In Fig. 3.5, the experimental transmission spectrum is shown as measured at 1560 nm wavelength. The transverse mode spacing between adjacent $\mathrm{TEM_{m0}}$ modes, which are preferentially excited when a horizontal misalignment of the injected laser is applied, and adjacent $\mathrm{TEM_{0n}}$ modes which are obtained by vertically misaligning the injected beam, is 78.9 and 164.6 MHz respectively at 1560 nm [46].

The quasi–concentric configuration in our cavity means that the beams are close to being tightly focused at the crossing region. The horizontal axis in particular is the one which is closest to instability and shows the largest discrepancy [46] with the theoretical prediction (see Fig. 3.6).

3.2 Laser amplification and interaction with atoms within the cavity

We have presented above the structure and spacing of the modes present in our bow–tie cavity in the paraxial approximation. Now, in this section, we intend to present to which extent the laser field injected into the cavity gets amplified at 1560 nm first, and later on in which way it allows to interact with rubidium atoms loaded into the science chamber at the center of the cavity.

3.2.1 Bow–tie cavity finesse

An optical resonator is an open system that suffers from losses via the coupling of the inner modes to the continuum of modes of the electromagnetic field outside. This coupling occurs through the mirrors, which leak some amount of the resonant cavity mode outwards depending on their quality. To quantify the quality of the bow-tie cavity itself, we use the widely used finesse figure of merit. The finesse is the ratio between the $\Delta\nu_{\mathrm{FSR}}$ which separates two identical longitudinally adjacent $\mathrm{TEM_{ij}}$ modes, and their full width at half maximum $\delta\nu_{\mathrm{FWHM}}$ of their linewidth, that is,

$$\mathcal{F} = \frac{\Delta\nu_{\mathrm{FSR}}}{\delta\nu_{\mathrm{FWHM}}}. \tag{3.21}$$

The larger this quantity is the sharper are the resonances in relation to their frequency separation, and the more roundtrips a photon does on average in its interior before being lost through transmission or diffusion.

For the particular case of our bow–tie cavity, the finesse is given by the following equation [54],

$$\mathcal{F}_{BT} = \frac{\pi r^2}{1 - r^4}, \tag{3.22}$$

where r is the ratio of the reflected electric field's amplitude to that of the incident amplitude of one cavity mirror. Neglecting mirror absorption, and using manufacturer ATFilms' transmission leak data $t^2 = 4.4 \times 10^{-4}$ for 1560 nm and $t^2 = 7.7 \times 10^{-6}$ one gets the theoretical reflection coefficients and finesses listed in Tab. 3.3.

$\lambda\ (nm)$	r^2	$\mathcal{F}_{BTC}$
1560	0.99956	4159.2
780	0.9999923	101670

Table 3.3: Theoretical reflection coefficients and finesses for 1560 and 780 nm radiations.

3.2.1.1 Finesse measurement from cavity spectroscopy

In our experiment, finesse at 1560 nm is an important parameter in relation to obtaining a sufficiently deep FORT, which is the all–optical method chosen to achieve the lowest temperature and most dense atomic samples when the BIARO experiment was designed. Therefore, the motivation for measuring the cavity finesse in the case of 1560 nm light was clear from the very beginning of the BIARO project.

Previously, the finesse measurement was achieved by scanning a sideband of a 1560 nm phase modulated laser via an electro–optic modulator (EOM). The velocity of the sweep could be precisely controlled thanks to a frequency synthesizer, and calibrated to infer the amount of time the transmitted sideband took to cross the resonance. This allowed to determine the FWHM linewidth which was found to be $\delta\omega_{1560} = 2\pi \times 0.546$ MHz. The measurement of the linewidth combined with the one for the FSR presented above, yields a value of 1560 nm finesse [54]

$$\mathcal{F}_{1560} = \frac{\Delta\omega_{\mathrm{FSR}}}{\delta\omega_{1560}} = 1788. \tag{3.23}$$

This lower value than the theoretically expected one of 4159.2 is related to additional losses on the mirrors, coming either from a lower reflectivity than the one provided by the mirror maker, or diffusion losses related to the reflection angle imposed by the bow–tie cavity geometry [46].

3.2.2 Cavity induced AC Stark shift in the two level approximation

The two–level atom model presented in Subsec. 1.1 is equally useful to explain the nature of another effect produced by the interaction of atoms with laser radiation. This is the so called AC Stark shift, which is responsible for the modification of the energy of the electronic levels in the atoms as opposed to the effect on the populations we focused on above, and which is at the heart of the dipole trap production technique [55] we use for trapping and cooling

neutral atoms to ultracold temperatures.

We intend to show this phenomenon first for the case of a two–level atom by rewriting Eqs. 1.5 in the rotating wave approximation for the new variables $\tilde{c}_1 = c_1 e^{-i(\omega-\omega_0)t/2}$ and $\tilde{c}_2 = c_2 e^{i(\omega-\omega_0)t/2}$, i.e. in a frame rotating at frequency ω. This gives,

$$\begin{aligned} i\dot{\tilde{c}}_1 &= \frac{1}{2}\left(\delta\tilde{c}_1 + \Omega\tilde{c}_2\right), \\ i\dot{\tilde{c}}_2 &= \frac{1}{2}\left(\Omega\tilde{c}_1 - \delta\tilde{c}_2\right), \end{aligned} \tag{3.24}$$

which is a system of two ordinary differential equations whose characteristic polynomial is $\lambda^2 - \delta^2/4 - \Omega^2/4$ and thus $\lambda = \pm(\sqrt{\delta^2+\Omega^2})/2$ its eigenvalues. This means that by increasing the laser intensity Ω, the bare atomic states get modified to give dressed states [56] for the system composed by the atoms plus the light.

Even ignoring the effect on $5P_{3/2}$ level's scalar polarizability all the electric dipole allowed transitions but the $5P_{3/2} \rightarrow 5S_{1/2}$ have, this simple two–level model of the AC Stark shift already accounts for the qualitative modification of ^{87}Rb's ground state under the far red detuned dipole trap present in our FORT (see Ann. A.). It is easy to see this by Taylor expanding λ around $\Omega = 0$ and preserving only quadratic terms, which physically means $\Omega \ll |\delta|$. We thus get

$$\lambda \approx \pm\left(\frac{\delta}{2} + \frac{\Omega^2}{4\delta}\right). \tag{3.25}$$

It follows from Eq. 3.25, where from Eqs. 3.24 positive and negative signs correspond to $\tilde{c}_1$ and $\tilde{c}_2$ respectively, that when $\delta < 0$, i.e. for a red detuned laser, the light will make the dressed states separate by $\hbar\Omega^2/2|\delta|$ from each other. This is in the same direction that the scalar polarizability term would shift the fine splitting of the D_2 line of ^{87}Rb if we considered its electronic structure was made only by $5S_{1/2}$ and $5P_{3/2}$ fine manifolds.

However, the structure of alkali atoms is made of many other electronic levels and thus the analysis of the AC Stark effect even qualitatively, needs to be done calculating all the contributions coming from them (see Ann. A.). This is particularly true when dealing with the gray molasses technique we use in our experiment, since the precise blue detuning required from $|5S_{1/2}, F = 1, 2\rangle \rightarrow |5P_{3/2}, F' = 2\rangle$ transitions for cooler and repumper respectively, is set predominantly by the multilevel AC Stark shift contribution produced by the intracavity 1560 nm FORT on the $5P_{3/2}$ manifold.

3.2.2.1 Ground state shift in the intra–cavity cross dipole FORT

The laser induced shift on a two level atom we studied above, and more specifically the multilevel extension at 1560 nm for the D_2 line in ^{87}Rb (see Ann. A.), explain the mechanism that allows us to trap and cool atoms farther through the gray molasses stage in our experiment. Nonetheless, the AC Stark shift on the ground state exactly corresponds to the dipole potential for a two level atom if the fine-structure is not resolved by the incident radiation [57], which is the case of 1560 nm laser with respect to the energy difference between $5P_{1/2}$ and $5P_{3/2}$ manifolds of ^{87}Rb. Then, if the atoms reside most of the time in the ground state, as happens once the atoms have been loaded and cooled down in the FORT, the dipole potential of interest to analyze the force imparted on the trapped atoms by the electric field of frequency ω and intensity I can be written classically as

$$U_d(\boldsymbol{r}) = -\frac{3\pi c^2}{2\omega_0^3}\left(\frac{\Gamma}{\omega_0-\omega}+\frac{\Gamma}{\omega_0+\omega}\right) I(\boldsymbol{r}), \tag{3.26}$$

where ω_0 is again the frequency difference between the ground and excited states of the two level atom, and Γ the damping rate of the transition ($\Gamma_{D_1} \simeq 2\pi\times$ 5.75 MHz and $\Gamma_{D_2} \simeq 2\pi\times$ 6.07 MHz [58]).

In order to asses the validity of Eq. 3.26 as a conservative potential, its magnitude should be compared to the scattering rate in the general case for any incident angular frequency ω, as opposed to the case in Subsec. 1.1 where we applied the rotating wave approximation. In the general case, a classical calculation as for Eq. 3.26 yields,

$$\Gamma_{scatt}(\boldsymbol{r}) = \frac{3\pi c^2}{2\hbar\omega_0^3}\left(\frac{\omega}{\omega_0}\right)^3\left(\frac{\Gamma}{\omega_0-\omega}+\frac{\Gamma}{\omega_0+\omega}\right)^2 I(\boldsymbol{r}). \tag{3.27}$$

For light at 1560 nm, the energy associated to the scattering rate is around eight orders of magnitude weaker than the dipole potential produced as shown in Fig. 3.7, which means we can safely ignore the heating produced by scattering of photons during the evaporation process which occurs on a timescale of few seconds.

We thus focus on the dipole potential at 1560 nm in the following, or equivalently $\omega = \omega_0/2$, for which the more explicit expression

$$U_d(\boldsymbol{r}) = -\frac{4\pi c^2\Gamma}{\omega_0^4} I(\boldsymbol{r}), \tag{3.28}$$

can be written.

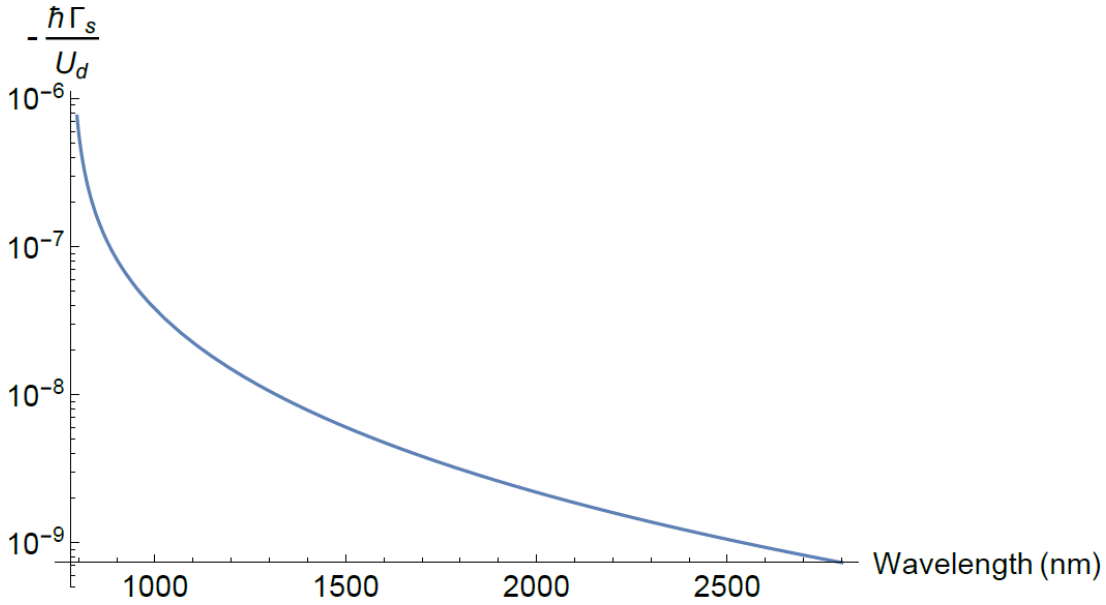

Figure 3.7: Energy associated to the scattering rate over dipole trap potential as a function of red detunning from the transition. At 1560 nm, the validity of the conservative potential approximation is apparent.

The main peculiarity of the crossed FORT in our experiment is the fact that it is created by a bow–tie cavity. This has some advantages but also important disadvantages common to cavities in general. The main advantage comes from the recycling of the power provided by the intra–cavity reflection, which means that with a moderate amount of power at the injection of the cavity, a large power is attained at the trapping region in the center where the cavity arms cross. A big drawback is however twofold, first the geometry of the cavity imposes a fixed trapping volume where the only adjustable parameter is the power injected into the cavity, and second, the angle at which both arms of the cavity cross is very tightly imposed due to the almost fixed nature of the cavity mirrors.

We consider next the electric field intensity profile produced by a single arm excited in the fundamental TEM_{00} mode,

$$I_m(x,y,z) = \frac{2P}{\pi w_{\parallel}(z) w_{\perp}(z)} \exp\left[-\frac{2x^2}{w_{\parallel}^2(z)} - \frac{2y^2}{w_{\perp}^2(z)}\right], \tag{3.29}$$

where P is the intra–cavity power, and $w_{\parallel/\perp}(z)$ the parallel and perpendicular Gaussian beam radii as defined in Subsec. 3.1.2. It is convenient for the second arm which crosses the first one at 90 degrees on the cavity center to interchange Cartesian coordinates x and z, while

close to the cavity center where both arms overlap we can also approximate parallel and perpendicular Gaussian beam radii by parallel and perpendicular waists (see Subsec. 3.1.2) $w_{\parallel/\perp}(0)$, respectively. We can then write,

$$I(x,y,z) = \frac{2P}{\pi w_{\parallel}(0) w_{\perp}(0)} \left[e^{-\frac{2x^2}{w_{\parallel}^2(0)}} + e^{-\frac{2z^2}{w_{\parallel}^2(0)}} \right] e^{-\frac{2y^2}{w_{\perp}^2(0)}}, \tag{3.30}$$

for the total intensity produced by both arms.

Substituting Eq. 3.30 in Eq. 3.28 and taking the potential produced by Earth's gravity into account, one gets the total dipole plus gravity potential ^{87}Rb atoms see as a function of intra–cavity power,

$$U_d(x,y,z) = -\frac{8Pc^2\Gamma}{\omega_0^4 w_{\parallel}(0) w_{\perp}(0)} \left[e^{-\frac{2x^2}{w_{\parallel}^2(0)}} + e^{-\frac{2z^2}{w_{\parallel}^2(0)}} \right] e^{-\frac{2y^2}{w_{\perp}^2(0)}} + mgy, \tag{3.31}$$

where m is the atomic mass and $-g$ the gravitational acceleration. This acceleration plays an important role at end of the stage that allows to get the coldest temperatures in our experiment, that is, at the end of the evaporative cooling process (see Subsec. 3.4 for details about the ramping down of the intracavity power) when the effect of the linear potential produced by gravity becomes comparable to the depth of the confining dipole potential in the vertical direction. In our cross dipole trap, this point sets a limit beyond which the evaporation procedure is no longer efficient (see Fig. 3.8). Intuitively, this happens when the dipole potential is not strong enough to counterbalance the gravitational one.

More formally, one can find the minimum of the potential in Eq. 3.31 to study the condition under which the counterbalancing stops. We denote the point where the minimum of the potential in Eq. 3.31 occurs by $\boldsymbol{r}_0 = (x_0, y_0, z_0)$, where $z_0 = x_0 = 0$, and y_0 is found by taking the partial derivative of the potential with respect to y and equaling it to zero,

$$\frac{\partial U_d(0,y,0)}{\partial y}\Big|_{y=y_0} = \frac{64Pc^2\Gamma}{\omega_0^4 w_{\parallel}(0) w_{\perp}^3(0)} y_0 e^{-\frac{2y_0^2}{w_{\perp}^2(0)}} + mg = 0. \tag{3.32}$$

This leads to the transcendental equation,

$$y_0 e^{-\frac{2y_0^2}{w_{\perp}^2(0)}} = -\frac{mg\omega_0^4 w_{\parallel}(0) w_{\perp}^3(0)}{64Pc^2\Gamma}, \tag{3.33}$$

which has a solution in terms of the Lambert function $W(v)$,

$$y_0 = -\frac{w_{\perp}(0)}{2}\sqrt{-W(v)}, \tag{3.34}$$

with $v = -[mg\omega_0^4 w_{\parallel}(0) w_{\perp}^2(0)/(32Pc^2\Gamma)]^2$.

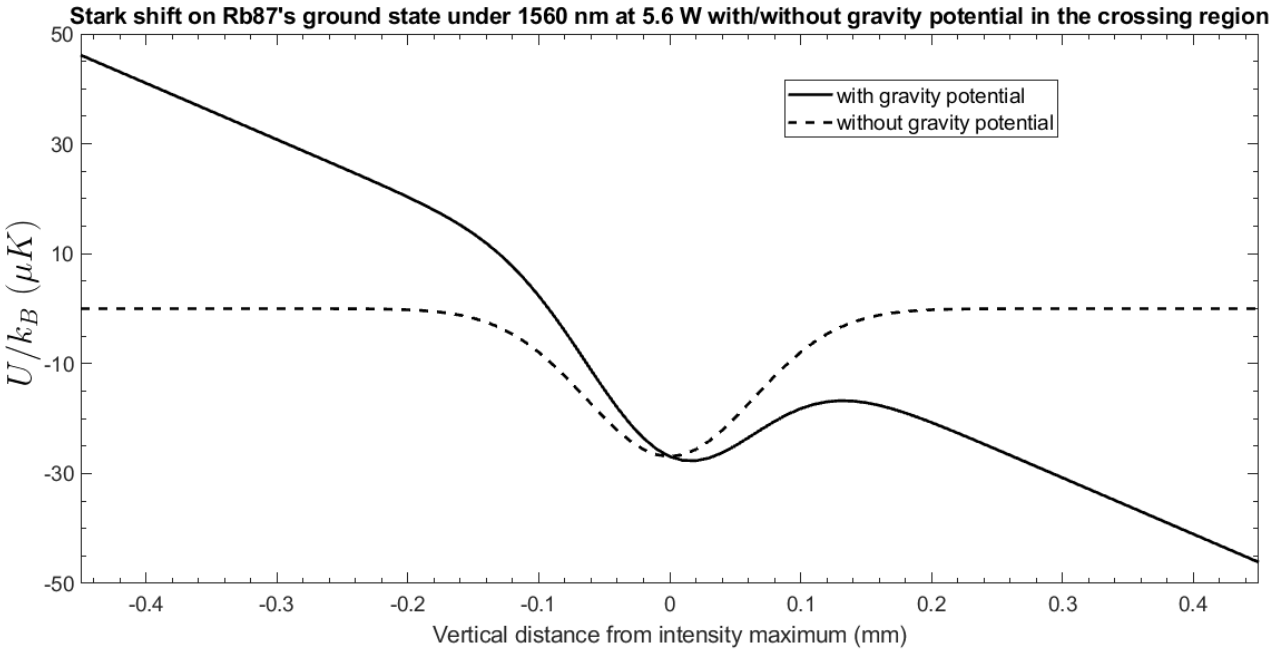

Figure 3.8: Dipole plus gravity potential seen by atoms at the end of the evaporation ramp in the center of our cavity.

The plot in Fig. 3.9 shows how y_0 changes as a function of intra–cavity power P, according to Eq. 3.34. The fact that $y_0 < 0$ means gravity induces a displacement of the center of the potential downwards. On the other hand, given that $v \in [-1/e, \infty)$ for it to satisfy the Lambert function, intra–cavity power P needs to obey,

$$\frac{Pc^2\Gamma}{mg\omega_0^4 w_{\parallel}(0) w_{\perp}^2(0)} \geq \sqrt{e}/32, \tag{3.35}$$

in order the dipole potential be a trapping one (see black vertical line in Fig. 3.9). This corresponds to a trap depth of 5 μK, that is, a factor of five less than the one in Fig. 3.8 which shows the more realistic limit at which the evaporation process is no longer efficient.

On the other hand, for y_0 to be a minimum the condition to fulfill is,

$$\frac{\partial^2 U_d(0,y,0)}{\partial y^2}\Big|_{y=y_0} = \frac{64Pc^2\Gamma}{\omega_0^4 w_{\parallel}(0) w_{\perp}^3(0)} \left[e^{-\frac{2y_0^2}{w_{\perp}^2(0)}} - \frac{4y_0^2}{w_{\perp}^2(0)} e^{-\frac{2y^2}{w_{\perp}^2(0)}} \right] > 0, \tag{3.36}$$

which implies $y_0 > -\omega_{\perp}(0)/2$ in accordance with the graph in Fig. 3.9.

Second derivatives of the potential are also useful to define the trapping frequencies of the dipole trap. By approximating the potential in Eq. 3.31 using Taylor series up to second order,

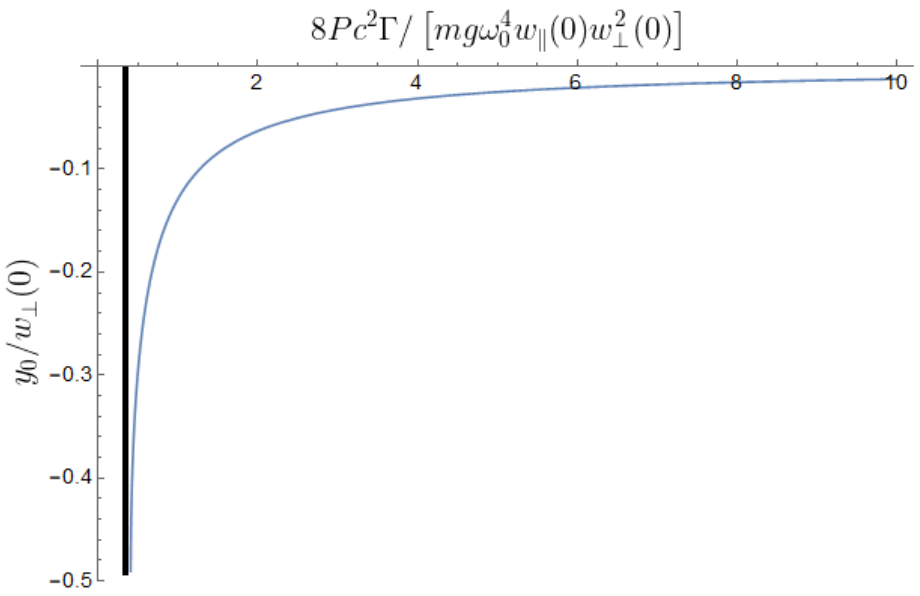

Figure 3.9: In blue, dependence on intra–cavity power P of the vertical position y_0 for the minimum of the potential. Vertical black line represents the value of the power below which there is no longer a trapping potential.

we can treat the problem as a harmonic one around the minimum of the trap $\boldsymbol{r}_0 = (x_0, y_0, z_0)$,

$$U_h(\boldsymbol{r}) = U_d(\boldsymbol{r}_0) + (\boldsymbol{r} - \boldsymbol{r}_0)^T \nabla U_d(\boldsymbol{r}_0) + \frac{1}{2}(\boldsymbol{r} - \boldsymbol{r}_0)^T \boldsymbol{H}(\boldsymbol{r}_0)(\boldsymbol{r} - \boldsymbol{r}_0) + O\left[(\boldsymbol{r} - \boldsymbol{r}_0)^3\right], \tag{3.37}$$

where $\boldsymbol{H}(\boldsymbol{r}_0)$ is the Hessian matrix of $U_d(\boldsymbol{r}_0)$ with elements $H_{ij}(\boldsymbol{r}_0) = \partial^2_{ij} U_d(\boldsymbol{r}_0)$, and T an operator which implies the multiplication of crossed terms. For large dipole trap powers, gravity can be neglected and the linear term drops out, while the constant term adds just an offset which does not change the form of the potential. We can then approximate the dipole potential by the potential created by a three dimensional harmonic oscillator,

$$U_h(\boldsymbol{r}) = -\frac{m}{2}\left(\omega_x^2 x^2 + \omega_y^2 y^2 + \omega_z^2 z^2\right), \tag{3.38}$$

where ω_x, ω_y and ω_z are the associated angular frequencies.

Finally, the angular frequencies can be calculated from the Hessian matrix which is real and symmetric, and thus diagonalizable. Defining,

$$U_0 = \frac{8Pc^2\Gamma}{\omega_0^4 w_\parallel(0) w_\perp(0)}, \tag{3.39}$$

and using $\omega_i = \sqrt{H_{ii}(\boldsymbol{r}_0)/m}$ with $i = x, y, z$, one finds the frequencies are proportional to the

square root of the power injected in the cavity, and inversely proportional to the waists,

$$\omega_x = \omega_z = \sqrt{\frac{4U_0}{mw_{\parallel}^2(0)}}, \tag{3.40a}$$

$$\omega_y = \sqrt{\frac{8U_0}{mw_{\perp}^2(0)}}. \tag{3.40b}$$

Indeed, the parameter U_0 which corresponds to the maximal depth of the trap, depends linearly on intracavity power. Intracavity power in turn depends on the laser power injected at the cavity entrance as well as on the coupling efficiency of the laser to the cavity (see Subsec. 3.1.2). Its precise value, however, is not easy to obtain since it cannot be measured directly.

Indirect measurements of both the power and the geometry of the intracavity mode were done in our cavity in the past [49]. The adopted method is based on the tomography of the differential Stark shift produced by light at 1560 nm injected in the cavity using a probe beam at 780 nm, which is swept to address atoms at different positions in the trap. By monitoring the detuning of the probe with respect to the bare transition, which can be done with great precision, one can infer the trapping intensity at a given position (see Ann. A.), including the maximum one present at the bottom of the trap, by measuring the position of the atoms in the trap simultaneously via absorption imaging with the same probe. This allowed to obtain $w_{\parallel}^{exp}(0) = 97 \pm 1$ μm, which is the value we use for our calculations. Furthermore, the power transmitted out of the cavity can be measured simultaneously, which allows to obtain the intracavity power to transmitted power ratio [46],

$$\frac{P}{P_{out}} = 2850. \tag{3.41}$$

At the maximum of the power, which is the power at which the evaporative cooling process is initiated (see Subsec. 3.4), we measure 19.9 mW of optical power in transmission. According to Eqs. 3.41 and 3.40, this output power corresponds to $\omega_x^{max} = \omega_z^{max} \simeq 2\pi \times 840$ Hz and $\omega_y^{max} \simeq 2\pi \times 905$ Hz.

3.2.2.2 Alignment of the cavity via imaging of the FORT arm overlap

An optimal overlap at the crossing of the two arms which form the dipole trap is of critical importance in order to have the right trapping potential at the center of the cavity. If we

consider the arms to be misaligned so that the top one lies $a/2$ above $y = 0$ and the bottom one the same amount below, then ignoring gravity again, the dipole potential can be written as [52],

$$U_a(\boldsymbol{r}) = -\frac{8Pc^3\Gamma}{\omega_0^4 w_\parallel(0) w_\perp(0)} \left\{ e^{-\left[\frac{2x^2}{w_\parallel^2(0)} + \frac{2ay}{w_\perp^2(0)}\right]} + e^{-\left[\frac{2z^2}{w_\parallel^2(0)} - \frac{2ay}{w_\perp^2(0)}\right]} \right\} e^{-\left[\frac{2y^2}{w_\perp^2(0)} + \frac{a^2}{2w_\perp^2(0)}\right]}. \tag{3.42}$$

Now computing the partial derivative with respect to y at $\boldsymbol{r}_0 = (0, y_0, 0)$ to find again the minimum of the potential along the vertical direction, we get

$$4y_0 \left[e^{-\frac{2ay_0}{w_\perp^2(0)}} + e^{\frac{2ay_0}{w_\perp^2(0)}} \right] + 2a \left[e^{-\frac{2ay_0}{w_\perp^2(0)}} - e^{+\frac{2ay_0}{w_\perp^2(0)}} \right] = 0, \tag{3.43}$$

which leads to another transcendental equation, namely,

$$\tanh\left(\frac{2ay_0}{w_\perp^2(0)}\right) = \frac{2y_0}{a}. \tag{3.44}$$

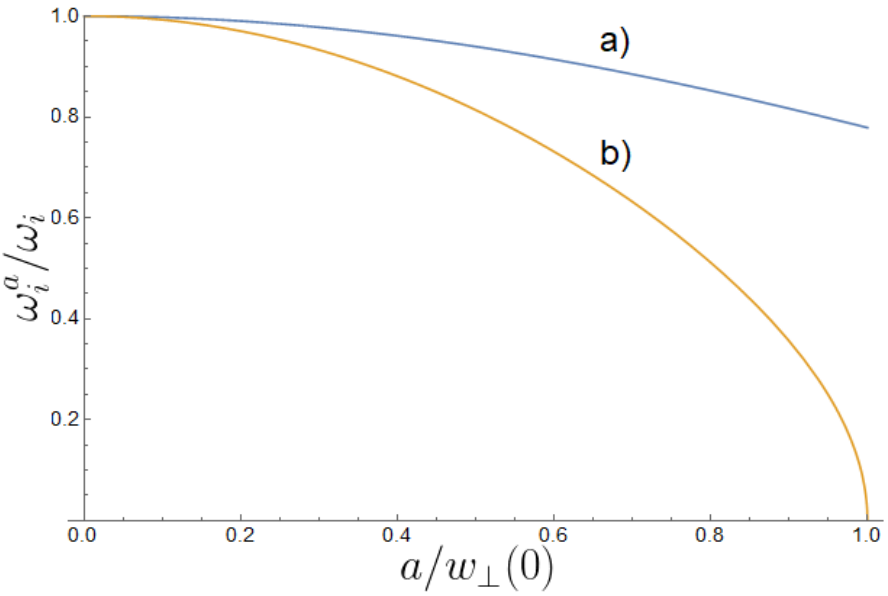

Figure 3.10: Trapping frequencies as a function of vertical misalignment of the cavity arms. a) corresponds to horizontal frequencies while b) shows how the vertical frequency gets modified.

When $a > w_\perp(0)$, the curves on the right hand side and the left hand side of Eq. 3.44 with y_0 as a variable, cross each other three times, that is, three critical points will exist corresponding to a double well potential in the vertical direction. This happens when the arms are very misaligned. When $a \leq w_\perp(0)$, on the other hand, there is a single crossing point at the origin $y_0 = 0$, and the potential remains a single well which is the case of interest

for us. In this case we find the modified trap frequencies ω_i^a take the following form,

$$\omega_x^a = \omega_z^a = \omega_x e^{-\frac{a^2}{4w_\perp^2(0)}}, \tag{3.45a}$$

$$\omega_y^a = \omega_y e^{-\frac{a^2}{4w_\perp^2(0)}} \sqrt{1 - \frac{a^2}{w_\perp^2(0)}}. \tag{3.45b}$$

Fig. 3.10 shows how the frequencies evolve when the distance a increases. Horizontal frequencies are less dependent on misalignment than the vertical one which vanishes when $a = w_\perp(0)$.

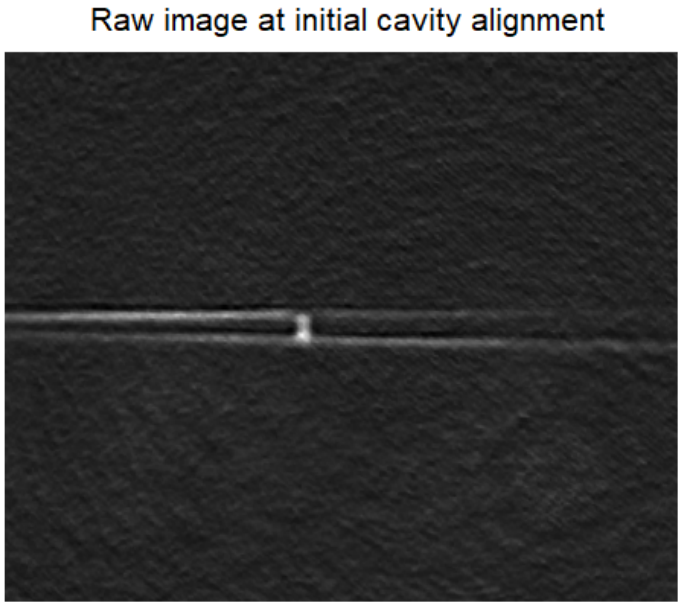

Figure 3.11: Initial cavity alignment as found when we installed the side imaging setup. Atoms are loaded in the FORT and released before 1 ms TOF.

During my PhD, the alignment of the cavity arms was monitored using the side camera described in Subsec. 2.3, while the relative position between the arms was modified using one of the two picomotors present on one of the cavity mirrors. To monitor the alignment, absorption imaging was used for atoms loaded in the FORT. After a time–of–flight (TOF) of 1 ms, most of them are located close to the crossing region between the arms, but the position of the arms themselves which also trap atoms, is equally visible. The alignment at which the cavity was found when it was first monitored during my PhD, using the new side imaging system, is visible in Fig. 3.11. The misalignment was so large that two separate clouds are clearly visible. Indeed, we were in the case of a double well potential, and thus a huge

correction had to be applied in the vertical direction.

To control the picomotors, which are produced by New Focus, we used an external joystick available from the same company. The joystick is connected to a block of picomotor drivers and a controller, identified by the model codes 8754, 8753 and 8752, respectively. An image of the whole kit with the Ethernet cables needed to connect the different components between them and to the picomotors is depicted in Fig. 3.12. The drivers are connected to a 24 V power supply and then the joystick and the controller are fed from the drivers with 5 V via two pins in the Ethernet cable. Each time the picomotor advances the mirror wheel by one step, a click is clearly audible and this practically allows to modulate the pressure one needs to apply on the joystick in the horizontal or vertical direction.

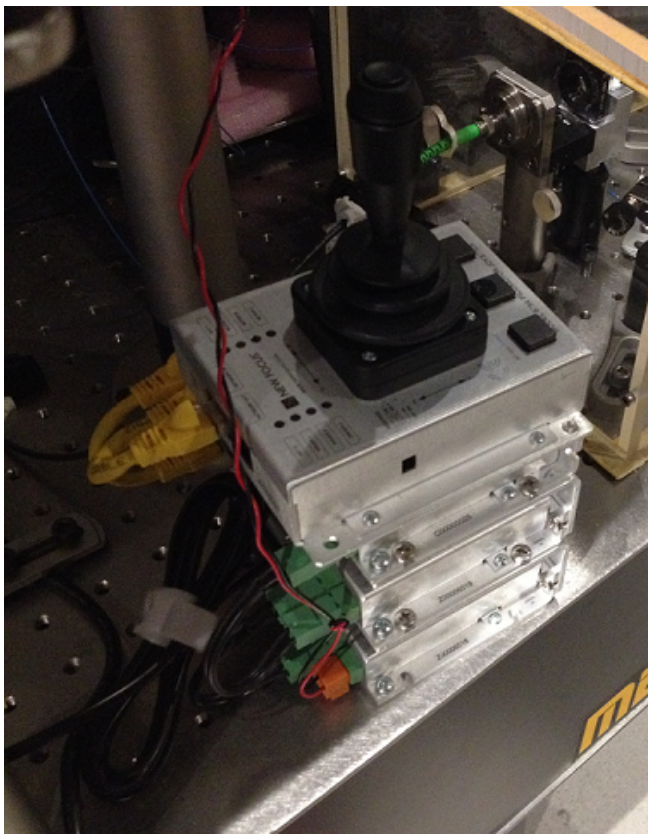

Figure 3.12: New Focus 8752, 8753 and 8754 picomotor control modules and Ethernet cables used to modify cavity alignment.

As explained in Subsec. 3.1.1, only one of the two picomotors controlling horizontal and vertical alignment works, and therefore the system is responsive only along the vertical direction which is fortunately the most important one. The other one, as expected, was not

producing any audible click at all.

Given the huge misalignment detected by the side imaging, we had to push the joystick upon hearing some hundreds of clicks, which corresponds to a few hundreds of μm. In the meantime, we continuously ran the experiment to load the FORT with atoms and image them in order to detect the correction on the alignment. The result of this coarse alignment process as well as an intermediate situation between the one depicted in Fig. 3.11 and the final one is shown in Fig. 3.13.

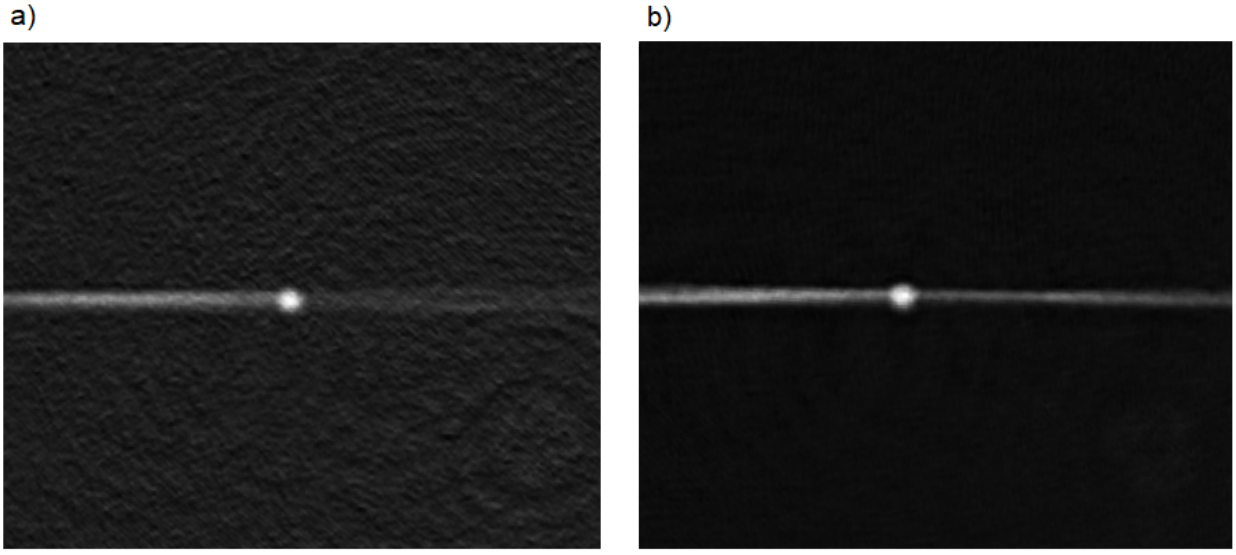

Figure 3.13: 1 ms TOF images of atoms trapped in the FORT for slightly misaligned cavity in a), and well aligned cavity in b).

Once the coarse alignment was finished, we focused on the fine one which is controlled through piezo–electric actuators attached to the three axes on a different cavity mirror (see Subsec. 3.1.1). The optimal coupling efficiency of the FORT to the cavity was lost during the coarse alignment process, and thus adjustments in the new 1560 nm injection setup, which is described in next Sec. 3.3, had to be performed. This is in essence an iterative process during which one needs to adjust the piezos and the injection setup one at a time, back and forth in order to achieve the best coupling efficiency.

3.3 Frequency locking of a diode laser to the cavity

A fundamental requirement for continuously injecting radiation into the cavity is to be able to adapt to the cavity's resonance frequency drifts permanently, otherwise the radiation will no longer be injected. This is done by creating an error signal that feeds–back both the laser's bias current and temperature in order to compensate for the drifts. However, regulating the laser's current and temperature to adapt to the cavity resonance is not entirely satisfying since the cavity resonances themselves do also drift with the temperature changes and vibrations produced in the surrounding environment. Therefore, in order to stabilize the frequency of the resonances the cavity length needs to be controlled, ideally by locking it to a spectroscopic signal. In our experiment this can be done by acting on the voltages controlling all the three piezo–electric actuators described in Subsec. 3.1.1 simultaneously. Generally, the system needs to apply corrections over a certain bandwidth, the larger this bandwidth is the more stable the frequency locking will be, not only because unitary gain will be attained at a larger frequency, but also and especially because the gain close to zero frequency will also be larger (see Ann. B. for more details).

On the other hand, we are interested in controlling the intracavity laser power in order to address the atoms trapped in the FORT in a controllable way, both when they are held in the FORT and therefore subjected to 1560 nm radiation, as well as to address them coherently via 780 nm light. It is on this second case when the stabilization of the cavity length becomes critical since to operate on the atoms in a reproducible way one must precisely know and control the detuning with respect to the atom transition.

After describing the frequency locking technique we use, we present the cavity injection setup we built at the beginning of my PhD. This was motivated by the fact that during previous work in our experiment, 1560 nm radiation was injected through a different cavity mirror from the one we currently use for the FORT. The old setup did not provide sufficient space for the new components to be added, and the flanges which were supporting it were weak and easily peaking up mechanical noise. Therefore, and in order to keep the old injection setup as reference, the decision to introduce an entirely new setup was made.

More importantly, the laser at use before for injecting 1560 nm light, is not adequate for

implementing optical molasses in our experiment, since this method requires turning off the magnetic field present during the MOT phase. Indeed, an old Distributed feedback (DFB) *Koheras* fiber laser was used to create the FORT at the time. This laser had an important limitation related to the low bandwidth of the piezo–electric actuators controlling the length of the laser–cavity. At the beginning, an AOM in double–pass configuration was used to increase the bandwidth, which allows faster correction of laser frequency by acting on the radio–frequency (RF) input signal of the AOM. This method, however, has the drawback of a low capture range limited by the range of frequencies over which the AOM is efficient. This range is, unfortunately, much lower than the roughly 500 MHz frequency shifts the turning off of the magnetic field created by the 3D–MOT coils produces on the cavity resonances before loading the FORT, and thus the double pass AOM technique is not suited for the in–trap gray molasses experiments we performed during our research.

Early in my PhD, a new solution was adopted, namely the introduction of a narrow linewidth 1560 nm diode laser which allows for frequency control via its bias current and temperature regulations alone. This allows a correction bandwidth no longer limited by piezo–electric actuators such as the ones present in the old DFB laser previously used to create the FORT in our bow–tie cavity. Before entering into more details about the actual setup, we describe in the following subsection the laser frequency correction technique we adopted in our new injection system.

3.3.1 Frequency stabilization using the Pound–Drever–Hall method

To frequency lock 1560 nm radiation to our bow–tie cavity, we use the Pound–Drever–Hall (PDH) technique [59], which is a method to stabilize the frequency of light emitted by a laser to the resonance of a cavity, provided an optical cavity that is more stable than the laser source. However in the particular case of our experiment, the objective is slightly different, since we do not intend to make the laser's frequency more stable by injecting it in the bow–tie cavity, but rather simply make the laser be injected even if neither the stability nor the linewidth of the cavity are better than the diode laser's ones.

In the realm of the PDH method, laser light is phase modulated at a larger frequency

than the linewidth of the cavity and directed to the injection, so that the carrier is the only one that can enter inside when it is close enough from the cavity resonance, and gets a phase change depending on its mismatch from it. The light reflected off is detected by a photodetector, where a signal that depends on the phase difference between the carrier and the sidebands appears. By mixing down this signal with a local oscillator that is in phase with the modulation, a measure of how far the laser carrier is off resonance with the cavity is obtained. We use the resulting electronic signal as feedback for active stabilization of the laser frequency by using a proportional-integral-derivative (PID) controller.

Let us now show the explicit form of the error signal in the weak modulation limit. By considering an incident electric field $E_0 e^{i\omega t}$ subjected to phase modulation $\beta \sin(\omega_m t)$ where $\beta \ll 1$, we get

$$\begin{aligned} E_i(t) &= E_0 e^{i[\omega t + \beta \sin(\omega_m t)]} = E_0 e^{i\omega t} \sum_{m=-\infty}^{\infty} J_m(\beta) e^{i\omega_m t} \\ &\approx E_0 e^{i\omega t} \left[J_0(\beta) + J_1(\beta) e^{i\omega_m t} + J_{-1}(\beta) e^{-i\omega_m t} \right], \end{aligned} \tag{3.46}$$

where $J_n(\beta)$ are the n-th Bessel functions of the first kind as in Subsec. 1.3.3. The part of the electric field that gets reflected out of the cavity gets an additional amplitude and phase change given by the complex reflection coefficient $R(\omega)$. The reflected field will take then the form

$$\begin{aligned} E_r(t) &= E_0 e^{i\omega t} \left[J_0(\beta) R(\omega) + J_1(\beta) R(\omega + \omega_m) e^{i\omega_m t} + J_{-1}(\beta) R(\omega - \omega_m) e^{-i\omega_m t} \right] \\ &= E_0 e^{i\omega t} \left\{ J_0(\beta) R(\omega) + J_1(\beta) \left[R(\omega + \omega_m) e^{i\omega_m t} - R(\omega - \omega_m) e^{-i\omega_m t} \right] \right\}. \end{aligned} \tag{3.47}$$

where we have used the relationship $J_{-n}(z) = (-1)^n J_n(z)$, valid for integer n.

The reflection signal becomes an electric current which is proportional to the optical power on the photodetector. This power, in turn, is proportional to the square of the electric field and thus

$$\begin{aligned} \frac{I_{ph}}{E_0^2} \propto \frac{E_r^*(t) E_r(t)}{E_0^2} &= \frac{\left[|R(\omega)| J_0(\beta) \right]^2 + \left[|R(\omega + \omega_m)|^2 + |R(\omega - \omega_m)|^2 \right] J_1^2(\beta)}{2} \\ &+ R^*(\omega) J_0(\beta) J_1(\beta) \left[R(\omega + \omega_m) e^{i\omega_m t} - R(\omega - \omega_m) e^{-i\omega_m t} \right] \\ &- J_1^2(\beta) R^*(\omega + \omega_m) R(\omega - \omega_m) e^{-i2\omega_m t} + c.c. \end{aligned} \tag{3.48}$$

After demodulation of the signal with the local oscillator in phase with the modulation, an

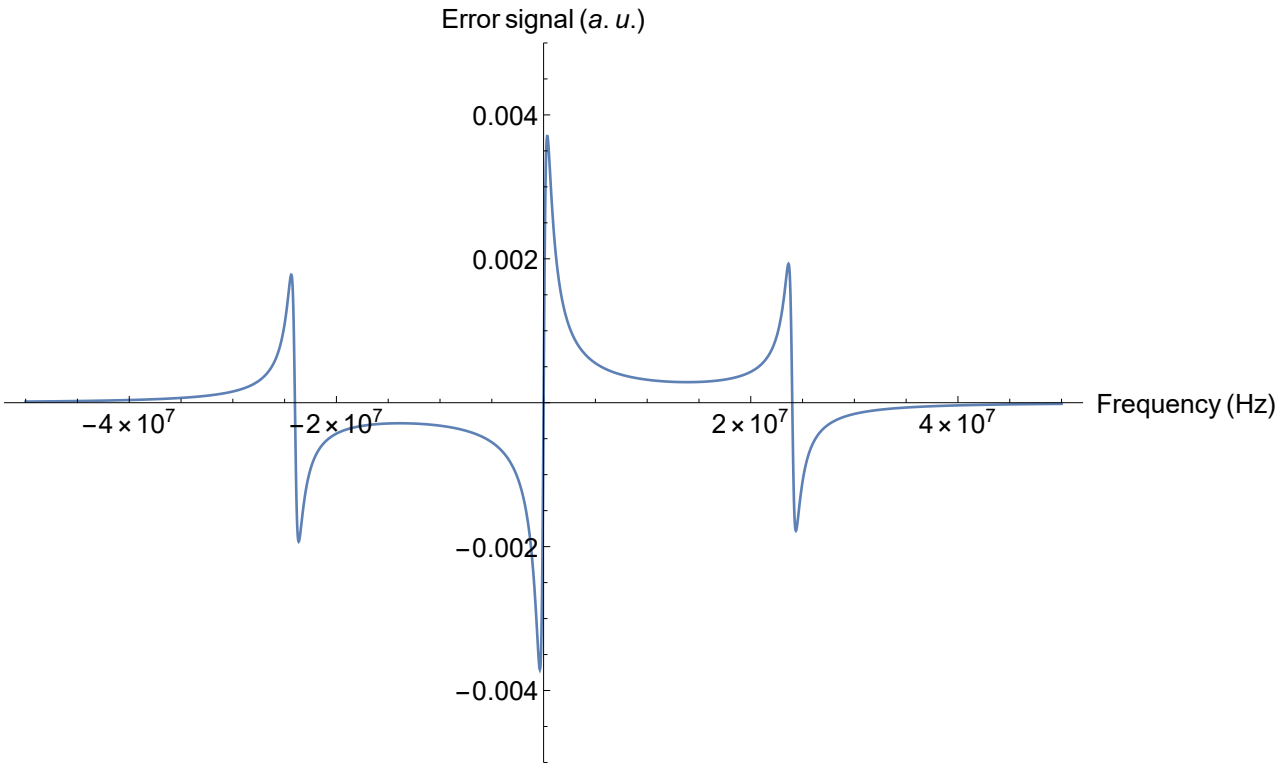

Figure 3.14: Theoretical PDH error signal in blue for 24.2 MHz modulation used in our setup.

error signal of the form

$$\epsilon_{PDH}(\omega) \propto R^*(\omega)R(\omega+\omega_m) - R(\omega)R^*(\omega-\omega_m) \tag{3.49}$$

is obtained. The complex reflection coefficient as given in Ref. [46] reads

$$R(\omega) = \frac{t^2 r^3 e^{i\omega L/c}}{1 - r^4 e^{i\omega L/c}}, \tag{3.50}$$

where t and r are again the ratios of the reflected and transmitted electric field's amplitudes to that of the incident amplitude of the mirrors, and L and c are the length of a full intracavity roundtrip and the speed of light in vacuum respectively. The real part of Eq. 3.49 is shown in Fig. 3.14 for the modulation frequency we impart on our laser radiation.

We next show how we experimentally apply the PDH method in our experiment and which are the actual components we use.

3.3.1.1 Implementation of the PDH method and injection setup on the bow–tie cavity

In our experiment, the phase modulation is created by a fibered Photline Technologies EOM. 80 % of the 1560 nm light produced by a narrow linewidth (1 kHz) RIO $Planex^{TM}$ diode is separated by a Comcore Technologies fibered splitter and injected into the EOM which phase–modulates the incident beam at a 24.2 MHz frequency, and at $\beta \simeq 0.8$ rad amplitude. A part of this RF signal is splitted and mixed with the reflection signal for demodulation in order to close the PDH loop which is governed by a PID circuit (more details in Ann. B.), providing the feed–back for both the current of the diode laser and the piezo–electric actuators controlling the bow–tie cavity length (see Fig. 3.15). This means that the later is locked to the laser at low frequency (<100 Hz) via one of the outputs of the PID circuit which was previously connected to a temperature stabilization unit from SYRTE–Observatoire de Paris to compensate for the slow drift of the error signal. The piezo–electric controller in turn comes from Mad City Labs. A comparator circuit compares the transmission signal out of the cavity with a digital control signal through a NAND gate, allowing to reengage the lock only when the desired cavity mode is present in the resonator.

The optic components used for the 1560 nm injection into the cavity are also visible in Fig. 3.15. In particular, an enlarging telescope (magnification 4) allows for optically mode matching to the TEM_{00} mode, followed by a cylindrical telescope that expands the horizontal direction using the 50-75 mm pair of cylindrical lenses mentioned above. The length on both telescopes needs to be adjusted very precisely in order to get the best coupling efficiency.

The signal reflected by the input mirror passes through a free-space Gooch $\&$ Housego AOM that is used to stabilize the power going onto a Thorlabs photodiode. This is done by an additional control loop governed by a proportional-integral (PI) control circuit (see Ann. B.), which is needed to ensure that the PDH error signal does not vary when a different amount of power is injected in the cavity. By taking the DC signal from the photodiode and by summing it with a control voltage that goes into the PI circuit, the free-space AOM is fed back via a voltage controlled oscillator (VCO) (see AOM drivers in Fig. 3.15).

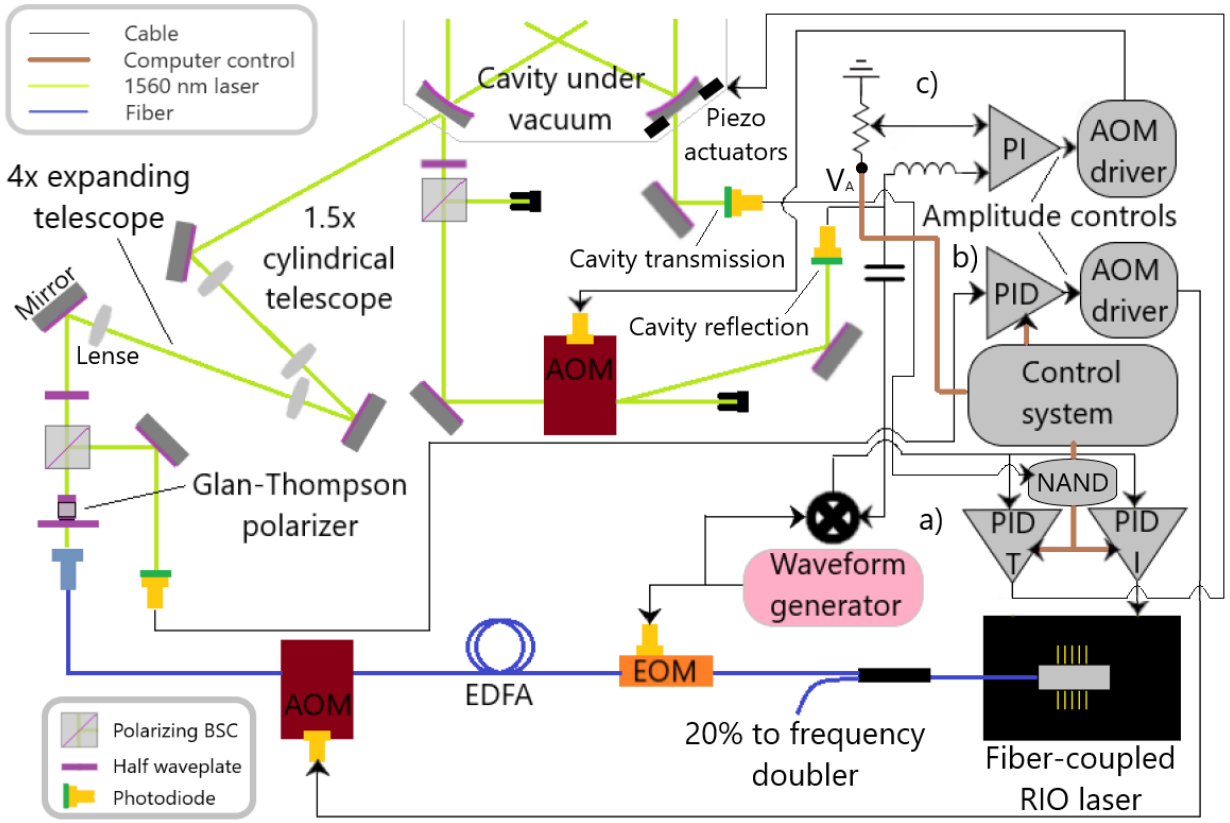

Figure 3.15: Cavity injection setup for 1560 nm laser. Power–stabilized radiation (see Subsec 3.4) is injected along the diagonal of the cavity, while a fraction of the reflected laser is detected by a photodiode to PDH frequency lock the RIO diode to the cavity resonance. This is done by control loop a), which takes into account the cavity transmission signal in order to determine via a NAND gate whether low or high gain is needed in the frequency lock circuit, while b) stabilizes power to the amount specified by the control system. Finally c) stabilizes power incident on the reflection photodiode in order the frequency lock error signal not to be dependent on the variation of power in the cavity.

3.4 Stabilization of the laser power and evaporation ramp

A main requirement to load and cool down atoms in the FORT is to be able to precisely control its power. The FORT always needs to be engaged in order the frequency stabilization to work, but on the meantime we are interested in minimizing its power when the initial cooling stages are implemented. The reason for this is the large AC differential Stark shift produced by 1560 nm light on ^{87}Rb, which strongly disturbs the cooling and repumping transitions (see Subsec. 3.2.2). The worst disturbance would occur when the atoms are imaged, since the imaging probe needs to be close to exact resonance with the whole atomic sample in order to get faithful images of the cloud. That is why before imaging the atoms, we do actually turn off the dipole trap. To do so, one can simply turn off the PID circuit governing the frequency lock, and once the image has been taken, turn it back on so that the laser gets injected into the cavity and the experiment is ready to run the next cycle.

But the turning on of the circuit followed by the automatic locking back to the cavity is obviously trickier than the reverse process. Once the frequency PID lock circuit is off, the laser starts to drift freely, and when turned back on it is usually too far away in frequency to be relocked automatically. Luckily, mechanical vibrations in the cavity produced by the 3DMOT coils, which are turned back on after the experimental sequence has finished, produce large enough oscillations for the laser to be found back on resonance. At that point the circuit is set to low gain and then the laser locks back to the cavity easier. Once the light has been injected and gone through the cavity, the transmission is detected as well, making the circuit automatically change to high gain and go to maximum stability thanks to the NAND gate described above. The pair of switches governing the gain and the power of the circuit, along with the circuit itself before it was introduced into a metal box for electromagnetic protection, are depicted in Fig. 3.16.

Experimentally, the output beam coming out of the EOM is amplified to up to 5W using a Keopsys erbium-doped fiber amplifier (EDFA) before entering a fibered AOM provided by AA Opto–Electronic. The latter allows to control the injected power into the cavity by sampling a small part of the laser light coming out from the AOM thanks to a polarizing beam splitter cube (PBSC), right after the Glan–Thompson polarizer depicted in Fig. 3.15. The signal

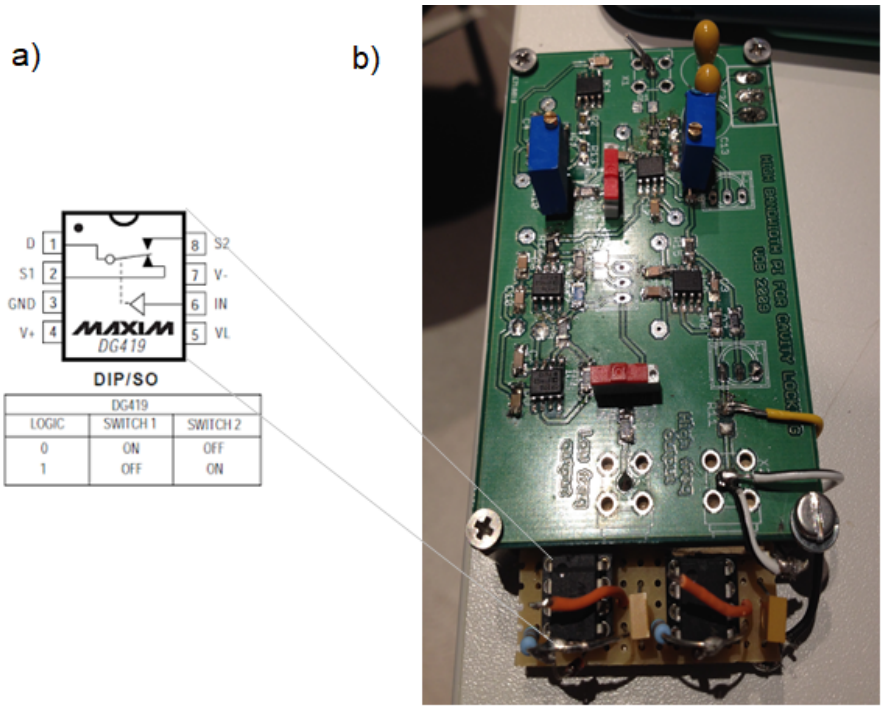

Figure 3.16: Schematic detail of gain and power switches for turning on and off the frequency lock circuit in a), while in b) frequency lock PID and switches after they were attached together.

detected in a Thorlabs photodiode was originally summed with a control voltage that is computer controlled before entering a PID circuit (see Ann. B.), which allows for stabilization of the power selected via computer.

At a later stage of the research however, an enhancement was added to the system, namely a direct digital synthesizer (DDS) allowing for the creation of arbitrary shaped functions when ramping down the dipole trap power. This device (model RSDG5082) can be loaded with functions written in comma separated values format (.csv), while its output is connected to a summing circuit in order to sum it with a computer controlled voltage. Since the introduction of the DDS, it has been the output of this summing circuit in turn the one which has been summed to the FORT power level signal in our experiment.

3.4.1 Optimization of evaporation ramp for maximum phase space density

Evaporative cooling is a broadly utilized technique to get the coldest temperatures while increasing atom phase space densities (PSD) [60, 61]. For dipole traps, it merely consists in decreasing the optical potential where the atoms have been loaded in small steps, so that the atoms, which have a Maxwell–Boltzmann distribution of energies E,

$$\mathcal{N}(E) = \mathcal{N}_0 \exp\left(-\frac{E}{k_B T}\right), \tag{3.51}$$

with $\mathcal{N}_0$ the lowest energy atoms for a given temperature T, are lost sequentially. This allows at each step, for the hottest atoms to escape, while collisions between the remaining colder ones which live deeper in the trap reestablish the thermal distribution, provided that the decrease of dipole trap power is done slowly enough.

Production of Bose–Einstein condensates (BECs) relying on this optical evaporation procedure alone for the evaporative cooling was first achieved at the beginning of this century [62]. In order to get a BEC, the temperature is not the only parameter to keep an eye on, but also the number of particles that are kept in the potential and the size of the atomic cloud. More precisely, one needs to increase the PSD in the center of the cloud, which takes the form [63],

$$\rho_{psd} = n_0 \left(\frac{h^2}{2\pi m k_B T}\right)^{3/2}, \tag{3.52}$$

where n_0 is the peak atom density in real space. Assuming the same Gaussian profile in all the three directions of space, the atom density is,

$$n(x, y, z) = n_0 \exp\left(-\frac{x^2 + y^2 + z^2}{2\sigma_c^2}\right), \tag{3.53}$$

where σ_c is the radius of the atomic density profile introduced in Subsec. 2.3. The peak atom density n_0 is related to the total number of atoms in the trap N by,

$$N = \int_{-\infty}^{\infty}\int_{-\infty}^{\infty}\int_{-\infty}^{\infty} n(x, y, z)dxdydz = n_0 \left(2\pi\sigma_c^2\right)^{3/2}. \tag{3.54}$$

By keeping track of temperature, atom numbers and size of the atomic cloud, we can deduce PSD and look then for the best strategy to decrease the dipole trap power in order to get the highest PSD at every step.

In our case, once we introduced the DDS controlled evaporation ramp in the experiment,

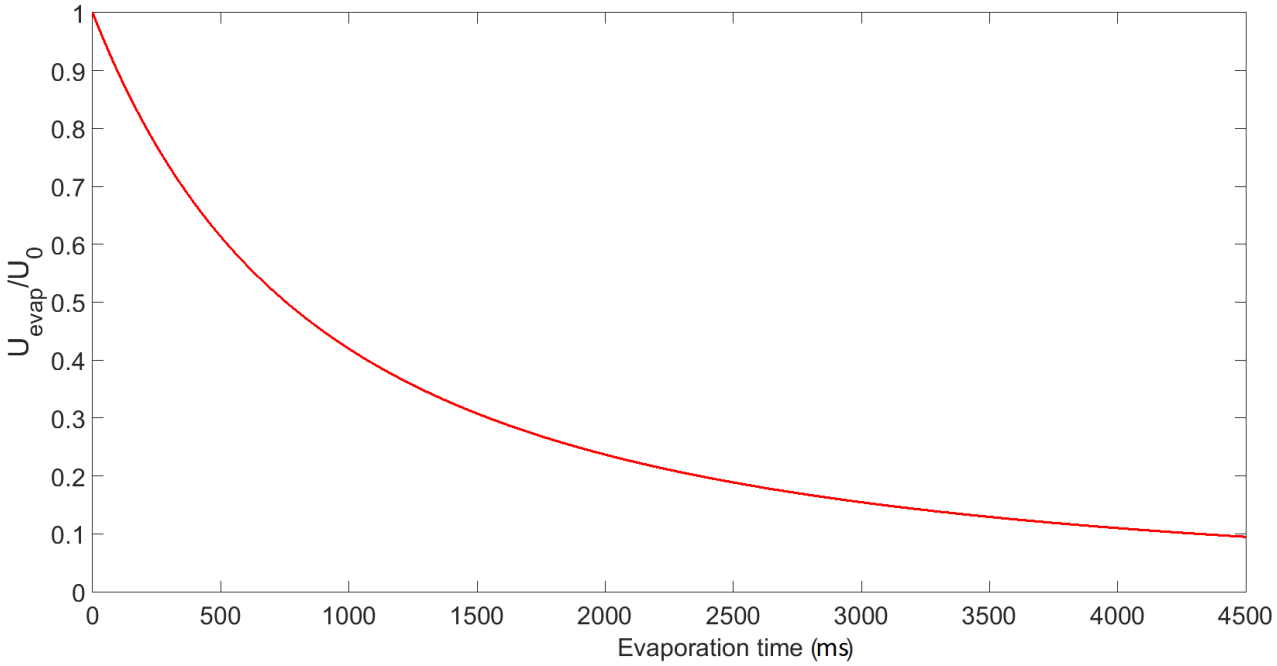

Figure 3.17: FORT power ramp down function in Eq. 3.55, with optimal evaporation parameters $\tau = 1500$ ms and $b = 1,7$ for maximum PSD.

the optimization of the evaporative cooling process became more straightforward. This was in essence due to a limitation we found in the control system when running the experimental sequences, namely the limited number of steps the analog ramp would allow us to introduce and which were forcing us to redefine the number of steps each time we wanted to bring the evaporation ramp farther down by a certain amount.

Being able to create the ramp by defining the desired evaporation function, then discretizing it and finally loading it into the DDS, made it easy for us to implement the ramp shape which was found to work best for the creation of a BEC in our experiment in the past [51]. These were empirically optimized following the formula,

$$U_{evap}(t) = \frac{U_0}{\left(1 + \frac{t}{\tau}\right)^b}, \tag{3.55}$$

where U_0 corresponds to the maximum FORT power injected before the evaporation starts, and τ and b are parameters to be optimized in order to get the largest PSD at the end of the evaporation. Both parameters were optimized by limiting the total ramping down duration on the DDS so that only a initial fraction of the ramp was run, and monitoring the PSD to find the parameters that would maximize it after this initial steepest fraction of the ramp (see

Fig. 3.17).

For a total ramp duration of 4.5 s, the optimal parameters we found are $\tau = 1500$ ms and $b = 1.7$. For 3 million atoms loaded initially in the trap via gray molasses (see Sec. 5.1), at a PSD of 10^{-4}, this ramp allowed us to achieve a final maximum PSD of 0.15 at $T = 265$ nK for 0.25 million atoms (see Fig. 3.18). Although this value of PSD is still almost one order of magnitude below the point at which condensation is achieved, the temperature of the atomic clouds is lower than the recoil limit one for ^{87}Rb ($T_r^{^{87}Rb} = 362$ nK [58]). This latter feature enables the observation of few–photon momentum signatures mediated by the cavity, as we shall show in Chapter 6.

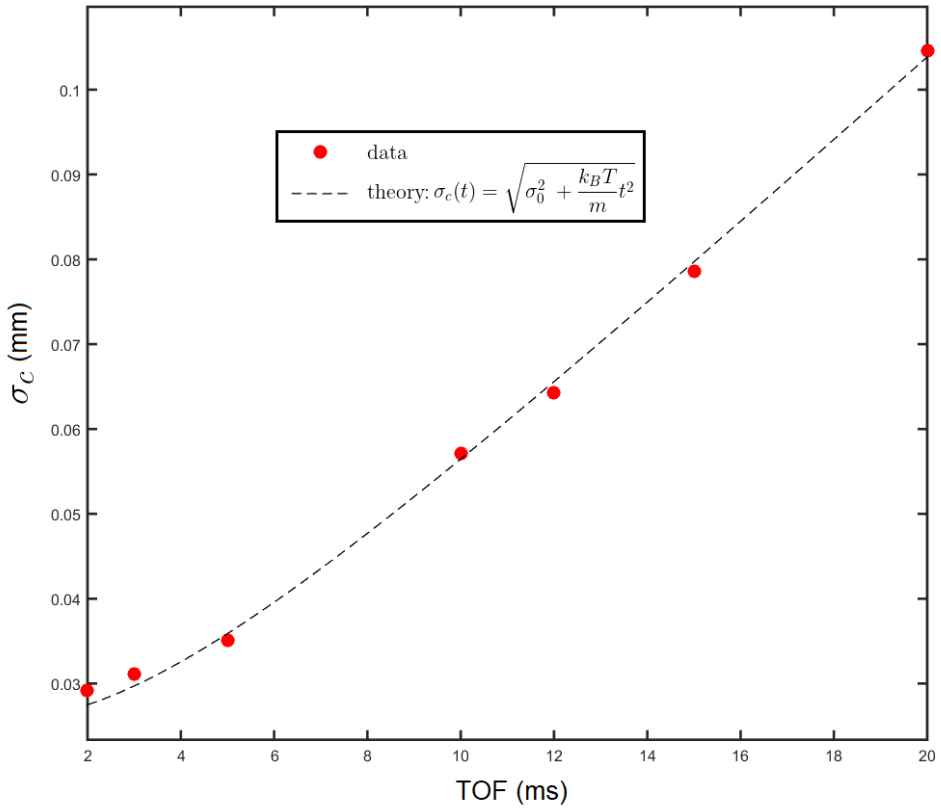

Figure 3.18: TOF expansion of the atomic cloud composed of 0.25 million atoms at the end of the evaporation ramp. Initial waist of the cloud is $\sigma_0 = 0.025$ mm and $T = 265$ nK, which corresponds to $\rho_{psd} = 0.15$.

Unfortunately, lowering the dipole trap potential farther down alone does not allow to make PSD larger. The reason for this is the detrimental effect gravity has on the vertical trapping power of the dipole trap, and which was studied in Subsec. 3.2.2. Experimentally, the

exact point at which the evaporation process is no longer efficient was observed clearly during our research. Indeed, when a slight lowering of the dipole trap potential from the condition in Fig. 3.18 was introduced, the number of particles found in the trap drastically reduced and even if the temperature of the sample was twice as low, the value of PSD stagnated (see Fig. 3.19).

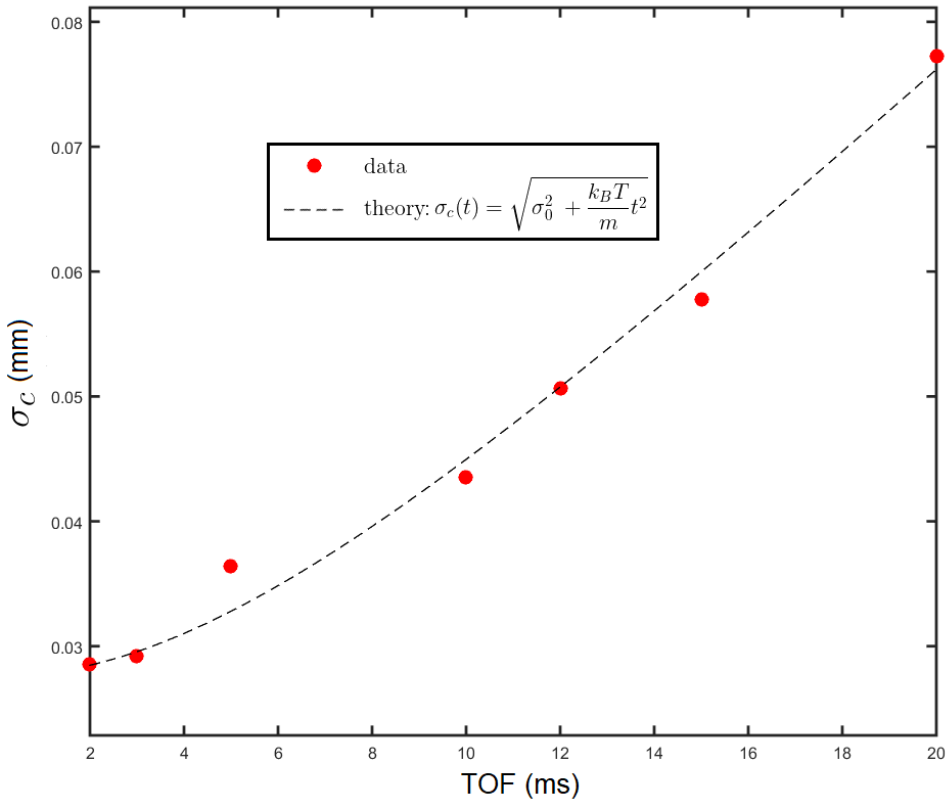

Figure 3.19: TOF expansion of the atomic cloud composed of 0.15 million atoms at the end of the evaporation ramp, with 10 % less final power than in Fig. 3.18. Initial waist of the cloud is now $\sigma_0 = 0.028$ mm and $T = 132$ nK, which corresponds to $\rho_{psd} = 0.13$.

In order to get larger PSD, one needs to compensate for the linear contribution that gravity adds to the potential and which effectively lowers the potential depth (see Fig. 3.8 above). A solution was adopted in our experiment in the past which consisted in superposing a vertical 1529 nm laser beam with the FORT at the cavity center in order to increase trapping frequencies in the plane of the cavity [52]. Moreover, this beam, known as dimple beam, can be used to neutralize the effect of gravity altogether by focusing the beam not on the

crossing region of the FORT arms but slightly above, so that the atoms trapped in the FORT are subjected to a linear vertical force counterbalancing gravity [51].

3.5 780 nm two–port cavity injection in counterpropagating directions

The enhancements introduced in the 1560 nm injection and locking setups not only allowed for robust operation of the dipole trap, but also provided us with a promising path for trying to inject 780 nm light continuously into the cavity. On the optics side, the increased coupling efficiency of the injected radiation to the cavity at 1560 nm was afforded by the use of cylindrical lenses. Therefore, we decided to follow the same cylindrical telescope optimization approach in order to increase the mode matching on the 780 nm injection setups as well, with the only difference being the values of the focal lengths chosen (see Subsec. 3.1.2). The coupling efficiencies achieved in this case are $P_{inj}/P_{tot} = 9 \pm 1$ % for both injection ports.

Before propagation in free space however, a few fiber components transport light towards the bow–tie cavity. After an EDFA amplification stage which amplifies 20 % of the 1560 nm light generated by the RIO $Planex^{TM}$ diode, 780 nm laser light is created by a frequency doubling periodically poled lithium niobate (PPLN) waveguide (see Fig. 3.20). This, along with two 200 MHz AA Opto-Electronic AOMs RF driven by a common VCO, ensures that 780 nm light can automatically be injected from both ports once the 1560 nm radiation is frequency locked to the cavity. Indeed, 780 nm light remains maximally injected for a few minutes after maximising its transmission by fine tuning the RF frequency on the AOMs. We attribute the slow drift with respect to 1560 nm laser to the difference in finesses between the two wavelengths (see Subsec. 3.5.1 below for the one at 780 nm). The drift is compensated every few experimental runs via analog voltage computer control of the RF frequency.

Additionally, a iXblue NIR–MPX800–LN–10 series fiber EOM allows to create sidebands separated by frequencies which can be multiples of the bow–tie cavity FSR (see Subsec. 3.2.1), and up to 10 GHz. We realized during our research that there is a feature of our cavity, namely the value of the FSR, which holds a particular relation with the hyperfine

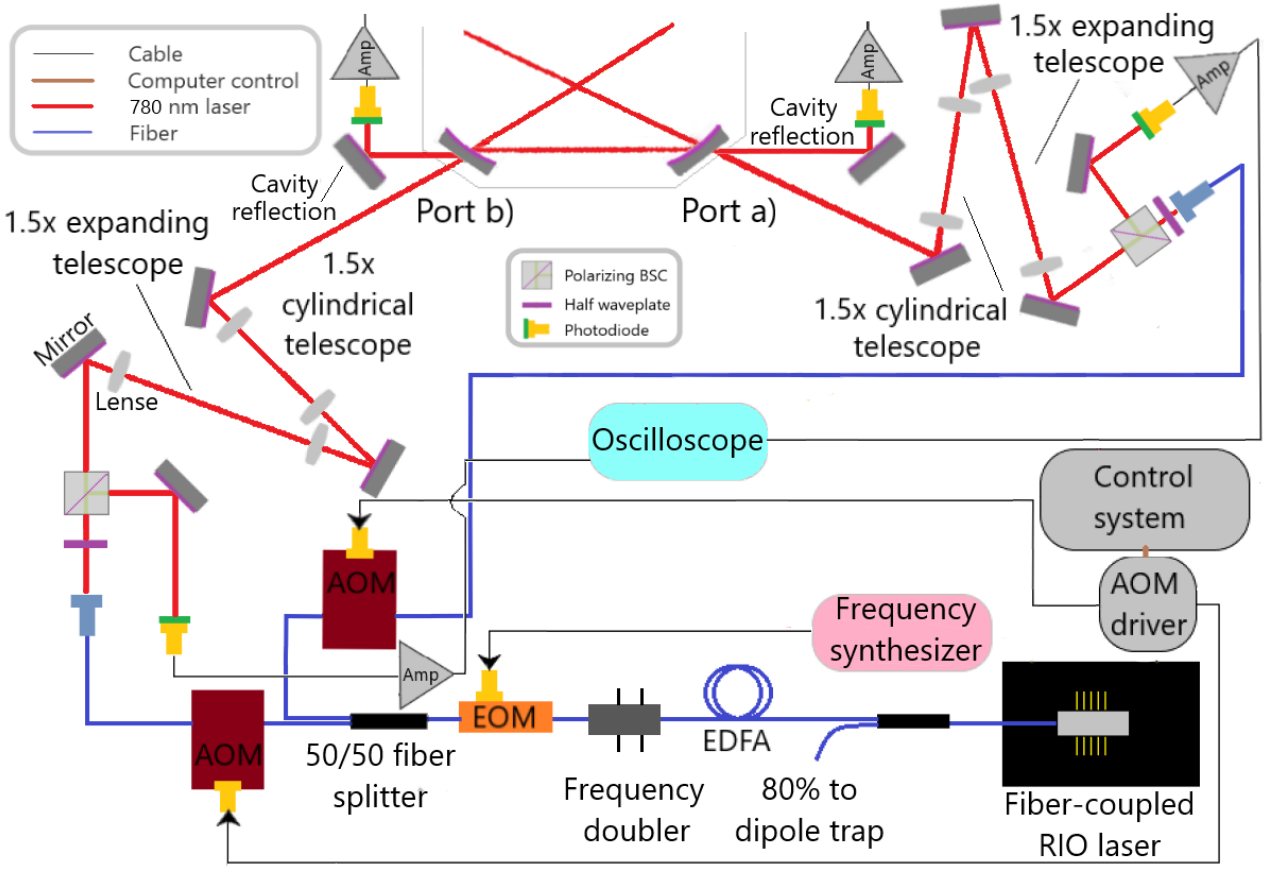

Figure 3.20: Cavity injection setup for 780 nm laser light. Two injection ports are utilized to achieve counterpropagating beams inside the cavity. Fiber EOM allows phase modulation in the few GHz level, while fiber AOMs are introducing 200 MHz shifts. Ordinary and cylindrical telescopes on both injection ports are identical, while reflection signal, and changes in polarization and power are monitored using a pair of photodiodes per port.

splitting of ^{87}Rb's ground state. Indeed, by multiplying $\Delta\omega_{\mathrm{FSR}} = 2\pi \times 976.2$ MHz by seven, we get a value which is slightly more than one MHz away from the hyperfine splitting. We determined the exact frequency needed for optimal injection of the carrier and the sidebands experimentally, by modulating the fibered EOM with an Anritsu 68017C frequency synthesizer allowing for sub–Hertz precision, and by monitoring the cavity transmitted signal at 1560 and 780 nm through a Thorlabs photodiode.

When the EOM is modulated at a frequency few MHz away from the hyperfine splitting (see Fig. 3.21a)) and at a modulation amplitude $\beta \simeq 1.7$ rad, while a scan is applied on the diode laser's current control, carrier and sideband transmission peaks are easily distinguished

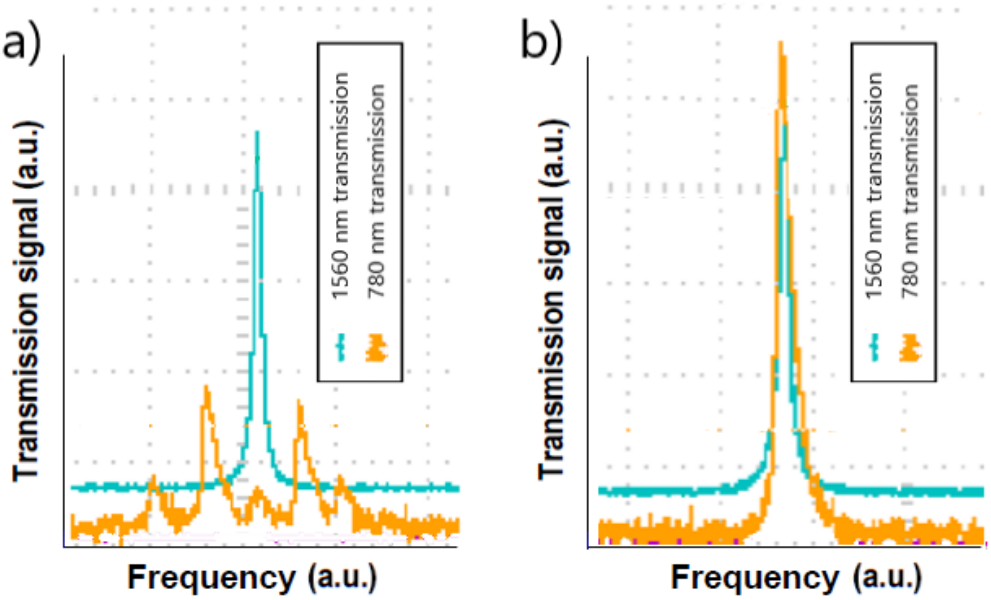

Figure 3.21: 1560 nm bow–tie cavity transmission in light blue and 780 nm in yellow when the later is phase–modulated at an amplitude $\beta \simeq 1.7$ rad, and at a frequency a) 6830.00 MHz, and b) 6834.26 MHz.

in the transmission signal. Below a couple of MHz away from the hyperfine splitting however, different transmission peaks which are separated by seven times the FSR can no longer be singled out. At $\omega_{\rm mod} = 2\pi \times 6834.26$ MHz, the detected transmission signal is maximum, which means sidebands are optimally injected at this phase modulation frequency.

3.5.1 Ring down measurement of finesse at 780 nm

The motivation for determining what the finesse is for 780 nm light was very strong for the purpose of this work. This is because, high finesse is a necessary condition if one wants to interact with ultracold atoms coherently. Given that we were expecting this finesse be of the order of $\sim 10^5$ (see Tab. 3.3 for the theoretical value), the method we chose to measure it was the ring down technique, which by suddenly turning off the injection of the laser into the cavity allows to measure the decay time τ of the intesity directly [64]. This decay time is related to $\delta\omega_{\rm FWHM}$ through the cavity losses $\alpha = 1/\tau$, where α is fitted from the decay rate of the measured intensity,

$$I = I_0 e^{-\alpha t}. \tag{3.56}$$

The ring down measurement relies on the introduction of a mechanism that allows cavity injection for 780 nm be turned off. Our choice was to use one of the fibered 200 MHz AOM that not only allows for fast turn off via TTL, but also modulates laser frequency so that it can be shifted to match the difference produced by the distinct positions of the 1560 and 780 nm coatings on the cavity mirrors.

An exponential decay fit of the recorded 780 nm light transmission data is shown in Fig. 3.22, where the first μs of decay is not considered since the switch–off time of the AOM takes approximately this long as revealed by the reflection signal (see yellow curve in Fig. 3.22a)). The 780 nm finesse using an average obtained from three measurements

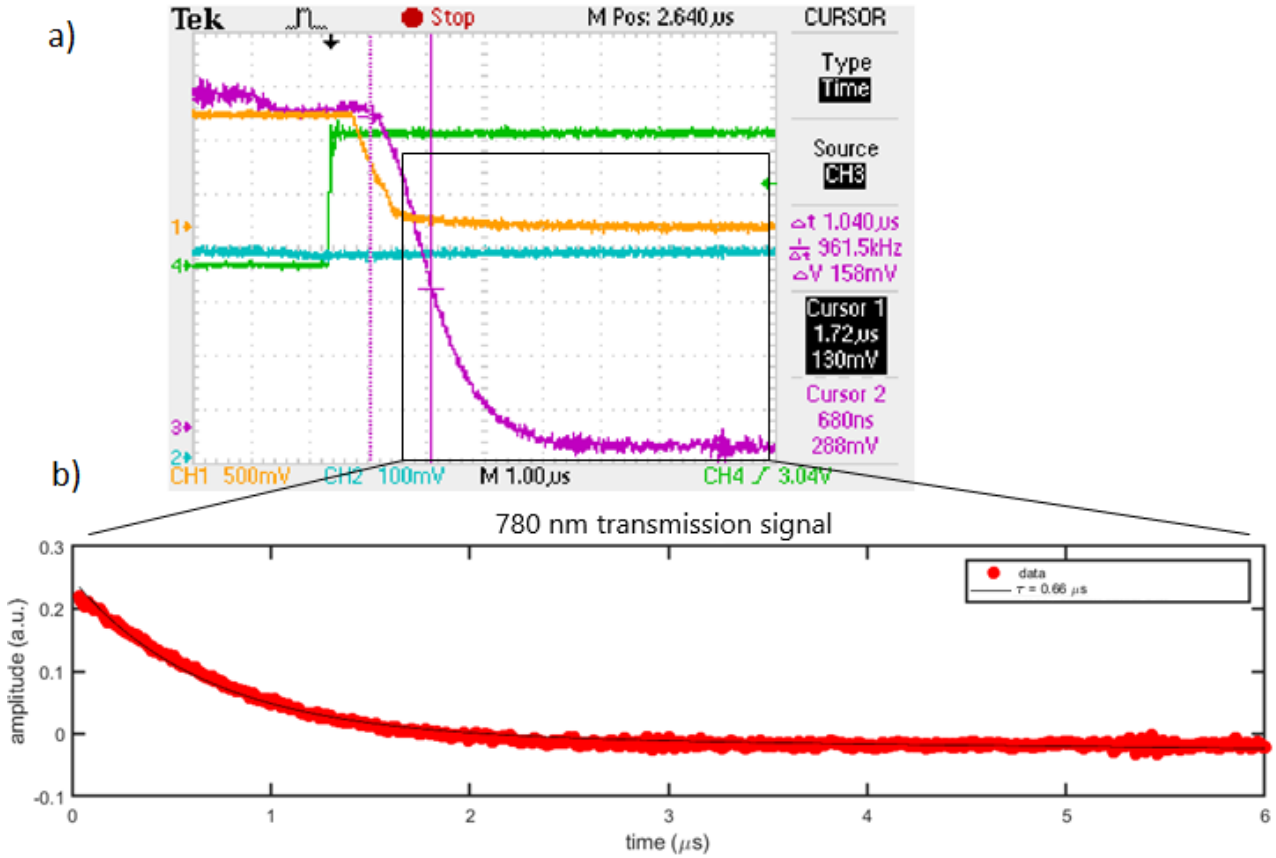

Figure 3.22: Ring down measurement and exponential decay fit. a) shows raw data with AOM TTL control signal in green, 1560 nm transmission signal in blue, 780 nm reflection signal in yellow and 780 nm transmission signal in purple. Raw data corresponding to 780 nm purple transmission signal from a) shown in red in b), where exponential decay fit is shown in black.

then yields,

$$\mathcal{F}_{780} = \frac{2\pi c}{\alpha L} = \frac{2\pi c\tau}{L} = 4050 \pm 165, \tag{3.57}$$

where the error is the standard error of the mean.

The value for the finesse in Eq. 3.57 and the one for the FSR presented in Subsec. 3.1.2 imply a FWHM linewidth of $\kappa = \Delta\omega_{\mathrm{FSR}}/\mathcal{F}_{780} = 2\pi \times (241 \pm 10)$ kHz for our bow–tie cavity at 780 nm, which is more than twice as narrower as the one achieved at 1560 nm (see Subsec. 3.2.1).

3.6 Concluding remarks

In this chapter, we have given a detailed description of our bow–tie cavity focusing on the improvements on the optical side, as well as specific insight on the mechanism explaining the trapping of atoms via the dipole force produced at 1560 nm. Finally, we would like to underline the improvement of frequency and power stabilization of laser light to the cavity at this wavelength, which has allowed us to inject frequency doubled 780 nm light continuously into our cavity for the first time, as long as the 1560 nm one is frequency locked to it. This key improvement, permitted us to measure the finesse at 780 nm, and has opened the possibility of closer to resonance atom–cavity interactions with the atoms loaded into the cavity mode volume as we show in the following Chapter 4.

Chapter 4

Atom–cavity coupling effects in a large volume bow–tie cavity

Unlike linear resonators, running or traveling–wave resonators are resonators where the intracavity field can propagate in two different directions without forming a standing wave. This type of resonators find relevant applications in laser technology, e.g. for second harmonic generation (SHG) [65] or in optical parametric oscillators (OPOs) [66]. However, loading cold atomic samples in their mode volume has not been that frequent as compared to the widespread use of simpler to construct Fabry–Perot cavities. Moreover, small mode volume is achieved more easily in two–mirror cavities, a feature that facilitates trapping [67] and cooling [68] of single atoms, while intracavity one dimensional optical lattices are obtained naturally [69] in these cavities, thanks to the boundary conditions imposed by the mirrors.

4.1 One and many atom strong coupling to optical cavities

Coupling atoms to cavities is interesting from a fundamental point of view. Since E. T. Jaynes and F. W. Cummings presented a fully quantum mechanical model [70] of an atom interacting with a single mode electromagnetic field in 1963, many physicists have been interested in exploring the validity of this model and more sophisticated ones such as the Tavis–Cummings one, which includes the presence of several atoms interacting with a single mode of the elec-

tromagnetic field. The motivation of using cavities for this purpose comes from the possibility of creating environments with small density of modes and narrow linewidth, a limit where the single–mode approximation may become valid. The atom then only radiates into this mode and can also re-absorb the emitted photon; in other words, the coupling between the field and the atom(s) becomes very strong, so that coherent interaction dominates over dissipation processes. It was in this regime that phenomena predicted only by the fully quantized model were observed for the first time in experiments with Rydberg atoms in a microwave cavity [71]. Indeed, the detected collapse and revivals of the Rabi oscillations when initializing the field in a coherent state showed that the Jaynes–Cummings Hamiltonian was a realizable model in the laboratory. Related ground–breaking experiments in cavity quantum electrodynamics (cQED) contributed in S. Haroche winning the Nobel prize in physics in 2012.

The single mode electric field produced in a cavity of mode volume V can be written quantum mechanically in terms of the creation and annihilation operators a and $a^\dagger$ as [72],

$$\mathbf{E}\left(\mathbf{r},t\right)=\hat{x}\sqrt{\frac{\hbar\omega}{2\epsilon_0 V}}\left[ae^{i(\mathbf{k}\cdot\mathbf{r}-\omega t)}+a^\dagger e^{-i(\mathbf{k}\cdot\mathbf{r}-\omega t)}\right], \tag{4.1}$$

where the electric field is polarized along direction x, and $\hbar\omega$ and ϵ_0 are the energy of a single photon and the free space permittivity respectively. An atom placed under such laser light field will experience a dipole force that can be cast into the following interaction Hamiltonian,

$$H_I=-\mathbf{E}\left(\mathbf{r},t\right)\cdot\mathbf{d}=-d\sqrt{\frac{\hbar\omega}{2\epsilon_0 V}}\left(\sigma_+ +\sigma_-\right)\left[ae^{i(\mathbf{k}\cdot\mathbf{r}-\omega t)}+a^\dagger e^{-i(\mathbf{k}\cdot\mathbf{r}-\omega t)}\right], \tag{4.2}$$

where $\mathbf{d}$ is the dipole operator with modulus d and its diagonal elements vanish from parity considerations as in Eq. 1.6 (see Sec. 1.1). The operators

$$\sigma_\pm=\frac{1}{2}\left(\sigma_x\pm i\sigma_y\right), \tag{4.3}$$

on the other hand, are the atomic transition operators derived from the Pauli operators. We can simply write them as $\sigma_+=|e\rangle\langle g|$ and $\sigma_-=|g\rangle\langle e|=\sigma_+^\dagger$, and keep numerical indexes for states of the field.

At this point, we consider the dipole approximation as in Sec. 1.1, and thus all high order terms but the trivial unity one on the Taylor expansion of the position complex exponential are neglected. To eliminate the time dependence, on the other hand, a unitary transformation to a rotating frame $H_I^{rot}=U_A^\dagger H_I U_A$ can be applied, where the unitary operator $U_A=e^{-iH_A t/\hbar}$

corresponds to the free Hamiltonian of the atom,

$$H_A = \Delta E_{ge}\sigma_+\sigma_- = \hbar\omega_0\sigma_+\sigma_-, \tag{4.4}$$

with $\Delta E_{ge} = \hbar\omega_0$ the energy difference between ground and excited states, and where the origin of the energy has been set at the ground state. The rotated interaction Hamiltonian then reads,

$$H_I^{rot} = -d\sqrt{\frac{\hbar\omega}{2\epsilon_0 V}}\left[\sigma_+ a e^{i(\omega_0-\omega)t} + \sigma_+ a^\dagger e^{i(\omega_0+\omega)t} + \sigma_- a e^{-i(\omega_0+\omega)t} + \sigma_- a^\dagger e^{-i(\omega_0-\omega)t}\right]. \tag{4.5}$$

This picture is useful for applying the rotating wave approximation we applied in Sub. 1.1. Similarly to there, here, we are interested in using laser light close to the atomic transition, so that $\omega \approx \omega_0$ and then terms containing $\pm(\omega_0 + \omega)$ can be safely neglected as before.

Thanks to this approximation, one can write down a time–independent Hamiltonian by making a second unitary transformation of the form $U_\Delta = e^{-i(\omega-\omega_0)\sigma_+\sigma_- t}$ on the rotated interaction Hamiltonian in Eq. 4.5. By considering the full Hamiltonian of the system, that is, the free Hamiltonians of the atom as well as the one corresponding to the single mode field in the cavity, we get the Jaynes–Cummings Hamiltonian

$$H_{JC} = \hbar\omega_0\sigma_+\sigma_- + \hbar\omega a^\dagger a - \hbar g\left(\sigma_+ a + \sigma_- a^\dagger\right), \tag{4.6}$$

where,

$$g = d\sqrt{\frac{\omega}{2\hbar\epsilon_0 V}}, \tag{4.7}$$

is the atom–cavity coupling, and $a^\dagger a$ is an Hermitian operator called the number operator, whose eigenstates $|n\rangle$ are states of the single mode field corresponding to n photons.

An explicit simple expression for Eq. 4.6 can be written in the basis of a subset of tensor product states $\S = \{|g,0\rangle, |e,0\rangle, |g,1\rangle ...\}$, namely using $|g,n\rangle$ and $|e,n-1\rangle$,

$$H_n = \hbar\begin{pmatrix} n\omega & -\sqrt{n}g \\ -\sqrt{n}g & n\omega - \delta \end{pmatrix}, \tag{4.8}$$

where $\delta = \omega_0 - \omega$ is the atom–cavity detuning. Diagonalization of Eq. 4.8 leads to eigenvalues

$$E_{\pm,n} = \hbar\left[n\omega - \frac{\delta}{2} \pm \sqrt{\left(\frac{\delta}{2}\right)^2 + ng^2}\right], \tag{4.9}$$

and eigenvectors,

$$|+,n\rangle = \sin\theta_n|e,n-1\rangle + \cos\theta_n|g,n\rangle, \tag{4.10a}$$

$$|-,n\rangle = \cos\theta_n|e,n-1\rangle - \sin\theta_n|g,n\rangle, \tag{4.10b}$$

where

$$\theta_n = \frac{1}{2}\arctan\left(\frac{2\sqrt{n}g}{\delta}\right). \tag{4.11}$$

The splitting of the dressed states in Eqs. 4.10 increases as δ and g become larger, and was clearly observed experimentally in the early 90s for mean number of atoms close to 1 [73]. Given that this splitting happens even when $n = 1$, and that it is also related to the rate at which energy is coherently transferred between the atom and the cavity under the presence of a single excitation [74], $2g$ is commonly known as the vacuum Rabi splitting.

4.1.1 Extension to many atoms coupled to a single mode: the Tavis–Cummings model

Despite the beauty and simplicity of the Jaynes–Cummings model, it is more often the case in the cold atoms community that researchers have to deal with many atoms coupled to optical cavities. Many atoms coupled to a single cavity mode allows for long range interactions between atoms mediated by the cavity, and have found applications not only in understanding the properties of many–body quantum systems which are hard to simulate by numerical methods [13], but also in more practical applications such as atom interferometry [75].

It is a natural extension of the Jaynes–Cummings model then to consider many atoms strongly coupled to a single mode. Such model is known as the Tavis–Cummings model [76], and extends the single to the many atoms case by substituting the single atomic transition operators by their collective counterparts of the form,

$$S_+ = \sum_i^N |e_i\rangle\langle g_i|, \tag{4.12}$$

$$S_- = \sum_i^N |g_i\rangle\langle e_i| = S_+^\dagger, \tag{4.13}$$

$$S_z = \frac{1}{2}\left(S_+ + S_-\right), \tag{4.14}$$

where N is the number of identical atoms. The Tavis–Cummings Hamiltonian can be then written as,

$$H_{TC} = \hbar\omega_0 S_z + \hbar\omega a^\dagger a - \hbar g\left(S_+ a + S_- a^\dagger\right). \tag{4.15}$$

If both the cavity and the atoms are in the ground state, the energy spectrum of Eq. 4.15 takes the form [77],

$$E_{\pm,N} = \hbar\left[\omega_0\left(1 - \frac{N}{2}\right) - \frac{\delta}{2} \pm \sqrt{\left(\frac{\delta}{2}\right)^2 + Ng^2}\right]. \tag{4.16}$$

By comparing this result to Eq. 4.9 at $n = 0$, we see that for the multi–atom case, the vacuum Rabi splitting gets an additional factor of $\sqrt{N}$, which means the normal–mode splitting can be then more easily resolved [78], and the coherent exchange of energy between the cavity and the atomic system will be greater too. Therefore, by increasing the number of atoms coupled to the cavity, the conditions to achieve the strong coupling regime can be relaxed.

For a single atom, this condition is given by the single atom cooperativity [79]

$$C = \frac{4g^2}{\kappa\Gamma} > 1, \tag{4.17}$$

where κ and Γ are the linewidths of the cavity and the atomic transition, respectively. It is of great interest then to use high–finesse cavities and narrow atomic transitions, as well as small volume cavities in order to achieve the condition in Eq. 4.17. With a few centimeter long cavities such as the one in our experiment, single atom strong coupling regime has not been achieved. In this case, strong coupling to the cavity can be obtained by loading many atoms into the mode volume instead [80], and then the collective cooperativity

$$C_N = \frac{4Ng^2}{\kappa\Gamma}, \tag{4.18}$$

can be considered.

4.2 Collective strong coupling of atoms to the bow–tie cavity

In our bow–tie cavity, collective strong coupling of the atoms to the cavity has not been demonstrated yet. However, from a theoretical point of view, experimental parameters do

allow for strong coupling as we shall show below.

4.2.1 Cavity mode volume and Rabi frequency

There are two cavity parameters which play a significant role in the coupling strength between the atoms and the cavity. One is the linewidth of the cavity, which has been measured and presented in Sec. 3.5. The other is the cavity mode volume, which appears in the denominator of the expression for the coupling constant g (see Eq. 4.7), and which we determine in the following.

It should be noted that the actual volume which is relevant for this calculation is not only the one overlapped by the cavity TEM_{00} mode volume at 780 nm, with the atoms loaded into the crossing region of the far off–resonant dipole trap (FORT) arms. Even if we always make intracavity 780 nm light interact with the atoms after these have been loaded into the FORT, and after an evaporation ramp of a few seconds, after which no atoms are found in the mode volume not spanned by the center of the cross, the integral that one should calculate is the one corresponding to the whole volume of the cavity mode [79] of length L and bow–tie side width s (see Subsec. 3.1.2),

$$\begin{aligned} V &= \int_{-\infty}^{\infty}\int_{-\infty}^{\infty}\int_{-L/2}^{L/2}\frac{I(x,y,z)}{I_0}dx\,dy\,dz \\ &= 2\int_{-\infty}^{\infty}\int_{-\infty}^{\infty}\int_{-s/\sqrt{2}}^{s/\sqrt{2}} e^{-\left\{\left[\frac{\sqrt{2}x}{w^{\parallel}_{780}(z)}\right]^2+\left[\frac{\sqrt{2}y}{w^{\perp}_{780}(z)}\right]^2\right\}}dx\,dy\,dz \\ &+ 2\int_{-\infty}^{\infty}\int_{-\infty}^{\infty}\int_{-s/2}^{s/2} e^{-\left\{\left[\frac{\sqrt{2}x}{w^{780}_{\parallel}(z)}\right]^2+\left[\frac{\sqrt{2}y}{w^{780}_{\perp}(z)}\right]^2\right\}}dx\,dy\,dz, \end{aligned} \tag{4.19}$$

where $w^{\parallel/\perp}_{780}$ are the parallel and perpendicular radii along the cross between the four mirrors of the cavity, and $w^{780}_{\parallel/\perp}$ the parallel and perpendicular radii in the two parallel sides of the square described by the cavity, all of them at 780 nm wavelength. Using the values in Tab. 3.1, and Tab. 3.2 we get $V = 9.7$ mm^3.

4.2.2 Single and collective atom–cavity coupling constants

Once the volume of the cavity has been determined, one can calculate the value of the atom–cavity coupling constant via Eq. 4.7. On the atom side, we use the electric dipole moment for the D_2 line of ^{87}Rb, i.e. $d_{D_2} = 4.228ea_0$ [58], while on the cavity side we have $\omega = 2\pi c/780.2$ nm. The single atom–cavity constant is then $g^{780}_{bow-tie} = 2\pi \times 65.8$ kHz, which is more than three times smaller than the cavity linewidth κ, and two orders of magnitude smaller than the D_2 transition linewidth Γ of ^{87}Rb.

It is clear then from Eq. 4.17, that the experimental parameters provided by our apparatus do not allow us to achieve a single atom cooperativity greater than one. Therefore, we will focus next on the multi–atom case and verify how much more favourable this situation becomes in the hope of entering the collective strong coupling regime.

4.2.2.1 Collective strong coupling

According to the expression for collective cooperativity in Eq. 4.18, collective strong coupling can be achieved starting approximately at hundred atoms or more.

On the other hand, the main purpose of the bow–tie cavity we work with in our experiment has mostly been to enhance 1560 nm power for the FORT which allows to get the lowest temperatures and highest PSD. However, given that both 1560 nm and 780 nm radiation are perfectly aligned inside the cavity, loading the FORT also ensures that hundreds of thousands and even millions of atoms can be positioned in the optimal place for them to interact with intracavity radiation closer to resonance. Therefore, collective strong coupling can in principle be achieved, and research in this direction may be conducted in the future.

In our experiment, however, cavity operation close to resonance with the atomic transition has been so far avoided on purpose. The main reason for this are large low frequency mechanical oscillations observed in the PDH error signal, which correspond to a minimum of 20 MHz drifts around the aimed frequency of the cavity. This was found by a voltage to frequency calibration conducted via beating of the PDH frequency locked 1560 nm radiation with the 1560 nm Koheras Adjustik fiber laser at the source of the repumper (see Sec. 2.1). The ultimate source of the large oscillations perturbing the cavity length are unknown, but

their frequency at 92 Hz and the fact that they are strongly excited when turning off the current going through the MOT coils makes us think they are purely mechanical. The mechanical excitation happens because the cavity is attached to the same titanium flange the MOT coils are attach to, but other sources of excitation are also suspected since the amplitude of the oscillations changes within the same day between the morning and the afternoon for example.

The solution we adopted to lock the cavity length to the injected laser frequency at 1560 nm via low–frequency feedback onto the piezo–electric actuators (see Sec. 3.3), does not get rid of the 92 Hz oscillations, but it does allow to select a large detuning δ between the D_2 line transition frequency and the cavity resonant 780 nm frequency doubled one (see Sec. 3.5), by modifying the current and temperature of the diode and making sure the beatnote frequency between the 1560 nm sources of the repumper and the cavity radiation is large. The larger, the better, since then not only the 20 MHz oscillations become negligible as compared to the large detuning, but also spontaneous emission is minimized and thus two–photon transitions we target in the interaction region at the center of the cavity become more relevant. Besides, the introduction of a fibered EOM to produce sidebands close to the hyperfine splitting of ^{87}Rb's ground state (see Sec. 3.5), farther requires δ to be large, so that the sidebands are also far from resonance with the atomic transition. We thus worked at a large red detuning $\Delta \simeq 2\pi \times 22.5$ GHz from halfway between cooler and repumper transitions (see Fig. 4.1), a value which still allows us to monitor the beatnote between the 1560 nm sources separated by approximately 13 GHz, using the spectrum analyzer.

From Subsec. 3.2.2 we find that at 22.5 GHz red detuning from the D_2 line, the scattering force contribution is more than four orders of magnitude weaker than the dipole force contribution already. Therefore, the interaction between the atoms and the cavity mode leaves the atoms in the internal ground state, while the atomic medium becomes dispersive, that is, a medium with a given refractive index which induces a phase shift on the cavity field [81]. The presence of the atoms in the case of a far detunned cavity mode introduces a shift on the resonant frequency of approximately [82],

$$\delta\omega \approx \frac{HNg^2}{\Delta}, \tag{4.20}$$

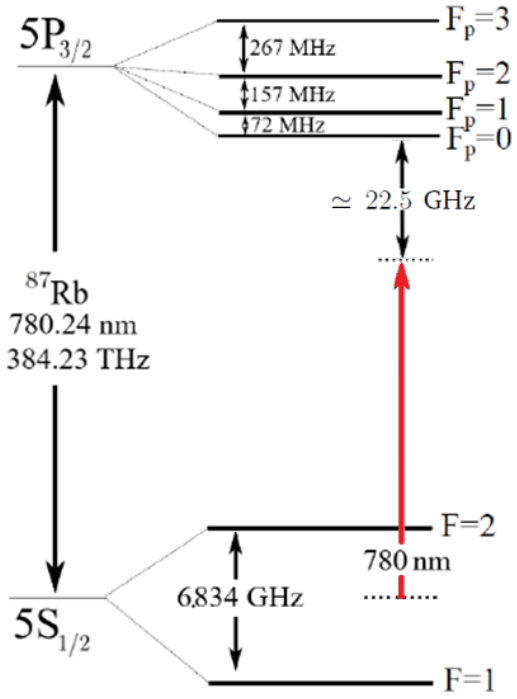

Figure 4.1: Large detuned 780 nm intracavity pulse frequency represented by red arrow, referenced to the D_2 line of ^{87}Rb.

under the rotating wave approximation ($\omega_0 \gg \Delta \gg \Gamma$), and where $H \in [0, 1]$ is an atomic distribution dependent collective coupling factor.

In our cavity, the shift induced by the atoms has been measured at the end of an evaporation ramp of 0.5 s, to ensure a large majority of the atoms left in the FORT are located in the mode volume of the 780 nm resonance. The transmission signal out of the cavity is detected for a set of pulse detunings around the resonant frequency for both the empty cavity and the cavity filled with atoms (see Fig. 4.2). The signals we obtained were fitted by Lorentzians,

$$L_T = \frac{\gamma}{\pi} \frac{\Delta\nu/2}{(\nu - \nu_0)^2 + (\Delta\nu/2)^2}, \tag{4.21}$$

where γ is an amplitude parameter, $\Delta\nu = \kappa/(2\pi)$ the FWHM linewidth and ν_0 a frequency offset which eventually permits to calculate the dispersive shift. By averaging over three sets of measurements for the empty cavity and over another three with atoms in the cavity mode we get,

$$\delta\omega = \omega - \omega_{atoms} = 2\pi \times (195 \pm 14) \text{ kHz}. \tag{4.22}$$

Substituting this value in Eq. 4.20 and considering $H = 1/2$ for a random distribution of

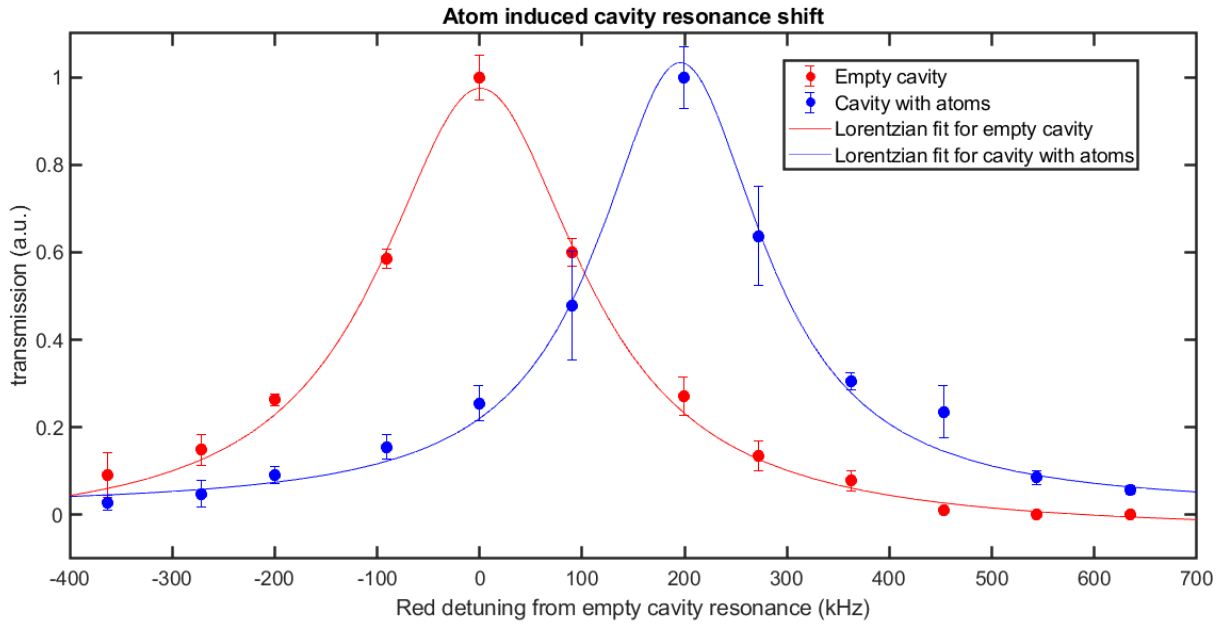

Figure 4.2: Transmission signal for a 0.2 ms cavity pulse and powers ranging between 0.15 and 0.4 mW, both for empty cavity and cavity filled with approximately 2 million atoms as measured via absorption imaging. Error bars are standard errors of the mean, obtained from three measurements for both cases, and Lorentzian fits are the ones obtained from the averages.

atoms, we get $N = (2.1 \pm 0.3) \times 10^6$, which is compatible with the number of atoms measured via time–of–flight (TOF).

4.3 Interarm coherent photon exchange processes in a bow–tie cavity

The possibility of injecting phase modulated laser light on the vicinity of the hyperfine splitting of ^{87}Rb's ground state, along with the bow–tie cavity mode geometry which offers four different directions of intracavity light propagation at the crossing region (see Fig. 4.3), allow for a rich environment of atom–cavity interactions. On the frequency side, the simultaneous injection of beams phase locked at $\omega_{\rm mod} \simeq 2\pi \times 6.834$ GHz, is a promising tool to create coherence between the two hyperfine ground states $|5S_{1/2}, F = 1, 2\rangle$, via two–photon transitions involving an intermediate virtual state $\simeq 22.5$ GHz red detuned from the D_2 line of ^{87}Rb. Momentum imparted by these photons onto atoms at the center of the trap can be detected

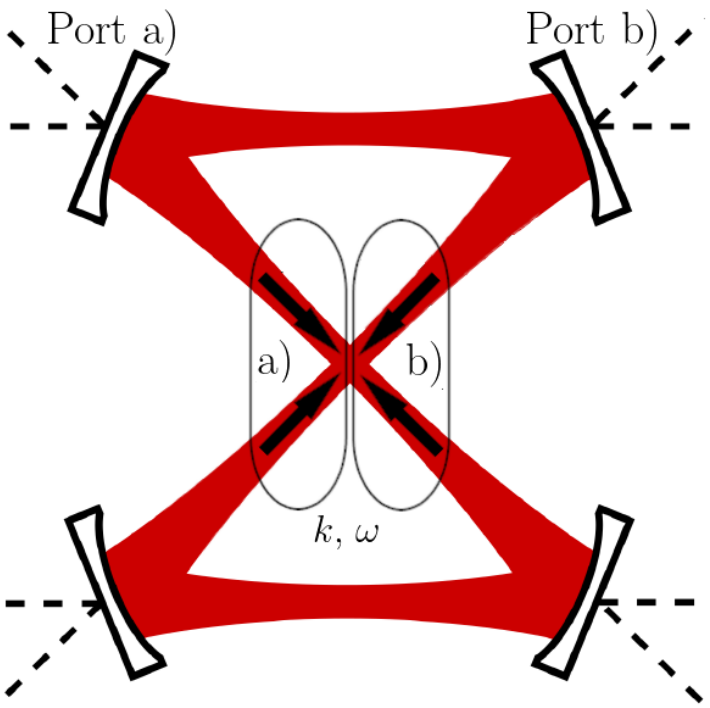

Figure 4.3: Top view of the bow–tie cavity with ports a) and b) injected and their associated intracavity traveling waves a) and b) with momentum per photon depicted by arrows. Each resonant photon of frequency ω carries momentum $\hbar k$.

by imaging the atoms themselves from above using the main imaging system.

When a single 780 nm port is injected, atoms at the crossing regions may absorb photons from two possible perpendicular directions (see Fig. 4.3). Assuming a perfect decoupling from the pump laser at the entrance of the cavity, both events are equally probable. Now if one also considers two–photon processes by adding the possibility of a simultaneous interaction with a second photon, Doppler detuning needs to be taken into account, depending on the velocity of the atoms. Two different scenarios are possible in our cavity: the simplest one on one hand, when the EOM on the injected pulse is off, will produce single frequency photons (within a linewidth of $\kappa = \Delta\omega_{\mathrm{FSR}}/\mathcal{F}_{780} = 2\pi \times 0.241$ MHz), which will thus lead to scattering involving two–photons of equal frequency (Rayleigh or Bragg scattering [83] for the counterpropagating emission case), connecting initial and final states of atoms with the same internal ground state; and on the other the EOM on scenario which can also lead to two–photon inelastic processes produced by distinct frequency absorbing and emitting photons inside the cavity [84].

When both photons at the two–photon process have equal frequencies, atoms absorbing and emitting them on the same cavity arm will undergo a transition which leaves them at the same internal state as the one they were on before the absorption–emission process. These atoms will not only conserve their kinetic energy, but they will also have the same final velocity as they initially had. On the contrary, atoms which absorb a photon from one arm and emit the second one on the other will get a kick on a direction at an angle of 45 degrees with both cavity arms, i.e. equidistant from both. Therefore, if a photon exchange process between arms occurs, its effect on the atoms can be possibly detected via TOF for sufficiently cold atoms (see Sec. 6.2).

4.3.1 Raman momentum exchange processes

Turning on the EOM to produce sidebands at the hyperfine splitting frequency of ^{87}Rb's ground state makes the analysis of the possible interactions more complex. Atoms will now not only undergo transitions from one of the two possible internal ground states to a same final one, but also those involving initial states $|5S_{1/2}, F = 1\rangle$ and final states $|5S_{1/2}, F = 2\rangle$, and vice–versa. However, from a practical point of view, given that the momentum recoil associated to the difference of energies between both photons is negligible compared to the one–photon recoil limit our atoms are at most cooled down to (see Sec. 3.4), not much difference from the Bragg scattering case is expected in terms of the amount by which the momentum of the atoms gets modified.

In order to prove the existence of Raman transitions, what we did was to check whether the presence of the EOM sidebands was actually making atoms undergo coherent transitions from one ground state to the other. This was done after a FORT evaporation ramp of 4.5 s described in Sec. 3.4, and by red detuning the pulse frequency by $\kappa/2$ from the atom–cavity resonance in order to avoid heating up the sample.

Even though above a few tenths of μs duration pulse, the difference on ground state population fractions between EOM on and off cases becomes apparent (see Fig. 4.4), the existence of Rabi oscillations could not be proved. What we can tell is that the pulse with the EOM off leaves the atoms mostly at the absolute ground state $|5S_{1/2}, F = 1\rangle$, no matter what

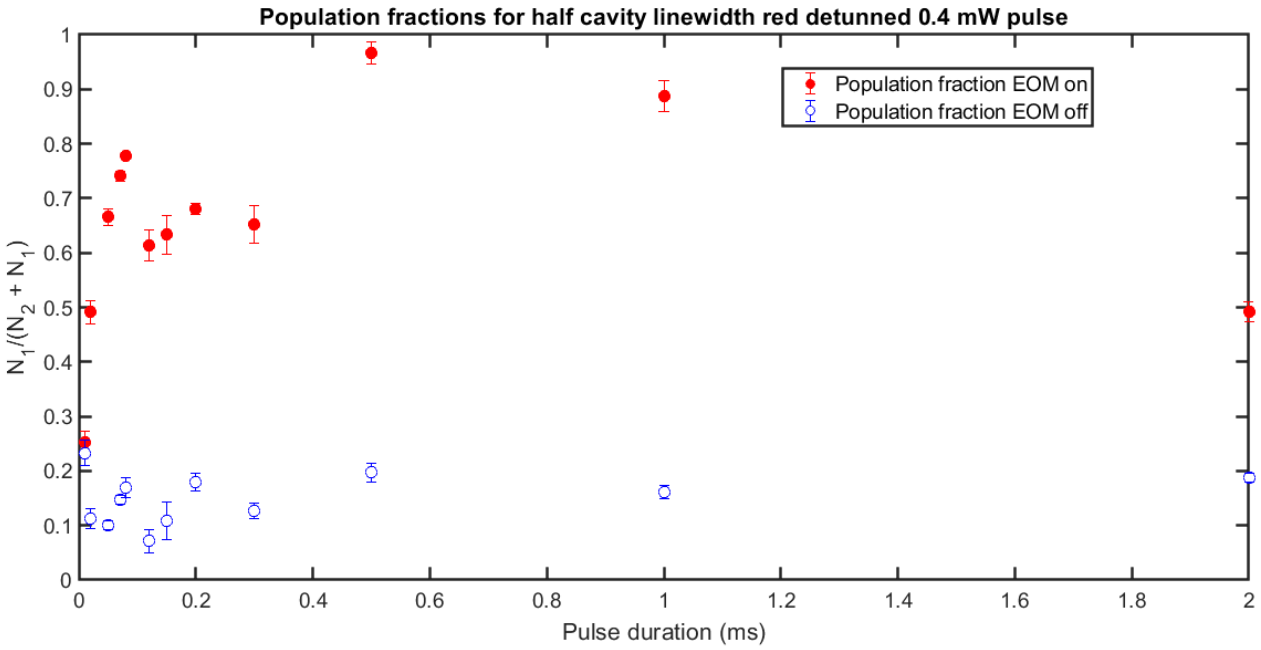

Figure 4.4: Population fractions of atoms in $|5S_{1/2}, F = 2\rangle$, divided by the total number of atoms detected on both $|5S_{1/2}, F = 1\rangle$ and $|5S_{1/2}, F = 2\rangle$, for changing pulse duration, when the EOM is run at $\beta \simeq 1.4$ rad modulation amplitude and $\omega_{\text{mod}} = 2\pi \times 6834.26$ MHz, vs when it is off.

pump duration is chosen, while switching on the EOM tranfers 95 % of the atoms onto the $|5S_{1/2}, F = 2\rangle$ manifold after half a millisecond.

4.4 Concluding remarks

At the beginning of this chapter, we have focused on the quantum mechanical models we are interested in studying using our cavity. Our calculations show the strong coupling regime is attainable provided that a few hundreds or more atoms are loaded into the mode volume at atomic resonance. Given that close to atomic resonance operation necessitates further cavity frequency stabilization, and given also that far off resonance pulses can reveal phenomena which are hardly visible on resonance, we have for now worked at tenths of GHz atom–cavity detuning.

The dispersive shift for a couple of million atoms loaded into the cavity mode volume at the crossing region has been measured. This measurement agrees with the number of atoms

detected via TOF. Finally, the effect of injecting phase–modulated light close to the Raman condition into the cavity filled with atoms has been studied. We find a large difference in the atomic ground state populations as compared to the single frequency beam injection case. Interestingly, the additional phase–locked repumping beam allows for the observation of clear two–photon induced recoil phenomena which will be described in Chapter 6.

Chapter 5

Dipole trap loading and atom cooling using gray molasses

The gray molasses technique is a powerful tool to achieve low temperature samples of ^{87}Rb atoms as explained in Sec. 1.3. The main reason for this is the possibility of cooling down atoms close to zero velocity states which are dark, and thus no longer go through absorption followed by spontaneous emission processes as happens with the bright states. The gray molasses process however, not only is a useful cooling technique for us, but also is the last process atoms are subjected to before we load them into the dipole trap. Given that the far off–resonant dipole trap (FORT) is always present in order the 1560 nm laser to be locked to the cavity, ideally, we want its effect to be minimal on the efficiency of the gray molasses process. In reality, however, and as mentioned in Subsec. 3.2.2, we must consider the AC Stark effect which explains the shift of energy levels in ^{87}Rb under the dipole trap, to correctly account for the effect on the gray molasses as we explain below.

As it became clear during this research, the Stark effect we need to consider for the gray molasses goes beyond the simple differential AC shift between the ground and excited fine manifolds of the D_2 line under 1560 nm, and this is what we will focus on in the second section of this chapter. Before that, we will introduce first the experimental procedure we utilize to perform the gray molasses FORT loading and cooling in our bow–tie cavity.

5.1 Gray molasses FORT loading: experimental procedure

The initial cooling stages in our experiment, whose working principle was presented in Subsec. 1.2, are done using the independent cooler and repumper lasers, and it is after the compressed MOT (cMOT) stage that the phase–locked repumper enters into action as we are going to show next.

5.1.1 MOT and cMOT stages

The ordinary MOT and cMOT cooling stages are described as they are executed during the FORT loading and cooling procedure. The sequence begins as follows,

- **2D and 3DMOT:** ^{87}Rb atoms are introduced into the 3DMOT chamber by a push beam in the 2DMOT device that is created by the same cooler and repumper light that feeds the 3DMOT cloud (see Fig. 2.1 above). The light coming from both lasers is overlapped on a single–mode polarisation-maintaining fiber. The cooler is detuned by $\Delta_c \simeq -3\Gamma$ from $|5S_{1/2}, F = 2\rangle \rightarrow |5P_{3/2}, F' = 3\rangle$ transition, whereas the repumper is on resonance with the $|5S_{1/2}, F = 1\rangle \rightarrow |5P_{3/2}, F' = 2\rangle$. The simultaneous action of both the 2D and 3D MOTs allows to load and trap $\sim 10^9$ atoms after 5 seconds. At that point, the 2DMOT beams and the push beam are stopped by a shutter that blocks the beam feeding the entire 2DMOT system, and the cooler is farther detuned to start the cMOT stage.

- **cMOT:** during 10 ms the cooler is detuned by $\Delta_{cmot} \simeq -6\Gamma$ from the cooler transition, and the power is reduced by a factor of 10, whereas the repumper is left unchanged both in frequency and power.

On the other hand, during these stages, the 1560 nm FORT is kept at $\simeq 3\%$ of the maximum power which is instead used during (see Subsec. 3.2.2) the first and second gray molasses loading and cooling stages as explained below. This creates a FORT depth of approximately 25 μK, which is still significantly greater than the power needed in order to keep the FORT locked to the cavity, which is required from the beginning of each experimental run, since the locking cannot be engaged at the middle of a running sequence.

5.1.2 Molasses stage and FORT power for optimal loading

It is at this point that the hyperfine Λ–scheme starts to be different from the ordinary molasses one. If one wants to proceed applying the ordinary molasses scheme then the independent repumper (i.e on the nominal $|5S_{1/2}, F = 1\rangle \rightarrow |5P_{3/2}, F' = 2\rangle$ transition frequency) should still be used. However, in order to get the repumper needed for the hyperfine Λ–scheme gray molasses configuration (see Subsec. 1.3.3) which gives the best loading and cooling, the ordinary repumper is turned off and the cooling laser is farther detuned until it remains $\sim 2\Gamma$ to the blue of the $|5S_{1/2}, F = 2\rangle \rightarrow |5P_{3/2}, F' = 2\rangle$ transition. In the meantime, the coherent repumper is turned on via the RF switch driving the EOM, so that the single laser source which produces the cooler plus the sidebands produced via phase–modulation are only used. At this point, power is farther reduced on the cooler both by reducing RF signal amplitude on the 113 MHz frequency AOM and also because the same beam now contains cooler and repumper frequencies.

Both ordinary and phase–locked repumper powers have been optimized to maximize the number of atoms loaded into the center of the cross shaped dipole trap. A reduction by a factor of four on the repumper power with respect to the cMOT stage was found to be best for the ordinary molasses. Most importantly for doing a true molasses, the magnetic field gradient needs to be turned off. This takes $\sim$2 ms, which is the time needed for the electric current producing the quadrupole field to be evacuated.

Once the EOM is turned on for the cooler and phase–locked repumper frequency generation in the hyperfine Λ–scheme, both are equally detuned from the $|5S_{1/2}, F = 2\rangle \rightarrow |5P_{3/2}, F' = 2\rangle$ and the $|5S_{1/2}, F = 1\rangle \rightarrow |5P_{3/2}, F' = 2\rangle$ transitions respectively, and the gray molasses process goes on for 8 ms. The optimal phase–modulation amplitude applied via the QUBIG free–space EOM producing the rempumping sideband (see Subsec. 1.2), was found to be $\beta \simeq 1.3$ rad, while data of number of atoms loaded obtained for changing phase–modulation frequency around the hyperfine ground splitting $\delta_{hf}^{^{87}Rb} = 2\pi \times 6.83468$ GHz is shown in Fig. 5.1, for different dipole trap powers at an absolute optimal detuning (see Sec. 5.3 below) of -43.5Γ from the $|5S_{1/2}, F = 2\rangle \rightarrow |5P_{3/2}, F' = 3\rangle$ transition. The observed resonance varies with increasing FORT power to the red by $\sim$50

kHz.

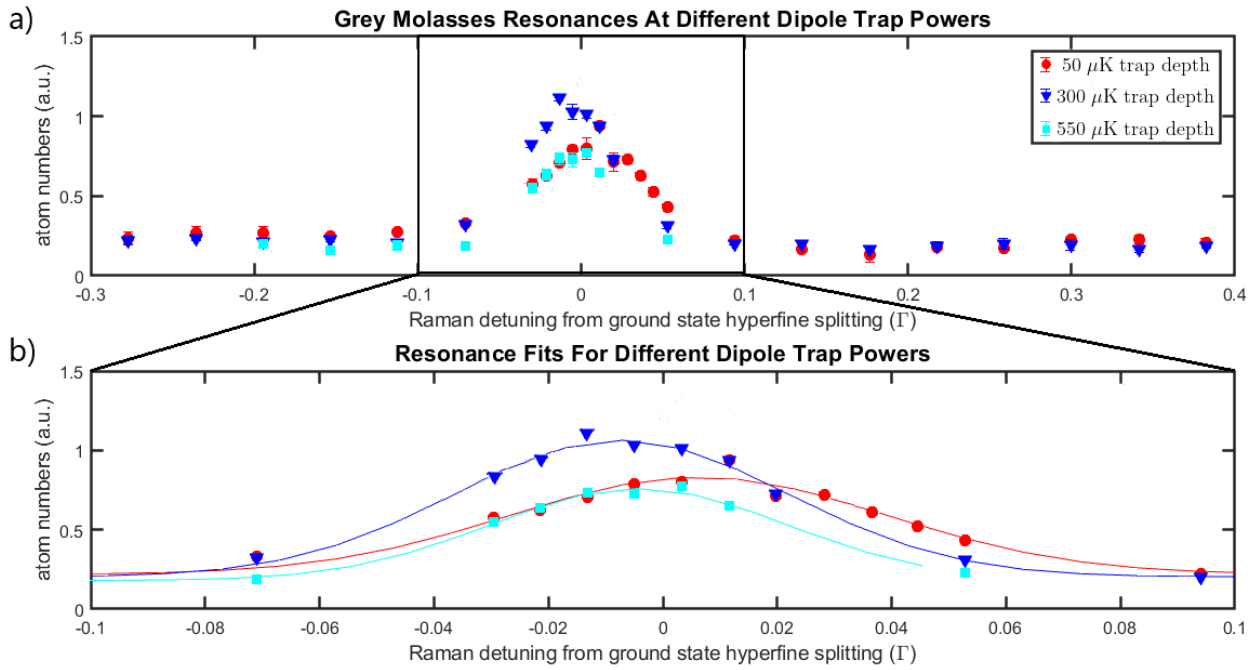

Figure 5.1: a) Loaded atom numbers as a function of the Raman detuning $\delta_{mod} = \omega_{mod} - \delta_{hf}^{^{87}Rb}$, where $\delta_{hf}^{^{87}Rb} = 2\pi \times 6.83468$ GHz, in units of the natural linewidth Γ of ^{87}Rb's D_2 line, for different dipole trap depths. b) Zoom–in of a) with Gaussian fits for each of the dipole trap powers.

A more precise view of the resonance when the FORT is off is given in Sec. 5.2 by looking at the maximum optical density at the center of the cloud. For optimal loading in turn, the FORT is ramped up to a trap depth of 170 μK in less than 1 ms. The dependence of the loading efficiency on FORT power is studied in Sec. 5.3, where we also show its relationship to scalar and tensor Stark shifts.

In order to keep as many atoms loaded as possible in the trap, the FORT is ramped up in power immediately after stopping the molasses, which is done via TTLs on the cooler and repumper AOM controllers. The cavity light in turn, is increased to a higher power by adjusting the RF power on the AOM at the output of the EDFA which amplifies the 1560 nm light (see Sec. 3.3). An optimal way to increase the depth loosing as few atoms as possible is by ramping up the dipole trap power following a logistic function of time,

$$U(t) = U_{mol} + \frac{U_0 - U_{mol}}{\exp\left[-b\,(t - t_0)\right] + 1}, \tag{5.1}$$

where U_{mol} is the FORT depth at the molasses stage and U_0 the one attained at the end of the ramping up process, while the parameter b can be safely increased to $b \simeq 0.8$ ms^{-1} before a noticeable reduction of atom numbers is observed for a final trap depth $U_0 \simeq 700$ μK.

5.1.3 Switching off the dipole trap and imaging

The dipole trap is switched off after a 500 ms hold time interval, by turning off the PDH feedback and the 1560 nm AOM, before initiating the time–of–flight (TOF) expansion phase.

Imaging starts by opening a shutter via TTL and by turning on an AOM which introduces the 123 MHz shift (see Subsec. 1.2) bringing the cooler to resonance with the $|5S_{1/2}, F = 2\rangle \rightarrow |5P_{3/2}, F' = 3\rangle$ transition. Before a TOF varying from 0.5 to 10 ms, shutters are opened considering a suitable shutter delay ($\simeq$ 20 ms). Afterwards, the CCD camera is triggered 10 μs before the delivery of a 50 μs imaging pulse, and 60 μs after the ordinary repumper has been turned on for 50 μs if imaging atoms at the $|5S_{1/2}, F = 1\rangle$ manifold is also desired. Otherwise, atoms on the $|5S_{1/2}, F = 2\rangle$ ground state alone will be detected. Once atoms have been imaged, the imaging and repumper AOMs are turned off and the respective shutters are closed again.

After 1 s, the system is prepared to take one image with no atoms for background subtraction purposes (see Subsec. 2.3). Before, the RF powers on the imaging and repumper AOMs are turned back on and the shutters are opened again. Finally, the imaging and repumper AOMs are turned off and the shutters are closed, including the one before the camera, so that a last image is taken without any repumper or imaging light at all in order to obtain the CCD background.

5.2 Raman frequency detuning at zero FORT power

The gray molasses technique we use in our experiment requires cooler and repumper be equally blue–detuned from the excited state for dark states to appear (see Subsec. 1.3.2). This can be guaranteed in our setup by phase–modulating the EOM which creates the rempumping sideband at the ground state hyperfine splitting frequency.

Sweeping the modulation frequency a few MHz around the hyperfine splitting value $\omega_{mod} = \delta_{hf}^{^{87}Rb} = 2\pi \times 6.83468$ GHz when the FORT is off revealed a narrow feature when the optical density of the cloud was measured (see Fig. 5.2). A narrow peak approximately

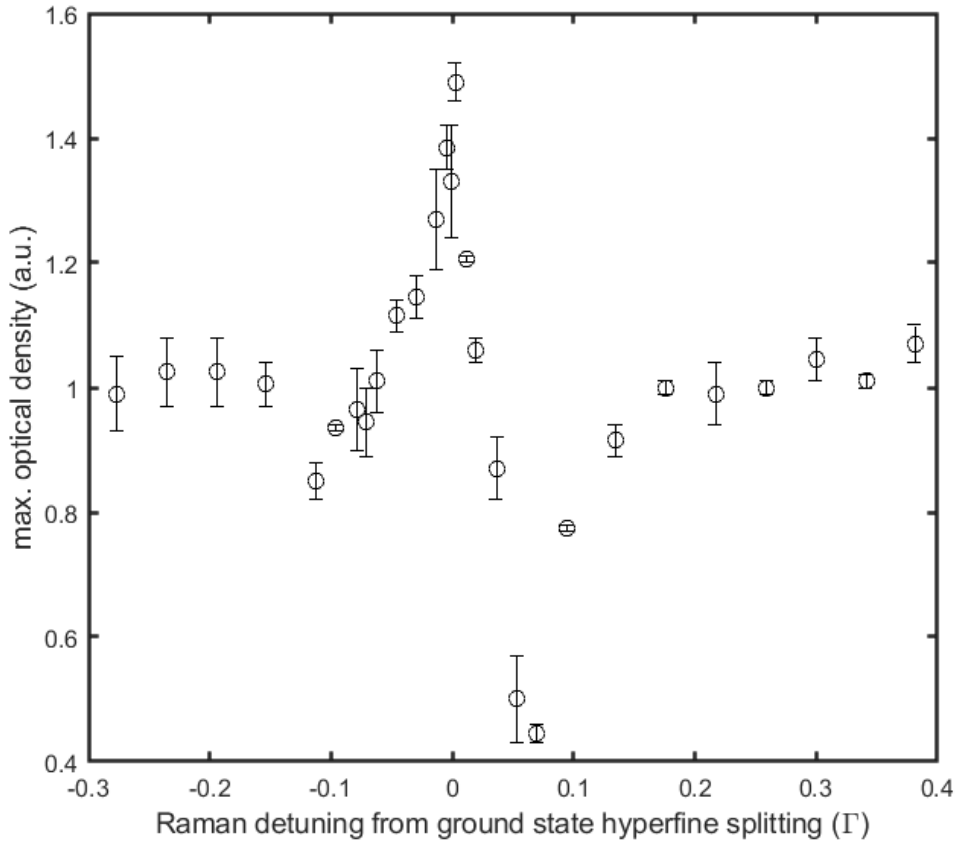

Figure 5.2: Optical density at the center of the cloud as a function of the Raman detuning $\delta_{mod} = \omega_{mod} - \delta_{hf}^{^{87}Rb}$, where $\delta_{hf}^{^{87}Rb} = 2\pi \times 6.83468$ GHz, when the FORT is off.

half a MHz wide is observed, the top of which indicates the detuning corresponding to the coldest temperature $\simeq$5 μK. Only $\simeq$300 kHz above this peak however, a deep minimum in the optical density is found which corresponds to an increase in temperature characteristic of hyperfine Λ–type gray molasses, clearly identified in lithium [43], sodium [44] and more recently in cesium [85]. Remarkably, the distance between the maximum and the minimum is much smaller than the linewidth Γ both in our case as well as in the cited ones, while the shape of the feature is well explained in the realm of CPT phenomena [86].

For non–zero FORT power, as shown in Fig. 5.1 for loaded atom numbers, a narrow

feature similar to the one in Fig. 5.2 cannot be resolved, while the ∼50 kHz red shift on the resonance obtained from the Gaussian fits is not well explained by either the scalar or the tensor AC Stark shifts, as we shall see below.

5.3 Stark shifts and dark states

There is however another detuning one needs to care about when addressing atoms in the cooler transition, namely the absolute detuning Δ from the $|5S_{1/2}, F = 2\rangle \rightarrow |5P_{3/2}, F' = 3\rangle$ transition in the case of ordinary Doppler cooling techniques. In this case, the cooler laser is usually detuned a few Γ to the red while the rempumper is on resonance with the $|5S_{1/2}, F = 1\rangle \rightarrow |5P_{3/2}, F' = 2\rangle$ transition. But the repumper is not allowed to interact with $|5P_{3/2}, F' = 3\rangle$ by the selection rules, since ΔF cannot be greater than one for a single photon transition. That is why in the gray molasses scenario, one should rather pay attention to the detuning of cooler and repumper from $|5S_{1/2}, F = 2\rangle \rightarrow |5P_{3/2}, F' = 2\rangle$ and $|5S_{1/2}, F = 1\rangle \rightarrow |5P_{3/2}, F' = 2\rangle$ transitions respectively.

Moreover, under the presence of the dipole trap the equivalence of considering the blue detuning from $|5S_{1/2}, F = 2\rangle \rightarrow |5P_{3/2}, F' = 2\rangle$, or the red detuning from $|5S_{1/2}, F = 2\rangle \rightarrow |5P_{3/2}, F' = 3\rangle$, does not hold as in free space anymore, since the splittings between hyperfine levels of the excited manifold get modified differently as the effect of the tensor polarizability term in the AC Stark shift becomes important (see Ann. A.), and the degeneracy of different Zeeman sublevels is partially lifted.

5.3.1 Scalar and tensor polarizability contributions on ^{87}Rb atoms under the FORT

In Subsec. 3.2.2, the dipole potential was treated considering the internal energies of atoms are made only of two levels. This is because once the evaporation process in the dipole trap has advanced for some hundreds of milliseconds, most atoms are found to be in the ground state, and thus shifts produced in the excited state are no longer relevant. This is not the case however during the gray molasses process, or during any of the preceding Doppler cooling

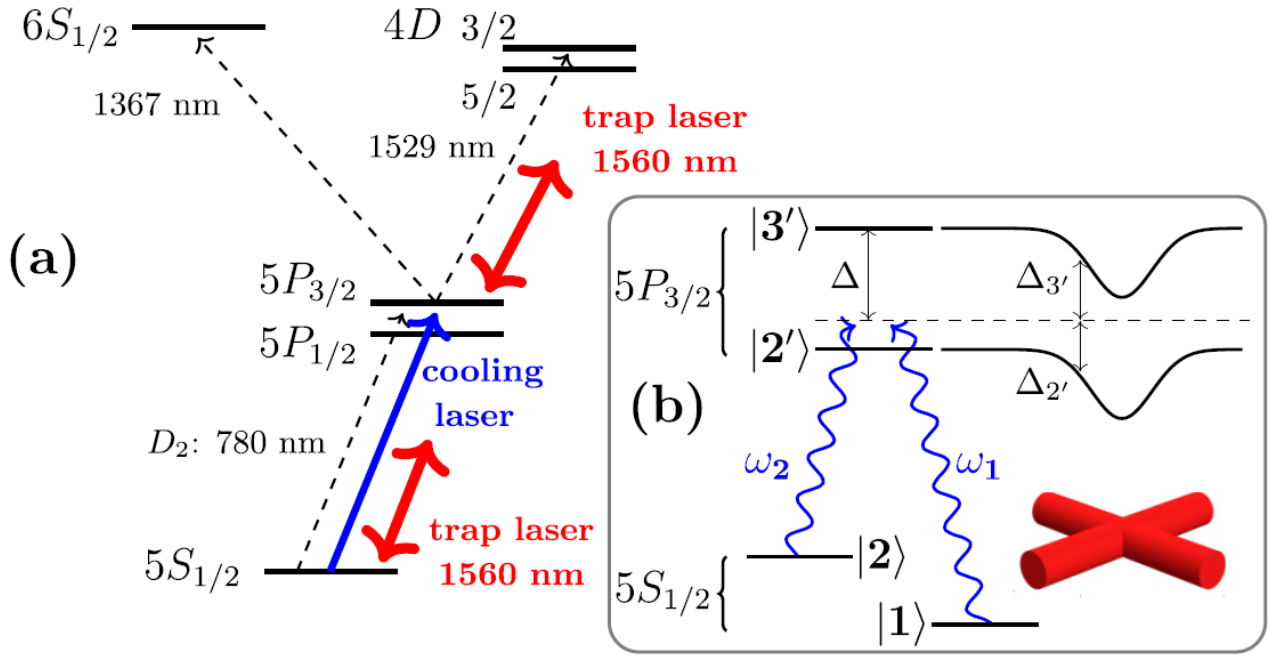

Figure 5.3: In a) relevant energy levels of ^{87}Rb showing both the laser on the cooling transition and the trap laser producing the FORT. In b) cooler and coherent repumper are shown in the context of the D_2 line, both with and without large differential light shift. Figure published in [16].

techniques on the cycling transition. In what concerns the latter ones, the effect of the large differential light shift produced by the 1560 nm during the loading of the dipole trap from the MOT was studied soon after our experiment was built [54]. This light shift is due to a resonance of the $5P_{3/2}$ manifold in the polarizability factors (see Ann. A.), with the higher lying excited states $4D_{3/2,5/2}$ close to 1529 nm, and to a lesser extent to the one with the state $6S_{1/2}$ at 1367 nm shown in Fig. 5.3, when 1560 nm light is used. It is easy to understand then why the shift is so much larger on the $5P_{3/2}$ manifold than it is on the $5S_{1/2}$ ground one when the FORT is turned on.

The term producing the partial lifting of degeneracy between different m_F sublevels however, was not considered at the time, since the main concern back then was to keep the cooler detuned between $|5S_{1/2}, F = 2\rangle \rightarrow |5P_{3/2}, F' = 2\rangle$ and $|5S_{1/2}, F = 2\rangle \rightarrow |5P_{3/2}, F' = 3\rangle$ transitions even when the large differential light shift was present. For that purpose, it was only made sure that detuning Δ from the bare upper transition was large enough to be also red–detuned in the FORT region when the dipole trap was set at higher power. In fact, the

differential light shift was utilized in order to accumulate atoms in the absolute ground state and realize a light shift induced dark spot [87], similar to a dark spot MOT [88]. In our case, it was not until we numerically simulated the AC Stark shift, taking into account both the scalar and tensor polarizability contributions, that we realized about the importance of the partial lifting of the degeneracy at high FORT power (see Ann. A.).

At the maximum power we apply experimentally (see Subsec. 3.2.2), we get 19.9 mW in transmission out of the cavity, which corresponds to trap frequencies of $\omega_x^{max} = \omega_z^{max} \simeq 2\pi \times 840$ Hz and $\omega_y^{max} \simeq 2\pi \times 905$ Hz, and a peak intensity of approximately 6 GW/m^2 at the crossing region of the FORT (see Ann. A.). In terms of trap depth, we get 700 μK at this power for atoms in the ground state as assumed in Subsec. 3.2.2, and for the excited state the corresponding shifts are plotted in Fig. 5.4. From the plot we see that

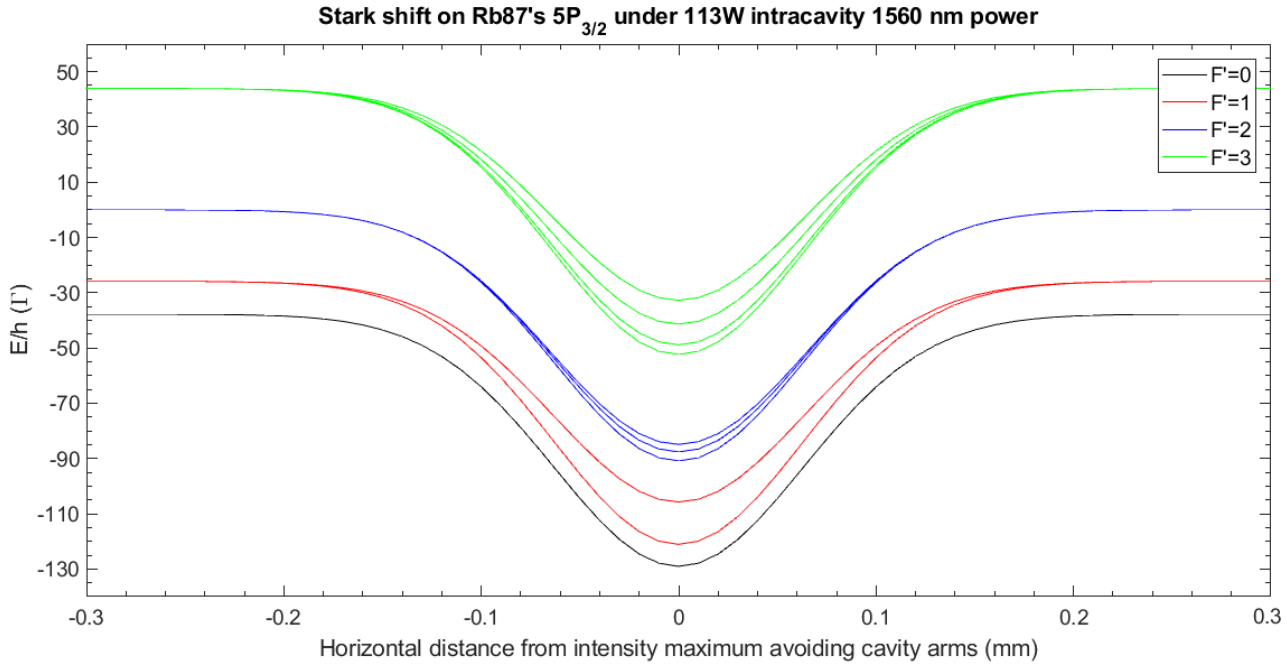

Figure 5.4: AC Stark shift on ^{87}Rb's $5P_{3/2}$ manifold under 1560 nm FORT at trap depth of 700 μK, in units of the natural linewidth Γ and as a function of horizontal distance from the maximum intensity point. For energies, the origin has been chosen at the bare $F' = 2$ level, which is the level of interest for our gray molasses scheme.

the shift on the $F' = 2$ manifold becomes larger than 80Γ, and Zeeman level splitting spans approximately 10Γ. We can consider these two values as the upper limits of Stark shift and splitting we are confronted with respectively in our experiment.

In practice, the shift created by the FORT on the energy levels was detected by measuring the number of atoms loaded in the trap as a function of the absolute detuning Δ of the Raman scheme. This was done while changing the power injected into the cavity at 1560 nm, and then the optimal power that maximized the number of atoms loaded into the trap could be found. In Fig. 5.5 the atom numbers we obtained for six different values of FORT power are plotted, measured by absorption imaging after a in–trap hold time of 500 ms. At the

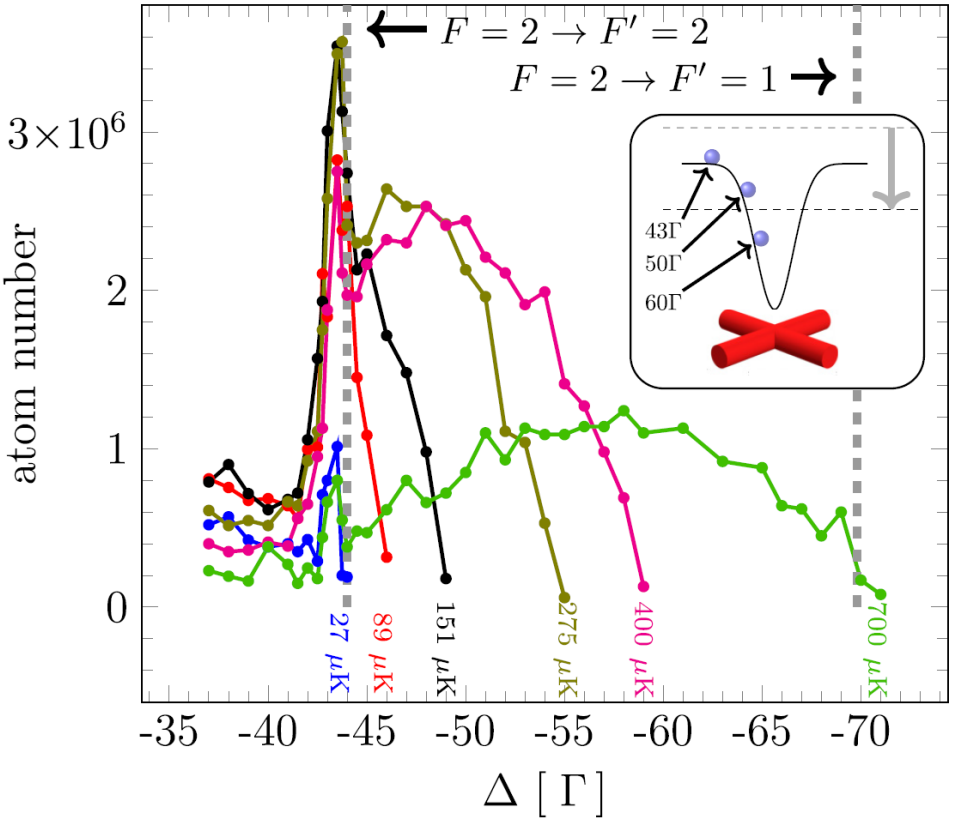

Figure 5.5: Number of atoms loaded into the FORT at large absolute detuning from the bare $|5S_{1/2}, F = 2\rangle \rightarrow |5P_{3/2}, F' = 3\rangle$ cooler transition, near $|5S_{1/2}, F = 1, 2\rangle \rightarrow |5P_{3/2}, F' = 2\rangle$ and between this and $|5S_{1/2}, F = 1, 2\rangle \rightarrow |5P_{3/2}, F' = 1\rangle$ cooler and repumper transitions for lasers at the Raman condition under different FORT depths indicated in colors. The sharp peak at -43.5Γ is given by atoms cooled just outside the FORT, while the broader farther detuned peak corresponds to atoms residing within the FORT volume. Inset: The radially changing FORT power results in a position dependent excited state light shift, represented for a FORT depth of 700 μK. Figure published in [16].

maximum trap depth of 700 μK, the range of detunings at which some loading is observed is

large, but the loading efficiency is low at every detuning as compared to lower FORT power. Off–resonant scattering from excited–state hyperfine levels not involved in the formation of dark states can hinder them, and the resulting decay rate will be strongly related to the energy shifts. Indeed, the dark state effective lifetime becomes dependent on the local intensity of the FORT field. However, the effect can be exploited to selectively cool the optically trapped atoms at specific radial positions, or to progressively cool the atoms in the FORT from its borders and towards its center as we shall see below.

Focusing now on the lower FORT power data sets, an interesting feature at -43.5Γ can be observed on all of them and even on the highest FORT power one, namely a narrow $\sim \Gamma$–wide peak on the number of loaded atoms. This suggests that cooling is mostly efficient outside and on the edges of the FORT, since the large detuning Δ is compatible with a blue detuning with respect to the unshifted $|5S_{1/2}, F = 1, 2\rangle \rightarrow |5P_{3/2}, F' = 2\rangle$ transitions. This peak sits atop a broader feature which does not abruptly end at the position of the $|5S_{1/2}, F = 1, 2\rangle \rightarrow |5P_{3/2}, F' = 2\rangle$ resonance. The broader feature shifts and broadens with increasing FORT power while the position of the sharp peak remains constant. This makes the outside and on the edges cooling assumption very plausible, while the broader feature corresponds to atoms loaded from within the trapping volume of the FORT: optimal detuning to cool these atoms is larger and position dependent, because of the excited state light shifts imposed by the FORT.

After these findings, we set the power on the FORT so as to maximize the loading peak at -43.5Γ, something which occurs at a FORT depth of 170 μK.

5.3.2 Possible dark states: from ZDSs to HDSs

The data presented so far were obtained by creating a rempumping sideband via phase–modulation of the cooler beam using an EOM (see Subsec. 1.3.2). But in our experiment, there is still the option to load the dipole trap using independent cooler and repumping lasers, with the latter on resonance with the $|5S_{1/2}, F = 1\rangle \rightarrow |5P_{3/2}, F' = 2\rangle$ rempumping transition (see Sec. 2.1).

From the point of view of the possible dark states which can be created utilizing one or the

other method, it is clear that HDSs (introduced in Sec. 1.3.3) can be only created with cooler and repumper in the Raman condition, since this condition is necessary in order to create coherence between sublevels belonging to different hyperfine states. Unfortunately, creating a pair of frequencies in the Raman condition using the independent repumper off resonance with the repumper transition, would require introducing several changes on the geometry and the electronics, in particular a phase locked loop (PLL) [89] would be needed in order to phase lock one laser onto the other. That is why the Raman condition in our experiment completely relies on the phase–modulation of the cooler. Nonetheless, as we shall see below, the independent cooler and repumper configuration does also show a sub–Doppler cooling feature which is satisfactorily explained by gray molasses cooling via ZDSs (introduced in Sec. 1.3.3).

The repumper at the Raman condition with the cooler, alows in principle for a larger variety of dark states, including both ZDSs and HDSs. The existence of the latter ones depends on the number of degenerate ground (N_g) and excited (N_e) Zeeman states [38, 90]: (i) for $N_g > N_e$, a dark state always exists provided the laser frequencies match the right detuning condition; (ii) for $N_g \leq N_e$, additional conditions on the complex Rabi frequencies must be satisfied. For instance, dark states where the connectivity between ground and excited states forms a loop exist if the phases of each complex Rabi frequencies sum to a multiple of 2π [90, 91]. These states are particularly relevant for gray molasses cooling because they can be eigenstates of the kinetic energy, thus stable both under free evolution and in presence of a slowly varying external potential.

The dark states for case (ii) then can exist in the usual $\sigma_+ - \sigma_-$ cooling configuration present in our experiment, provided that lasers tuned to the cooling $|5S_{1/2}, F = 2\rangle \rightarrow |5P_{3/2}, F' = 2\rangle$ and repumping $|5S_{1/2}, F = 1\rangle \rightarrow |5P_{3/2}, F' = 2\rangle$ transitions are phase–locked to fulfil the phase requirements on the Rabi frequencies. In addition, the excited Zeeman states $|F' = 2, m_{F'}\rangle$ must be degenerate e.g. at zero magnetic field or when the connected states experience the same light shifts in the presence of far off–resonance light (see example in Fig. 5.6). A numerical approach to ascertain the precise dark states involved in our configuration under light at 1560 nm is presented in Subsec. 5.3.3.

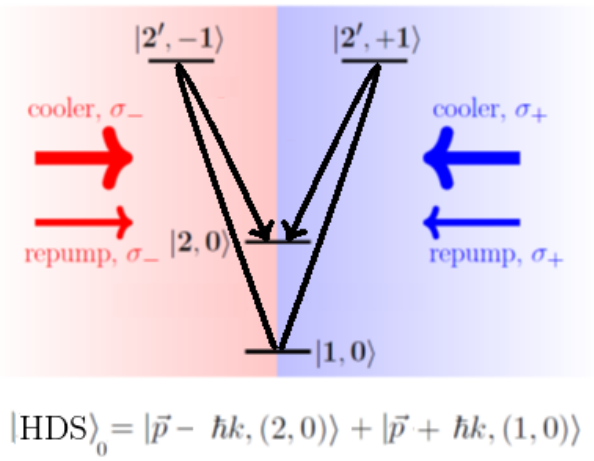

Figure 5.6: Example of case (ii) HDS in the $\sigma_+ - \sigma_-$ cooling configuration present in our experiment, for which the loop is connecting ground states whose $m_F = 0$. The excited states also experience the same light shifts in the presence of far off resonance light, given that they share the same $|m_{F'}|$ value.

5.3.3 Theoretical framework and determination of dark states

To investigate the formation of dark states, a one dimensional model of the gray molasses [31, 43] that includes the presence of two counterpropagating beams with opposite circular polarization, each carrying both cooler and repumper frequency, was used by our Italian collaborator Prof. Francesco Minardi.

The considered Hamiltonian is a sum of three terms: (i) the atomic Hamiltonian H_{at}, taking into account only the $5S_{1/2}$ and $5P_{3/2}$ manifolds connected by the D_2 line; (ii) the molasses Hamiltonian H_{mol}, modeling the interaction of the atom with the cooler and repumper light; and (iii) the scalar and tensor Stark Hamiltonians H_{dip}, describing the interaction of the atom with the dipole trap light at 1560 nm, causing scalar and tensor light shifts. However, for the computer simulations used to reproduce our dipole trap loading results, we considered the specific case of zero power for the FORT [16], which is valid for atoms at the edges of the trap. Furthermore, a fully time-dependent model, which is beyond the scope of the work presented here, should consider the FORT intensity increase during the few ms long gray molasses phase. By ignoring the last term (iii) in what follows then, we get

$$H = H_{\mathrm{at}} + H_{\mathrm{mol}}, \tag{5.2}$$

with

$$H_{\rm at} = \sum_{n=5S_{1/2},5P_{3/2}} \sum_{n,F,m_F} E\left(n,F,m_F\right)|n,F,m_F\rangle\langle m,F,m_F| \tag{5.3}$$

$$H_{\rm mol} = -\frac{\hbar}{2}\left[\left(\Omega_R e^{-i\omega_R t}+\Omega_C e^{-i\omega_C t}\right)\left(\hat{e}_+ e^{ikz}+\hat{e}_- e^{-ikz}\right)\hat{\Sigma}_+ + H.c.\right]. \tag{5.4}$$

In the $H_{\rm at}$ term, $E(n,F,m_F)$ denotes the energies of the ground and excited hyperfine manifolds, hereafter indicated with $5S$ and $5P$, with the definition $E(5S,1,m_F)=0$.

In $H_{\rm mol}$, $\Omega_{R(C)} \equiv \Gamma\sqrt{I_{R(C)}/\left(2I_s^0\right)}$ is the repumper (cooler) Rabi frequency in terms of the saturation intensity $I_s^0 = 1.67$ mW/cm^2 and the excited state linewidth $\Gamma = 2\pi\times$ 6.067 MHz, $\hat{\Sigma}_{+/-}$ are the raising operators of atomic levels whose matrix elements are derived from the 3–j and 6–j Wigner coefficients (see Ann. A. for the explicit form), and $\omega_{R(C)}$ is the repumper (cooler) angular frequency. Each molasses beam carries the repumper and cooler components, with Rabi frequencies $\Omega_C = 4.2\,\Gamma$ and $\Omega_R = 1.2\,\Gamma$, corresponding to the total intensities, i.e. summed on the six beams found in standard 3DMOTs. Eq. (5.4) is farther simplified by neglecting the coupling of the cooler with the $F=1\rightarrow F'$ transitions, due to very large detuning ($\sim 10^3\,\Gamma$), and likewise the coupling of the repumper with $F=2\rightarrow F'$ transitions,

$$H_{\rm mol} \simeq -\frac{\hbar}{2}\left[\left(\Omega_R e^{-i\omega_R t}P_e\hat{\Sigma}_+P_1+\Omega_C e^{-i\omega_C t}P_e\hat{\Sigma}_+P_2\right)\left(\hat{e}_+ e^{ikz}+\hat{e}_- e^{-ikz}\right)+H.c.\right]. \tag{5.5}$$

By applying the unitary transformation,

$$U = P_1 + \exp\left[i\left(\omega_R-\omega_C\right)t\right]P_2 + \exp\left[i\omega_R t\right]P_e$$

where P_1, P_2, P_e are the projectors on the ground lower $\{|5S,1,m_F\rangle\}$, ground upper $\{|5S,2,m_F\rangle\}$, and electronic excited $\{|5P,F',m'_f\rangle\}$ hyperfine levels, respectively, the Hamiltonian is modified as follows: (i) the time-dependence of $H_{\rm mol}$ drops, and (ii) the atomic energy levels are shifted $E'(5S,1,m_F)=0$, $E'(5S,2,m_F)=E(5S,2,m_F)-\hbar(\omega_R-\omega_C)$, $E'(5P,F,m_F)=E(5P,F,m_F)-\hbar\omega_R$.

The frequency difference $\omega_R-\omega_C$ is set to match the hyperfine separation of a free atom and then the Hamiltonian for different values of the position z is diagonalized. At each position, dark states are identified as those whose projection in the excited level $5P$ is below an arbitrary threshold value, chosen equal to 0.1, i.e. a given eigenstate $|\psi\rangle$ of the total Hamiltonian is considered dark if $\langle\psi|\,P_e\,|\psi\rangle < 0.1$, which is equivalent to require a scattering rate

below $0.1\,\Gamma$. In the σ_+/σ_- configuration of the 1D model, the light shifts are uniform in space, i.e. independent of z. At each point the polarization of the molasses lasers field is linear, with direction varying periodically in space so as to wind like a helix (see Subsec. 1.3.2). As a consequence, it is expected that the number of dark states does not depend on the position z.

In the set of dark states, a farther selection can be made by keeping only those composed of hyperfine states $|F, m_F = \pm 1\rangle$ and discarding those formed by $|F, \pm 2\rangle$ and $|F, 0\rangle$. The former are linear superpositions of states with momenta $p \pm \hbar k$, that can be stable under kinetic energy evolution for sufficiently small p. On the other hand, the latter are superpositions of states with momenta $p, p \pm 2\hbar k$, that cannot be eigenstates of the kinetic energy. For molasses times longer than the inverse kinetic energy associated to the two–photon transitions, $t_{mol} > (2\hbar k^2/m)^{-1} \simeq 10\,\mu$s, the latter states become bright.

To calculate the expected relative populations of the $F = 1$ and $F = 2$ hyperfine levels at the end of the molasses, only the dark states selected as described are taken into account: for each of the states $|D_j\rangle$, $p_{1,j} = \langle D_j| P_1 |D_j\rangle$ and $p_{2,j} = \langle D_j| P_2 |D_j\rangle$ are evaluated, and the relative population $N_2/(N_1 + N_2) = \sum_j p_{2,j}/(p_{1,j} + p_{2,j})$ is defined, implicitly assuming that all dark states are equally populated.

5.4 Gray molasses FORT loading and cooling: results

We have so far presented the experimental procedure accompanied by some preliminary results which allowed us to set the optimal parameters for the loading of the FORT, and the theoretical picture of possible dark states to be expected in our experiment. We intend in this section to present the FORT loading results that confirm our assumptions, as well as to describe an in–trap cooling technique which builds on these results.

5.4.1 Gray molasses FORT loading efficiency

The measured loading efficiency in the dipole trap as a function of the red detuning of the cooler from the $F = 2 \rightarrow F' = 3$ transition is plotted in Fig. 5.7a), for both the ordinary independent repumper (blue points) and the Raman condition molasses (red points) config-

urations. In Fig. 5.7b) on the other hand, the purple points which are numerically simulated following Subsec. 5.3.3, report the relative population in the specific case for zero power of the FORT. Thus this configuration approximates the condition experienced by the atoms roaming the edges of the FORT trap.

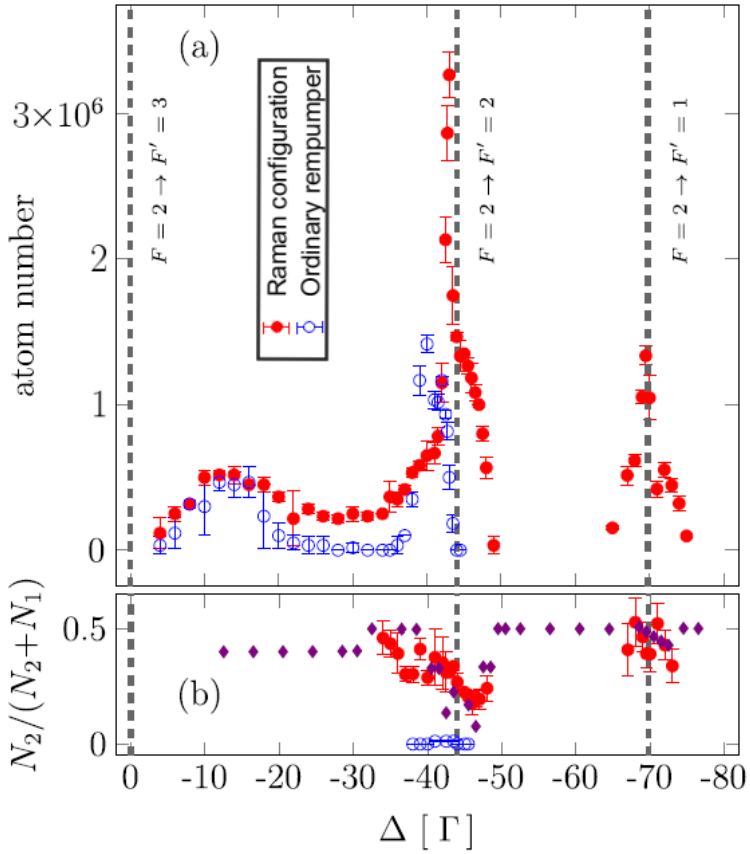

Figure 5.7: a) Number of atoms loaded into the FORT at optimal depth 170 μK, as a function of detuning of the cooler from the $F = 2 \rightarrow F' = 2$ cycling transition, for both ordinary and Raman scheme repumper configurations. The numbers are measured after the dipole trap has been held up for 500 ms, and a TOF of 2 ms. b) Population fraction of atoms in $F = 2$ with the repumper in the two configurations as above; $N_{1,2}$ indicate the atomic populations of the $F = 1, 2$ manifolds. The purple points result from a numerical evaluation of the DSs forming at each detuning (see Subsec. 5.3.3). Figure published in [16].

We can identify three regions: (i) $|\Delta|/\Gamma < 30$, where standard $F = 2 \rightarrow F' = 3$ sub–Doppler cooling takes place, leading to optimum loading at $|\Delta|/\Gamma \simeq 15$ for both configurations; (ii) $30 < |\Delta|/\Gamma < 60$, where gray molasses occurs on the $F = 2 \rightarrow F' = 2$ transition; and (iii) $|\Delta|/\Gamma > 60$, where gray molasses occurs on the $F = 2 \rightarrow F' = 1$ transition.

In the first configuration, only ZDSs can form. Gray molasses leads to a 2.5 times more efficient loading at -40 Γ, i.e. blue–detuned from the $F = 2 \rightarrow F' = 2$ transition, than the loading at $|\Delta|/\Gamma \simeq 15$. This coincides with an optimum in density when the cooling is applied without the FORT. We find that almost all the atoms are in the $F = 1$ manifold (blue points in Fig. 5.7b)) even though the ZDSs are in the $F = 2$ manifold. This can be understood as the effect of the repumper weakly coupling the dark states [22], leading to eventual decay in $F = 1$.

In the second configuration we observe a more efficient loading, with an outstanding narrow peak at -43.5 Γ, seven times higher than standard red–detuned molasses and more than twice higher than the one corresponding to ZDS gray molasses. A similar peak is also observed at -69 Γ, i.e. blue–detuned from the $F = 2 \rightarrow F' = 1$ transition, although its loading efficiency is lower due to at least in part the ramping process of absolute detuning from the MOT frequencies, which involves crossing the $F = 2 \rightarrow F' = 2$ transition with associated heating. The atomic population in this region is more balanced for all detunings (red points in Fig. 5.7b)), which suggests all atoms are in balanced HDSs, mediated either by the symmetric excited state $m_{F'} = \pm 1$ (as in Fig. 5.6), or via $m_{F'} = 0$.

The sharpness of the peak at -43.5 Γ occurs due to a competition between the enhanced atomic densities outside the FORT and the effect of the light shifts on atoms approaching the FORT frontier, and its position at -43.5 Γ does not change with the FORT power as reported above in Fig. 5.5. The peak ultimately arises from a volumetric effect, while the shape of the broader loading curve is a convolution of the atomic density distribution and the spatial profile of the FORT. A similar double structure can be resolved in the blue data points, where only ZDSs can form, but the associated peak at -40 Γ is much less intense. Moreover, the broader feature in this case does not penetrate the vertical line representing the $F = 2 \rightarrow F' = 2$ transition, which indicates that the ordinary repumper configuration is not compatible with cooling atoms inside the FORT volume.

The finding of a more efficient loading with HDSs than with ZDSs also agrees with the greater proximity of the HDS peak to the $F = 2 \rightarrow F' = 2$ transition thanks to the involvement of states with zero momentum in this case, which results in lower temperatures and more efficient loading of the FORT.

5.4.2 Farther detuned molasses for high power in–FORT cooling

Optically trapped atoms experience position dependent excited state light shifts, in relation to the local FORT power. Changing the detuning of HDS cooling will hence address atoms at different places in the optical potential creating spatially dependent HDSs. The position of an atom within a conservative trap is also energy dependent, with higher momentum/energy states spending more time near the edges where the light shift is smaller, while lower momentum/energy states residing near the center where the light shift is larger. Therefore at any particular detuning only atoms of a particular momentum/energy will be optimally cooled. This opens up the possibility of an altogether different type of cooling: by starting with small detunings, hotter atoms at the edges of the FORT will selectively cool, falling deeper into the FORT where a farther shift in the Raman beams to larger detunings will cool the atoms to even lower momentum/energy states. Excited state effects will be minimized, since the protocol relies on dark states, and remarkably, no atoms are lost in the process, given that the energy is carried away via spontaneous emission and not by evaporation (described in Sec. 3.4).

To investigate this possibility, we ramped up the FORT depth to 535 μK after the atom loading following a function of the form of Eq. 5.1, to increase the excited state light shifts and, thereby, the energy selectivity. We sweep the detuning in 6 ms from -55 Γ to -68 Γ and observe a temperature reduction from 198 μK to 48 μK with no atom loss (Fig. 5.8). A slower sweep does not lower the final temperature, whereas increasing the final detuning beyond $-68\,\Gamma$ results in a complete atom loss as the laser frequency becomes resonant with the $F = 2 \rightarrow F' = 2$ transition at the center of the FORT.

Higher energy sensitivity can be achieved by farther increasing the FORT depth. However, for large shifts, while the Raman beams are detuned to cool atoms near the edges of the FORT, atoms in the center find themselves closer to the $F = 2 \rightarrow F' = 3$ transition, an effect which can impede the formation of HDSs and eventually cause heating. This effect represents the main limitation to our present scheme but it also points to a straightforward remedy, i.e. perform the scheme on the $|5S_{1/2}, F = 1, 2\rangle \rightarrow |5P_{1/2}, F' = 2\rangle$ transitions of the D_1 line which contain no higher $F' = 3$ state.

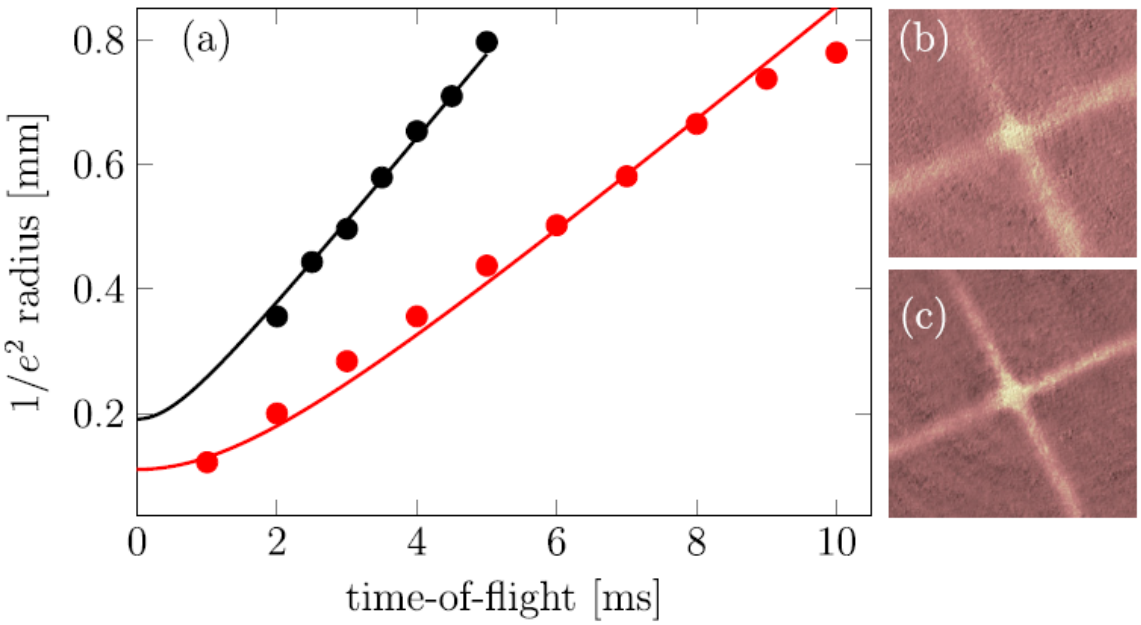

Figure 5.8: a) Ballistic expansion of the atomic cloud released from the FORT: cloud size versus TOF. The fits (solid lines) yield a temperature of 198 μK before the cooling sweep (black points) and 48 μK after it (red points). Absorption images of the atoms before b) and after c) the cooling sweep, taken with a TOF of 700 μs. The atom number in the cross configuration is $\simeq 3\times10^6$, with no significant difference between the two cases. Figure published in [16].

Nonetheless, the experimental scheme presented in this chapter, using the same D_2 line as here, has already proved its power for the production of all–optical Bose–Einstein condensates (BEC) in microgravity [92]. The 1550 nm FORT used in this case leads to very similar light shifts as the ones presented in this chapter, while in their experiment the Λ–enhanced gray molasses cooling enables a fourfold increase on the number of atoms loaded as compared to the numbers obtained with a molasses produced using independent cooler and repumper. This eventually permits to initiate the evaporation ramp with more atoms and reach phase space densities (PSD) allowing for condensation at the end of the process, under both gravity and microgravity.

Chapter 6

Interarm photon exchange processes with ultra–cold atoms

Injecting 780 nm laser light into the cavity has permitted us to observe atom–cavity coupling with atoms loaded onto the far off–resonant dipole trap (FORT). Signatures of this coupling together with the effect on atomic internal ground state populations for phase–modulated and unmodulated light has been presented in Chapter 4. In the current chapter, we will present more recent results which build upon the two–photon coherent scattering processes described above and which are still preliminary at the time of completion of this manuscript.

6.1 Interaction of atoms with carrier and sideband pulses: experimental procedure

Before injecting the 780 nm pulse into the cavity, a sample of cold atoms needs to be created and loaded at the center of the FORT, where the interaction with the 780 nm intracavity light occurs. We make the atoms interact with the pulses once sufficiently cold atomic samples for observing few photon coherent phenomena have been made available. In order to ensure this condition, a FORT evaporation ramp of 4.5 s is applied, which provides us with a couple of hundred thousand atoms at temperatures slightly below 0.5 μK (see Sec. 3.3). In what concerns the preceding cooling and loading procedure, this is entirely based on the gray

molasses technique described in Sec. 5.1, and thus we shall only focus on the creation of the 780 nm light pulse in what follows.

The light pulses we inject are never shorter than 20 μs in duration, and then we avoid increasing the uncertainty of the pulse frequency above the range of frequencies on the order of the linewidth of the cavity.

6.1.1 AOM pulse injection control and phase–modulation via EOM

It is at the end of the previously described 4.5 s evaporation ramp (see Sec. 3.3), when the dipole trap depth is approximately 25 μK, that we deliver the 780 nm pulse into the cavity. There are two time duration parameters which are computer controlled: the first is the duration of the pulse, while the second is the extra interval during which the atoms are kept in the optical dipole trap after the 780nm pulse, so that when the latter parameter is zero both the FORT and the 780 nm pulse are turned off simultaneously. Both time parameters, as well as the power and the frequency which allows to change the pulse detuning from the cavity resonance, are controlled via the 200 MHz fiber AOMs introduced in Sec. 3.5, while the dipole trap turning off control remains unchanged.

Before being split and entering the AOMs, the 780 nm light goes through a fiber EOM (see Sec. 3.5) that allows to create sidebands which are resonant seven times the cavity free spectral range (FSR) away from the carrier. This one is red detuned by $\Delta \simeq 2\pi \times 22.5$ GHz from halfway between cooler and repumper transitions in order to avoid spontaneous emission for the series of experiments described in this chapter.

6.1.2 Atom–cavity resonance and off–resonant pulses

The transmission signal out of the cavity, in turn, is detected via a photodiode. The intensity of the signal along with the reflected signal intensity off the injection mirror, gives a direct measure of how far detuned δ_{AC} the injected pulse is from the atom–cavity resonance. We have presented in Sec. 4.2 the dispersive shift from the empty cavity resonance produced by the atom–cavity interaction, which is on the order of hundreds of kHz at most for the red detuning Δ of the pulse we use from the atomic transition.

For each experimental run, and once the coarse AOM frequency control on the voltage controlled oscillator (VCO) has been manually tuned so as the pulse to be on the proximity of the atom–cavity resonance ($\delta_{AC} \simeq 0$), the desired precise detuning is selected via analog control of the VCO frequency, which allows for a resolution of ~ 10 kHz as found from the voltage to frequency calibration inferred from the cavity linewidth κ and the empty cavity spectroscopy (see Subsecs. 3.5.1 and 4.2.2).

The sequence ends by turning off the FORT and imaging via time–of–flight (TOF) in the same way as described in Subsec. 5.1.3.

6.2 Momentum distribution studies via absorption imaging

The 780 nm pulses injected in the cavity interact with cold atoms trapped in the optical dipole trap. Thanks to the imaging system in our experiment, which implements absorption imaging detection, several properties of these atoms can be studied. TOF is, in particular, the technique we use and the one which provides us with information about the momentum distribution of atoms at the center of the cavity. The effect produced by the 780 nm pulse on the momentum of the atoms needs to be distinguished from the TOF expansion due to the finite temperature of the atoms, and thus the colder our atoms are the easier will be to distinguish any effects produced by the momentum imparted by the cavity pulses. These pulses are shorter or at most, their duration is of the order of the TOF duration for the longest pulses when the shortest TOF durations are applied.

Thanks to the temperature of the atoms being comparable to the recoil limit one for ^{87}Rb after the FORT evaporation ramp has come to an end (see Sec. 3.3), the effect of the pulses on the atoms as observed by TOF expansion are clearly apparent as we shall see next.

6.2.1 Red– vs blue–detuned, atom–cavity interactions

Once the capacity to inject pulses detuned from the atom–cavity resonance with a resolution of approximately 10 kHz was demonstrated, we started to explore the effect of these pulses on the atoms after a TOF expansion of 2 ms. A pulse duration of 200 μs was chosen, while

the injected power was kept at 50 μW on atom–cavity resonance. We chose the latter value due to the optical power limitation on the fiber EOM input, which allows to inject no more than 0.5 mW per injection port, and thus obliges to use low–power on resonance if one wants to keep the transmission power out of the cavity constant when injecting at a few hundreds of kHz detuning.

After an initial exploration on the close vicinity of atom–cavity resonance, we observed a clear qualitative difference between $\delta_{AC} < 0$ and $\delta_{AC} > 0$ frequency detuning cases. We

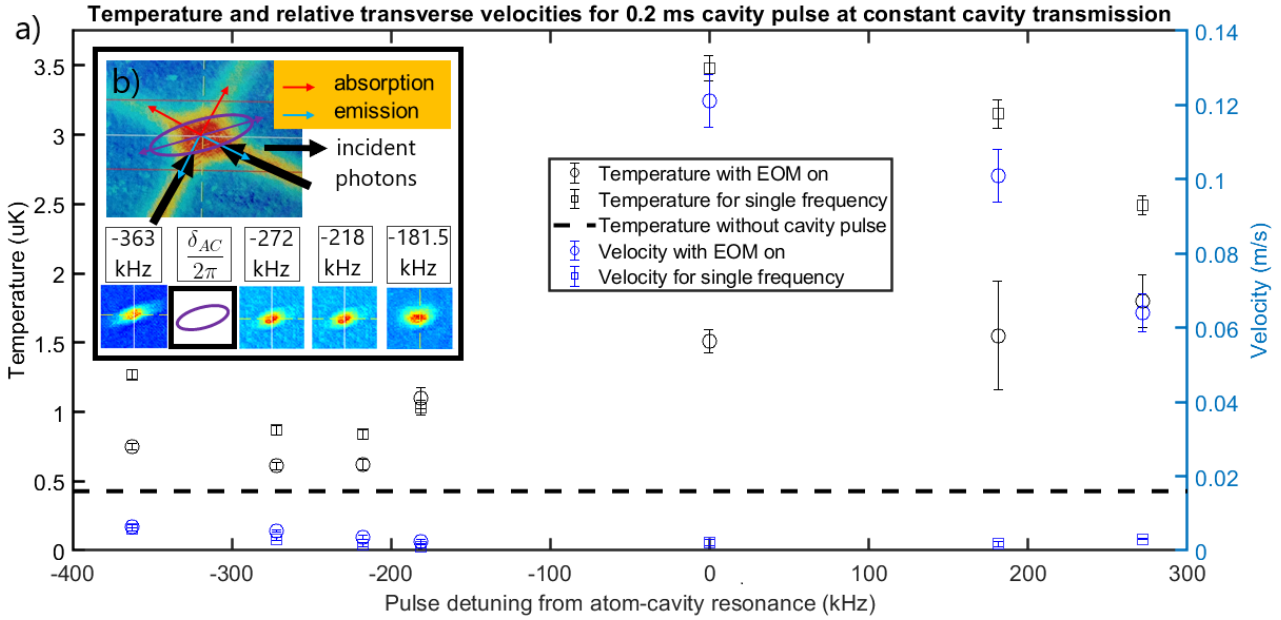

Figure 6.1: a) Temperature and velocity of atoms as a function of detuning from atom–cavity resonance both when the EOM is on at $\beta \simeq 1.4$ rad modulation amplitude and $\omega_{\text{mod}} = 2\pi \times 6834.26$ MHz, and when it is off. Inset b) shows a TOF image of $\sim$3 million atoms at the top before the FORT evaporation ramp has been initiated, and four images at the bottom with $\sim$0.2 million atoms each after the ramp and the 780 nm pulse have been applied. Frequency values appearing above each of the four images are detunings $\delta_{AC}/(2\pi)$ plotted in the red detuned region ($\delta_{AC} < 0$) of a). Large black arrows represent the momentum carried by the intracavity 780 nm photons when a single port is injected, while smaller red and blue vectors represent momentum imparted to atoms when two–photon absorption–emission processes happen, respectively. Finally, each purple vector equidistant from two cavity arms is a sum of a red and a blue vector, and represents one of the two possible total momentum changes of an atom experiencing a two–photon process involving the interarm photon exchange described in Sec. 4.3, while the purple ellipse represents the shape the atomic cloud acquires after TOF.

could identify two regions (see Fig. 6.1): (i) the blue side of the resonance ($\delta_{AC} > 0$) where

the atoms are heated by more than a factor of three with respect to the case of not injecting the 780 nm pulse, and where a large momentum is imparted to the atoms when the EOM is on; and (ii) the red side ($\delta_{AC} < 0$) where very little heating is observed, and where the atomic cloud is elongated along the direction at 45 degrees from the cavity arms (see inset b) in Fig. 6.1).

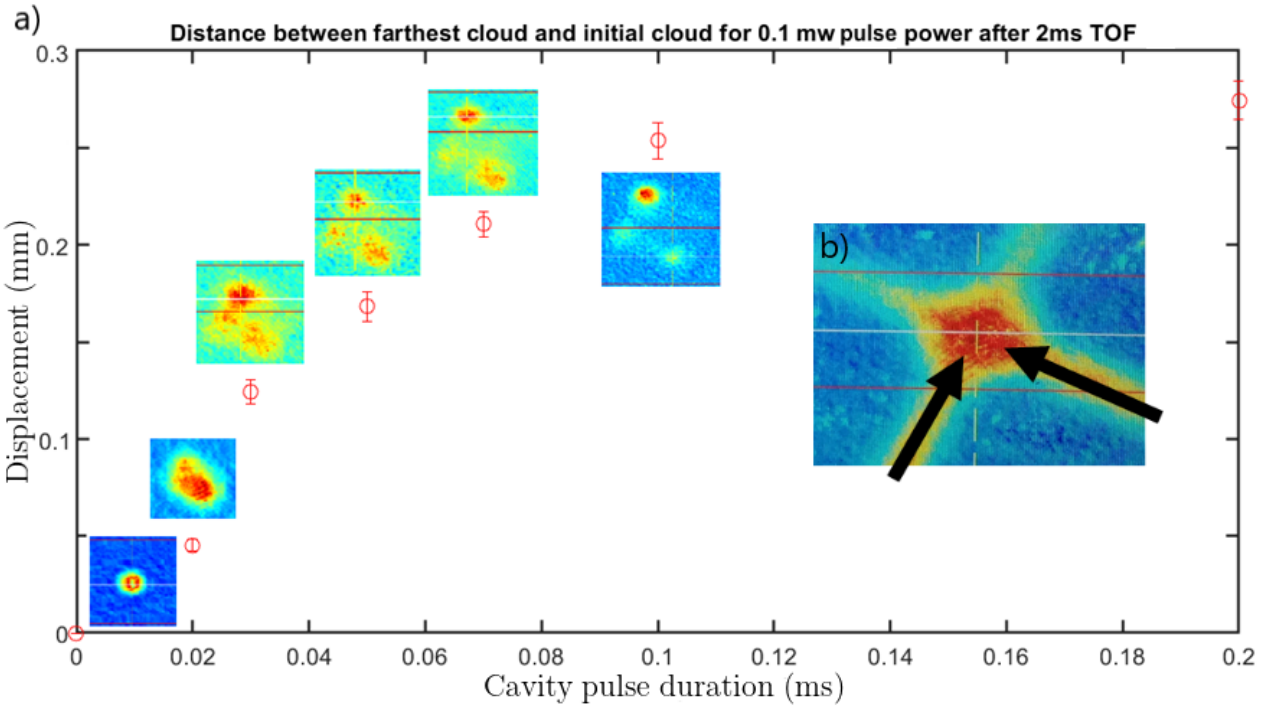

Figure 6.2: a) Close to resonance displacement of the farthest atomic cloud from the immobile one in the center (appearing at the bottom right of each of the small TOF images), as a function of 780 nm pulse duration at $\beta \simeq 1.4$ rad EOM modulation amplitude and $\omega_{\text{mod}} = 2\pi \times 6834.26$ MHz modulation frequency. TOF images for most of the data points are shown close to them. Inset b) shows the same pre-evaporation ramp TOF image as in Fig. 6.1 for ∼3 million atoms for comparison, with the black arrows indicating again the momentum imparted by the incident 780 nm photons.

In region (i), the observation of a large imparted momentum on the atoms when the EOM is on only, suggests that a mechanism involving the excitation of more than one $\text{TEM}_{00}^{\text{p}}$ cavity mode, with p the longitudinal mode order, exists. However, the difference $\Delta\text{p} = \text{p}-\text{p}'$ in this case seems not to be related to the hyperfine splitting of the ground state of ^{87}Rb, since the large momentum transfer is also observed for EOM modulation frequencies which are multiples of the FSR different from seven. At a modulation frequency seven times that of the FSR

frequency, the observed farthest atomic cloud displacements at atom–cavity resonance for changing pulse durations, and TOF images corresponding to nearby data points, are shown in Fig. 6.2. This latter figure equally explains the way in which the velocity data points in Fig. 6.1 are obtained for on resonance and blue detuned (region (i)) cases. The velocities reported therein for those cases are obtained by dividing the displacement of the farthest atomic cloud by the TOF time the displacement from the stationary cloud took, and by averaging over velocities obtained using four different TOF values for each data point. The reported on resonance and blue detuned temperatures in turn, are those of the stationary atomic clouds at the center of the cavity.

Above a couple of hundreds of μs pulse duration, the observed displacement saturates, while at very short pulse durations it becomes difficult to determine where the border separating different atomic clouds actually is in the TOF images. Moreover, as pointed out above, the linewidth of the pulse becomes larger than the linewidth of the cavity resonance as the pulse duration approaches $\sim$10 μs, which reduces the effective power of the pulse given that the intracavity (atom–cavity) resonant power will have not reached a steady state at those timescales.

For region (ii), the momentum distribution of atoms shows an interesting feature. As one goes farther away from resonance and increases the power of the pump so that the intracavity power stays constant, the elongation at 45 degrees becomes larger as quantified by the velocity imparted to the atoms which expand following the shape of an ellipse. The velocity is obtained by measuring first the TOF expansion of the smallest radius of the elliptically shaped cloud, and then subtracting this expansion to the expansion of the largest axis. The smallest radius TOF expansion provides us with temperature information, while the differential expansion between large and small radii allows us to deduce the range of velocities the atoms are accelerated to by the pulse which clearly induces interarm photon exchange processes introduced in Sec. 4.3. The fact that differential velocities are of the same order of magnitude as the single–photon recoil velocity of the atoms ($v_r^{^{87}Rb} = 0.0059$ m/s [58]), makes the assumption of two–photon transitions occurring plausible.

Initially, we attributed the fact that signatures of interarm two–photon processes only appear in region (ii) to the frequency of the pump being smaller than the intracavity field

frequency in this region [93]. Given that the cavity is evacuating energy via transmission at a higher frequency than the one at which it is being injected with, the field needs to borrow energy from the atoms and thus reduces their heating which is otherwise observed on atom–cavity resonance as well as in region (i). A more complete explanation which I found once the manuscript had been handed in to the jury is presented in the following subsection.

6.2.2 Momentum distributions from emission of photons into the counterpropagating cavity mode

The interarm photon exchange scenario presented in Sec. 4.3 explains well the elliptical feature observed in the TOF data obtained in region (ii) of Fig. 6.1. For the emission of photons in that section however, it was assumed that photons are only emitted on the same direction as that of the laser light injected into the cavity. But given that our cavity also accepts modes travelling on the counterpropagating direction, emission onto those empty modes will be favoured as well. The momentum imparted to atoms loaded on the center of the cavity after absorption followed by counterprogating emission events is depicted in Fig. 6.3.

The four possible two–photon processes appearing in Fig. 6.3 provide an explanation of the TOF patterns observed in region (i) of Fig. 6.1 (and in Fig. 6.2). This implies in particular, the coherent nature of the process observed on the blue side of the atom–cavity resonance, in spite of the much higher number of photons involved in this case as compared to what is found in region (ii). In other words, momentum transfer is induced by pairs of photons not only for red–detuned pulses from atom–cavity resonance, but also for blue–detuned ones, with the difference that in the former case the emitted photons are travelling in the direction copropagating with respect to the pulse, while in the latter they are emitted in the counterpropagating empty cavity mode.

Finally, the counterpropagating emission also permits to understand why this kind of emission is only observed on the blue side of the atom–cavity resonance: as atoms get accelerated along the cavity arms, the photons from the pulse are of a lower frequency in their rest frame than in the lab frame, and thus the counterpropagating photons they emit will also be of this

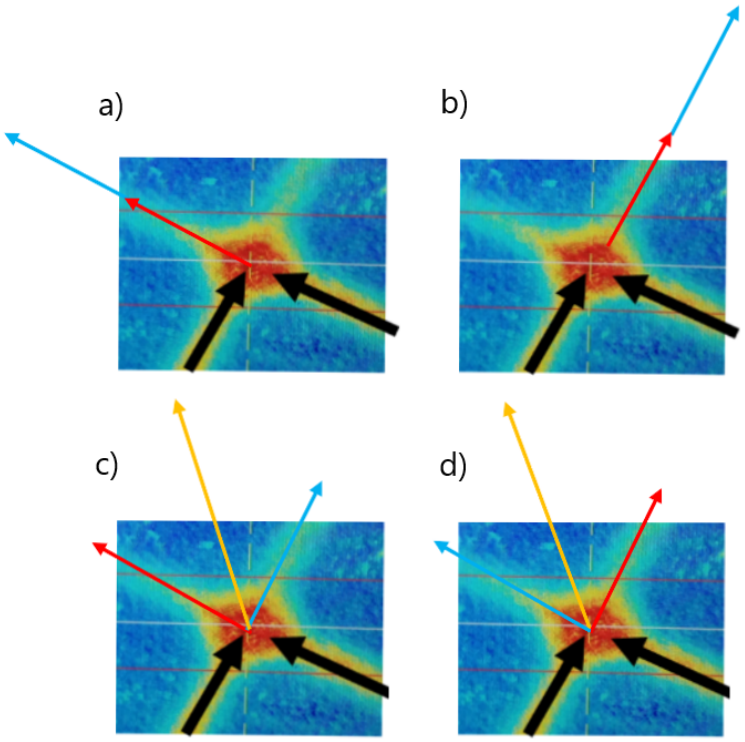

Figure 6.3: Large black arrows impinging on atoms at the center of the cross represent the momentum carried by the intracavity 780 nm photons when a single port is injected, while thinner red and blue vectors represent momentum imparted to the atoms when two–photon absorption–emission processes happen respectively as in Fig. 6.1, although there momentum from emission is depicted on the opposite direction. Finally, each yellow vector equidistant from two cavity arms in c) and d) is a sum of a red and a blue vector, and represents the total momentum change of an atom experiencing a two–photon process involving an interarm photon exchange with emission in the counterpropagating direction with respect to the pulse.

lower frequency. These emitted photons are then doubly Doppler shifted in the lab frame with respect to the incident pulse photons. Eventually, the velocity the atoms can attain is limited by the linewidth of the cavity on one hand, and the initial atom–cavity detuning at use on the other, since the further detuned to the blue the pulse is in the vicinity of the resonance, the longer will the atoms be able to emit into the cavity mode as they accelerate and thus the higher will their final velocity be when the emission starts to be out of cavity resonance at large enough velocities.

The Doppler shift corresponding to the measured maximum velocity along one arm

($v_{max} \simeq 0.12/\sqrt{2}$ m/s from Fig. 6.1) is,

$$\Delta\omega_{\rm D} = \frac{v_{max}}{c}\omega_{pulse} \simeq 2\pi \times 110\,{\rm kHz}, \tag{6.1}$$

that is $\sim$ 10 % away from one half the value of the cavity linewidth κ, which ultimately sets the limit for the maximum (double) Doppler shift attainable for atoms emitting into the cavity mode. Two–photon processes involving an interarm photon exchange (c) and d) cases in Fig. 6.3) lead to $\simeq \sqrt{2}$ times as much magnitude of the atom velocity as the single arm processes (a) and b) cases in Fig. 6.3) since they take advantage from twice as many scattering events in total before the Doppler limit is attained.

Approximately one linewidth to the red from where the maximum velocity is observed (see Fig. 6.1), emission into the counterpropagating cavity mode is completely inhibited, since the atoms emit completely out of resonance in this direction as soon as they are accelerated by a tiny amount.

6.3 Results: towards coherent splitting of cold atomic clouds

Data for the red detuned from atom–cavity resonance pulse presented so far obeys well the cavity interarm photon exchange scenario introduced in Sec. 4.3. We will now present a more quantitative analysis of the copropagating photon emission exchange process observed in our cavity by studying finer properties of the TOF distributions.

6.3.1 Sum of Gaussian fits for multiphoton momentum effects

Even if the ellipse and its equation, which were used to model the TOF expansion of the cloud in Sec 6.2, provide us with a good qualitative understanding of the effect the pulse produces on the atoms, in order to quantify farther the imparted momentum and obtain fine details of the TOF images too, we had to take a closer look on the raw data provided by the CCD camera. To do so, the fits files from the control system computer were extracted and manipulated so that they could be rotated by the inclination of approximately 20 degrees the

atomic cloud ellipses show with respect to the horizontal axis.

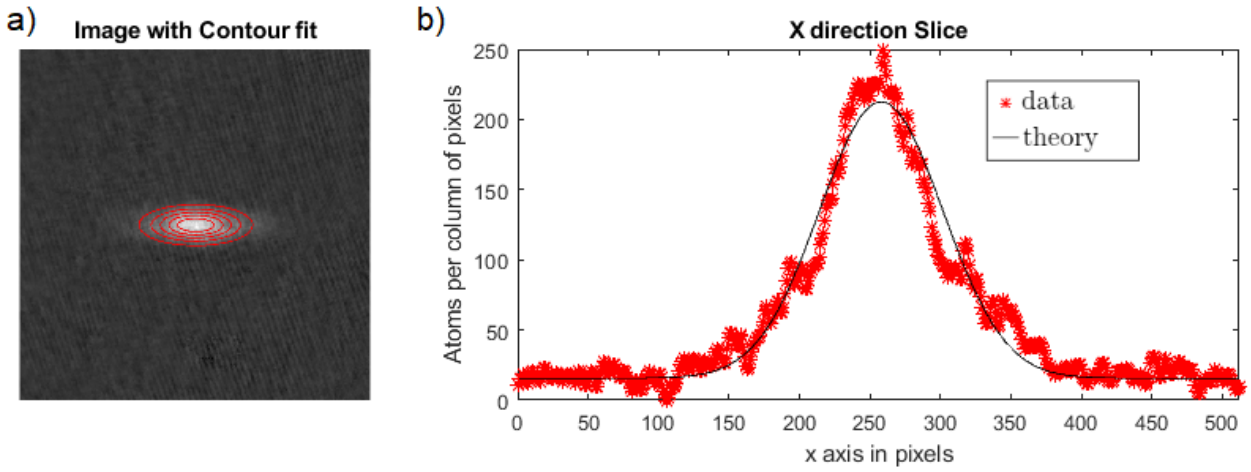

Figure 6.4: a) Two dimensional Gaussian contour fit after rotation of atomic cloud image by $\simeq 20$ degrees, for 2 ms TOF. b) shows number of atom average over ten horizontal pixel rows closest to the center as a function of horizontal position and the best single Gaussian fit which is however not satisfactory.

After rotation and Gaussian refitting, we obtained plots providing us with information about the long axis profile of the ellipse and its Gaussian fit. An example of such plot is depicted in Fig. 6.4 for an atomic cloud of approximately 0.25 million atoms and a pulse duration of 500 μs. The raw data and its contour fits are shown in a), while in b) an average over ten rows closest to the center has been fitted by a Gaussian along the long axis of the ellipse. This Gaussian fit is clearly at odds with the profile of the atomic sample which shows two bumps symmetrically positioned with respect to the maximum intensity region.

The presence of similarly shaped side bumps over many samples, under different conditions of pulse power and duration for changing TOFs has been observed for clouds expanding elliptically. The hypothesis that such shape is produced by two or more photon transitions can be farther verified by trying a fit containing the sum of three Gaussian functions instead of one. The result for the sample in Fig. 6.4 is shown in Fig. 6.5, where in a) the sum of a three Gaussian fit has been utilized while in b) a sum of two Gaussians has been fitted to the data remaining after the subtraction of the main Gaussian from a).

The location of the two side clouds on the other hand, provides us with more precise information about the momentum imparted to the atoms that split from the initial cloud.

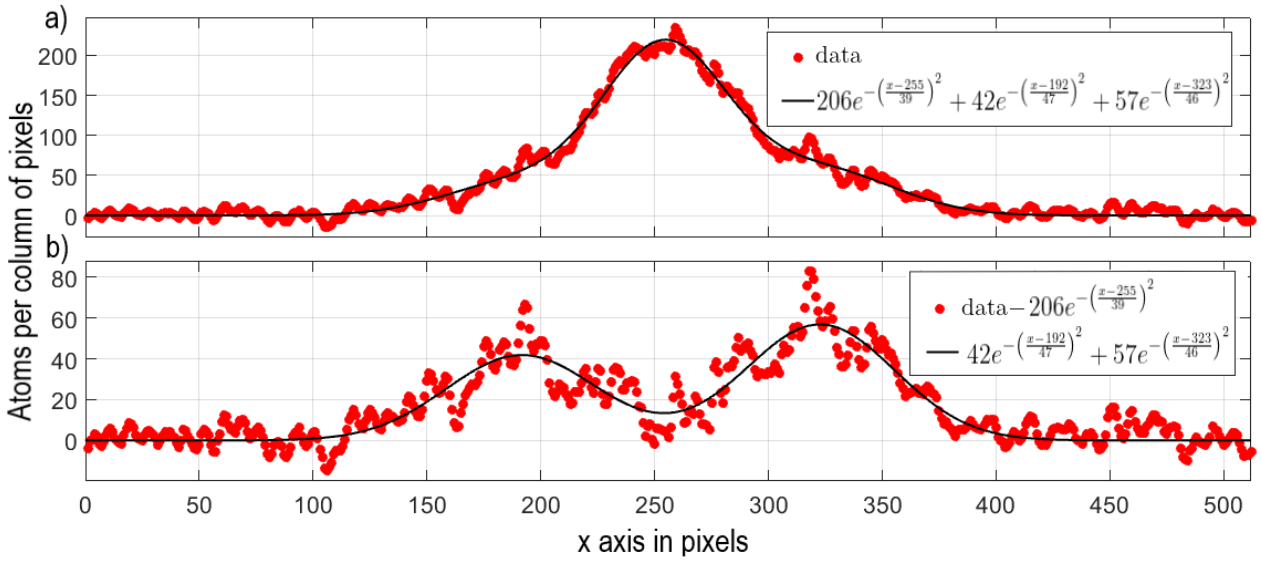

Figure 6.5: a) Sum of three Gaussian fit to the same data as the one presented in Fig. 6.4. b) shows a sum of two Gaussian fit to the sample data left after the center Gaussian from a) has been subtracted to the complete sample.

However, increasing the duration of the cavity pulse to 0.5 ms comes at the price of increasing the atomic cloud temperature to $\simeq$ 2.5 μK, obtained again via small axis TOF expansion of the elliptical clouds. The velocity of the bumps on the large axis in turn is $\simeq$ 0.06 m/s which corresponds to 7 times the one–photon recoil momentum imparted by each of the arms, that is 7 photons absorbed from one arm and 7 emitted on the other on average.

We can integrate the function achieved from the fitting of the two Gaussians along x, over the regions delimited by the local minimum between left and right blobs, and thus calculate the number of atoms on each of the side clouds. The result for 20 samples on which the splitting could be detected is depicted in Fig. 6.6. The data indicates that the split clouds show a large variation on the difference of atom numbers $|N_2\text{-}N_1|$ between the clouds from shot to shot. For comparison, we also plot the boundaries of the quantum projection noise (QPN) limit [94] for the lowest uncertainty classical process possible, i.e. without quantum advantage. In this case the best achievable atom number uncertainty to atom number ratio is limited by,

$$\frac{\Delta N}{N} = \frac{1}{2\sqrt{N}}. \tag{6.2}$$

This classical lowest uncertainty limit gives a means of comparing our splitter to the case in

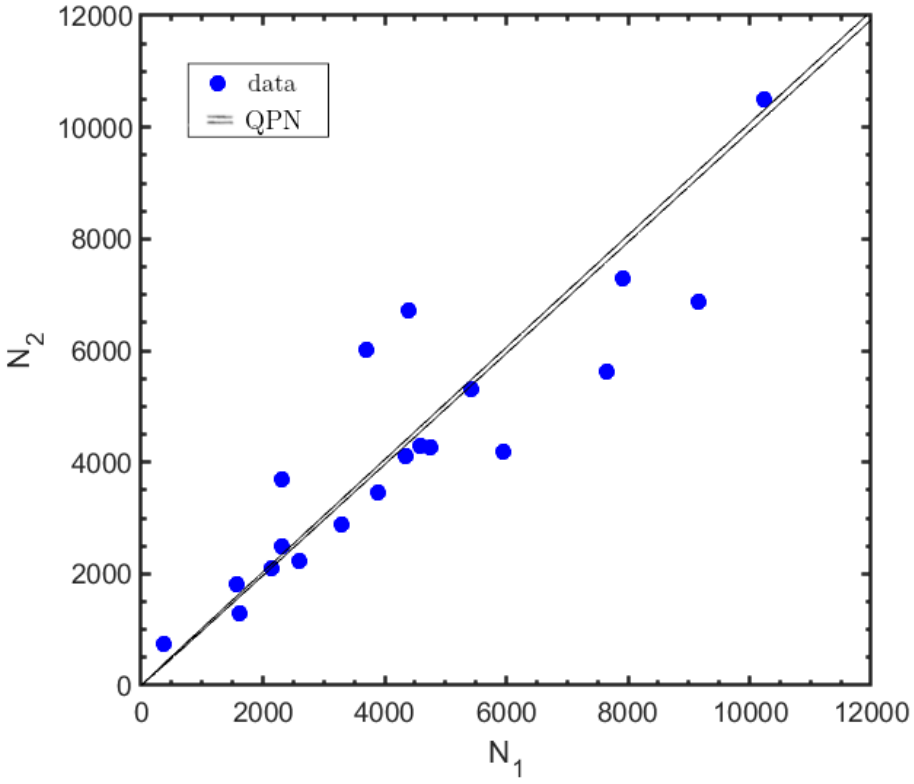

Figure 6.6: Number of atoms on the left cloud as a function of number of atoms on the right cloud for twenty samples on which the splitting could be detected. Black diagonal lines represent QPN boundaries $\Delta N = \pm\sqrt{N}/2$, centered around perfect splitting $N_2 = N_1$.

which one can get an advantage by using quantum correlated states (see e.g. [95, 96]) that can lead to the ideal quantum correlated splitter's noise figure laying within the boundaries of the area delimited by the two lines in Fig. 6.6.

On the other hand, the total number of atoms $N = N_1 + N_2$ splitting from the initial cloud varies significantly from a detected minimum of 6 % to a maximum of 69 %. It is clear then that the technical noise is too large at our current level of control, and that a finer one of pulse power and detuning is needed in order to make the cold atom cloud splitter more predictable.

6.3.2 Higher order multiphoton momentum signatures

More recent parameter exploration has allowed us to detect additional features on the elliptical atomic clouds when pulse durations greater than $\simeq$1 ms are utilized, and which were not visible on the initial samples achieved at 200 μs and 500 μs. The samples obtained at larger pulse duration appear more elongated after TOF expansion, and careful analysis of the intensity profile shows at least two more smaller clouds appearing on the sides of the two other ones detected for smaller pulse duration (see Fig. 6.7). In a), the data obtained after a TOF expansion of 2 ms has been fitted using a function made of five Gaussians, while in b) the central Gaussian has been subtracted to the data and then a four Gaussian fit has been applied to the remaining sample. Finally in c) the two Gaussians closest to the center Gaussian have been subtracted to the sample left in b), and the result has been fitted using a sum of two Gaussian functions. These farther from the center side clouds reveal the existence of a higher order momentum exchange process which requires a deeper investigation.

Even if it is difficult to tell what the precise nature of the two detected additional clouds is at this stage of the research, one can think about at least two different scenarios: (i) it seems reasonable to consider that after a longer interaction time with the pulse, atoms at the two side clouds appearing for example in Fig. 6.5, may also interact with the two arms of the cavity, leading to four more clouds. Two of them will propagate faster than their parent ones since they have undergone more interarm photon interactions absorbing and emitting photons on the same arms as their parents have, and are thus visible at a larger distance after TOF expansion. The other two however, should be the ones that have been subjected to absorption–emission processes involving arms in reverse order, and should thus get accelerated on the opposite direction. Therefore, they may get overlapped with the atoms left at the initial central cloud and that is why they could be more difficult to detect in TOF; a more direct explanation (ii) in greater accordance with what we actually see consists in assuming that two simultaneous parallel processes occur with different budgets of interchanged photons, which thus lead to two pairs of counterpropagating clouds, i.e. one slower pair centered around velocities $\pm v_s$ and another faster pair centered around velocities $\pm v_f$.

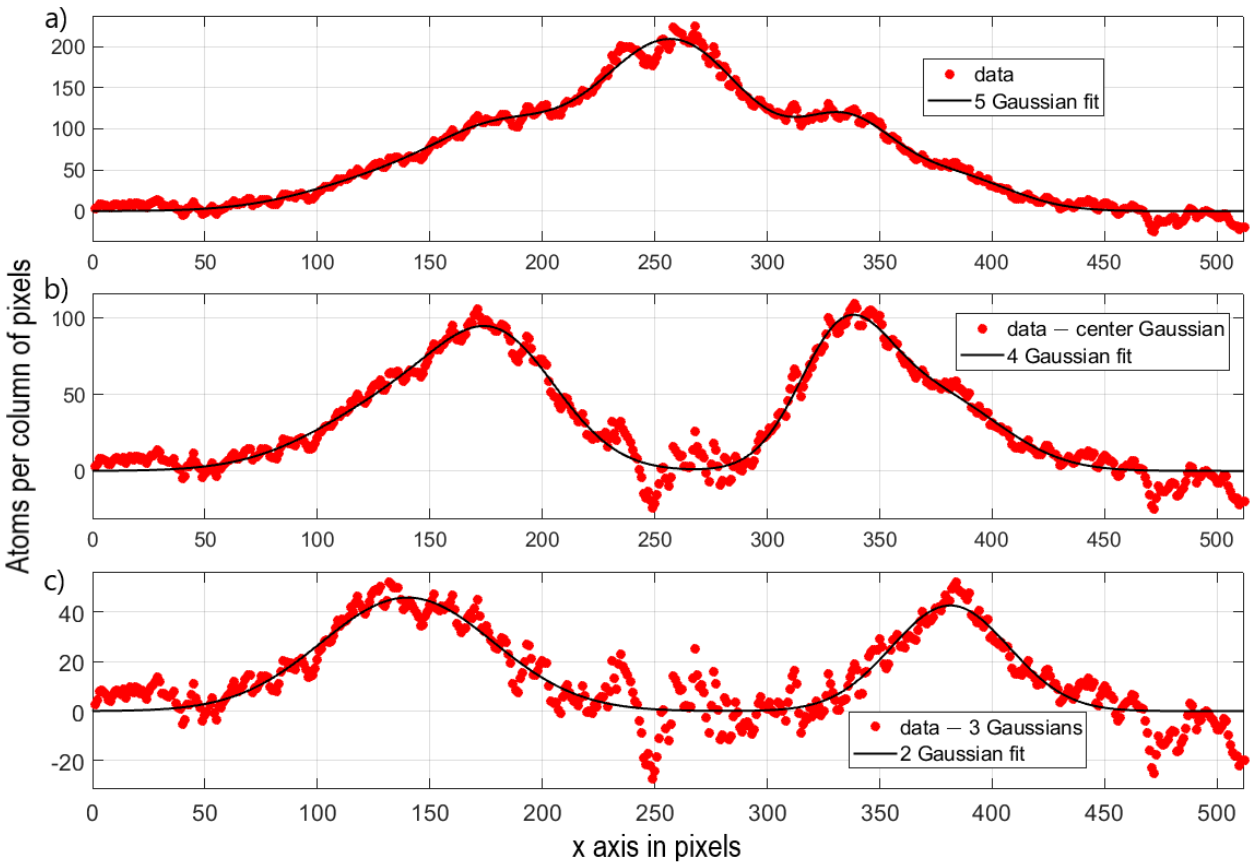

Figure 6.7: a) Sum of five Gaussian fit of a sample obtained under 1 ms pulse duration. b) shows a sum of four Gaussian fit to the sample data left after the center Gaussian from a) has been subtracted to the complete sample. Finally c) shows a sum of two Gaussian fit to the sample data left after the center Gaussian from a) and the next two side Gaussians from b) have been subtracted to the complete sample.

Following (ii), one can calculate as in Subsec. 6.3.1 the number of photons absorbed and emitted on each cavity arm. We measure a second order bump velocity of $\simeq$0.1 m/s which corresponds to 12 times the one–photon recoil momentum imparted by each of the arms. This is close to having twice as many photons interacting with the atomic cloud per arm as in the single pair of side bumps scenario.

6.4 Concluding remarks

In this chapter, we have presented and characterized atom–photon interactions mediated by a bow–tie cavity. The phenomena we describe could only be detected for far red–detuned

pulses from the atomic transition, which speaks of the importance of avoiding spontaneous emission, while the large dependence on the fine pulse detuning from atom–cavity resonance is well explained via the Doppler shift allowed by the cavity linewidth we measured for 780 nm light.

So far our investigations focused on the red–side of the atom–cavity resonance predominantly, since the few photon character of the momentum distributions induced by the pulse on that side makes the observed phenomena potentially more interesting and useful. In the future, addressing this same side with colder and eventually condensed atomic samples could be tested by either utilizing pulses farther detuned from the atomic transition, or by trying to load atomic samples closer to quantum degeneracy.

We have omitted from our discussion the effect the dipole trap produces on the atom dynamics during the 780 nm pulse delivery. A deeper understanding of the splitting phenomena we observe could be achieved if the trapping character of the FORT was accounted for in the model, something which is beyond the scope of this manuscript given the incipient nature of the research at the time of writing.

Discussion and outlook

In this thesis, we have presented the work we carried out during my PhD, which led to the coupling of ultracold ^{87}Rb atoms to a bow–tie optical cavity, after being loaded and cooled by an hyperfine Λ–enhanced gray molasses cooling technique.

Hyperfine gray molasses dipole trap loading and cooling

The results related to the implementation of a gray molasses dipole trap loading and cooling technique utilizing hyperfine dark states (HDSs) are shown in Chapter 5. We have demonstrated that this new type of atom cooling can be used to efficiently load a far off–resonant optical dipole trap (FORT), which entails addressing atoms under the presence of large and degeneracy lifting differential AC Stark shifts. Furthermore, an intra–FORT velocity–selective cooling technique has been demonstrated leading to a fourfold temperature reduction while conserving loaded atom numbers.

The method which does not rely on closed, cycling transitions, offers new opportunities in the production of ultra–cold atomic and molecular gases thanks to high speed and no atom loss. In the particular case of rubidium, it has already been pivotal in the production of an all–optical Bose–Einstein condensate (BEC) in microgravity [92], while degenerate Fermi gases of polar molecules involving ^{87}Rb have also been obtained [97] using the same hyperfine Λ–enhanced gray molasses technique [45].

Farther improvements could be achieved by switching to the D_1 line of ^{87}Rb which contains no higher $F' = 3$ state and by performing HDS–mediated cooling there, which could permit the generation of ultracold gases in unusual environments [98], or become a complementary alternative for all–optical degenerate gases production [99, 100].

Interarm photon exchange processes with ultra–cold atoms

A second line of research has been studied in Chapters 4 and 6. This line is devoted to exploring the possibilities the 780 nm resonance of our bow–tie cavity offers with respect to the coupling of cold atoms loaded in the center of the FORT. The cavity finesse and volume allow in principle for collective strong coupling of atoms to the cavity. This may be an avenue which will be opened in the future provided that closer to the atomic resonance operation becomes attainable.

So far, we have focused on investigating atom–cavity interactions on a farther detuned condition from atomic resonance, which has afforded us the possibility to interact with the cold atoms without heating them up enormously. The particular cavity length which creates a free spectral range $\sim$50 kHz away from being a divisor of the ground hyperfine splitting of ^{87}Rb, along with the bow–tie geometry of the cavity which makes interarm photon exchange processes possible, has permitted to explore coherent two–photon momentum transfer phenomena in an original scenario. The effect of pulse delivery at 780 nm could be more clearly identified with farther–detuned pulses from atomic resonance, and if even colder atomic samples were available, in particular the effect on not merely ultracold but also quantum degenerate clouds would surely be cleaner and more interesting.

Future work on improving the electronics could allow to stabilize the power of 780 nm light injected into the cavity and permit to operate the pulses in a more reproducible way. Given that a new control system [101] governing the experiment will be introduced in due time, the 780 nm power injection control might as well be added nearby.

Appendix

A. Stark effect of 1560 nm laser light on the D_2 line of ^{87}Rb

Alkali metals' ground states have a closed shell that does not contribute to the angular momentum, and an outer valence electron whose state is completely determined by its orbital angular momentum **L** and spin angular momentum **S**. These two couple to each other and form the total electronic angular momentum $\mathbf{J} = \mathbf{L} + \mathbf{S}$ giving rise to the fine structure of the atom. This phenomenon leads to different energies for each quantum number *J*, since the eigenvalues of the spin-orbit interaction $H_{so} = A\mathbf{L} \cdot \mathbf{S}$ depend on the orientation of **L** with respect to **S**.

Furthermore, the electronic angular momentum **J** itself couples to the nuclear one **I** to form the total angular momentum $\mathbf{F} = \mathbf{I}+\mathbf{J}$. Atomic nuclei having nuclear spin equal or larger than one also produce an electric quadrupole moment [102]. The hyperfine interaction then reads

$$H_{hf} = B_1 \mathbf{I} \cdot \mathbf{J} + B_2 \frac{3(\mathbf{I} \cdot \mathbf{J})^2 + 1.5\mathbf{I} \cdot \mathbf{J} - I(I+1)J(J+1)}{2I(2I-1)J(2J-1)}, \tag{9.3}$$

and splits energy levels corresponding to different values of the quantum number *F*, tipically in the order of MHz or few GHz which is much less than the splitting in the order of THz produced by the spin-orbit interaction. The AC Stark interaction perturbes the hyperfine structure at most.

A. I. Weak field AC Stark effect

When the intensity of the applied field does not exceed approximately $10^{10}\ W/m^2$, crossings between different hyperfine levels are not expected [58]. On the other hand, the Hamiltonian

H_{hf} in Eq. 9.3 is diagonal on the total angular momentum basis $\{|FM\rangle\}$, but the AC Stark Hamiltonian is not as we show next. Therefore, one needs to diagonalize the full Hamiltonian in order to find the new eigenvalues.

Stark shifts are explained by the eigenvalues of the interaction Hamiltonian

$$H_I = -\mathbf{d}\cdot\mathbf{E}, \tag{9.4}$$

where **E** is the applied electric field and **d** the electric-dipole operator. First-order perturbation of Eq. 9.4 gives a zero contribution because diagonal elements of the dipole operator vanish for systems with an inversion center such as atoms. The second-order contribution to the AC Stark shift of a level v, on the other hand, can be written as

$$\begin{aligned}\Delta E &= \sum_k \frac{\langle J_v m_v|H_I|J_k m_k\rangle\langle J_k m_k|H_I|J_v m_v\rangle}{E_v - E_k} \\ &= \sum_k \frac{\langle IJFM|H_I|I_k J_k F_k M_k\rangle\langle I_k J_k F_k M_k|H_I|I'J'F'M'\rangle}{E_v - E_k},\end{aligned} \tag{9.5}$$

where the sum over k includes all states allowed by electric-dipole transition selection rules. Note also that Eq. 9.5 is no longer a sum of diagonal terms when including second-order perturbations, and $\{|I'J'F'M'\rangle\}$ has been introduced.

However, given that Eq. 9.4 does not affect the nuclear spin and given also that the fine structure is far from mixing at the electric field values present in our experiment, Eq. 9.5 can be simplified to

$$\begin{aligned}\Delta E &= \sum_k \frac{\langle FM|H_I|F_k M_k\rangle\langle F_k M_k|H_I|F'M'\rangle}{E_v - E_k} \\ &= \langle FM|H_{II}|F'M'\rangle\end{aligned} \tag{9.6}$$

where

$$H_{II} = H_I\left(\sum_k \frac{|F_k M_k\rangle\langle F_k M_k|}{E_v - E_k}\right)H_I. \tag{9.7}$$

Now, if the applied electric field is non-zero only in the z direction, then Eq. 9.6 becomes diagonal in M and therefore

$$\Delta E_{F,F',M} = \langle FM|H_{II}|F'M\rangle. \tag{9.8}$$

An explicit expression for the AC Stark shift can be written in terms of the scalar and

tensor polarizabilities [103], which for an electric field of magnitude $|\mathbf{E}|$ reads [104],

$$\Delta E_{F,F',M} = \langle FM|H_{II}|F'M\rangle = -\frac{1}{2}\alpha_0(\omega)|\mathbf{E}|^2\delta_{F,F'} - \frac{1}{2}\alpha_2(\omega)|\mathbf{E}|^2\langle FM|Q|F'M\rangle, \tag{9.9}$$

where

$$\alpha_0(\omega) = \frac{2}{3(2J_v+1)}\sum_k \frac{\langle J_v||\mathbf{d}||J_k\rangle^2(E_v-E_k)}{(E_v-E_k)^2-\omega^2}, \tag{9.10}$$

and

$$\begin{aligned}\alpha_2(\omega) &= -\sqrt{\frac{40J_v(2J_v-1)}{3(J_v+1)(2J_v+1)(2J_v+3)}} \\ &\times\sum_k(-1)^{J_v+J_k+1}\begin{Bmatrix} J_v & 1 & J_k \\ 1 & J_v & 2\end{Bmatrix}\frac{\langle J_v||\mathbf{d}||J_k\rangle^2(E_v-E_k)}{(E_v-E_k)^2-\omega^2},\end{aligned} \tag{9.11}$$

are the scalar and tensor polarizabilities respectively, and

$$\begin{aligned}\langle FM|Q|F'M\rangle &= \sqrt{\frac{(J_v+1)(2J_v+1)(2J_v+3)(2F+1)(2F'+1)}{J_v(2J_v-1)}} \\ &\times(-1)^{I+J+F-F'-M}\begin{pmatrix} F & 2 & F' \\ M & 0 & -M\end{pmatrix}\begin{Bmatrix} F & 2 & F' \\ J_v & I & J_v\end{Bmatrix}.\end{aligned} \tag{9.12}$$

Here, matrices delimited by $()$ and $\{\}$ are 3–j and 6–j symbols respectively, whose elements are Wigner coefficients. They lead to a Q matrix showing rows and columns labeled by F and F' for each submatrix corresponding to a magnetic sublevel M [105]. As mentioned above, in order to get the AC Stark shifts, what is needed is to diagonilize $H = H_{hf} + H_I$ altogether, something that we present in the following section for the specific case of ^{87}Rb which we use in our experiment.

A. II. Case of ^{87}Rb under a 1560 nm laser

We are going to apply the theory presented in the previous section to the case of ^{87}Rb now. The relevant atomic structure of this atom is depicted in Fig. 9.8. The frequency of the incident radiation is half of that of the ^{87}Rb's D_2 transition line, which is close to the D_1 line that corresponds to the first excited fine level. For electric dipole allowed transitions, this and the second excited fine level corresponding to the D_1 and the D_2 lines respectively, are the only ones that contribute to the AC Stark effect on the ground state $5S_{1/2}$. However, in order to know how the D_2 line gets modified, we are also interested in calculating the AC Stark

Transition	Wavelength (nm)	$\langle J_v \|\| \mathbf{d} \|\| J_k \rangle$ (C·m)
$5S_{1/2} \rightarrow 5P_{1/2}$	794.979	3.6635×10^{-29}
$5S_{1/2} \rightarrow 5P_{3/2}$	780.241	5.0675×10^{-29}
$5P_{3/2} \rightarrow 6S_{1/2}$	1366.875	5.1269×10^{-29}
$5P_{3/2} \rightarrow 4D_{3/2}$	1529.261	3.0802×10^{-29}
$5P_{3/2} \rightarrow 4D_{5/2}$	1529.366	9.2406×10^{-29}

Table 9.1: ^{87}Rb's relevant electric dipole allowed transitions from the D_2 line and their corresponding wavelengths and dipole elements. Note that the latter are given in S.I. units d[C·m] $= ea_0 d[ea_0] = 8.47835 \times 10^{-30} d[ea_0]$.

effect on the excited state $5P_{3/2}$. Therefore, we also list the relevant dipole elements for this excited state in Tab. 9.1.

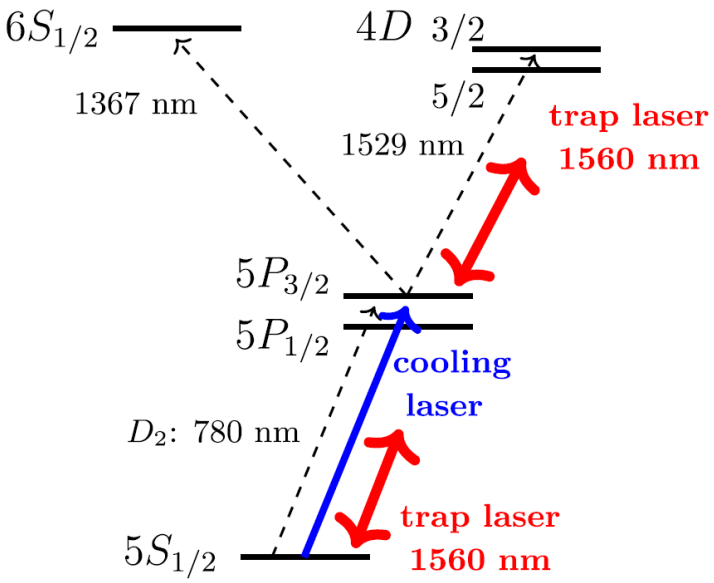

Figure 9.8: ^{87}Rb's most relevant energy levels of the electronic structure for 1560 nm incident light (Fig. published in [16]).

In Tab. 9.2 we list the values for the scalar and tensor polarizabilities of $5S_{1/2}$ and $5P_{3/2}$ states. These lead to a scalar polarizability ratio β of

$$\beta = \frac{\alpha_{5P_{1/2}}}{\alpha_{5S_{1/2}}} = 48.19. \tag{9.13}$$

Next we show the explicit Q matrix in Eq. 9.12 for the ^{87}Rb's $5P_{3/2}$ excited state. The nuclear spin I equals $3/2$ for ^{87}Rb and, along with $J = 3/2$, a 16×16 matrix is defined by the following sub-blocks centered on the diagonal, corresponding to $m_F = \pm 3$, $m_F = \pm 2$,

State	α_0(1560 nm)((C·m^2)/V)	α_2(1560 nm)((C·m^2)/V)
$5S_{1/2}$	6.802×10^{-39}	0 (for $J_v = 1/2$)
$5P_{3/2}$	3.278×10^{-37}	-4.240×10^{-38}

Table 9.2: ^{87}Rb's scalar and tensor polarizabilities for $5S_{1/2}$ and $5P_{3/2}$ states when shined with 1560 nm light.

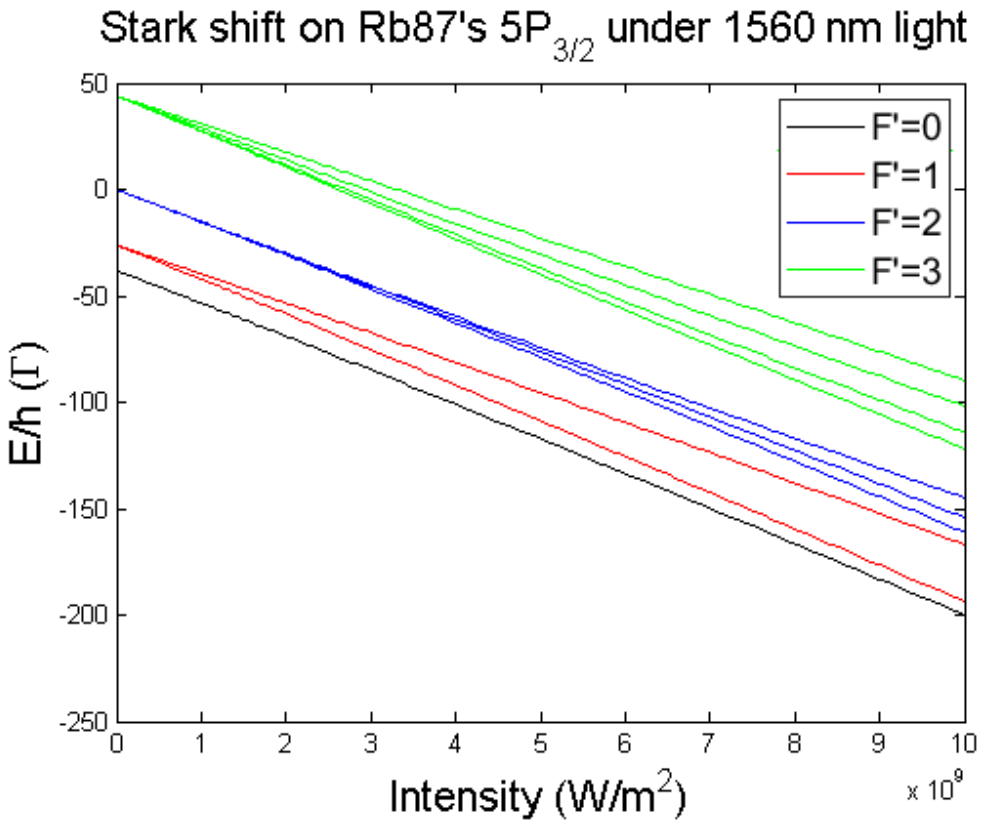

Figure 9.9: Numerical simulation of the AC Stark shifts on ^{87}Rb's $5P_{3/2}$ in units of the D_2 linewidth and as a function of the electric field intensity $I = 2c\epsilon_0|\mathbf{E}|$.

$m_F = \pm 1$ and $m_F = 0$.

$$\begin{pmatrix} 1 \end{pmatrix}, \tag{9.14}$$

$$\begin{pmatrix} 0 & \mp 1 \\ \mp 1 & 0 \end{pmatrix}, \tag{9.15}$$

$$\begin{pmatrix} -0.6 & \mp 0.6325 & 0.4899 \\ \mp 0.6325 & 0 & \mp 0.7746 \\ 0.4899 & \mp 0.7746 & -0.4 \end{pmatrix}, \tag{9.16}$$

$$\begin{pmatrix} -0.8 & 0 & 0.6 & 0 \\ 0 & 0 & 0 & 1 \\ 0.6 & 0 & 0.8 & 0 \\ 0 & 1 & 0 & 0 \end{pmatrix}, \tag{9.17}$$

respectively. The rest of the elements are zero. Substituting the polarizabilities in Eq. 9.9 and diagonilizing the 16×16 matrix given by the diagonal parts H_{hf} and the scalar polarizability contribution in H_I, plus the non-diagonal tensor contribution, one gets the AC Stark energy shifts.

A numerical simulation of these shifts for different values of the electric field intensity $I = 2c\epsilon_0|\mathbf{E}|$ is depicted in Fig. 9.9. The degeneracy of the $5P_{3/2}$ state is partially lifted (note the splitting of curves with increasing electric field intensity for most of the colors in Fig. 9.9) following different $|m_F|$ values.

B. PID controller for active stabilization of laser radiation to the cavity

The Pound–Drever–Hall (PDH) [59] feedback loop supplies corrections to the laser within some electronic bandwidth, following the path that goes from the laser to the cavity, to the detector, to the electronic gain stage that we describe below, and back to the laser.

B. I. Frequency locking via current, temperature and cavity length control

The PID controller we use for PDH laser frequency stabilization on our system is composed of proportional, integral and derivative parts depicted in Fig. 9.10. The values of the components were optimized experimentally by looking both at the low and high frequency responses of the lock. Additionally, a temperature stabilization low frequency stage has been introduced to prevent the slow drift of the error signal when the laser is locked to the cavity.

Later in the research, we used the low frequency stage to stabilize the cavity length via the piezo–electric actuators' voltage control, since temperature variations happening at low frequency do intrinsically change the cavity length which is the parameter governing the absolute frequency of the cavity resonances. Stabilizing the cavity length not only allows to compensate for the slow drift on frequency produced by the temperature change, but also allows to compensate for some of the vibrations produced at a higher frequency up to some tenths of Hz.

The simulated Bode plot expressing the magnitude and the phase of the frequency response of the PID is depicted in Fig. 9.11 in log-log scale. The derivative section on the left of Fig. 9.11 provides an increase of the gain at high frequency which compensates for the cavity roll–off starting at $\sim$500 KHz (whose effect is not included in Fig. 9.11), and is also responsible for the phase approaching 90 degrees at high frequency. One has to take into account that as a consequence of the loop components that act as low-pass filters, at high enough frequency, the correction signal can be 180 degrees shifted from negative feedback, which will make the correction signal move the system further away from resonance and

make the loop unstable. Therefore, ideally, one should ensure that the loop gain has already gone below unity gain, or 0 dB, in the frequency range at which this occurs.

Let us summarize the main points that have to be kept in mind when optimizing the frequency and phase responses by the following list of rules–of–thumb,

- At the unity–gain point, the phase margin (PM $= \phi - (-180^{o})$) of the loop should be greater than 45 degrees.

- At the unity–gain point, the slope of the magnitude transfer function should not decrease by much more that 20 dB per decade of frequency.

- Above $\sim$500 KHz, our butterfly cavity acts as an integrator and adds a -20 dB/dec. slope to the system.

A small fraction of the error signal has been extracted before the mixer in order to view it on a RF spectrum analyzer. The image we obtained is depicted in Fig. 9.12. It shows a center peak at the modulation frequency with noise sidebands on both sides. The width between these sidebands, which lay approximately 1.2 MHz apart, is the electronic feedback bandwidth over which corrections are imposed.

B. II. Electronic switches for gain and circuit switch off control

Additionally, our PID circuit for laser frequency stabilization contains a pair of Maxim DG419 electronic switches which are TTL controlled externally using the control system (see Fig. 9.13). One of the purposes is to turn off the circuit to ensure there is no laser going into the cavity when TOF images of the atoms are taken. By turning off the circuit, the RIO laser producing the dipole trap will no longer receive feedback and will therefore go out of lock. The other related purpose is to change the gain of the PID to lower values at low frequency and relock the dipole trap more easily once the atoms have been imaged and the PID circuit has been turned back on.

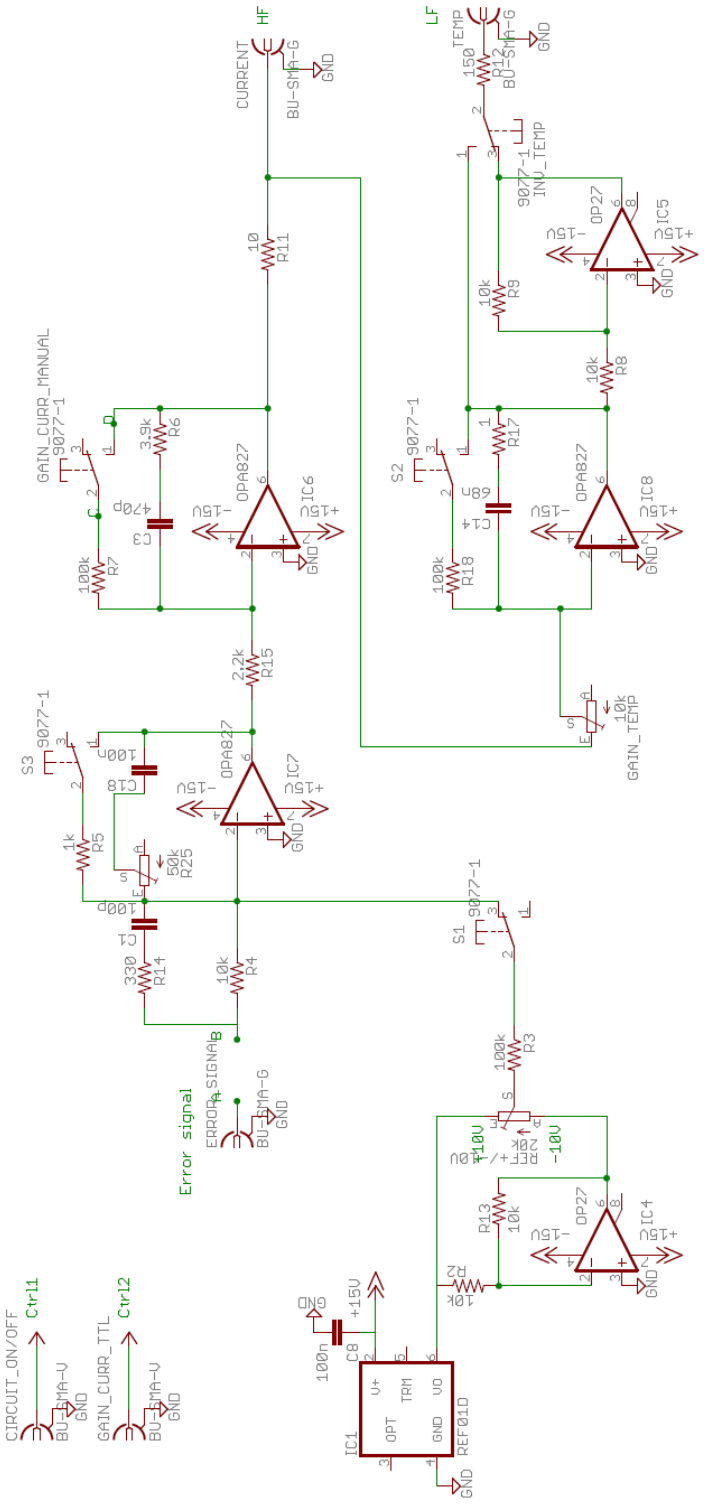

Figure 9.10: PID circuit we implemented in our frequency lock PDH scheme, with both bias current and low frequency stabilization stages for the laser and cavity. Diagram created with EAGLE.

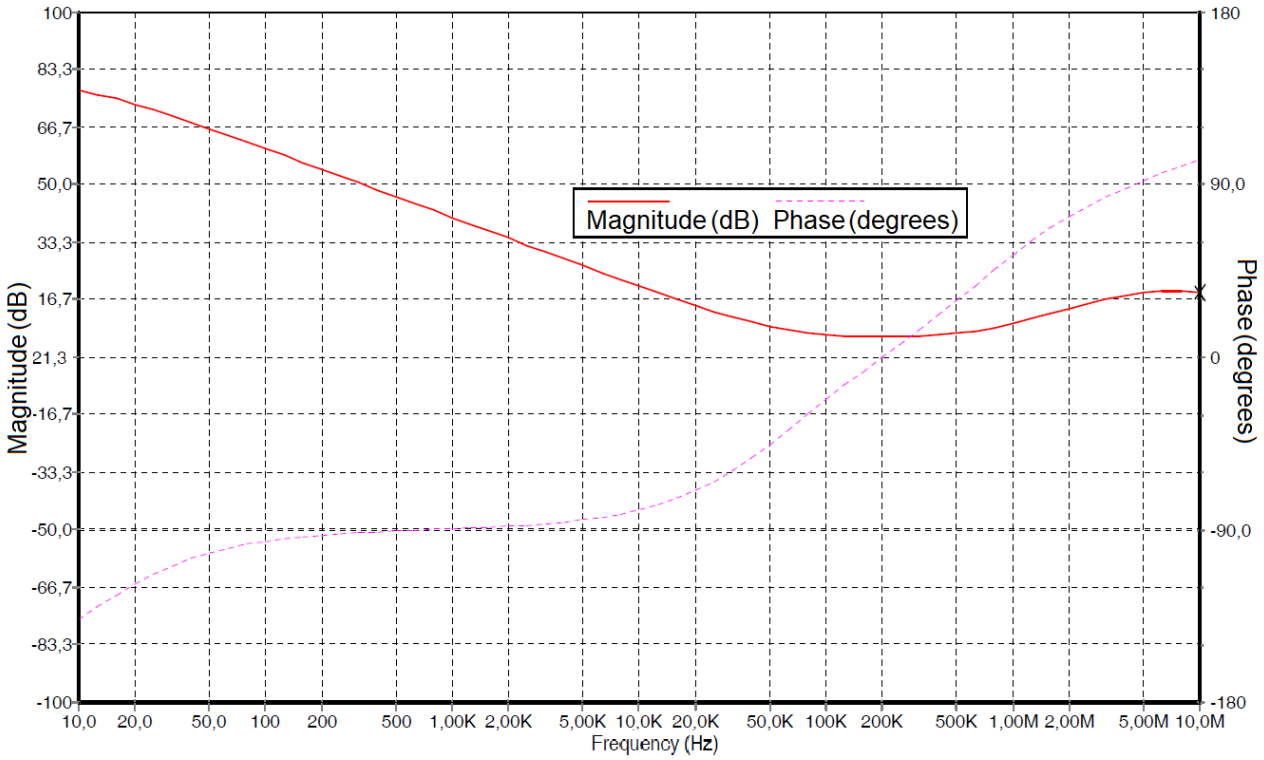

Figure 9.11: Bode plot for the circuit in Fig. 9.10, expressing both magnitude and phase of the gain. The derivative part is responsible for both an increase in the gain at high frequency and the phase approaching 90 degrees. The phase value at -90 degrees on the most part of the bandwidth on the other hand, comes from the integral nature of the circuit. The picture was created using 5Spice Analysis Software [106].

B. III. Stabilization of PDH reflection signal

To ensure the PDH reflection signal's amplitude does not vary over time when a different amount of power is selected for cavity injection, we introduced an additional control loop which amplitude controls the free-space Gooch & Housego AOM via a voltage controlled oscillator (VCO), right before the laser impinges upon the PDH reflection photodiode. The PI circuit governing the loop is depicted in Fig. 9.14.

B. IV. PID for cavity injection power stabilization

It is of vital interest to be able to control precisely the amount of power injected into the cavity, since the purpose of our 1560 nm laser is to create a dipole trap whose power needs

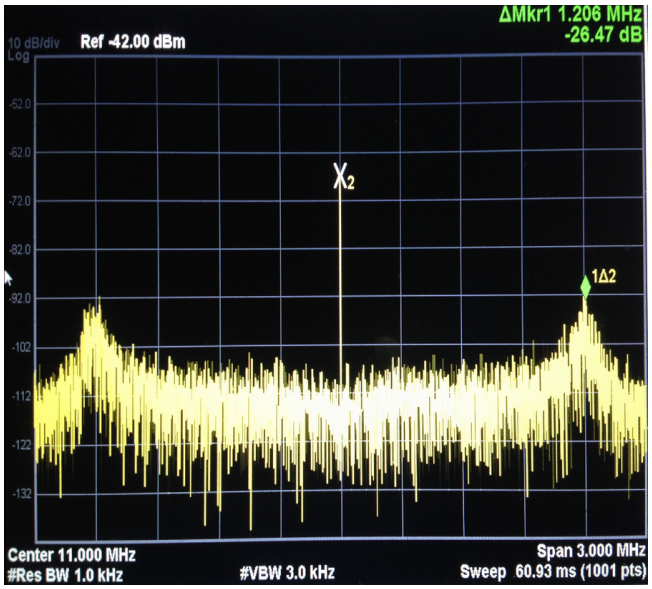

Figure 9.12: Spectral power at the mixer input (see Sec. 3.3) centered at 11 MHz, which was the modulation frequency at use when the frequency lock to the cavity was being tested. It shows noise sidebands peaking at 1.2 MHz indicating the servo bandwidth approximately this wide.

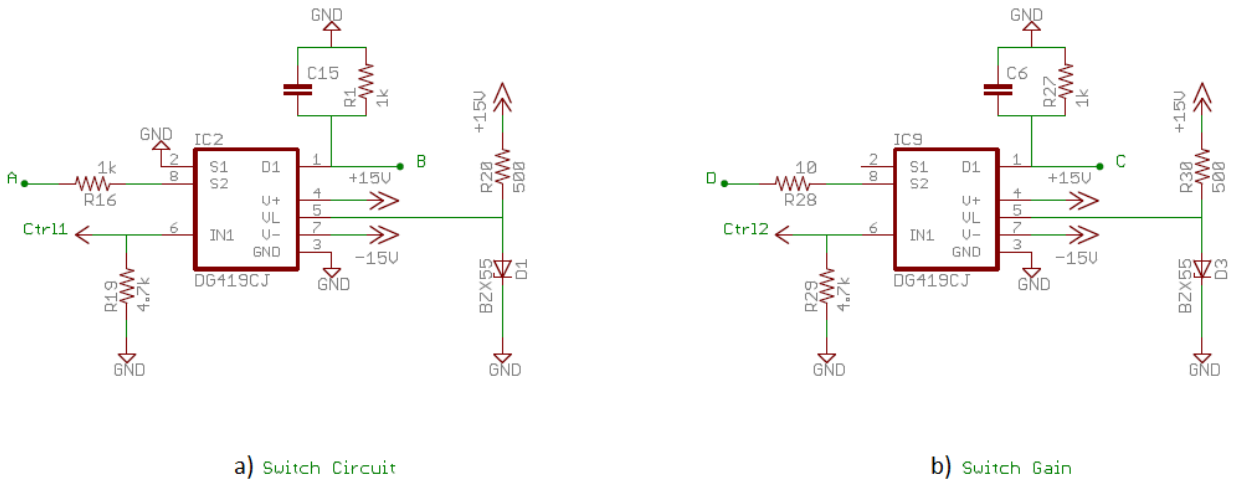

Figure 9.13: Circuit a) and gain b) switches show connections A, B, C and D which correspond to their counterparts in Fig. 9.10. Diagram created with EAGLE.

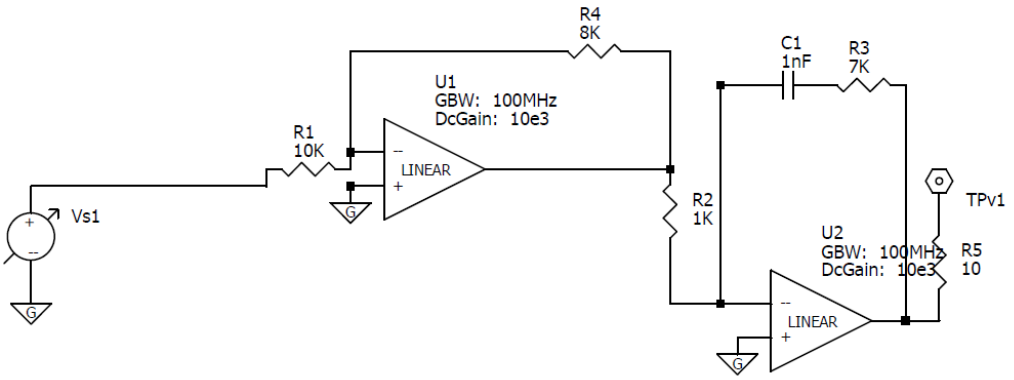

Figure 9.14: PI circuit for stabilization of PDH reflection signal. The picture was created using 5Spice Analysis Software [106].

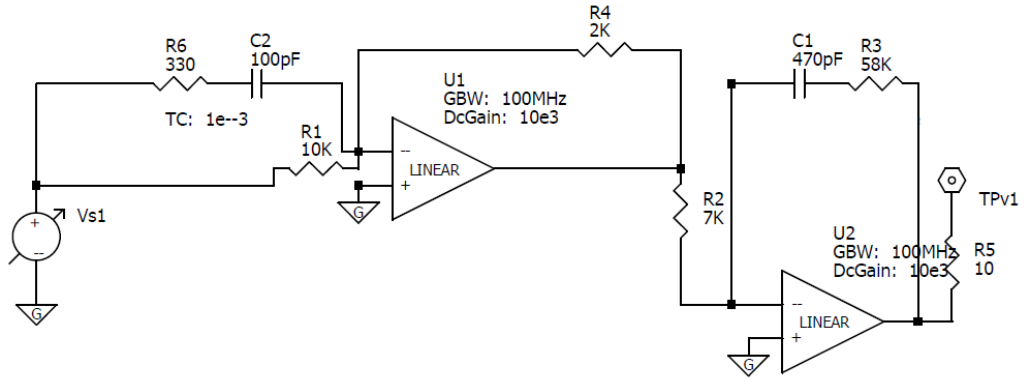

Figure 9.15: PID circuit for dipole trap power stabilization. The picture was created using 5Spice Analysis Software [106].

to be chosen with care depending on which cooling stage the atoms in the cavity volume are subjected to. This power is controlled by a fiber AA Opto-Electronic AOM through a 110 MHz RF signal whose amplitude depends on the corrections sent by a PID circuit.

The PID's input is fed by signals coming both from a Thorlabs photodetector, to which part of the 1560 nm laser beam is directed after a Glan–Thompson polarizer (see Sec. 3.3) and a polarizing beam–splitter (PBS), and the analog control ramp which provides the voltage selected on the control system computer. A summing amplifier adds both signals before taking them into the proportional, integral and derivative stages. The circuit containing these stages is depicted in Fig. 9.15.

C. Coauthored publications

- All-Optical Bose-Einstein Condensates in Microgravity. G. Condon, M. Rabault, B. Barrett, L. Chichet, R. Arguel, H. Eneriz, D. S. Naik, A. Bertoldi, B. Battelier, A. Landragin, and P. Bouyer, Physical Review Letters **123**, 240402 (2019).

- Loading and cooling in an optical trap via hyperfine dark states. D. S. Naik, H. Eneriz, M. Carey, T Freegarde, F. Minardi, B. Battelier, P. Bouyer, and A. Bertoldi, Physical Review Research **2**, 013212 (2020).

- A control hardware based on a field programmable gate array for experiments in atomic physics. A. Bertoldi, C. H. Feng, H. Eneriz, M. Carey, D. S. Naik, J. Junca, X. Zou, D. O. Sabulsky, B. Canuel, P. Bouyer, and M. Prevedelli. Review of Scientific Instruments, **91**, 033203 (2020).

Bibliography

[1] L. Mandel. The case for and against semiclassical radiation theory. *Progress in Opt.*, 13:27, 1976.

[2] H. J. Kimble, M. Dagenais, and L. Mandel. Photon antibunching in resonance fluorescence. *Phys. Rev. Lett.*, 39:691, 1977.

[3] M. C. Teich and B. E. A. Saleh. Observation of sub–poisson franck–hertz light at 253.7 nm. *J. Opt. Soc. Am. B*, 2:275, 1985.

[4] E. M. Purcell. Spontaneous emission probabilities at radio frequency. *Phys. Rev.*, 69: 681, 1946.

[5] P. Goy, J. M. Raimond, M. Gross, and S. Haroche. Observation of cavity–enhanced single–atom spontaneous emission. *Phys. Rev. Lett.*, 50:1903, 1983.

[6] M. H. Anderson, J. R. Ensher, R. Matthews, C. E. Wieman, and E. A. Cornell. Observation of Bose-Einstein condensation in a dilute atomic vapor. *Science*, 269:198, 1995.

[7] K.B. Davis, M.O. Mewes, M. R. Andrews, N. J. van Druten, D. S. Durfee, D. M. Kurn, and W. Ketterle. Bose–Einstein condensation in a gas of sodium atoms. *Phys. Rev. Lett.*, 75:3969, 1995.

[8] D. G. Fried, T. C. Killian, L. Willmann, David Landhuis, Stephen C. Moss, Daniel Kleppner, and Thomas J. Greytak. Bose-Einstein condensation of atomic hydrogen. *Phys. Rev. Lett.*, 81:3811, 1998.

[9] K. M. R. van der Stam, E. D. van Ooijena, R. Meppelink, J. M. Vogels, and P. van der Straten. Large atom number Bose-Einstein condensate of sodium. *Rev. of Sci. Ins.*, 78: 013102, 2007.

[10] A. Öttl, S. Ritter, M. Koḧl, and T. Esslinger. Correlations and counting statistics of an atom laser. *Phys. Rev. Lett.*, 95:090404, 2005.

[11] S. Slama, S. Bux, G. Krenz, C. Zimmermann, and Ph. W. Courteille. Superradiant Rayleigh scattering and collective atomic recoil lasing in a ring cavity. *Phys. Rev. Lett.*, 98:053603, 2007.

[12] S Gopalakrishnan, B. L. Lev, and P. M. Goldbart. Emergent crystallinity and frustration with Bose-Einstein condensates in multimode cavities. *Nature Physics*, 5:845, 2009.

[13] K. Baumann, C. Guerlin, F. Brennecke, and T. Esslinger. Dicke quantum phase transition with a superfluid gas in an optical cavity. *Nature*, 464:1301, 2010.

[14] F. Brennecke, S. Ritter, T. Donner, and T. Esslinger. Cavity optomechanics with a Bose-Einstein condensate. *Science*, 322:235, 2008.

[15] J. D. Miller, R. A. Cline, and D. J. Heinzen. Far-off-resonance optical trapping of atoms. *Phys. Rev. A*, 47:R4567, 1993.

[16] D. S. Naik, H. Eneriz-Imaz, M. Carey, T. Freegarde, F. Minardi, B. Battelier, P. Bouyer, and A. Bertoldi. Loading and cooling in an optical trap via hyperfine dark states. *Phys. Rev. Research*, 2:013212, 2020.

[17] J. Dalibard and C. Cohen-Tannoudji. Laser cooling below the Doppler limit by polarization gradients. *J. Opt. Soc. Am. B*, 6:2023, 1989.

[18] F. Arecchi and R. Bonifacio. Theory of optical maser amplifiers. *J. Quantum Electron.*, 1:169, 1965.

[19] L. Allen and J. H. Eberly. Optical resonance and two–level atoms. *J. Wiley and Sons*, 1975.

[20] S. Chu, L. Hollberg, J. E. Bjorkholm, A. Cable, and A. Ashkin. Three–dimensional viscous confinement and cooling of atoms by resonance radiation pressure. *Phys. Rev. Lett.*, 55:48, 1985.

[21] S. Stenholm. The semiclassical theory of laser cooling. *Rev. Mod. Phys.*, 58:699, 1986.

[22] P. D. Lett, R. N. Watts, C. I. Westbrook, W. D. Phillips, P. L. Gould, and H. J. Metcalf. Observation of atoms laser cooled below the Doppler limit. *Phys. Rev. Lett.*, 61:169, 1988.

[23] E. L. Raab, M. Prentiss, Alex Cable, Steven Chu, and D. E. Pritchard. Trapping of neutral sodium atoms with radiation pressure. *Phys. Rev. Lett.*, 59:2631, 1987.

[24] E. Arimondo and G. Orriols. Nonabsorbing atomic coherences by coherent two–photon transitions in a three–level optical pumping. *Nuovo Cimento Lett.*, 17:333, 1976.

[25] H. R. Gray, R. M. Whitley, and C. R. Stroud Jr. Coherent trapping of atomic populations. *Opt. Lett.*, 3:218, 1978.

[26] A. Aspect, E. Arimondo, R. Kaiser, N. Vansteenkiste, and C. Cohen-Tannoudji. Laser cooling below the one-photon recoil energy by velocity–selective coherent population trapping. *Phys. Rev. Lett.*, 61:826, 1988.

[27] H. J. Metcalf and P. van der Straten. Laser cooling and trapping. *Springer-Verlag*, 1999.

[28] F. Bardou, J. P. Bouchaud, O. Emile, A. Aspect, and C. Cohen-Tannoudji. Subrecoil laser cooling and Lévy flights. *Phys. Rev. Lett.*, 72:203, 1994.

[29] A. Aspect, E. Arimondo, R. Kaiser, N. Vansteenkiste, and C. Cohen-Tannoudji. Laser cooling below the one-photon recoil energy by velocity–selective coherent population trapping: theoretical analysis. *J. Opt. Soc. Am. B*, 6:2112, 1989.

[30] M. S. Shahriar, P. R. Hemmer, M. G. Prentiss, P. Marte, J. Mervis, D. P. Katz, N. P. Bigelow, and T. Cai. Continuous polarization-gradient precooling-assisted velocity-selective coherent population trapping. *Phys. Rev. A*, 48:R4035, 1993.

[31] M. Weidemüller, T. Esslinger, M. A. Ol'shanii, A. Hemmerich, and T. W. Hänsch. A novel scheme for efficient cooling below the photon recoil limit. *Europhys. Lett.*, 27: 109, 1994.

[32] D. Grischkowsky, M. M. T. Loy, and P. F. Liao. Adiabatic following model for two-photon transitions: Nonlinear mixing and pulse propagation. *Phys. Rev. A*, 12:2514, 1975.

[33] E. Brion, L. H. Pedersen, and K. Mølmer. Adiabatic elimination in a lambda system. *J. Phys. A: Math. Theor.*, 40:1033, 2007.

[34] D. Boiron, C. Triché, D. R. Meacher, P. Verkerk, and G. Grynberg. Three-dimensional cooling of cesium atoms in four–beam gray optical molasses. *Phys. Rev. A*, 52:R3425, 1995.

[35] T. Esslinger, F. Sander, A. Hemmerich, and T. W. Hänsch. Purely optical dark lattice. *Opt. Lett.*, 21:991, 1996.

[36] M. Widmer, M. J. Bellanca, W. Buell, H. Metcalf, M. Doery, and E. Vredenbreg. Measurement of force-assisted population accumulation in dark states. *Opt. Lett.*, 21:606, 1996.

[37] A. Hemmerich, M. Weidemüller, T. Esslinger, C. Zimmermann, and T. W. Hänsch. Trapping atoms in a dark optical lattice. *Phys. Rev. Lett.*, 75:37, 1995.

[38] F. Papoff, F. Mauri, and E. Arimondo. Transient velocity–selective coherent population trapping in one dimension. *J. Opt. Soc. Am. B*, 9:321, 1992.

[39] R. G. Brewer and E. L. Hahn. Coherent two-photon processes: Transient and steady-state cases. *Phys. Rev. A*, 11:1641, 1975.

[40] Y. Li and M. Xiao. Electromagnetically induced transparency in a three–level Λ–type system in rubidium atoms. *Phys. Rev. A*, 51:R2703, 1995.

[41] H. Y. Ling, Y. Li, and M. Xiao. Coherent population trapping and electromagnetically induced transparency in multi–Zeeman–sublevel atoms. *Phys. Rev. A*, 53:1014, 1996.

[42] D. Rio Fernandes, F. Sievers, N. Kretzschmar, S. Wu, C. Salomon, and F. Chevy. Sub–Doppler laser cooling of fermionic ^{40}K atoms in three-dimensional gray optical molasses. *Europhys. Lett.*, 100:63001, 2012.

[43] A. T. Grier, I. Ferrier-Barbut, B. S. Rem, M. Delehaye, L. Khaykovich, F. Chevy, and C. Salomon. Λ–enhanced sub–Doppler cooling of lithium atoms in D_1 gray molasses. *Phys. Rev. A*, 87:063411, 2013.

[44] G. Colzi, G. Durastante, E. Fava, S. Serafini, G. Lamporesi, and G. Ferrari. Sub–Doppler cooling of sodium atoms in gray molasses. *Phys. Rev. A*, 93:023421, 2016.

[45] S. Rosi, A. Burchianti, S. Conclave, D. S. Naik, G. Roati C. Fort, and F. Minardi. Λ–enhanced grey molasses on the D_2 transition of Rubidium–87 atoms. *Sci. Rep.*, 8:1301, 2018.

[46] S. Bernon. Trapping and nondemolition measurement of cold atoms in a high–finesse ring cavity. *PhD thesis, Ecole Polytechnique*, 2011.

[47] P. D. Lett, W. D. Phillips, S. L. Rolston, C. E. Tanner, R. N. Watts, and C. I. Westbrook. Optical molasses. *J. Opt. Soc. Am. B*, 6:2084, 1989.

[48] C. S. Adams and E. Riis. Laser cooling and manipulation of neutral particles. *The New Optics*, 1997.

[49] A. Bertoldi, S. Bernon, T. Vanderbruggen, A. Landragin, and P Bouyer. In situ characterization of an optical cavity using atomich light shifts. *Opt. Lett.*, 35:3769, 2010.

[50] D. S. Weiss, E. Riis, Y. Shevy, P. J. Ungar, and S. Chu. Optical molasses and multilevel atoms: experiment. *J. Opt. Soc. Am. B*, 6:2072, 1989.

[51] D. S. Naik, G. Kuyumjyan, D. Pandey, P. Bouyer, and A. Bertoldi. Bose–Einstein condensate array in a malleable optical trap formed in a traveling wave cavity. *Quantum Sci. Technol.*, 3:045009, 2018.

[52] T. Vanderbruggen. Détection non–destructive pour l'interférométrie atomique et condensation de Bose–Einstein dans une cavité optique de haute finesse. *PhD thesis, Paris–Sud University*, 2012.

[53] A. E. Siegman. Lasers. *University Science Books*, 1986.

[54] S. Bernon, T. Vanderbruggen, R. Kohlhaas, A. Bertoldi, A. Landragin, and P. Bouyer. Heterodyne non–demolition measurements on cold atomic samples: towards the preparation of non–classical states for atom interferometry. *New J. Phys.*, 13:065021, 2011.

[55] S. Chu, J. E. Bjorkholm, A. Ashkin, and A. Cable. Experimental observation of optically trapped atoms. *Phys. Rev. Lett.*, 57:314, 1986.

[56] C. Cohen-Tannoudji and S. Reynaud. Dressed-atom description of resonance fluorescence and absorption spectra of a multi-level atom in an intense laser beam. *J. Phys. B: At. Mol. Phys.*, 10:345, 1977.

[57] R. Grimm, Weideüller, and Y.B. Ovchinnikov. Dipole traps for neutral atoms. *Adv. in At. Mol. Opt. Phys.*, 42:95, 2000.

[58] D. A. Steck. Rubidium 87 D line data. *Available online at http://steck.us/alkalidata (revision 2.1.5)*, 2015.

[59] R. W. P. Drever, J. L. Hall, F. V. Kowalski, J. Hough, G. M. Ford, A. J. Munley, and H. Ward. Laser phase and frequency stabilization using an optical resonator. *Appl. Phys. B*, 31:97, 1983.

[60] K. B. Davis, M. O. Mewes, M. A. Joffe, M. R. Andrews, and W. Ketterle. Evaporative cooling of sodium atoms. *Phys. Rev. Lett.*, 74:5202, 1995.

[61] W. Ketterle and N.J. VanDruten. Evaporative cooling of trapped atoms. *Adv. in At. Mol. Opt. Phys.*, 37:181, 1996.

[62] M. D. Barrett, J. A. Sauer, and M. S. Chapman. All-optical formation of an atomic Bose-Einstein condensate. *Phys. Rev. Lett.*, 87:010404, 2001.

[63] M. Inguscio, S. Stringari, and C.E. Wieman. Proceedings of the international school of physics, Enrico Fermi course. *IOS Press*, 1999.

[64] G. Rempe, R. J. Thompson, H. J. Kimble, and R. Lalezari. Measurement of ultralow losses in an optical interferometer. *Opt. Lett.*, 17:363, 1992.

[65] A. Ashkin, G. Boyd, and J. Dziedzic. Resonant optical second harmonic generation and mixing. *J. Quantum Electron.*, 2:109, 1966.

[66] J. A. Giordmaine and Robert C. Miller. Tunable coherent parametric oscillation in $LiNbO_3$ at optical frequencies. *Phys. Rev. Lett.*, 14:973, 1965.

[67] J. Ye, D. W. Vernooy, and H. J. Kimble. Trapping of single atoms in cavity QED. *Phys. Rev. Lett.*, 83:4987, 1999.

[68] P. Maunz, T. Puppe, I. Schuster, N. Syassen, P. W. H. Pinkse, and G. Rempe. Cavity cooling of a single atom. *Nature*, 428:50, 2004.

[69] J. Lee, G. Vrijsen, I. Teper, O. Hosten, and M. A. Kasevich. Many-atom cavity QED system with homogeneous atom–cavity coupling. *Opt. Lett.*, 39:4005, 2014.

[70] E. T. Jaynes and F.W. Cummings. Comparison of quantum and semiclassical radiation theories with application to the beam maser. *Proc. of the IEEE*, 51:89, 1963.

[71] G. Rempe, H. Walther, and N. Klein. Observation of quantum collapse and revival in a one–atom maser. *Phys. Rev. Lett.*, 58:353, 1987.

[72] C. C. Gerry and P. L. Night. Introductory quantum optics. *Cambridge University Press*, 2005.

[73] R. J. Thompson, G. Rempe, and H. J. Kimble. Observation of normal-mode splitting for an atom in an optical cavity. *Phys. Rev. Lett.*, 68:1132, 1992.

[74] M. Brune, F. Schmidt-Kaler, A. Maali, J. Dreyer, E. Hagley, J. M. Raimond, and S. Haroche. Quantum Rabi oscillation: a direct test of field quantization in a cavity. *Phys. Rev. Lett.*, 76:1800, 1996.

[75] O. Hosten, N. J. Engelsen, R. Krishnakumar, and M. A. Kasevich. Measurement noise 100 times lower than the quantum–projection limit using entangled atoms. *Nature*, 529:505, 2016.

[76] M. Tavis and F.W. Cummings. Approximate solutions for an N–molecule–radiation–field Hamiltonian. *Phys. Rev.*, 188:692, 1969.

[77] G. S. Agarwal. Vacuum–field rabi splittings in microwave absorption by rydberg atoms in a cavity. *Phys. Rev. Lett.*, 53:1732, 1984.

[78] M. G. Raizen, R. J. Thompson, R. J. Brecha, H. J. Kimble, and H. J. Carmichael. Normal–mode splitting and linewidth averaging for two–state atoms in an optical cavity. *Phys. Rev. Lett.*, 63:240, 1989.

[79] H. J. Kimble. Strong interactions of single atoms and photons in cavity QED. *Phys. Scr.*, T76:127, 1998.

[80] J. Klinner, M. Lindholdt, B. Nagorny, and A. Hemmerich. Normal mode splitting and mechanical effects of an optical lattice in a ring cavity. *Phys. Rev. Lett.*, 96:023002, 2006.

[81] H. Ritsch, P. Domokos, F. Brennecke, and T. Esslinger. Cold atoms in cavity-generated dynamical optical potentials. *Rev. Mod. Phys.*, 85:553, 2013.

[82] H. Tanji-Suzuki, I. D.Leroux, M. H. Schleier-Smith, M. Cetina, A. T. Grier J. Simon, and V. Vuletić. Interaction between atomic ensembles and optical resonators: Classical description. *Adv. in At. Mol. Opt. Phys.*, 60:201, 2011.

[83] P. J. Martin, B. G. Oldaker, A. H. Miklich, and D. E. Pritchard. Bragg scattering of atoms from a standing light wave. *Phys. Rev. Lett.*, 60:515, 1988.

[84] G. Vrijsen, O. Hosten, J. Lee, S. Bernon, and M. A. Kasevich. Raman lasing with a cold atom gain medium in a high–finesse optical cavity. *Phys. Rev. Lett.*, 107:063904, 2011.

[85] Y. F. Hsiao, Y. J. Lin, and Y. C. Chen. Λ-enhanced gray-molasses cooling of cesium atoms on the D_2 line. *Phys. Rev. A*, 98:033419, 2018.

[86] B. Lounis and C. Cohen-Tannoudji. Coherent population trapping and Fano profiles. *J. Phys. II France*, 2:579, 1992.

[87] J. F. Clément. Réalisation d'un condensat de Bose–Einstein dans un piège dipolaire optique à 1565 nm. *PhD thesis, Paris–Sud University*, 2008.

[88] W. Ketterle, K. B. Davisand, M. A. Joffe, A. Martin, and D. E. Pritchard. High densities of cold atoms in a dark spontaneous–force optical trap. *Phys. Rev. Lett.*, 70:2253, 1993.

[89] L.H. Enloe and J.L. Rodda. Laser phase–locked loop. *Proc. of the IEEE*, 53:165, 1963.

[90] D. Finkelstein-Shapiro, S. Felicetti, T. Hansen, T. Pullerits, and A. Keller. Classification of dark states in multilevel dissipative systems. *Phys. Rev. A*, 99:053829, 2019.

[91] D. V. Kosachiov, B. G. Matisov, and Y. V. Rozhdestvensky. Coherent phenomena in multilevel systems with closed interaction contour. *J. Phys. B: At. Mol. Opt. Phys.*, 25: 2473, 1992.

[92] G. Condon, M. Rabault, B. Barrett, L. Chichet, R. Arguel, H. Eneriz-Imaz, D. Naik, A. Bertoldi, B. Battelier, P. Bouyer, and A. Landragin. All-optical Bose-Einstein condensates in microgravity. *Phys. Rev. Lett.*, 123:240402, 2019.

[93] H. W. Chan, A. T. Black, and V. Vuletić. Observation of collective–emission–induced cooling of atoms in an optical cavity. *Phys. Rev. Lett.*, 90:063003, 2003.

[94] D. J. Wineland, J. J. Bollinger, W. M. Itano, and D. J. Heinzen. Squeezed atomic states and projection noise in spectroscopy. *Phys. Rev. A*, 50:67, 1994.

[95] C. Gross, T. Zibold, E. Nicklas, J. Estève, and M. K. Oberthaler. Nonlinear atom interferometer surpasses classical precision limit. *Nature*, 464:1165, 2010.

[96] The LIGO Scientific Collaboration. A gravitational wave observatory operating beyond the quantum shot-noise limit. *Nature Physics*, 7:962, 2011.

[97] L. De Marco, G. Valtolina, K. Matsuda, W. G. Tobias, J. P. Covey, and J. Ye. A degenerate fermi gas of polar molecules. *Science*, 363:853, 2019.

[98] D. Becker et al. Space-borne Bose-Einstein condensation for precision interferometry. *Nature*, 562:391, 2018.

[99] J.Hu, A. Urvoy, Z. Vendeiro, V. Crépel, W. Chen, and V. Vuletić. Creation of a Bose-condensed gas of ^{87}Rb by laser cooling. *Science*, 358:1078, 2017.

[100] A. Urvoy, Z. Vendeiro, J. Ramette, A. Adiyatullin, and V. Vuletić. Direct laser cooling to Bose-Einstein condensation in a dipole trap. *Phys. Rev. Lett.*, 122:203202, 2019.

[101] A. Bertoldi, C.H. Feng, H. Eneriz, M. Carey, D. S. Naik, J. Junca, X. Zou, D. O. Sabulsky, B. Canuel, P. Bouyer, and M. Prevedelli. A control hardware based on a field programmable gate array for experiments in atomic physics. *Rev. of Sci. Ins.*, 91:033203, 2020.

[102] H. A. Enge. Introduction to nuclear physics. *Addison Wesley*, 1966.

[103] J. R. P. Angel and P. G. H. Sandars. The hyperfine structure Stark effect. *Proc. Roy. Soc. A*, 305:125, 1968.

[104] B. Arora, M. S. Safronova, and C. W. Clark. Magic wavelengths for the np–ns transitions in alkali–metal atoms. *Phys. Rev. A*, 76:052509, 2007.

[105] R. W. Schmieder. Matrix elements of the quadratic Stark effect on atoms with hyperfine structure. *Am. J. Phys.*, 40:297, 1972.

[106] R. P. Andresen. 5spice Analysis Software. *Available online at http://www.5spice.com (version 1.67)*, 2012.